Lawrence Berkeley Laboratory
UNIVERSITY OF CALIFORNIA

CHEMICAL SCIENCES DIVISION

Study of Clusters Using Negative Ion Photodetachment Spectroscopy

Y. Zhao
(Ph.D. Thesis)

December 1995

DISCLAIMER

Study of Clusters Using Negative Ion Photodetachment Spectroscopy

Yuexing Zhao
Ph.D. Thesis

Department of Chemistry
University of California

and

Chemical Sciences Division
Lawrence Berkeley Laboratory
University of California
Berkeley, California 94720

December 1995

Study of Clusters Using Negative Ion Photodetachment Spectroscopy
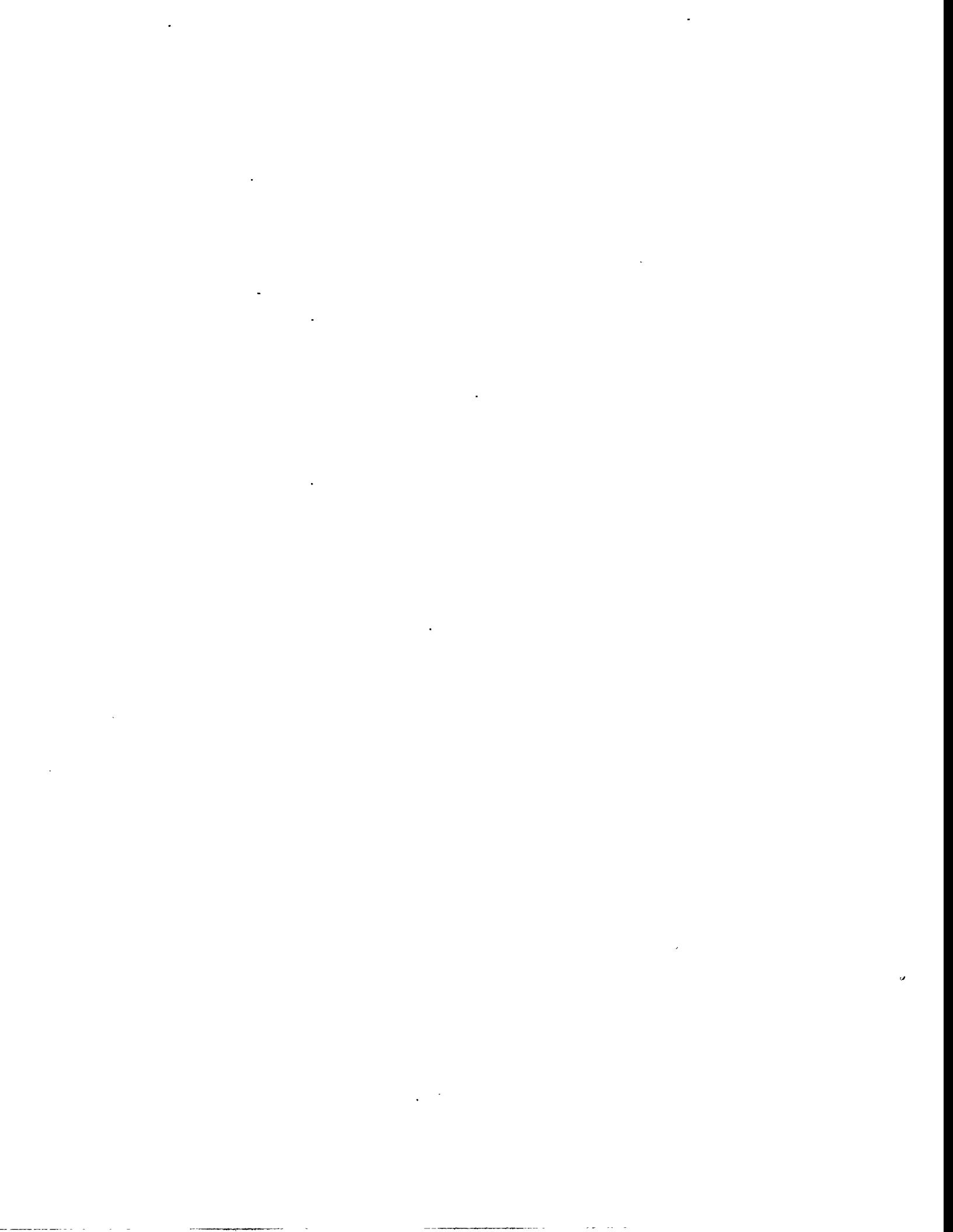
by Yuexing Zhao

Abstract

Study of Clusters Using Negative Ion Photodetachment Spectroscopy

by

Yuexing Zhao

Doctor of Philosophy in Chemistry

University of California, Berkeley

Professor Daniel M. Neumark, Chair

The weak van der Waals interaction between an open-shell halogen atom and a closed-shell atom or molecule has been investigated using zero electron kinetic energy (ZEKE) spectroscopy. This technique is also applied to study the low-lying electronic states in GaAs and GaAs$^-$. In addition, the spectroscopy and electron detachment dynamics of several small carbon cluster anions are studied using resonant multiphoton detachment spectroscopy.

ZEKE spectroscopy is a photodetachment technique well suited for small cluster study, as it combines mass selection with good spectroscopic resolution (2-3 cm^{-1}). The vibrational structures of the weak van der Waals bonds I—CO_2, Rg—X (Ar-Br, Ar-I, and Kr-I) are well resolved in the ZEKE spectra of the corresponding anions. Potential energy curves are constructed from the observed vibrational structures for the open-shell — closed-shell interaction in the neutrals and the closed-shell — closed-shell interaction in the anions. Photodetachment of I$^-$$CO_2$ is found to yield the T-shaped I•CO_2 neutral.

Several low-lying triplet and singlet electronic states of GaAs are observed in the ZEKE spectrum of GaAs$^-$. Transitions from two anion electronic states are seen, and the $^2\Sigma^+$ state is found to be the ground state. This simple diatomic has rather complex electronic structure; ZEKE spectroscopy provides the relative term energies and vibrational frequencies of the low-lying electronic states.

The $^2\Pi \leftarrow X^2\Pi$ electronic transitions of the small carbon cluster anions, C_4^-, C_6^-, C_8^-, are studied using resonant multiphoton detachment spectroscopy. Vibrationally resolved spectra are observed in the one-color experiments, providing spectroscopic information on the $^2\Pi$ and $X^2\Pi$ electronic states. In the case of C_4^-, a rotationally resolved spectrum is obtained in a 2-color resonant 2-photon detachment experiment, resulting in accurately determined molecular constants for the $C^2\Pi_u$ and $X^2\Pi_g$ electronic states of C_4^-. The electron detachment dynamics of the multiphoton process is also investigated. The measured electron kinetic energy distributions, in the cases of C_4^- and C_6^-, show characteristics of thermionic emission. In the cases of C_6^- and C_8^-, delayed electron emission is observed following photon absorption. It is concluded that resonant multiphoton detachment occurs via thermionic emission following photon absorption, fast internal conversion and energy randomization.

Out m

2

Dedicated to my parents (Zhao Jinrui and Xu xiulian)

and sister Caizhu

Table of Contents

Chapter 3. Study of the ArBr⁻, ArI⁻, KrI⁻ anions and the corresponding neutral van der Waals complexes by anion zero electron kinetic energy spectroscopy

Chapter 4. Study of the low-lying electronic states of GaAs and GaAs⁻ using negative ion photodetachment spectroscopy. 112

Chapter 5. Rotationally resolved spectrum of the $C^2\Pi_u \leftarrow X^2\Pi_g$ electronic

transition of C_4^- via resonant 2-photon detachment spectroscopy

Chapter 6. Spectroscopy and electron detachment dynamics of small carbon cluster anions (C_4^-, C_6^-, C_8^-).

      A. Assignment of resonant multiphoton detachment spectra of C_6^-

Acknowledgments

I feel very fortunate to have been able to work in Professor Daniel M. Neumark's research group. Dan has always come up with great ideas about the experiments and data analysis, and his scientific motivation and enthusiasm have had a very positive effect on his graduate students including myself. His guidance and support over the last several years have played an essential part in completing the work described in this dissertation. Having come from a different cultural background, where I was more used to doing things as instructed, I had some difficulty in taking strong personal initiative towards achieving results and solving problems. Working in Dan's lab has certainly helped me a great deal on that aspect, which I am sure will benefit me greatly in my future career.

Thanks also go to many of my wonderful co-workers. Dr. Caroline Arnold taught me how to run the ZEKE experiment. Her efficiency and scientific drive have provided as an exemplary model for me. Ivan Yourshaw joined the ZEKE project two years after me, and he quickly acquired a thorough understanding of the experiment. The experience of working with Ivan has been really rewarding and productive. I wish the best of luck to him and Mike Furlanetto, who recently joined our project, in implementing the stimulated Raman pumping technique. Dr. Georg Reiser, probably the only person who has worked on both the anion and neutral ZEKE experiments, and Dr. Esther de Beer brought fresh scientific approaches to the project as postdocs. Most of the experiments described in this dissertation were done on the ZEKE apparatus which were originally built by Dr. Theo Kitsopoulos and his co-workers.

There are other group members that deserve mention. Dave Osborn deserves a lot of credit for managing the workstations. Dr. Don Arnold and Dr. Steve Bradforth helped me get started with analyzing data on the UNIX computers. Cangshan Xu, my fellow country man, helped a lot on matters related to PC's. In the Berkeley Chinese student and scholar community, he actually is better known as *The PC Doctor*. Eun Ha Kim joined the group the same time that I did, and it has been a pleasure to work with her. It is quite exciting to watch Jeff Greenblatt and Marty Zanni build the femtosecond photoelectron spectrometer and make it work. Several people who recently joined the group, Travis Taylor, Hyeon Choi, Dr. David Mordaunt, and Ryan Bise, brought fresh new look to our research group. It has been really fun to work with them.

Additional thanks go to my preliminary exam committee: Prof. Paul Alivisatos, Prof. Roger Falcone, Prof. Bill Lester, and Prof. Herb Strauss; — the exam was a good learning experience.

Before I came to Berkeley, I spent more than a year as a graduate student in Professor Gao Zi's lab at Fudan University. Although my research project was interrupted by the famous 1989 Chinese student democracy movement, the experience I gained in her research program was invaluable.

Outside the school environment, many friends have played a significant role in forming my Berkeley experience. During my first two years in Berkeley, housemates Scott and Eric were of great help in improving my spoken English and my understanding of American culture. Like themselves, I now have opinions on many important issues, and at the same time, try to be open-minded about the different values. Bing, Wei, George,

Shigeru, and many other fellow Berkeley Chinese students shared with me similar interests, background, and experience as foreign students, and at times, provided support to each other. My most special thanks go to Lisa. Over the last year and half, Lisa has made a real difference in my life. I thank her for her love, care, and support. Although she does not think she was a big help to my research, she has certainly made everything I do more worthwhile; and I still cannot say she is wrong on "C_6 is linear 80% of time, and cyclic 20% of time". Every time I look at it, C_6 is linear. I would also like to thank Lisa's parents, grandparents, and Joyce for their hospitality and many terrific dinners.

Finally, I would like to thank my family. Given the standard of living in rural China, in order to support me and my sister Caijiao throughout the school years, my parents and sister Caizhu worked extremely hard and made tremendous sacrifices over the years; — and for this very reason, I dedicate this thesis to them.

Chapter 1. Introduction

The following chapters describe experimental studies of several small clusters, both weakly bound van der Waals clusters and strongly bound carbon clusters and the GaAs binary complex. Two different negative ion photodetachment spectroscopy methods are used to study these species. Chapters 2-4 describe the study of I•CO_2 , Rg-X (rare gas halogen), and GaAs using negative ion zero electron kinetic energy (ZEKE) spectroscopy; chapters 5-6 describe the study of small carbon cluster anions using resonant multiphoton detachment spectroscopy.

Experimentally, one of the most difficult aspects of cluster study has been the ambiguity regarding species identity. Most cluster sources simultaneously generate a distribution of cluster sizes; for the neutral species, it is not possible to separate out the species of interest prior to spectroscopic investigation. This difficulty is resolved if one starts out from making negative ions. Negative ions can be mass-selected, thereby eliminating any ambiguity regarding species identity. Moreover, many neutral clusters, in particular, neutral clusters with open-shell electronic structures, have electron affinities between 2-4 eV; therefore the corresponding anions can be photodetached using UV-visible lasers. Photoelectron spectroscopy of negative ions, including ZEKE spectroscopy, provides valuable spectroscopic information on the low-lying electronic

states and vibrational structures of the neutral species. In the case when the negative ion has an allowed electronic transition below detachment threshold, resonant multiphoton detachment spectroscopy can be applied to obtain detailed spectroscopic information of the negative ion.

This chapter focuses on the principles of ZEKE spectroscopy and resonant multiphoton detachment spectroscopy and their application toward cluster study. The experimental techniques will also be briefly discussed. Fixed-frequency anion photoelectron spectroscopy (PES) is the most commonly used negative ion photodetachment approach to cluster study, and it is closely relevant to the ZEKE technique. Therefore, the PES approach will be discussed first.

I. Principles of anion photoelectron spectroscopy and ZEKE spectroscopy

The fixed-frequency anion photoelectron spectroscopy (PES) and the ZEKE spectroscopy both start with the generation of an internally cold, mass-selected negative ion beam, but they differ in photodetachment and electron detection schemes. The ZEKE approach affords significantly better spectroscopic resolution than the PES. However, compared to the fixed-frequency PES, more restrictive propensity rules apply to the ZEKE technique; moreover, for a given negative ion, typically it takes much less time to obtain the fixed frequency photoelectron spectrum than the ZEKE spectrum.

A. PES

Anion photoelectron spectroscopy involves the measurement of kinetic energies of photoelectrons ejected by a laser beam in order to determine the electron affinity EA, intensities and angular distributions of these electrons and to use this information as a probe to elucidate the electronic and vibrational structure of the neutral and anion. Figure 1.1 shows a schematic of the energetics involved in this technique. The photoelectron kinetic energies (eKE) are given by

$$eKE = h\upsilon - EA - (T_e' + E_{v'}^0) + (T_e'' + E_{v''}^0), \qquad \text{Eq. (1.1)}$$

where $h\upsilon$ is the photon energy, EA is the adiabatic electron energy of the neutral, T_e' and T_e'' are the term energies of neutral and anion electronic states, respectively, and $E_{v'}^0$ and $E_{v''}^0$ are the vibrational energies with respect to the zero point energies of the neutral and anion states, respectively. Because energy levels in the neutral and anion are quantized, the photoelectron spectrum, i.e., the electron intensities *vs.* eKE, shows the peaks that correspond to transitions between the anion and neutral states.

Compared to an optical transition, the electronic selection rules for photodetachment are much less restrictive.[1,2] All transitions involving ejection of an electron from a single molecular orbital of the anion are allowed; transitions involving ejection and/or excitation of more than one electron are only allowed through configuration interaction. A simple argument based on the use of a one-electron dipole operator has been provided by Rabalais.[1] The electronic transition dipole moment, d_e is given by,

3

$$d_e \propto \left| \left\langle \phi'' \middle| r_e \middle| \phi_e \right\rangle \right|^2 , \qquad \text{Eq. (1.2)}$$

where ϕ'' is the wavefunction of the anion molecular orbital from which the electron is detached, r_e is the one-electron dipole operator, and ϕ_e is wavefunction of the free electron. A transition is allowed if the product of the irreducible representations Γ of the species in Eq. (1.2), $\Gamma(\phi'') \times \Gamma(r_e) \times \Gamma(\phi_e)$, is totally symmetric with respect to all symmetry elements of the molecular point group for at least one component of r_e, i.e., $x, y,$ or z. Since the orbital angular momentum of the detached electron is unrestricted in the photoelectron spectrum, the irreducible representations of $\Gamma(\phi'') \times \Gamma(r_e) \times \Gamma(\phi_e)$ always contain a totally symmetric component. The spin selection rules for photodetachment are straightforward. For instance, if the anion ground state is a singlet electronic state, the neutral state has to be a doublet electronic state.

The less restrictive electronic selection rules of photoelectron spectroscopy make it possible to observe transitions to the electronic states that are forbidden in direct absorption or emission experiments (*a.k.a.* dark states).

In the photoelectron spectrum, the peak positions are determined by Eq. (1.1); the peak intensities, within the Franck-Condon approximation, are proportional to the Franck-Condon factors,

$$Intensity \propto \left| \left\langle v'' \middle| v' \right\rangle \right|^2 , \qquad \text{Eq. (1.3)}$$

where $\langle v''|$ and $|v'\rangle$ are the vibrational wave functions of the anion and neutral states, respectively. In order to have non-zero Franck-Condon factors, the product of the anion and neutral vibrational wavefunctions in Eq. (1.3) has to include the totally symmetric

4

representation of the point group to which the anion and neutral belong. If the anion is initially in the ground state, then only those transitions to the neutral vibrational states of totally symmetric modes and those of double-quanta excitations of the asymmetric modes are symmetry-allowed. If the anion and neutral belong to the same point group, then typically only transitions to the vibrational states of totally symmetric modes are observed in the photoelectron spectrum. Based on the Franck-Condon simulation of the peak intensities in the photoelectron spectrum, the displacement of the anion wave function along the appropriate neutral coordinate can be obtained. In some cases, including all diatomic species, the displacements obtained in this manner can be transformed into actual bond distance and, for polyatomic molecules, bond angle differences between the anion and neutral geometries.

Peak widths in the photoelectron spectrum are determined by either experimental resolution, unresolved underlying structures, or the lifetime of the neutral sates. The energy resolution of the electron time-of-flight analyzer in the spectrometer used in the studies presented in this work is 8 meV at 0.65 eV eKE and degrades as $(eKE)^{3/2}$ at higher eKE's. Although this resolution is typically sufficient to resolve the electronic structures and vibrational progressions of large frequencies, it is insufficient to discern vibrational structures in the low-frequency modes, such as those in the weakly bound van der Waals clusters. The ZEKE technique, on the other hand, offers considerably higher resolution due to its different electron detection scheme.

B. ZEKE

The energetics involved in this technique are illustrated in Figure 1.2. Mass-selected negative ions are photodetached with a tunable pulsed dye laser beam rather than a fixed-frequency laser, and only those photoelectrons with nearly zero electron kinetic energy are detected. The method of selectively detecting low kinetic energy electrons is similar to the techniques developed by Müller-Dethlefs *et al.*[3] for threshold photoionization of neutrals.

Separation of energetic electrons from the ZEKE electrons is achieved by a delayed detection scheme coupled with spatial and temporal filtering, the details of which will be given later. The energy resolution of the negative ion ZEKE technique is 2 to 3 cm^{-1}, which is mainly limited by space charge effects.

In a ZEKE experiment, one scans the wavelength of the dye laser and collect the ZEKE electron signal; peaks are observed when the photon energy is resonant with the energy difference between the neutral and anion states. Although the ZEKE detection scheme is very different from the PES, the same principles of photoelectron spectroscopy apply. For example, the peak intensities in a ZEKE spectrum will also be determined by the Franck-Condon factors, or Eq. (1.3).

However, not all the electronic transitions that are observed in a PES spectrum can be observed in the ZEKE spectrum. The ability to acquire ZEKE spectra is contingent on the photodetachment cross section near threshold. The Wigner threshold law[4] gives that near threshold, the photodetachment cross section for an atomic anion goes as

$$\sigma \propto \sigma_0 \left(E_{h\upsilon} - E_{threshold} \right)^{l+1/2},$$ Eq. (1.4)

where $E_{h\upsilon}$ - $E_{threshold}$ is the difference between an anion and neutral level, and l is the orbital angular momentum of the detached electron. For $l=0$ (s-wave detachment), the cross section rises sharply above threshold, but for $l \geq 1$ (p, d, ... -wave detachment), the cross section is very small near threshold. Therefore, the ZEKE technique is insensitive to transitions other than those involving s-wave detachment.

For an atomic system, it is easy to determine which anions will photodetach via s-wave. For linearly polarized light, removal of an electron from a p-orbital results in s-wave detachment ($l=0$). For molecular anions, Getlman et al.[5] and Reed et al.[6] extended the threshold law to diatomic and polyatomic anions with the end result that anion molecular orbitals that transform as x, y, or z in the molecular point group can yield s-wave photoelectrons. In fact, these results can be easily obtained from Eq. (1.2). For s-wave detachment, $\Gamma(\phi_e)$ is always totally symmetric. In order to make the product, $\Gamma(\phi'')\times\Gamma(r_e)\times\Gamma(\phi_e)$, totally symmetric, under the restriction of s-wave detachment, $\Gamma(\phi'')$ has to be the same as at least one of $\Gamma(r_e)$.

For homonuclear diatomic species, such as Si_2^- and Ge_2^-, the π_u and σ_u orbitals transform as (x,y) and z, respectively, therefore, only photodetachment from these two types of molecular orbitals are active in the ZEKE technique. Transitions involving removal of an electron from the π_g and σ_g orbitals can not be observed in ZEKE spectra. On the other hand, for a heteronuclear diatomic species, such as $GaAs^-$, g/u symmetry does not apply, so all transitions involving removal of an electron from a π or σ orbital are

7

active in the ZEKE technique. Experimental results on photodetachment of $GaAs^-$, when compared to our previous work on Si_2^- and Ge_2^-, are consistent with this analysis.

II. Applications of negative ion ZEKE spectroscopy toward cluster study

The combination of mass-selection and good spectroscopic resolution makes ZEKE spectroscopy particularly advantageous in studying the spectroscopy and structures of clusters. In the past, ZEKE spectroscopy has been used to study a series of small carbon and silicon clusters and group III-V semiconductors.[7] ZEKE spectroscopy has also been used to study the transition state of the I + HI reaction by photodetaching the stable anion precursor IHI^-.[8] Here we provide a few more examples of how negative ion ZEKE spectroscopy can be applied to study very different clusters.

A. Weakly bound clusters

The study of weakly bound clusters, including van der Waals clusters, is of fundamental interest and has been studied extensively in recent years.[9] The vibrational frequency of a typical van der Waals bond is on the order of a few tens of wavenumbers. Fixed-frequency PES does not have sufficient energy resolution to resolve the vibrational structure; ZEKE spectroscopy, on the other hand, is ideally suited to study the vibrational

structure of the weakly bound clusters provided that the neutral cluster has positive electron affinity. The closed shell - closed shell interaction, such as that in the rare gas - rare gas (Rg-Rg) clusters, has been extensively studied using various experimental techniques.[10] However, the open shell - closed shell interaction, especially the interaction between an open shell atom and a closed shell species, is not as well characterized. ZEKE spectroscopy provides a means of studying this type of interaction with vibrational resolution. From a practical standpoint of view, the open shell - closed shell van der Waals clusters typically have positive electron affinities because their corresponding anions have closed shell structures and are more stable than the neutrals.

Chapter 2 gives the detailed descriptions and analysis of the ZEKE spectra of I^- CO_2. Vibrational frequencies of the I — CO_2 bond stretch are determined for the anion and neutral. The $\angle OCO$ angle is found to change upon photodetachment. In chapter 3, the information obtained from the ZEKE spectra of several rare gas halides, along with the results from scattering experiments,[11] is used to construct the potential energy curves of the neutral and anion species.

B. Strongly bound clusters

ZEKE spectroscopy provides a powerful probe of the electronically complex small semiconductor clusters. Chapter 4 describes the PES and ZEKE spectra of $GaAs^-$. PES and ZEKE spectra provide complementary information that allows characterization of the low-lying electronic states in the neutral and anion. This work is a continuation of our

9

earlier work on similar systems, such as Ge_2^-/Ge_2 and Si_2^-/Si_2.[7] Just as other studies on small semiconductor clusters, high level *ab initio* calculations done by others[12] are an essential tool in assigning our spectra.

III. Application of resonant multiphoton detachment spectroscopy toward the study of carbon cluster anions

Ever since it came into being in the early 1970s, resonant multiphoton ionization spectroscopy has been widely used to study neutral and positive ion species.[13] The analogous technique, resonant multiphoton detachment spectroscopy of negative ions, has been applied, for example, to study the B←X electronic transition of C_2^-.[14] However, compared to resonant multiphoton ionization studies, the application of this technique toward negative ion study has been much less common; this is largely due to the fact that many negative ions do not have an allowed electronic transition below the detachment threshold.

In a resonant 2-photon detachment process, in the simplest case, the first photon excites the anion to an excited electronic state which lies below the neutral ground state, the second photon then photodetaches the excited anion. The first photon has to be resonant with the specific electronic transition, the second photon should have at least enough energy to photodetach the excited anion. This process is illustrated in Figure 1.3a. The two photons may have the same frequency (the one-color experiment), or different frequencies (the two-color experiment). A spectrum of the anion electronic transition can

10

be obtained by scanning the laser wavelength of the first photon while recording the electron signal intensity. Compared to absorption or emission spectroscopy, this technique offers better sensitivity because the electron detection efficiency can be very high.

The sensitivity of this technique is also much better than that of the ZEKE spectroscopy; in the resonant multiphoton detachment technique, all the photodetached electrons are collected, regardless of their kinetic energies. However, these two techniques are really quite different in many ways. First, from the ZEKE spectra, one learns about the neutral cluster and the anion ground state; from the resonant multiphoton detachment spectra, one mainly learns about the electronic transition of the anion. Second, in a resonant multiphoton detachment process, the first step is an optical transition; more restrictive electronic selection rules may apply.

The two steps in a resonant 2-photon detachment process may have very different cross sections. Typically, one would expect the first transition to have a larger cross section because it is an allowed optical transition. The cross section between two bound states is usually several orders of magnitude larger than that for photodetachment. Therefore, in the one-color scheme, in order to achieve sufficient detachment, the first transition may have to be saturated which leads to power-broadening in the spectrum. The power-broadening problem can be solved by using a two-color scheme in which the excitation laser photon density is significantly reduced and the detachment laser, which may have high intensity, detaches the excited anion.

Such a two-color detachment scheme is used to study the spectroscopy of C_4^- with rotational resolution. The results of this work are described in chapter 5.

Figure 1.3 illustrate different variations of the resonant 2-photon detachment mechanism of a negative ion. Figure 1.3a shows the direct 2-step detachment process. However, as shown in Figure 1.3b, the second photon may further excite the anion to an excited state that lies above the neutral ground state. Electron detachment then occurs via autodetachment. After absorbing the first photon, the excited state may relax to a different state or back to the ground state via internal conversion or radiative emission. Energy relaxation may also occur for the excited anion state above the detachment threshold. This situation is shown in Figure 1.3c. If energy randomization occurs faster than electron detachment, then a vibronically *hot* anion is created and electron detachment becomes a statistical process. The electron kinetic energy (eKE) distribution can be measured to discern the direct or statistical detachment mechanism.

Chapter 6 describes the results of a series of resonant multiphoton detachment experiments on C_4^-, C_6^-, and C_8^-, which reveal interesting information on the spectroscopy and electron detachment dynamics of these species.

IV. Experimental techniques

Since full descriptions of the ZEKE apparatus can be found in the dissertations of Theofanis Kitsopoulos[15] and Caroline Arnold,[7] previous students on this project, only a brief description of the apparatus and data collection will be given for introductory

purposes. In the following chapters, details of each experiment will accompany the data presentation and discussion.

A schematic diagram of the experimental apparatus is shown in Figure 1.4. The experiment begins with the formation of negative ions. In the experiments described in this dissertation, ions were formed using three different techniques: (1) electron dissociative attachment, (2) laser vaporization, and (3) pulsed discharge. The first of these, developed in the Lineberger laboratory,[16] generates ions at the intersection of a pulsed molecular beam and a 1 keV electron beam near the orifice of the pulsed valve through a variety of dissociative attachment and clustering processes. I^-CO_2 and $Rg-X^-$ ions were produced by this method. The second ion source is a Smalley-type cluster source where a rotating and translating rod is vaporized with a laser pulse and the resulting plasma, containing the negative ions, is entrained in the carrier gas pulse from the molecular beam valve. $GaAs^-$ was produced by this method. Although carbon cluster anions were produced with the second type of ion source in our earlier studies, the carbon cluster anions reported in this dissertation were produced with the third type of ion source, i.e., the discharge source. The discharge electrodes are attached to the face plate of the pulsed molecular beam valve, and a pulse of gas mix, such as acetylene in Ne, is discharged by an electric pulse of 600-800 V magnitude. The molecules are dissociated during the discharge and clusters form in subsequent clustering processes.

The next stage of the experiment separates the ion of interest from the other ions formed in the source region by time-of-flight mass spectrometry. A beam-modulated mass spectrometer[17] provides a mass resolution of $M/\Delta M \sim 250$.

After the ions have separated spatially according to their mass, they enter the detector region where they are selectively photodetached by a properly timed laser pulse. The laser beam comes from a dye laser pumped by a XeCl excimer laser. For the ZEKE technique, as shown in Figure 1.4, photodetachment takes place at the first pair of laser windows. The anions are detached in a field free region, between the first two of a series of metal plates which have apertures in the center; a gentle electric field (1-3 V/cm) is applied to the metal plates after a delay on the order of 200 to 600 ns. During the delay, energetic electrons scatter away from the neutrals and undetached anions, while the ZEKE electrons remain close to the neutrals and undetached anions. Those energetic electrons that are scattered sideways do not make through the apertures of the metal plates after extraction; those that are either forward-scattered or backward-scattered acquire different amount of kinetic energy during the pulsed extraction, and they separate our from the ZEKE electrons by time-of-flight. Discrimination against the energetic electrons is then achieved by gated integration of the ZEKE electron signal. The resolution of the ZEKE technique is 2 cm^{-1} for atomic systems.

For the resonant multiphoton detachment experiments, the ion - laser interaction takes place at the second pair of laser windows, directly underneath the dual multichannel plate electron detector. In the two-color experiments, the second laser beam comes from another dye laser pumped by a Nd:YAG laser. In these experiments, all the detached electrons are collected by perpendicularly extracting the produced electrons with a weak electric field. Electrons that reach the detector are collected using a gated detection scheme.

[1] J. W. Rabalais, *Principles of Ultraviolet Photoelectron Spectroscopy*, (Wiley, New York, 1977).

[2] J. Berkowitz, *Photoabsorption, Photoionization and Photoelectron Spectroscopy*, (Academic Press, New York, 1979).

[3] K. Müller-Dethlefs, M. Sander, and E. W. Schlag, Z. Naturforsch, **39a**, 1089 (1984); Chem. Phys. Lett. **12**, 291 (1984).

[4] E. P. Wigner, Phys. Rev. **73**, 1002 (1948).

[5] S. Geltman, Phys. Rev. **112**, 176 (1958); L. M. Branscomb, D. S. Burch, S. J. Smith, and S. Geltman, Phys. Rev. **111**, 504 (1958).

[6] K. J. Reed, A. H. Zimmerman, H. C. Anderson, and J. I. Brauman, J. Chem. Phys. **64**, 1368 (1976).

[7] C. C. Arnold, Ph. D. Thesis, University of California, Berkeley, (1994).

[8] I. M. Waller, T. N. Kitsopoulos, and D. M. Neumark, J. Phys. Chem. **94**, 2240 (1990).

[9] For example, G. C. Maitland, M. Rigby, E . B. Smith, and W . A. Wakeham, *Intermolecular Forces* (Oxford University, Oxford, 1981).

[10] R. A. Aziz, in *Inert Gases*, edited by M. L. Klein (Springer, Berlin, 1984), pp. 5-86.

[11] P. Casavecchia, G. He, R. K. Sparks, and Y. T. Lee, J. Chem. Phys. **75**, 710 (1981); **77**, 1878 (1982).

[12] K. Balasubramanian, J. Mol. Spec. **139**, 405 (1990).

[13] V. S. Letokhov, *Laser Photoionization Spectroscopy*, (Academic Press, Orlando, 1987) and the listed references.

[14] W. C. Lineberger and T. A. Patterson, Chem. Phys. Lett. **13**, 40 (1972).

[15] T. N. Kitsopoulos, Ph. D. Thesis, University of California, Berkeley, (1991).

[16] M. A. Johnson, M. L. Alexander, and W. C. Lineberger, Chem. Phys. Lett. **122**, 285 (1984).

[17] J. M. Bakker, J. Phys. E **6**, 785 (1973); J. Phys. E **7**, 364 (1974).

Anion Photoelectron Spectroscopy

$$M^- + h\upsilon \rightarrow M + e^-$$

Figure 1.1

Anion ZEKE Spectroscopy

$$M^- + h\upsilon \rightarrow M + e^-$$

Figure 1.2

Resonant Two-Photon Detachment Mechanisms

Figure 1.3

Negative Ion ZEKE Spectrometer

Figure 1.4

Chapter 2. Study of the I•CO$_2$ van der Waals Complex by Threshold Photodetachment Spectroscopy of I⁻CO$_2$

Abstract

Photodetachment of the I⁻CO$_2$ anion accesses the three lowest-lying electronic states of the I•CO$_2$ van der Waals complex. High resolution threshold photodetachment (ZEKE) spectroscopy reveals progressions in the low frequency C-I van der Waals stretch in each electronic state, providing a detailed spectroscopic probe of the interaction between a halogen atom and a closed shell molecule. From our data, we construct one-dimensional potential energy functions for each neutral state as well as for the anion, and these are compared to rare gas-halogen and rare gas-halide potentials.

I. Introduction

The development of intermolecular potentials between weakly interacting species has received much attention in recent years. A host of spectroscopic and scattering-based experiments have been performed to probe these fundamental interactions. While the most commonly studied examples are the interactions between closed-shell atoms and molecules, the more complex potentials between open-shell and closed shell species are also of considerable interest. The simplest examples of these are rare gas-halides (Rg-X), which have been studied extensively because of their importance in excimer lasers. More complicated systems include the van der Waals complexes between rare gas atoms and molecular radicals, such as ArOH[1,2,3] and ArNO.[4] In this paper we present results for the I•CO_2 complex, which we study by high resolution photodetachment spectroscopy of the I⁻CO_2 anion. Since the I•CO_2 and Rg-X interactions have much in common, our experiment is best understood in the context of the somewhat simpler Rg-X systems.

In contrast to the isotropic interaction between two closed-shell atoms, the potential between a rare gas and halogen atom is complicated by spin-orbit and orientation effects due to the open-shell nature of the halogen atom.[5,6] These effects lead to the three electronic states shown in the correlation diagram, Figure 1. At infinite Rg-X separations, we have the two $^2P_{3/2}$ and $^2P_{1/2}$ spin-orbit levels of the halogen atom. As the separation decreases, the electrostatic interactions between the two atoms becomes increasingly important, resulting in a splitting of the $^2P_{3/2}$ level. The overall interaction is best described by Hund's case (c) coupling at large distances, where the spin-orbit interaction dominates, and by Hund's case (a) coupling at small

21

distances, where electrostatic effects are dominant. Typically, all three curves have shallow minima, and the determination of the well depths and locations is one of the prime targets of any investigation of Rg-X species. Haberland[5] and Aquilanti et al.[6] have shown that, if the spin-orbit interaction is independent of distance, then the potential energy curves associated with the three electronic-states are not independent; from two of the curves, the third may be calculated.

Previous experimental work on Rg-X systems include both scattering experiments and spectroscopic studies. Lee and co-workers[7] have extracted Rg-X potential energy curves in a series of differential cross section measurements, while Aquilanti et al.[8] have measured integral cross sections for several Rg-X pairs as a function of collision energy to obtain this information. As for spectroscopic studies, except for an absorption experiment by Smith and Kobrinsky,[9] all the gas phase experiments on Rg-X complexes have been implemented by using emission spectroscopy. Spontaneous emission spectra have been recorded by Ewing and Brau,[10] Thrush,[11] Tellinghuisen et al.,[12] and Casassa et al.[13] With the exception of several band systems in XeF and XeCl,[12,10] all of the observed spectra show only the diffuse structure characteristic of bound-free transitions. More structure has been observed in the emission[14,15,16] and predissociation[17] spectra of the series of heteronuclear cations HeNe$^+$, NeAr$^+$, etc. Each of these is isoelectronic to an Rg-X pair and has the same qualitative electronic structure, although the ground states of the ions are far more strongly bound than the corresponding Rg-X species. Rare gas diatomic cations have also been studied by photoionization and photoelectron spectroscopy[18,19,20] of the corresponding neutral van der Waals molecule.

The approach used in our laboratory to study the I•CO_2 complex is most akin to the last approach.[19,20] We perform high resolution threshold photodetachment (ZEKE) spectroscopy on ICO_2. This work is a continuation of our lower resolution photoelectron spectroscopy studies of I$(CO_2)_n$ clusters.[21] Photodetachment of ICO_2 accesses three neutral electronic states analogous to those shown in Figure 1, and the resolution of the spectra reported here is sufficient to resolve vibrational progressions due to the I-CO_2 van der Waals stretch for each electronic state. From this data we construct one-dimensional potential energy curves for the anion and the three neutral states. The previous photoelectron spectrum showed that the ICO_2 anion is bound by about 0.2 eV, and the neutral states are expected to be bound by considerably less. Hence, the situation is reversed from the rare gas diatom photoelectron spectra mentioned above, in which the cation resulting from photoionization is more strongly bound than the neutral van der Waals molecule.

II. Experimental

The high resolution threshold photodetachment spectrometer (also called a Zero Electron Kinetic Energy or ZEKE spectrometer) has been described in detail previously.[22] Briefly, an internally cold ICO_2 beam is generated by expanding a 2-4% mixture of HI in CO_2 gas (or the mixture of CO_2 and He gas) through a pulsed molecular beam valve, typically with a backing pressure of 60 psi, and then crossing the molecular beam with a 1 keV electron beam just outside the valve orifice. Negative ions are formed through dissociative attachment and clustering processes in the continuum flow region of the free-jet expansion and their internal

degrees of freedom are cooled as expansion progresses. We achieved a vibrational temperature of approximately 65 K in this case. The negative ions that pass through a 2 mm diameter skimmer are collinearly accelerated to 1 keV and mass-selected with a 1 meter long beam-modulated time-of-flight mass spectrometer.[23] The mass-selected ions then enter the detection region where they are photodetached by an excimer-pumped dye laser. QUI and Rhodamine 590 laser dyes were used and the latter was doubled with a BBO crystal.

Only those electrons produced with nearly zero kinetic energy are detected by using a detection scheme based on the design of Muller-Dethlefs et $al.$[24] for ZEKE photoionization of neutral species. First, a delay of 120-200 ns subsequent to photodetachment allows the more energetic electrons and the threshold electrons to separate. A weak field (~ 5 V/cm) is then applied collinearly to extract the photoelectrons. Finally ZEKE electrons are selectively detected by using a combination of spatial and temporal filtering. The ultimate resolution of the instrument is 0.3 meV. However, under the operating conditions used in these experiments the resolution was approximately 1.0 meV. The electron signal is normalized to laser power and the ion signal.

III. Results

A. Spectrum and general features

The threshold photodetachment spectrum of I^-CO_2 is shown in Figures 2a and 2b. The lower resolution (~ 80 cm^{-1}, dotted lines) photoelectron spectrum of Arnold et $al.$[21] is superimposed for comparison. Both spectra consist of two distinct bands separated

approximately by the $I(^2P)$ spin-orbit splitting (0.943 eV). We refer to these two bands as the $I(^2P_{3/2})\bullet CO_2$ band (Figure 2a) and, at higher energy, the $I(^2P_{1/2})\bullet CO_2$ band (Figure 2b). In the photoelectron spectrum, both bands consisted of a short progression of peaks spaced by 670 ± 50 cm^{-1}. This spacing is equal to the CO_2 bend frequency (667 cm^{-1}), and these peaks were assigned to progressions in the CO_2 bend in the neutral complex (the ν_2 mode) which arise because the CO_2 is slightly bent in the anion (175°) but linear in the neutral. The anion is expected to be have a C_{2v} structure with the I^- bound to the C atom, and we attributed the bent CO_2 moiety to a small amount of charge transfer from the I^- to the CO_2 LUMO.[21]   The threshold photodetachment spectra show considerably more structure. The $I(^2P_{3/2})\bullet CO_2$ band now consists of four sub-bands, labeled A, Ap, B, and Bp in Figure 2a. Bands Ap and B lie to the blue of band A by 225 cm^{-1} and 662 cm^{-1} (the CO_2 bend frequency), respectively, and band Bp lies about 225 cm^{-1} to the blue of band B. Each of these bands shows additional low frequency structure. In band A, we observe a progression with spacings starting at 37 cm^{-1} and gradually decreasing to the blue; the origin of this progression is indicated by an arrow. The peaks are 9 - 12 cm^{-1} wide (FWHM). We also observe two smaller peaks in band A to the red of the origin which are separated by 64 cm^{-1}. These appear to be anion hot bands, since their intensities vary with source conditions. The low frequency structure in band A is essentially mirrored in band B, although the intensity in considerably less. In band Ap, the peak spacings are smaller than in band A, and a continuum appears at the high energy side of the band. Again, the overall appearance of band Bp is similar but the intensity is less. In the $I(^2P_{1/2})\bullet CO_2$ band (Figure 2b), we observe only two sub-bands labeled C and D. The band origins are separated by 697 cm^{-1}, and each band consists of a progression of peaks whose

spacing decreases from ~30 cm^{-1} towards the blue, eventually resulting in an apparent continuum.

B. Spectrum assignments

The overall features in the I·CO$_2$ ZEKE spectrum can be readily explained in terms of the electronic and vibrational structure of the I·CO$_2$ complex. We first consider the significance of the spacings near 670 cm^{-1} observed between several pairs of sub-bands. Based on our interpretation of the photoelectron spectrum,[21] this is the frequency of the ν_2 CO$_2$ bending mode in the I·CO$_2$ complex. From the comparison of the ZEKE spectrum to the photoelectron spectrum, we assign sub-bands A and Ap in the I($^2P_{3/2}$)·CO$_2$ band and sub-band C in the I($^2P_{1/2}$)·CO$_2$ band to transitions to the $\nu_2=0$ bending level of the neutral complex, and sub-bands B, Bp, and C to transitions to the $\nu_2=1$ level.

This assignment requires an explanation of why there are two sub-bands corresponding to each ν_2 level in the I($^2P_{3/2}$)·CO$_2$ band but not in the I($^2P_{1/2}$)·CO$_2$ band. This is an electronic effect which can be explained with reference to the correlation diagram in Figure 1. Specifically, at sufficiently small distance, the electrostatic interaction between the I atom and CO$_2$ molecule should split the I($^2P_{3/2}$) atomic level into two levels with $\Omega=1/2$ and $\Omega=3/2$, (the X1/2 and I3/2 states) whereas the I($^2P_{1/2}$) level is not split by this interaction, leaving only a single $\Omega=1/2$ level (the II1/2 state). Here Ω is the projection of the total electronic angular momentum on the C-I axis. Strictly speaking, it is defined only for a diatomic molecule, but it should be an approximately good quantum number considering the relatively weak interaction between the I atom and CO$_2$ molecule.

26

In any case, we interpret the threshold photodetachment spectrum to mean that the 225 cm^{-1} interval between bands A and Ap and bands B and Bp is the splitting between the X1/2 and I3/2 levels of the I•CO_2 complex. This assignment is supported by the absence of a comparable splitting in the I($^2P_{1/2}$)•CO_2 band. We therefore assign bands A, Ap, and C to transitions to the X1/2, I3/2, and II1/2 levels of the I•CO_2 complex with $\nu_2 = 0$, and bands B, Bp, and D to the analogous transitions with $\nu_2 = 1$. Note that we are clearly in the Hund's case (c) regime; the electrostatically induced splitting is not only less than the I atom spin-orbit splitting, it is also less than the CO_2 bend frequency. Figure 3 shows the anion and neutral potential energy curves responsible for the bands in the ZEKE spectrum. These curves are discussed in more detail below.

We next consider the low frequency vibrational progressions seen in each of the sub-bands. With peak spacings in the range of 30 cm^{-1}, these must be progressions in one of the van der Waals modes of the I•CO_2 complex. Extended progressions in photodetachment spectroscopy generally involve totally symmetric vibrational modes. If the neutral complex is T-shaped with the I atom weakly bound to the C atom, then the only totally symmetric van der Waals mode is the C-I stretch (the ν_3 mode). This is a reasonable assignment, since photodetachment should affect the C-I bond length and one therefore expects extensive progressions in this mode. This assignment implies that the hot bands in band A represent a progression in the C-I stretch of the anion. The higher frequency, 64 cm^{-1}, is consistent with the stronger binding expected in the anion. Other possible I•CO_2 geometries are discussed in the last section of this paper.

The van der Waals progressions in the sub-bands corresponding to the various electronic states of the neutral are quite different. Band A (X1/2 state) shows the most pronounced structure, while in band Ap (I3/2 state), the progression is shorter, the peak spacing is smaller, and there appears to be a continuum towards the blue. The progression in band C (II1/2 state) is intermediate in length and peak spacing. This suggests that the well depths for the three electronic state decrease in the order X1/2 > II1/2 > I3/2, a result predicted in the previous work on Rg-X potentials. The other notable result is that the appearance of the van der Waals progression is largely independent of v_2, the bending quantum in the neutral vibration. For example, apart from overall intensities, bands A and B are quite similar (although not identical) in appearance. This means the vibrational wavefunction for the two modes can be written as

$$\Psi_{v2,v3}(Q_2, Q_3) \cong \psi_{v_2}(Q_2)\psi_{v_3}(Q_3) \tag{1}$$

where $\psi_{v2}(Q_2)$ may depend weakly on v_3 and *vice versa.*

The positions and assignments of peaks in each band are tabulated in Tables I and II. Band Bp is not listed due to its low intensity; individual peaks could not be picked out readily.

IV. Analysis

Based on the qualitative assignments discussed in the previous section, we can construct potential energy curves for ΓCO_2 and the three electronic states of $I \bullet CO_2$ from which the experimental spectra can be simulated. This section describes the simulation method

28

and the form of the resulting potential energy curves. We restrict ourselves to a determination of the one-dimensional potential energy curves along the C-I (v_3) van der Waals stretch coordinate that reproduce the individual sub-bands in Figures 2a and 2b. This approach is reasonable in light of Eq. 1 above, although it neglects any coupling of the C-I stretch to the low frequency van der Waals bending modes.

A. Method of calculation

For a given set of model potentials for the anion and neutral, we simulate the spectrum by (a) solving for the eigenvalues and eigenfunctions supported on each potential, and (b) calculating the Franck-Condon overlap between the first few anion v_3 levels and the bound and continuum levels supported by the neutral potential energy curves. We use a discrete variable representation (DVR) to determine the eigenvalues and eigenfunctions.[25,26,27] Our implementation of the DVR to the problem at hand has been described elsewhere.[28] We use a standard version in which the DVR points are determined by diagonalization of the position operator in a one-dimensional harmonic oscillator basis (Gauss-Hermite quadrature). Even for our relatively simple problem, the DVR offers a great increase in speed as we do not have to set up and diagonalize a new Hamiltonian matrix for each model potential.

The one somewhat nonstandard aspect of our calculation is that we need to treat continuum as well as bound state wavefunctions. To simulate the continuum transitions, we use the approach outlined in Ref. 28. When we use the DVR procedure to determine eigenvalues supported by a potential with a shallow well, we obtain a discrete energy spectrum both above and below the dissociation continuum; the discrete levels above the dissociation limit are an artifact resulting from using localized (i.e. harmonic oscillator) basis functions. If

29

the number of basis functions is changed, the continuum "eigenvalues" change substantially, while the bound eigenvalues are relatively unaffected. Therefore, by doing the DVR and Frank-Condon calculations at several different basis sizes, summing the results together, and convoluting the resulting stick spectra with our experimental resolution, we generated a simulated spectrum which is discrete below the dissociation continuum and continuous above it. The full simulation requires summing between eight and twelve simulations in our case. The accuracy of this method was checked by comparing the full simulation to the results of a one-dimensional time-dependent wave packet calculation[29] using the same potential energy curves; the two methods yield identical results.

B. Nature of the potential energy curves

It is desirable to use the simplest potential energy functions needed to fit our spectra. The long-range attractive forces are well-understood for the neutral and anion. For the various $I \bullet CO_2$ states, the leading term in the potential at long range is the $-1/r^6$ term due to the van der Waals attraction, while for $I^- CO_2$, the long-range attraction goes as $-1/r^4$ due to charge-quadrupole and charge-induced dipole interactions with a contribution from a $-1/r^6$ term due to the large polarizability of I^-. There is considerably less agreement on the form of the potential at closer range, and, for example, one can choose for the neutral functional forms ranging from the Lennard-Jones (12-6) potential to the considerably more involved functions developed by Lee,[7] Aquilanti,[8] and their co-workers.

We experimented with several anion and neutral potential energy functions to see which gave the best results for band A, since it is the most structured and intense band in the spectrum and includes the most distinct anion hot bands. The following procedure was used. Given a

functional form for the neutral potential (the X1/2 state), the parameters were varied so that the bound states energies agreed with the experimental peak spacings (band A has no observable continuum transitions). The parameters in the anion potential were then adjusted to match the absolute peak positions, the hot band transition energies, and the intensity distribution of all the peaks.

Although we were able to reproduce the peak spacings in band A fairly well using the Lennard-Jones(12-6) potential for the neutral, the best simulation of peak positions and intensities was obtained with the Maitland-Smith (n-6) potential[30] for the neutral:

$$U(r^*) = \frac{\varepsilon}{n-6}\left[6(r^*)^n - n(r^*)^6\right] \tag{2}$$

Here $r^* = r/r_m$, where r_m is the distance at the potential minimum energy ε. The key feature of this potential is that n varies with r^* according to

$$n = m + \gamma(r^* - 1) \tag{3}$$

where m and γ are adjustable parameters. The Maitland-Smith type potential is a simple potential form but is flexible enough to fit our data. The exponent of the repulsive part varies with distance depending on the sign of γ, while the attractive part is still represented by the $-1/r^6$ term. Notice the Lennard-Jones (12-6) form is obtained when m is set to 12 and γ is set to zero. Using Eq.2 we obtain the best match with experiment for $\varepsilon = 44.5$ meV, $r_m = 3.99$ Å, m = 11.8 and $\gamma = -2.5$ for the neutral X1/2 state.

Once the well depth ε_X of the X1/2 state has been determined, we can immediately extract the well depth ε_a of the anion potential from the following formula:

31

$$v_{00} + \omega_0^a + \varepsilon_X - \omega_0^X = \varepsilon_a + EA(I) \qquad (4)$$

Here $v_{00} = 3.225$ eV is the energy of the origin transition for band A, $EA(I) = 3.0591$ eV is the electron affinity of atomic iodine, and ω and ω are the zero point energies of the anion state and the neutral X1/2 state, respectively. Eq. 4 is evident from Figure 3. From our X1/2 state potential we find $\omega = 20$ cm^{-1}, and we estimate $\omega = 32$ cm^{-1} from the hot band spacings in band A. From this we obtain $\varepsilon_a = 212$ meV.

To construct the full anion potential, we use a variation of Eq. 2:

$$U(r^*) = \frac{\varepsilon_a}{n-4}(4(r^*)^n - n(r^*)^{-4}) \qquad (5)$$

which we refer to as the Maitland-Smith (n-4) potential. Compared to the neutral potential, the attractive part for the anion is represented by the $-1/r^4$ term. The best simulation of band A is obtained with $r_m = 3.772$ Å, $m = 9$, and $\gamma = 1.5$. Note that r_m for the anion is smaller than for the neutral X1/2 state. Simulations with r_m larger in the anion than the neutral yielded insufficient intensities in the high v_3 peaks. Given the anion potential and the neutral X1/2 potential established from simulation of band A, the hot band transition intensities in band A are best reproduced by using 65 K as the anion vibrational temperature.

Once the anion well depth is determined, we can use energy balance equations similar to Eq. 4 to find the well depths for the potential energy curves responsible for bands Ap, B, C and D, using the experimentally measured band origins. (Figure 3 is again a useful reference.) The zero point energies needed to extract the well depths can be estimated from the peak spacings in each band. The well depths obtained by this method are listed in Table III.

Finally, using the anion potential obtained above, we can construct the full potential energy curves for the excited states responsible for bands Ap, B, C, and D. We found we could simulate bands C and D with a simple Lennard-Jones (12-6) potential, but the Maitland-Smith (n-6) form was required to simulate bands Ap and B. The potential parameters for the excited states are tabulated in Table III. Note that the well depth for the band C potential is 4.5 meV deeper than for the band D potential. This indicates that the attraction between $I(^2P_{1/2})$ and CO_2 is slightly reduced for bend-excited CO_2, effectively increasing the CO_2 bend frequency in the $I(^2P_{1/2}) \bullet CO_2$ complex.

Figure 4 shows the simulated and experimental spectra. Because we ignored the CO_2 bending mode in our simulation, the simulated bands are simply scaled by multiplying the peak intensities in each band by a constant so that we can compare the simulated data to the experimental results. The four potentials for the neutral states X1/2, I3/2 and II1/2 with $v_2 = 0$ (corresponding to band A, AP and C) and the anion state are drawn in Figure 5.

It is important to consider the possible errors in the potential energy functions and parameters, in particular, the values for ε and r_m. We can estimate the uncertainties in these two parameters by systematically varying them parameters and observing when the agreement between the simulated and experimental spectra degrades. The estimated maximum uncertainties are ±8% in ε for the neutral states and r_m for all the states and ±2% in ε for the negative ion state. As for the full potential energy functions, our spectra probe the attractive wells and (for bands Ap, C, and D) the repulsive wall a few hundred cm^{-1}'s above the dissociation limit. We believe that these regions of the curves are well-characterized. However, our experiment is clearly not sensitive to the repulsive wall at higher energies, and

the characterization of this region of the potential will have to await scattering measurements of the differential and total cross sections.

Another independent check on our well depths can be obtained by applying the method of LeRoy and Bernstein,[31] who showed that the dissociation energy can be obtained given the long-range attractive potential and the energies of several vibrational levels near the dissociation limit. This analysis has recently been used by Brucat and co-workers[32] to obtain dissociation energies for rare gas-transition metal cations. If we apply this to the neutral states, using a $-1/r^6$ attractive potential, we obtain $\varepsilon = 36$ meV for band A, 19 mev for band Ap, and 34 meV for band C. The results for band Ap and C are fairly close (~ 2 meV) to the values in Table III, while the result for band A differs, the well depth for band A is off by 10 meV. The greater deviation for band A is not surprising, since we actually do not observe vibrational levels up to the dissociation limit as we do for the other two bands.

V. Discussion

In this section, we examine in more detail some features of the I^-CO_2 and $I \bullet CO_2$ potential energy curves obtained in the previous section. The first point to consider is the change in the C-I bond length upon photodetachment. For weakly bound molecules or ions, the length of the weak bond is determined by the strength of the attractive interaction and the sizes of the atoms most involved in the bond. In our case, these two factors compete: the anion is more strongly bound than the neutral, but I^- is larger than I in the sense that the polarizability of I^- is larger. Our analysis does in fact show that the C-I bond length in the

34

anion is 0.22 Å smaller than the neutral X1/2 state, the most strongly bound neutral state. This result is consistent with previous work on Rg-X systems.[6,7,8,33] With the exception of XeF and XeCl,[10,12] the bond lengths are shorter in the anion than in the neutral.

One question raised by our analysis is the validity of the one-dimensional approach, in which we essentially treat the CO_2 molecule as if it were an atom. One check on this is provided by the work of Haberland[5] and Aquilanti *et al.*[6] on Rg-X systems. They showed that given two of the three adiabatic Rg-X potentials, the third can be calculated if one assumes the spin-orbit constant is independent of the internuclear distance. (See Eq. (12) below.) If we use their expressions, and calculate the I3/2 potential from our X1/2 and II1/2 curves, we find $\varepsilon=23$ meV and $r_m=4.19$ Å. These are close but not identical to the results in Table III ($\varepsilon=17.3$ meV and $r_m=4.15$ Å). Some of this discrepancy may occur because the spin-orbit coupling is not a constant, and some may occur because CO_2 is not an atom. Nonetheless, the values for r_m and ε are sufficiently close that we believe our one-dimensional analysis is appropriate. This means we can further analyze our potentials in terms of the formalism developed for Rg-X species.

In the absence of spin-orbit coupling, the interaction potential between a rare gas and halogen atom can be written as[6]

$$V(r,\theta) = V_0(r) + V_2(r) P_2(\cos\theta) \tag{6}$$

where r is the internuclear distance and θ is the angle between the unfilled p-orbital on the halogen atom and the internuclear axis. Thus, $V_2(r)$ represents the anisotropic interaction between two atoms due to an unfilled orbital on one of the atoms. $V_0(r)$ and $V_2(r)$ are related to the potentials $V_\Sigma(r)$ and $V_\Pi(r)$ that describe the Σ and Π states resulting from the Rg + X interaction without spin-orbit coupling by

35

$$V_0 = \frac{1}{3}(V_\Sigma + 2V_\Pi); \qquad V_2 = \frac{5}{3}(V_\Sigma - V_\Pi) \qquad (7)$$

Once either V_Σ and V_Π or V_0 and V_2 are specified, along with the spin-orbit coupling constant Δ, one can find the three potentials $V(X1/2)$, $V(I3/2)$, $V(II1/2)$:[5,6]

$$(8)$$

$$V(X1/2) = V_0 + \frac{V_2}{10} + \frac{\Delta}{2} - \frac{1}{2}(\frac{9}{25}V_2^2 + \Delta^2 - \frac{2}{5}V_2\Delta)^{1/2}$$

$$V(I3/2) = V_0 - \frac{V_2}{5}$$

$$V(II,1/2) = V_0 + \frac{V_2}{10} + \frac{\Delta}{2} + \frac{1}{2}(\frac{9}{25}V_2^2 + \Delta^2 - \frac{2}{5}V_2\Delta)^{1/2}$$

Conversely, given two of the three potentials $V(X1/2)$, $V(I3/2)$, $V(II1/2)$, one can determine V_Σ, V_Π, V_0, and V_2.

If we do this using our $V(X1/2)$ and $V(II1/2)$ potentials for $I \bullet CO_2$ (with $v_2=0$), we obtain the curves for V_Σ, V_Π, V_0, and V_2 shown in Figure 6. We find that for $V_0(r)$, $\varepsilon = 32$ meV and $r_m = 4.08$ Å, while $V_2(r)$ is purely attractive. This means that as the I and CO_2 approach, the unfilled p orbital prefers to lie along the C-I axis. A similar tendency also can be seen by comparing the $V_\Sigma(r)$ and $V_\Pi(r)$ curves: the well is noticeably deeper for the Σ state. These anisotropic effects strongly resemble those in Rg-X potentials.[7,8] Figure 6 shows that $|V_2/\Delta|$ is small (≤ 0.15) over the range of R_{C-I} probed in our experiment, indicating, as expected, that we are in the Hund's case (c) coupling regime; the transition from case(c) to case (a) occurs in the neighborhood of $|V_2/\Delta| = 1$.

In Table IV, we compare our well depths and r_m values for $I \cdot CO_2$ with those for similar Rg-X species. The polarizability of CO_2 is less than that of Xe and about equal to that of Kr,[34] and this is consistent with the r_m values: $r_m(XeI) > r_m(KrI) \approx r_m(I \cdot CO_2)$. However, the $I \cdot CO_2$ well for the ground X1/2 state is noticeably deeper than for XeI and KrI. The greater well depth is most likely due to the interaction of the CO_2 quadrupole moment with the I atom polarizability. This interaction apparently has a larger effect on the well depth than on r_m. Although the binding energies for XeI– or KrI– have not been experimentally determined, Cappelletti et al.[35] have proposed simple correlation formulae for ion-neutral interactions which depend only on polarizabilities. They find $\varepsilon = 133$ meV and $r_m = 4.27$ Å for XeI–, and $\varepsilon = 90$ mev and $r_m = 4.17$ Å for KrI–. It is clear that the binding in $I–CO_2$ (211 meV, 3.77 Å) is considerably stronger, presumably due to a combination of the charge-quadrupole interaction and charge transfer from the I– to the CO_2.

We close the discussion by considering in more detail our assumption of T-shaped equilibrium geometry for $I \cdot CO_2$. For $I–CO_2$, it is certainly reasonable to expect the I– to bind to the C atom. This is the geometry favored by the charge-quadrupole interaction, and it also facilitates charge transfer from the I– to the LUMO of CO_2 (which is why the CO_2 is slightly bent in the anion[21]). The case of the neutral complex seems, *a priori*, more ambiguous. If the I atom acts as an electron donor, it will be attracted to the C atom, while if it acts as an electron acceptor, it will bind to one of the O atoms, resulting in a linear complex. Thus, for example, $Ar \cdot CO_2$ is T-shaped,[36,37] while $CO_2 \cdot HF$ is linear.[38]

Our experiment shows strong evidence for at least a local minimum at the T-shaped geometry of $I \cdot CO_2$. If this were not the case, we would expect to see an extended progression

in the van der Waals bending mode as well as in the stretch, whereas our spectra show only a single van der Waals progression. While one could argue that this progression is due entirely to the Van der Waals bend and not the stretch, the preceding discussion has shown very strong analogies between the potential energy curves needed to reproduce our spectra and those which describe the Rg-X interaction. It therefore seems unreasonable to attribute the low frequency progressions to anything other than the Van der Waals stretch. However, we cannot rule out the existence of another minimum at the linear $I \bullet CO_2$ geometry.

VI. Conclusions

We have shown that threshold photodetachment spectroscopy of an anion cluster can provide a detailed probe of weakly bound neutral van der Waals complexes involving open-shell atoms. Specifically, the threshold photodetachment spectrum of $I^- CO_2$ probes all three electronic states resulting from the electronically anisotropic interaction of $I(^2P_{3/2,1/2})$ with a CO_2 molecule. For each electronic state, we observe extensive progressions in the low frequency C-I van der Waals stretching mode, and we also probe the continuum above the $I + CO_2$ dissociation threshold for two of the three electronic states. From this information, we are able to construct potential energy curves for the anion and the three neutral electronic states.

Now that we have demonstrated the feasibility of applying this method to a polyatomic open-shell van der Waals complex, we plan to look at some of the diatomic Rg-X species via photodetachment of RgX−. Such experiments would provide a stringent test of the potential energy functions for these species derived from scattering experiments.

38

Acknowledgments

References:

1 J. Goodman and L. E. Brus, *J. Chem. Phys.*, 1977, 67, 4858.

2 M. T. Berry, M. R. Brustein and M. I. Lester, *Chem. Phys. Lett*, 1988, 153, 17; *J. Chem. Phys.*, 1989, 90, 5878.

3 J. M. Bowman, B. Gazdy, P. Schaefer and M. C. Heaven, *J. Phys. Chem.*, 1990, 94, 2226; B-C Chang, L. Yu, D. Cullin, B. Rehfuss, J. Williamson, T. A. Miller, W. Fawzy, X. Zheng, S. Fei and M. Heaven, *J. Chem. Phys.*, 1991, 95, 7086.

4 P. D. A. Mills, C. M. Western and B. J. Howard, *J. Phys. Chem.*, 1986, 90, 4961.

5 H. Haberland, *Z. Phys. A*, 1982, 307, 35.

6 V. Aqualanti and G. Grossi, *J. Chem. Phys.*, 1980, 73, 1165; V. Aquilanti, G. Liuti, F. Pirani and F. Vecchiocattivi, *J. Chem. Soc., Faraday Trans. 2*, 1989, 85, 955.

7 C. H. Becker, P. Casavecchia and Y. T, Lee, *J. Chem. Phys.*, 1978, 69, 2377; *ibid.*, 1979, 70, 2986; C. H. Becker, J. J. Valentini, P. Casavecchia, S. J. Sibener and Y. T. Lee, *Chem. Phys. Lett.*, 1979, 61, 1; P. Casavecchia, G. He, R. K. Sparks and Y. T. Lee, *J. Chem. Phys.*, 1981, 75, 710; P. Casavecchia, G. He, R. Sparks and Y. T. Lee, *ibid.*, 1982, 77, 1878.

8 V. Aquilanti, R. Condori, and F. Pirani, *J. Chem. Phys.*, 1988, 89, 6157; V. Aquilanti, R. Condori, D. Cappelletti, V. Lorent and F. Pirani, *Chem. Phys.*, 1990, 145, 293; V. Aquilanti, D. Cappelletti, V. Lorent, E. Luzzatti and F. Pirani, *Chem. Phys. Lett.*, 1992, 192, 153.

9 A. L. Smith and P.C. Kobrinsky, *J. Mol. Spectrosc.*, 1978, 69, 1.

10 J. J. Ewing and C. A. Brau, *Phys. Rev. A*, 1975, 12, 129; C. A. Brau and J. J. Ewing, *J. Chem. Phys.*, 1975, 63, 4640; J. J. Ewing and C. A. Brau, *Appl. Phys. Lett.*, 1975, 27, 350; C. A. Brau and J. J. Ewing, *ibid.*, 1975, 27, 435.

11 M. F. Golde and B. Thrush, *Chem. Phys. Lett.*, 1974, 29, 486.

12 J. Tellinghuisen, J. M. Hoffman, G. C. Tisone and A. K. Hays, *J. Chem. Phys.*, 1976, 64, 2484; J. Tellinghuisen, G. C. Tisone, J. M. Hoffman and A. K. Hays, *ibid.*, 1976, 64, 4796; J. Tellinghuisen, A. K. Hays, J. M. Hoffman and G. C. Tisone, *ibid.*, 1976, 65, 4473; P. C. Tellinghuisen, J. Tellinghuisen, J. A. Coxon, J. E. Velazco and D. W. Sester, *ibid.*, 1978, 68, 5187; A. Sur, A. Hui and J. Tellinghuisen, *J. Mol. Spectrosc.*, 1979, 74, 465.

13 M. P. Casassa, M. F. Golde and A. Kvaran, *Chem. Phys. Lett.*, 1978, 59, 51.

14 I. Dabrowski and G. Herzberg, *J. Mol. Spectrosc.*, 1978, 73, 183; I. Dabrowski and G. Herzberg, K. Yoshino, *ibid.*, 1981, 89, 491.

15 Y. Tanaka, K. Yoshino and D. E. Freeman, *J. Chem. Phys.*, 1975, 62, 4484.

16 K. P. Huber and R. H. Lipson, *J. Mol. Spectrosc.*, 1986, 119, 433.

17 A. Carrington and T. P. Softley, *Chem. Phys.*, 1985, 92, 199.

18 C. Y. Ng, P. W. Tiedemann, B. H. Mahan and Y. T. Lee, *J. Chem. Phys.*, 1977, 66, 5737.

19 P. M. Dehmer and J. L. Dehmer, *J. Chem. Phys.*, 1978, 68, 3462; S. T. Pratt and P. M. Dehmer, *J. Chem. Phys.*, 1982, 76, 3433.

20 K. Norwood, G. Luo and C. Y. Ng, *J. Chem. Phys.*, 1989, 90, 4689.

21 D. W. Arnold, S. E. Bradforth, E. H. Kim and D. M. Neumark, *J. Chem. Phys.* 1992, 95, xxxx.

22 T. N. Kitsopoulos, I. M. Waller, J. G. Loeser and D. M. Neumark, *Chem. Phys. Lett.*, 1989, 159, 300; C. J. Chick, Y. Zhao and D. M. Neumark, to appear on *J. Chem. Phys.*.

23 J. M. Bakker, *J. Phys. E,* 1973, 6, 785.

24 K. Müller-Dethlefs, M. Sander and E. W. Schlag, *Z. Naturforsch*, 1984, 39a, 1089; *Chem. Phys. Lett.*, 1984, 12, 291; K. Müller-Dethlefs and E. W. Schlag, *Ann. Rev. Phys. Chem.*, 1991, 42, 109.

25 D. O. Harris, G. G. Engerholm and W. D. Gwinn, *J. Chem. Phys.*, 1965, 43, 1515.

26 A. S. Dickinson and P. R. Certain, *j. Chem. Phys.*, 1968, 49, 4209.

27 J. C. Light, I. P. Hamilton and J. V. Lill, *J. Chem. Phys.*, 1985, 82, 1400.

28 R. B. Metz, *Ph.D Thesis, University of California, Berkeley,* 1991.

29 S. E. Bradforth, A. Weaver, D. W. Arnold, R. B. Metz and D. M. Neumark, *J. Chem. Phys.*, 1990, 92, 7205.

30 G. C. Maitland and E. B. Smith, *Chem. Phys. Lett.*, 1973, 22, 443.

31 R. J. LeRoy and R. B. Bernstein, *J. Chem. Phys.*, 1970, 52, 3869.

32 D. Lessen and P.J. Brucat, *J. Chem. Phys.*, 1989, 91, 4522.

33 C. C. Kirkpatrick and L. A. Viehland, *Chem. Phys.*, 1985, 98, 221.

34 T. M. Miller, *Handbook of Chemistry and Physics*, 71st Edition, CRC Press, pp. E72-E78.

35 D. Cappelletti, G. Liuti and F. Pirani, *Chem. Phys. Lett.*, 1991, 183, 297.

36 J. M. Steed, T. A. Dixon, and W. Klemperer, *J. Chem. Phys.*, 1979, 70, 4095.

37 G. T. Fraser, A. S. Pine and R. D. Suenram, *J. Chem. Phys.*, 1988, 88, 6157.

38 F. A. Baiocchi, T. A. Dixon, C. H. Joyner, and W. Klemperer, *J. Chem. Phys.*, 1981, 74, 6544.

Table I. Peak positions, relative energies, and assignments for Figure 2a ($I(^2P_{3/2})\bullet CO_2$ band).

Band	Position (nm)	Vacuum Wavenumbers (cm^{-1})	Relative Energy (cm^{-1})	Assignment
A	386.25	25882	-129	3_2^0
	385.30	25946	-65	3_1^0
	384.35	26011	0	Origin[a] ($2_0^0 3_0^0$)
	383.80	26048	37	3_0^1
	383.30	26082	71	3_0^2
	382.85	26113	102	3_0^3
	382.40	26143	132	3_0^4
	382.03	26169	158	3_0^5
	381.68	26193	182	3_0^6
Ap	381.05	26236	0	Origin($2_0^0 3_0^0$)
	380.75	26257	21	3_0^1
	380.45	26278	42	3_0^2
	380.17	26297	61	3_0^3
	379.91	26315	79	3_0^4
	379.70	26329	93	3_0^5
B	375.71	26608	-65	3_1^0
	374.80	26673	0	Origin($2_0^1 3_0^0$)

374.26	26711	38	3_0^1
373.77	26746	73	3_0^2
373.31	26779	106	3_0^3

[a] This corresponds to an electron affinity of 3.225 (0.001) eV.

Table II. Peak positions, relative energies, and assignments for Figure 2b ($I(^2P_{1/2}) \bullet CO_2$ band).

Band	Position (nm)	Vacuum Wavenumbers (cm^{-1})	Relative Energy (cm^{-1})	Assignment
C	297.65	33586	-125	3_2^0
	297.10	33648	-63	3_1^0
	296.84	33678	-33	3_1^1
	296.55	33711	0	Origin($2_0^0 3_0^0$)
	296.26	33744	33	3_0^1
	295.99	33775	64	3_0^2
	295.77	33800	89	3_0^3
	295.54	33826	115	3_0^4
	295.39	33844	133	3_0^5
D	290.54	34408	0	Origin($2_0^1 3_0^0$)
	290.29	34438	30	3_0^1
	290.08	34463	55	3_0^2
	289.88	34486	78	3_0^3

45

Table III. Potential parameters for the anion and the neutral states obtained from the simulation. The potential forms are those discussed in the text.

State (band)	X1/2 (A)	(B)	I3/2 (Ap)	II1/2 (C)	(D)	Anion
ε(meV)	44.5	44.5	17.0	32.0	27.5	212.0
r_m(Å)	3.990	3.995	4.147	4.083	4.090	3.773
m	11.8	11.8	14.0	12.0	12.0	9.0
γ	-2.5	-2.5	9.5	0.	0.	1.5

Table IV.   Comparisons of our well depth ε's and r_m values for I•CO_2 with those for a few similar Rg-X species.

System	Ref.	V(X1/2)		V(I3/2)		V(II1/2)	
		ε (meV)	r_m (Å)	ε (meV)	r_m (Å)	ε (meV)	r_m (Å)
I-CO_2	this work	44.5	3.99	17.0	4.15	32.0	4.08
I-Xe	[7]	30.0	4.30	20.5	4.60		
I-Kr	[7]	24.0	4.05	16.	4.32		
Br-Xe	[7]	28.0	3.80	18.4	4.11		
Cl-Xe	[8]	35.4	3.23	17.0	4.21	20.0	4.09

Figure Captions

Figure 1. Schematic correlation diagram showing the three electronic states arising from rare gas (Rg) + halogen (X) interaction. In order of increasing energy, these are called the X1/2, I3/2, and II1/2 states.

Figure 2. Threshold photodetachment spectrum of I–CO_2 (solid lines) and photoelectron spectrum (from Ref. 21) of I^-CO_2 (dotted lines). (a) is the $I(^2P_{3/2})\bullet CO_2$ band and (b) is the $I(^2P_{1/2})\bullet CO_2$ band. The arrows indicate the band origins.

Figure 3. Illustration of the potential energy curves responsible for the bands in Figure 2. The bottom potential energy curve corresponds to the anion state, while the remaining curves, in order of increasing energy, correspond to the following neutral states: X1/2 (band A), I3/2 (band Ap), X1/2 (band B, v_2=1), I3/2 (band Bp, v_2=1), II1/2 (band C) and, II1/2 (band D,v_2=1). ε_X and ε_a are the well depths for the neutral X1/2 state and the anion state, respectively; v_{00} is the origin transition energy for band A; EA is the electron affinity of I; Δ is the $I(^2P)$ spin-orbit splitting constant and ω the bending frequency of CO_2.

Figure 4. Frank-Condon simulation of the threshold photodetachment spectrum of I^-CO_2. The solid lines are the simulated results, the dotted lines are the experimental results.

48

Figure 5. The anion and three neutral adiabatic potential energy curves resulting from our fit to the $v_2=0$ bands in the spectrum. Note that the Y-axis scale for the anion potential is larger than that for the neutral potentials.

Figure 6. Plot of the potentials $V_0(r)$, $V_2(r)$ $V_\Sigma(r)$, and $V_\Pi(r)$ obtained from the potentials in Figure 5. See Eqs. (7), (8) in the text.
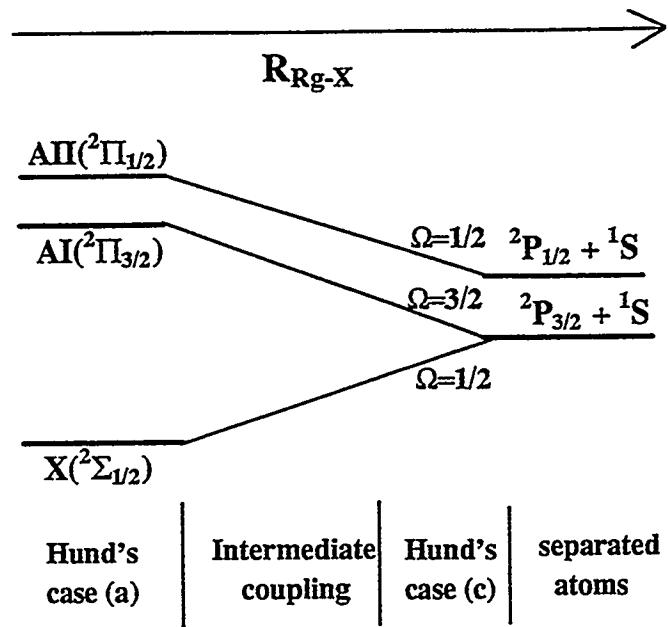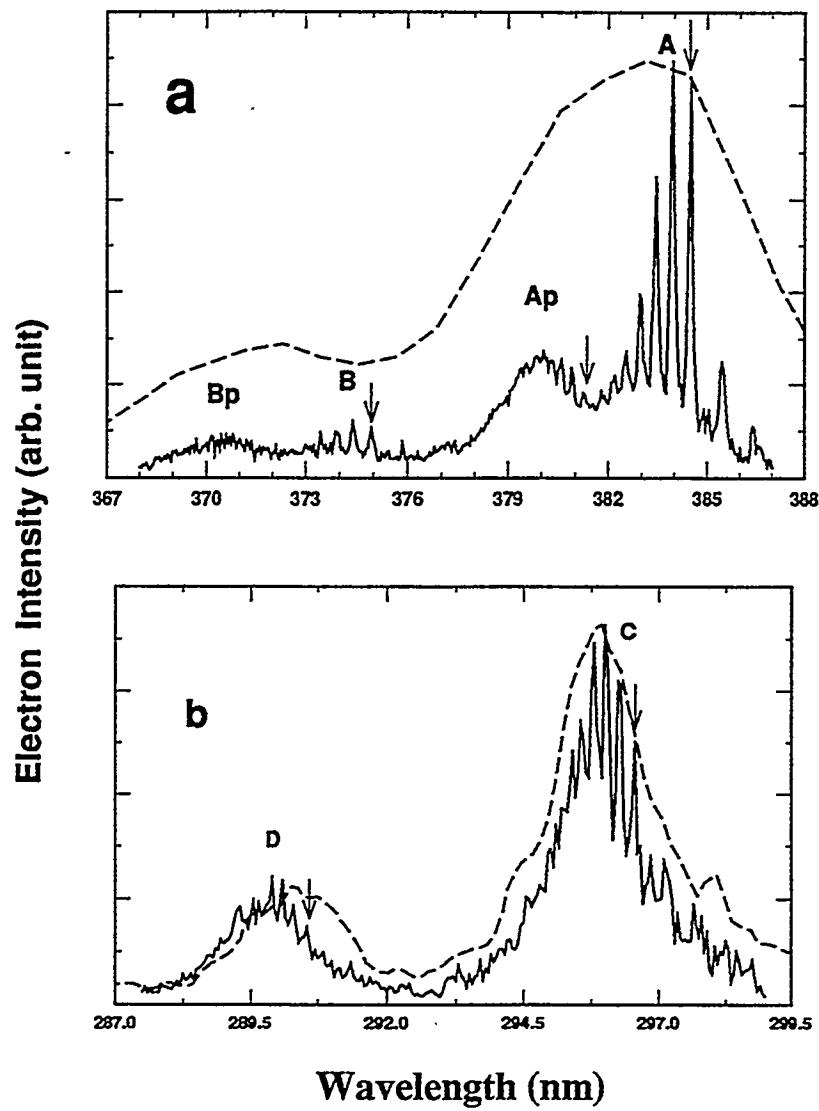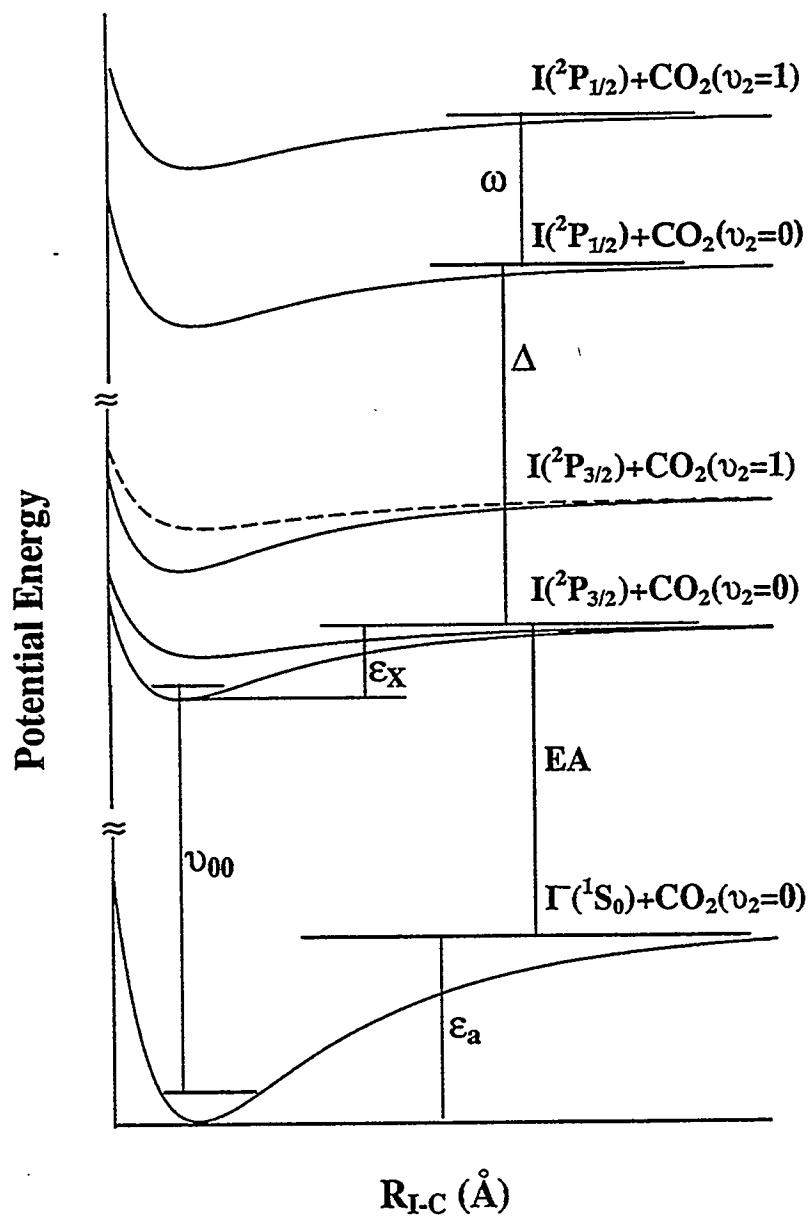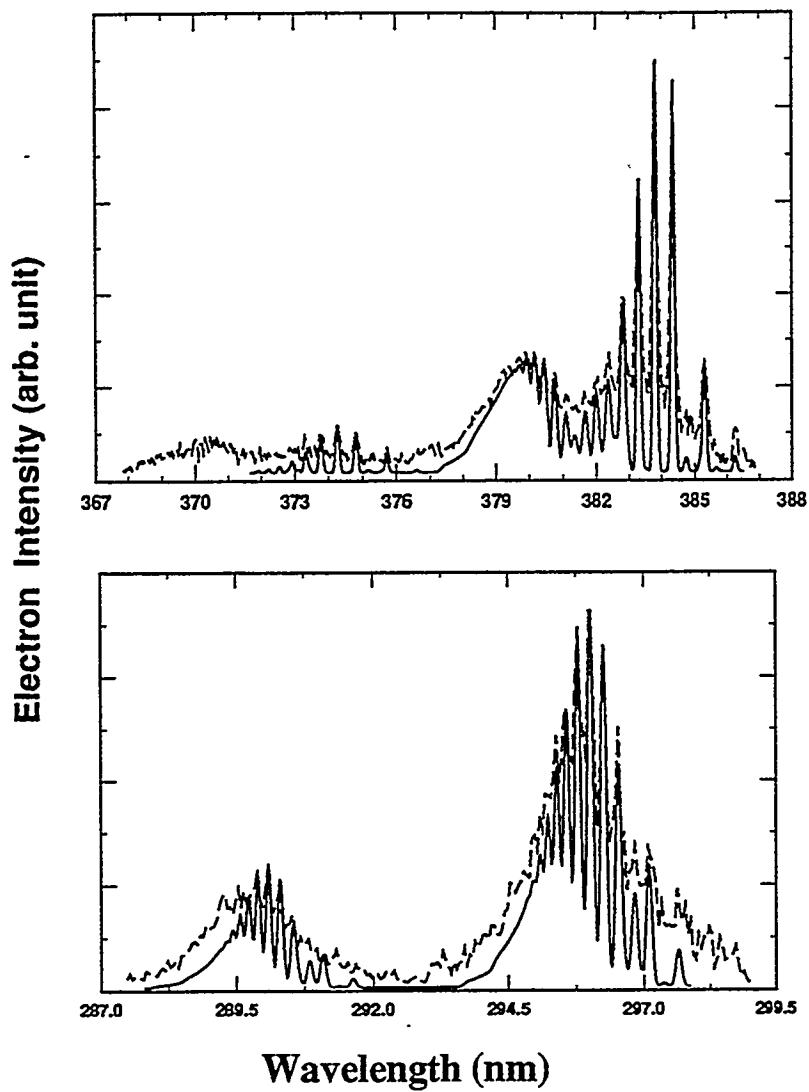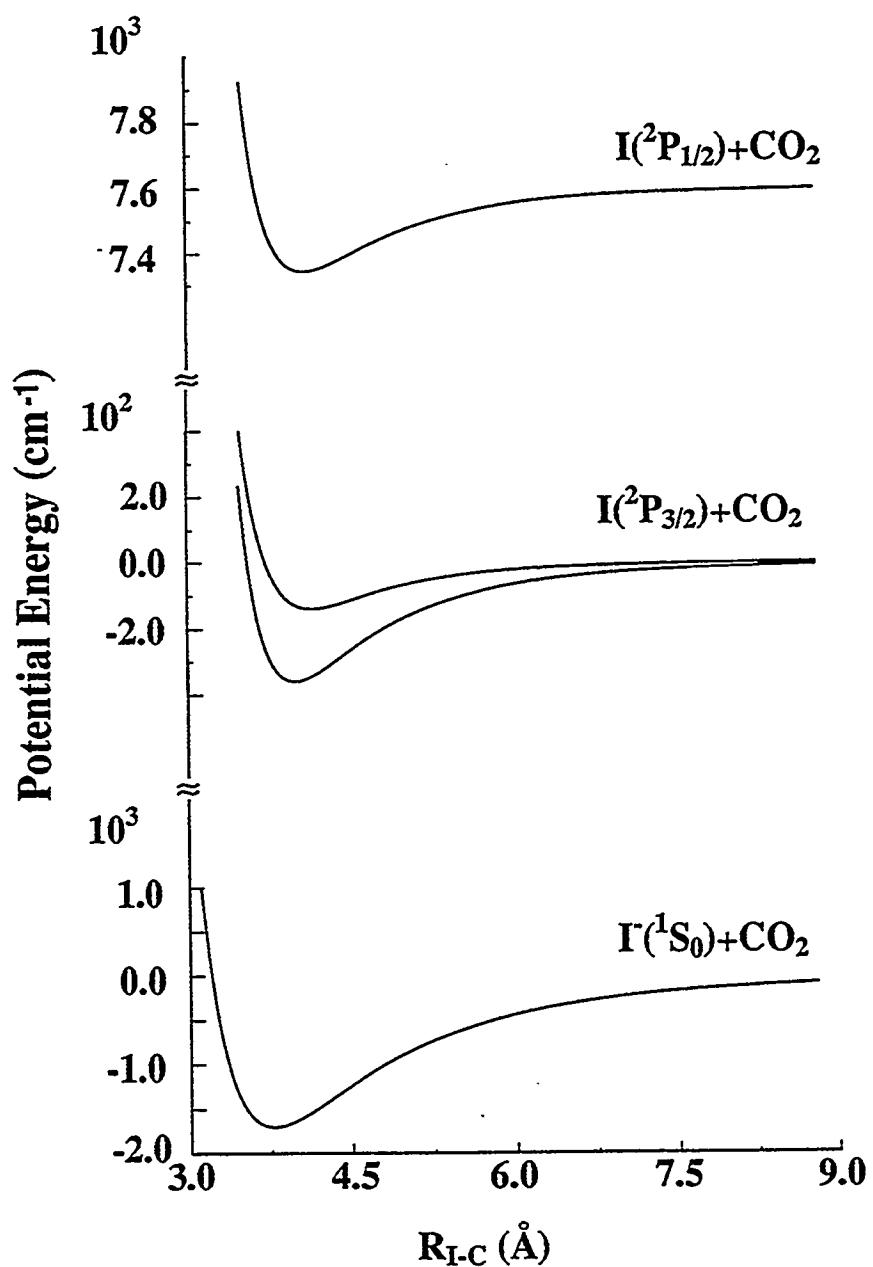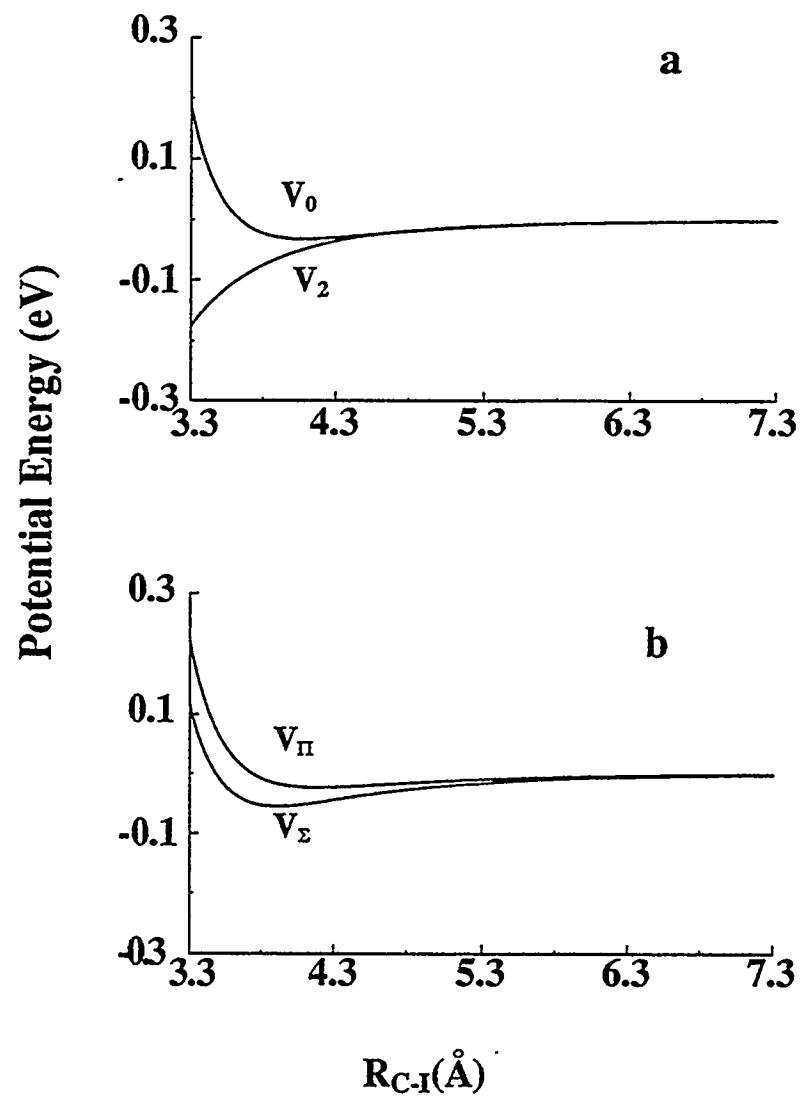
R_{Rg-X}

$A\Pi(^2\Pi_{1/2})$

$AI(^2\Pi_{3/2})$

$\Omega=1/2$ $^2P_{1/2} + {}^1S$

$\Omega=3/2$ $^2P_{3/2} + {}^1S$

$\Omega=1/2$

$X(^2\Sigma_{1/2})$

| Hund's case (a) | Intermediate coupling | Hund's case (c) | separated atoms |

Figure 2.1

Figure 2.2

51

Potential Energy (y-axis)

$I(^2P_{1/2})+CO_2(\upsilon_2=1)$

ω

$I(^2P_{1/2})+CO_2(\upsilon_2=0)$

Δ

$I(^2P_{3/2})+CO_2(\upsilon_2=1)$

$I(^2P_{3/2})+CO_2(\upsilon_2=0)$

ε_X

EA

υ_{00}

$I^-(^1S_0)+CO_2(\upsilon_2=0)$

ε_a

R_{I-C} (Å)

Figure 2.3

52

Figure 2.4

53

Figure 2.5

54

Figure 2.6

55

Chapter 3. Study of the ArBr⁻, ArI⁻, and KrI⁻ anions and the corresponding neutral van der Waals complexes by anion zero electron kinetic energy spectroscopy

Abstract

Three rare gas halide (RgX⁻) anions, ArBr⁻, ArI⁻, and KrI⁻, and the corresponding open-shell van der Waals complexes, ArBr, ArI, and KrI, were studied with anion zero electron kinetic energy (ZEKE) spectroscopy. Photodetachment of each anion accesses the three lowest-lying electronic states (the $X1/2$, $I3/2$, and $II1/2$ states) of the neutral complex. The spectra for each system reveal well-resolved progressions in the low frequency vibrations of the anion and the three neutral electronic states, providing a detailed spectroscopic probe of the Rg•X⁻ and Rg•X interaction potentials. The line shapes observed in the ZEKE spectra are analyzed in terms of the line strengths of the underlying rotational transitions. From our data, we construct the potential energy curve for each neutral state as well as for the anion, and these interaction potentials are compared to potentials obtained from scattering and ion mobility experiments.

I. Introduction

The determination of the potential energy function between weakly interacting species has been a central goal of a wide range of scattering and spectroscopy studies over the last several years. As a result of this effort, the interactions between closed shell atomic and molecular neutral species have been characterized in considerable detail.[1,2] On the other hand, potential energy functions between open and closed shell species or between neutrals and ions are generally much less well understood. These latter two types of interactions are the subject of this paper. We report a zero electron kinetic energy (ZEKE) spectroscopy study of several rare gas halide (RgX⁻) anions. The resulting spectra provide a detailed probe not only of the RgX⁻ potential energy function, but also of the potential energy functions for the ground and low-lying excited electronic states of the neutral RgX van der Waals complex. Results are presented here for the ArBr, ArI, and KrI complexes.

The RgX⁻ potentials are of interest as they determine the diffusion and mobility of ions in plasmas and discharges. The primary interest in the neutral RgX species derives from their importance in excimer lasers, in which the lasing transition occurs between a strongly bound excited state, largely ionic in character, and the weakly bound ground state of the complex. The neutral species are also of interest as prototypical open-shell complexes. In contrast to the isotropic interaction between two closed-shell atoms, the interaction potential between a rare gas and a halogen atom is complicated by spin-orbit and orientation effects due to the open-shell nature of the halogen atom.[3,4] Specifically, the interaction between an X(^{2}P) and rare gas atom results in three low-lying electronic states, all of which weakly bound by van der Waals

57

forces. The lower two states (the X1/2 and I3/2 states) correlate to ground state $X(^2P_{3/2})$ + Rg products, while the higher II1/2 state correlates to $X^*(^2P_{1/2})$ + Rg products.

All three states are accessible via photodetachment of the RgX⁻ anion and can therefore be characterized in our experiment. The resolution of our negative ion ZEKE spectrometer(2-5 cm⁻¹ under conditions used here) is sufficient to resolve transitions between anion and neutral vibrational levels, thereby providing a detailed probe of the anion and three neutral states. The work presented here is an extension of an earlier paper[5] in which the van der Waals states of the I•CO_2 complex were studied by ZEKE spectroscopy of the I⁻CO_2 anion.

The properties of RgX complexes have been studied previously in scattering and spectroscopy experiments. Scattering experiments have been most useful in characterizing the van der Waals states of these species. In a series of differential cross section measurements, Lee and co-workers[6,7] obtained the X1/2 and I3/2 potential energy curves of several RgX complexes. These experiments have been carried out on the whole series of Rg (Ar,Kr,Xe) - X (F,Cl,Br,I) interactions except for ArCl, KrCl and ArI. In a complementary set of experiments, Aquilanti et al.[8,9,10] have measured Rg-F and Rg-Cl (Rg=He,Ne,Ar,Kr,Xe) elastic scattering integral cross sections using magnetically state-selected X atoms.

In addition to the scattering experiments, several spectroscopic methods have been used to probe RgX complexes. Spontaneous emission spectra from the strongly bound ionic excited states to the van der Waals states have been recorded for several KrX and XeX species by Setser and coworkers,[11] Ewing and Brau,[12] and Tellinghuisen and coworkers.[13] Golde and coworkers[14] have measured spontaneous emission spectra of ArCl and ArBr. The XeF

electronic absorption spectrum was obtained by Smith and Kobrinsky.[15] Solgadi[16] and

Smalley[17] have studied XeCl and XeF, respectively, with laser induced fluorescence (LIF).

Photoassociation spectra of KrF and XeI have recently been obtained by Eden and

coworkers.[18] In general, these spectroscopic studies have provided considerably more

information on the ionic excited states than on the van der Waals states; only the XeF and

XeCl spectra show discrete structure associated with bound levels of the ground state. The

ionic states have also been studied theoretically; the *ab initio* configuration interaction

calculations by Hay and Dunning[19] provided a particularly clear picture of these excited states,

and greatly facilitated the assignment of the features observed in the emission spectra.

However, *ab initio* calculations have been less useful in describing the weaker ground state

interactions.

The RgX⁻ anions have not been nearly as well studied as the neutrals. Potential energy

functions for several of these have been derived from the ion mobility studies by Albritton,[20]

McDaniel,[21,22] Viehland[23] and their coworkers. Empirical, semi-empirical, and *ab initio*

potential energy functions for these species have been proposed by several research groups.[24]

The results presented here are the first observation of vibrational energy levels in RgX⁻

anions and the ArBr, ArI, and KrI van der Waals states. From this data, we can extract

potential energy functions for the anion and three neutral van der Waals states. These are

compared to the potential energy functions obtained previously by other investigators. Among

the three systems we report here, ArBr and KrI have been studied by Lee and coworkers[7]

while the interaction potentials of the ArI complex have not been reported previously. Overall,

we find reasonable agreement with Lee's X1/2 and I3/2 potentials. The scattering experiments

provide no information on the $\Pi 1/2$ potentials because of the negligible populations of the Br and I $^2P_{1/2}$ states, from which the $\Pi 1/2$ state derives. We find considerably more disagreement with the previously published anion potentials.

II. Experimental

The negative ion high resolution threshold photodetachment (ZEKE) spectrometer has been described in detail previously.[25] A cold RgX⁻ beam is generated by expanding a 1-2% mixture of HBr or HI in rare gas (Ar or Kr) (or the mixture of Ar (or Kr) and He gas) through a pulsed molecular beam valve, typically with a backing pressure of 60 psi, and then crossing the molecular beam with a 1 keV electron beam just outside the valve orifice. Negative ions are formed through dissociative attachment and clustering processes in the continuum flow region of the free-jet expansion and their internal degrees of freedom are cooled as the expansion progresses. The negative ions that pass through a 2 mm diameter skimmer are collinearly accelerated to 1 keV and mass-selected with a 1 meter long beam-modulated time-of-flight mass spectrometer.[26] The mass-selected ions then enter the detection region where they are photodetached by an excimer-pumped dye laser. For photodetachment of ArBr⁻, DMQ and Rhodamine 640 laser dyes were used and the latter was doubled with a KDP crystal; for ArI⁻, BBQ, DPS and Rhodamine 610 dyes were used and the last one was doubled with a β-barium borate (BBO) crystal. For KrI⁻, DPS and Rhodamine 610 dyes were used and again the latter was doubled with a BBO crystal.

Only those electrons produced with nearly zero kinetic energy are detected using a scheme based on the design of Müller-Dethlefs et al.[27] for ZEKE photoionization of neutral species. First, a delay of 150-300 ns subsequent to photodetachment allows the more energetic electrons and the threshold electrons to separate. Then a weak field (2-5 V/cm) is applied collinearly to extract the photoelectrons. Finally ZEKE electrons are selectively detected by using a combination of spatial and temporal filtering. The ultimate resolution of the instrument is 0.3 meV. However, under the operating conditions used in these experiments the resolution was 0.4 - 0.6 meV. The electron signal is normalized to laser power and the ion signal.

III. Results

The ZEKE spectra of ArBr⁻, ArI⁻ and KrI⁻ are shown in Figures 1, 2, and 3, respectively. The spectrum of each complex consists of two distinct groups of features separated approximately by the spin-orbit splitting of the halogen atom $X(^2P)$ (0.457 eV for Br and 0.943 eV for I). It appears that the features at lower photon energies consist of two close-lying bands, referred to, in order of increasing energy, as bands A and B. The highest energy band is labeled band C.

Each band consists of a single intense peak with several smaller peaks on either side. Peak spacings within a band range from 6 cm⁻¹ to 26 cm⁻¹. These spacings are consistent with the transitions expected between the various anion and neutral vibrational levels. The largest peak in each band is taken to be the origin and is marked with an arrow. Typically, peaks to the blue of the origin peaks are spaced by ca. 20 cm⁻¹. When more than one peak is observed,

such as in band B of the ArBr$^-$ and KrI$^-$ spectra, the spacing decreases towards the blue side. The peaks to the red of the origin peaks have smaller spacings, and the spacings appear to be more irregular. Since band A and band B are very close to each other in energy, one cannot determine at first glance the band to which the peaks between peak 1 and peak 2 belong. In bands A and C, the intensities of the peaks to the red of the origins depend on source conditions, which indicates that these peaks are `hot band' transitions from vibrationally excited anion states. The most significant difference among spectra of the different species is the length of progression in each corresponding band. For instance, we only observe one peak to the blue of peak 2 in the ArI$^-$ spectrum, while more extended progressions are seen in band B of the ArBr$^-$ and KrI$^-$ spectra.

The peak widths are between 6-9 cm^{-1} (FWHM). Peaks in different bands show slightly different peak shapes. Typically, it appears that peaks in band A have a slight tail towards the blue while peaks in bands B and C are more symmetric; this is most evident in the KrI$^-$ spectrum, Figure 3. Peak widths are also dependent on the source conditions. As discussed in Section IVc, the peak shapes are related to the rotational sub-band profiles, and consequently depend on the anion rotational temperature and the rotational constants in the anion and neutral.

In assigning the RgX$^-$ ZEKE spectra, we first explain the band structure in terms of transitions from the anion to different neutral electronic states. Model potentials for the relevant states are shown in Figure 4. As pointed out earlier, there are three neutral electronic states labeled by the quantum number Ω, the projection of the electronic spin and orbital angular momentum onto the internuclear axis. At very large internuclear distance, the X1/2

and I3/2 states correlate to the $X(^2P_{3/2})$ + Rg ($^1S_0$) asymptote, while the II1/2 state correlates to the higher-lying $X^*(^2P_{1/2})$ + Rg($^1S_0$) asymptote. These two asymptotes are separated in energy by the spin-orbit splitting of the corresponding halogen atom. Because the well depths of the neutral adiabatic potentials are expected to be much smaller than the spin-orbit splitting of $Br(^2P)$ or $I(^2P)$, transitions to the II1/2 neutral state should be considerably higher in energy than those to the X1/2 and I3/2 states. We assign the peaks observed in band C to transitions from the anion state to the II1/2 neutral electronic state. Peaks in band A and B are then assigned to transitions to X1/2 and I3/2 neutral states, respectively. Note that we are clearly in the Hund's case (c) regime; the electrostatically induced splitting (*i.e.*, the energy separation between band A and band B) is much less than the spin-orbit splitting of the Br or I atom.

We next consider the vibrational structure in each band. The peaks to the blue of the origin peak are assigned to a progression in the neutral van der Waals vibration (1-0, 2-0, 3-0, etc.). This yields vdW vibrational frequencies on the order of 20 cm^{-1}, consistent with what one would expect based on the potentials derived from Lee's crossed beams experiments. The anions should be more strongly bound than the neutrals, and the anion vibrational frequencies should be higher. Hence the more closely spaced peaks to the red of the origins are assigned primarily to sequence bands (1-1, 2-2, etc.) and other hot band transitions. Based on this, the rest of the peaks are assigned by analyzing the peak spacings. The positions and assignments of peaks in each band are tabulated in Tables I, II and III.

There is considerable variation in the appearance of this vibrational structure among the different spectra. According to the Franck-Condon principle, the length of a progression is determined by the relative position and shape of the corresponding anion and neutral potential

63

energy curves. For instance, in the ArBr⁻, band A consists entirely of sequence band transitions, band B consists only of a progression in the neutral, and band C shows both types of transitions. This indicates the anion equilibrium geometry is closest to that of the X1/2 state and furthest from that of the I1/2 state. The more quantitative extraction of potentials from these spectra is discussed below.

IV. Analysis

The RgX⁻ ZEKE spectra can be analyzed to obtain potential energy functions for the anion and three neutral electronic states accessed in the spectra. This section describes the simulation method and the form of the resulting potential energy curves. We also address in this section another aspect of our spectra, the asymmetric, non-Gaussian peak shapes. These peak shapes are explained in terms of a combination of the ZEKE instrumental line shape and unresolved underlying rotational structure.

A. Method of calculation of the Franck-Condon factors

In our analysis of the ZEKE spectra, interaction potentials are obtained by an iterative fitting procedure. For a given set of anion and neutral potentials, the spectra are simulated by (a) calculating the eigenvalues and eigenfunctions supported by each potential; (b) calculating the Franck-Condon overlap between the first few anion vibrational levels and the levels supported by the neutral potential energy curves, and (c) comparing the peak positions and intensities in the Franck-Condon simulation to the experimental spectrum.

64

The model potentials need to be varied many times to optimize the fit between the simulated and experimental spectra, so an efficient theoretical scheme to calculate the eigenvalues and eigenvectors is required. We use a discrete variable representation (DVR) to determine the eigenvalues and eigenfunctions. This method was first proposed by Harris *et al.*[28] and has been extended by Light *et al.*.[29] Our implementation of the DVR to the problem at hand has been described elsewhere.[30] We use a standard version in which the DVR points are determined by diagonalization of the position operator in a one-dimensional harmonic oscillator basis. Even for the one dimensional calculation, the DVR offers a great increase in speed as the potential energy part of the Hamiltonian matrix is diagonal in DVR basis and we do not have to set up and diagonalize a new Hamiltonian matrix for each model potential.

B.   Nature of the potential energy curves

It is desirable to use potential energy functions that are flexible enough to fit all the vibrational features in our spectra. All aspects of the vibrational structure, including the peak spacings and intensities must be reproduced in the simulations. Over the years, many sophisticated potential energy functions have been developed to account for the extensive experimental results on rare gas-rare gas interactions,[1,2] and these can be used for the rare gas-halogen systems as well. Moreover, these functions can be adapted to the rare gas halide anions by appropriate modification of the long range attraction.

Lee and co-workers[6,7] have published potential functions for the X1/2 and I3/2 states of ArBr and KrI based on their differential cross section measurements. Since these are a convenient starting point for our analysis, we decided to use the same functional form as they did, namely, the MMSV (Morse-Morse-switching function-van der Waals) potential. This is

an extremely flexible piecewise potential. In reduced form, with $x = r/r_m$ and $f(x) = V(r)/\varepsilon$, the MMSV potential for each neutral RgX state is given by

$$
\begin{aligned}
f(x) \ = \ & \exp[2\beta_1(1-x)] - 2\exp[\beta_1(1-x)], \quad 0 < x \le 1, \\
= \ & \exp[2\beta_2(1-x) - 2\exp[\beta_2(1-x)] \equiv M_2(x), \quad 1 < x \le x_1, \\
= \ & SW(x)M_2(x) + [1 - SW(x)]W(x), \quad x_1 < x < x_2, \\
= \ & -C_{6r}x^{-6} - C_{8r}x^{-8} \equiv W(x), \quad x_2 \le x < \infty,
\end{aligned}
\tag{1}
$$

The switching function $SW(x)$ is given by

$$
SW(x) \ = \ \frac{1}{2}\left[\cos\frac{\pi(x - x_1)}{(x_2 - x_1)} + 1\right],
\tag{2}
$$

and the long range attraction constants are given by

$$
C_{6r} \ = \ C_6/(\varepsilon r_m^6), \quad C_{8r} \ = \ C_8/(\varepsilon r_m^8);
\tag{3}
$$

Here ε is the well depth and r_m the internuclear distance of the potential minimum. C_6 and C_8 are the dispersion coefficients which account for the induced dipole-induced dipole and the induced dipole-induced quadrupole interactions, respectively. Any other constants of the same order or higher order are neglected because of their very small contributions.

In the cases of ArBr and KrI neutral states, we use the C_6 and C_8 constants which were previously used by Lee and coworkers.[7] For the states which were not studied in their experiments, we estimate the C_6 and C_8 constants the same way as they did. The C_6 constants are estimated from the Slater-Kirkwood formula[31] for the effective number of electrons and polarizabilities. The relevant polarizabilities are: Br 3.05 Å^3, I 5.35 Å^3, Ar 1.64 Å^3, and Kr

66

2.48 Å^3.[32] The C_8 constants of ArKr, ArXe and KrXe are used for ArBr, ArI and KrI, respectively. The C_8 constants for the unlike rare gas pairs are estimated by applying the combining rules based on Cohen and Pack.[33] These values are consistent with those calculated based on the method of Koutselos et al.[34]

For the anion potential, the leading long range attraction term should be dominated by a $-1/r^4$ term with a significant contribution from a $-1/r^6$ term. We adapt the same MMSV potential form for the anion electronic state except the last (fourth) piece of the potential form, which now should be written as:

$$f(x) = -B_{4r}x^{-4} - B_{6r}x^{-6} \equiv W(x), \quad x_2 \leq x < \infty, \tag{4}$$

where

$$B_{4r} = B_4 / (\varepsilon r_m^4), \quad B_{6r} = B_6 / (\varepsilon r_m^6); \tag{5}$$

and

$$B_4 = -q^2 \alpha_B / 2, \quad B_6 = -q^2 \alpha_q^B / 2 + C_6; \tag{6}$$

Here q is the negative charge on the X$^-$, while α_B and α are the dipole and quadrupole polarizability of the rare gas atom, respectively. The B_6 constant consists of contributions from two terms: the charge-induced quadrupole interaction and the induced dipole-induced dipole interaction. When estimating the latter, the following anion polarizability values are used: Br$^-$ 5.22 Å^3, I$-$7.81 Å^3.[35]

Since only transitions between several low-lying anion and neutral vibrational levels are observed, our simulation is not sensitive to the very long range part of the potential or the

repulsive part of the potential with energies well above the asymptote. The long range part of the potential mainly affects the vibrational levels close to the dissociation limit. Therefore, during our simulation, C_6, C_8, B_6, and B_8 are left unchanged at the estimated values.

In addition to fixing the long range attraction constants, there is one extra restriction on the potential parameters of the involved potentials. Once one of the four well depths is determined, we can immediately extract the other three well depths from the known or experimentally determined energetics. For example, if ε_X is known for the X1/2 state, ε_a of the anion potential is determined from:

$$ v_{00} + \omega_0^a + \varepsilon_X - \omega_0^X \;=\; \varepsilon_a + EA \tag{7} $$

Here, v_{00} is the energy of the origin transition for band A, EA is the electron affinity of the halogen atom, (3.3636 eV for Br,[36] 3.0591 eV for I[37]) and ω and ω are the zero point energies of the anion state and the neutral X1/2 state, respectively. This relation is made clear in Figure 4. The zero point energies can be estimated based on vibrational frequencies we obtained in the assignments, or from the DVR calculation of the corresponding potentials. In any case, the error involved in the difference of the zero point energies should be very small compared to the energy scale of the well depth. Once the anion well depth is determined, the well depths of the I3/2 and II1/2 neutral states are extracted by the same method.

In simulating the ArBr⁻ and KrI⁻ spectra, we start with the X1/2 and I3/2 potentials from reference 7. The initial estimate for the anion potential function is obtained by fitting the peak positions and intensities in bands A and B. The initial potential for the II1/2 neutral state is then constructed by simulating band C. The initial potentials for all neutral and anion states

are subsequently optimized to obtain the best fit between the experimental and simulated spectra in all three bands. However, as discussed in Section IVd, it is difficult to determine absolute values for r_m and ε from our spectra. We therefore fix these parameters for the X1/2 states of ArBr and KrI at the same values found by Lee and co-workers.[7]

There are no reported experimental results for the ArI complex. We therefore require a means of accurately estimating r_m and ε for one of the neutral electronic states. This is done by modification of the simple correlation formulae for r_m and ε in terms of atomic polarizabilities (in $Å^3$) proposed by Pirani *et al.*:[38]

$$R_m = 1.767\frac{\alpha_A^{1/3} + \alpha_B^{1/3}}{(\alpha_A \alpha_B)^{\gamma}}\ (Å),\quad \varepsilon = 0.72\frac{C_6}{R_m^6}\ (meV)$$

$$where\quad \gamma = 0.095$$

(8)

As will be discussed in Section V, Eqs. 8 should apply to the II1/2 state when the halogen spin-orbit splitting is large. Nonetheless, a slight modification of the numerical coefficients (1.728 for R_m, 0.78 for ε) is necessary to reproduce our values of r_m and ε for the II1/2 states of ArBr and KrI, and we use Eqs. 8 with these modified coefficients to determine r_m and ε for the II1/2 state of ArI. We then determine the anion potential and the potentials for the X1/2 and I3/2 states applying the same procedure used for ArBr and KrI.

The Franck-Condon calculation generates a vibrational stick spectrum. To obtain a simulation that can be compared to the experimental spectrum, the stick spectrum must be convoluted with the factors that result in a non-zero finite experimental line width. These are considered in the following section.

69

C. Peak shape and rotational analysis

As mentioned previously, the peak shapes of the ZEKE spectra are asymmetric and change from band to band. In addition, the peak widths vary with source conditions. We explain the peak shape and width in terms of the asymmetric ZEKE experimental peak shape combined with the effect of the unresolved rotational structure associated with each vibrational transition. Both effects are discussed in this section, with the main focus on how one treats the rotational contribution to the peak widths.

The ejected electron has spin s=1/2 and orbital angular momentum l=0 (only s-wave photodetachment is observed in anion ZEKE experiments[25]). Hence, the anion → neutral rotational selection rules are $\Delta J=\pm 1/2, \pm 3/2$. Since individual rotational lines are not resolved in our spectra, several assumptions are required to simulate these transitions. For calculating the energies of the rotational transitions in each band, equilibrium rotational constants B_e are assumed, using the r_m values from the potentials obtained in the vibrational analysis discussed above.

The more difficult aspect of the rotational analysis involves calculating the relative intensities of the rotational transitions in each band. Xie and Zare[39] derived an expression for the photoionization probability of a diatomic molecule conforming to Hund's case (b) in terms of a generalized rotational line strength factor and the reduced multipole moments. Here we adapt this approach to a Hund's case (c) molecule. The results are valid for photodetachment as well as photoionization. Although we do not resolve individual rotations in the spectra presented in this paper, the results presented below should be useful for future investigations in

70

which rotational structure is resolved. Moreover, the final expressions obtained are quite simple, and result in a very satisfactory fitting of the peak shapes.

The eigenstates of a case (c) molecule are represented by

$$|nJ\Omega Mv\rangle = |J\Omega M\rangle|n\Omega\rangle|v\rangle \qquad (9)$$

where the angular momentum quantum numbers are defined in Table IV; v is the vibrational quantum number, and n represents the remaining quantum numbers. On the right side of 9 we have assumed the Born-Oppenheimer approximation and independence of rotational from vibrational degrees of freedom to separate the eigenstate into rotational, electronic and vibrational parts. The detached electron is assumed to be well approximated asymptotically by a partial wave expansion in a spherically symmetric potential.[40] The eigenstate of a given electron partial wave in the coupled representation appropriate to case (c) is $|jm\rangle$, where j is the total (orbital and spin) angular momentum of the electron partial wave, and m its projection in the space-fixed frame. The electronic dipole operator transforms as a spherical tensor, $T(1, \mu_0)$, under rotation. The photodetachment probability for a given electron angular momentum from rotational state J^- of the anion to state J of the neutral is then (neglecting constants and the vibrational eigenvectors):

$$P_j(J^-,J) \propto \sum_{m} \sum_{M,M^-} |<J\Omega M|<n\Omega|<jm|T(1,\mu_0)|n^-\Omega^->|J^-\Omega^-M^->|^2 \quad (10)$$

We transform the dipole operator and electron eigenstates to the molecule fixed frame using the Wigner rotation matrices as defined by Zare[41][p.85]:

$$T(1,\mu_o) = \sum_{\mu} D^{I}_{\mu_o\mu}(R)T(1,\mu)$$

$$<jm| = \sum_{\omega} \left[D^{j}_{m\omega}(R)\right]^{\dagger}<j\omega|$$

(11)

where R stands for the Euler angles ϕ, θ and χ, and the angular momentum quantum numbers are defined in Table IV.

The rotational eigenfunctions are

$$|J^{-}\Omega^{-}M^{-}> = \left(\frac{2J^{-}+1}{8\pi^{2}}\right)^{\frac{1}{2}} D^{J^{-}}_{M^{-}\Omega^{-}}(R)$$

$$< J\Omega M| = \left(\frac{2J+1}{8\pi^{2}}\right)^{\frac{1}{2}}\left[D^{J}_{M\Omega}(R)\right]^{\dagger}$$

(12)

Substituting Eqs. (11) and (12) into Eq. (10) gives

$$P_{j}(J^{-},J) \propto \frac{(2J+1)(2J^{-}+1)}{(8\pi^{2})^{2}}\sum_{m}\sum_{M,M^{-}}\left|(-1)^{M-\Omega+m+\mu_{o}+M^{-}-\Omega^{-}} x \sum_{\mu,\omega}\right.$$

$$(-1)^{-\omega-\mu}\left(\int D^{J}_{M\Omega}(R)D^{j}_{m\omega}(R)D^{1}_{-\mu_{o}-\mu}(R)D^{J^{-}}_{-M^{-}-\Omega^{-}}(R)dR\right)$$

(13)

$$\left. x <n\Omega|<j\omega|T(1,\mu)|n^{-}\Omega^{-}>\right|^{2}$$

where all the dependence on angular nuclear coordinates is contained in the integral over the four rotation matrices.

To evaluate the integral over the four rotation matrices, we expand those from the detached electron and dipole operator in a Clebsch-Gordon series[41][pp.98-100]

72

$$D^j_{m\omega}(R)D^1_{-\mu_0-\mu} = (-1)^{p-q}\sum_k (2k+1)\begin{pmatrix} j & 1 & k \\ m & -\mu_0 & p \end{pmatrix}\begin{pmatrix} j & 1 & k \\ \omega & -\mu & q \end{pmatrix}D^k_{-p-q}(R) \quad (14)$$

with

$$k = 1+j, ..., |1-j|$$

$$p = \mu_0 - m$$

$$q = \mu - \omega$$

Substituting this into Eq. (13) we obtain an integral over three rotation matrices[41][p.103]

$$\int D^J_{M\Omega}(R)D^k_{-p-q}(R)D^{J^-}_{-M^- -\Omega^-}(R)dR = 8\pi^2\begin{pmatrix} J^- & k & J \\ M^- & p & -M \end{pmatrix}\begin{pmatrix} J^- & k & J \\ \Omega^- & q & -\Omega \end{pmatrix} \quad (15)$$

Using Eqs. (14) and (15) in Eq. (13) we obtain

$$P_j(J^-,J) \propto (2J+1)(2J^-+1)\sum_m\sum_{M,M^-}\left|(-1)^{M-\Omega+m+\mu_0+M^- -\Omega^-+p}\right.$$

$$\times\sum_k(2k+1)\begin{pmatrix} j & 1 & k \\ m & -\mu_0 & p \end{pmatrix}\begin{pmatrix} J^- & k & J \\ M^- & p & -M \end{pmatrix}\begin{pmatrix} J^- & k & J \\ \Omega & \Omega-\Omega^- & -\Omega \end{pmatrix} \quad (16)$$

$$\times\sum_{\mu,\omega}(-1)^{\mu-\omega-q}\begin{pmatrix} j & 1 & k \\ \omega & -\mu & q \end{pmatrix}\left.< n\Omega/< j\omega/T(1,\mu)/n^- \Omega^- >\right|^2$$

The condition $q = \Omega - \Omega^-$ (ie. $\mu+\Omega^- = \omega+\Omega$) determines the electronic selection rules.

The M and M^- dependent terms in the square of the sum over k for a given k' and k'' give rise to sums

$$\sum_{M,M^-} \begin{pmatrix} J^- & k' & J \\ M^- & p & -M \end{pmatrix} \begin{pmatrix} J^- & k'' & J \\ M^- & p & -M \end{pmatrix} = \frac{1}{2k'+1} \delta_{k'k''} \qquad (17)$$

so that the cross terms vanish,[39] leaving

$$P_j(J^-,J) \propto \frac{1}{3} \sum_k S_k(J^-,J) |\mu_j(k,q)|^2 \qquad (18)$$

Here, following Xie and Zare,[39] we define the rotational line strength factor

$$S_k(J^-,J) = (2J+1)(2J^-+1) \times \left| \begin{pmatrix} J^- & k & J \\ \Omega^- & \Omega - \Omega^- & -\Omega \end{pmatrix} \right|^2 \qquad (19)$$

which contains all the J and J^- dependence, and a generalized multipole transition moment:

$$|\mu_j(k,q)|^2 = (2k+1) \left| \sum_{\mu,\omega} (-1)^{-\mu-\omega-q} \begin{pmatrix} j & 1 & k \\ \omega & -\mu & q \end{pmatrix} \times \langle n\Omega | \langle j\omega | T(1,\mu) | n^-\Omega^- \rangle \right|^2 \qquad (20)$$

In anion ZEKE spectroscopy, $j=1/2$ (because $l=0$ for the detached electron) and 18 becomes

$$P_{\frac{1}{2}}(J^-,J) \propto C_{\frac{1}{2}} S_{\frac{1}{2}}(J^-,J) + S_{\frac{3}{2}}(J^-,J) \qquad (21)$$

with

$$C_{1/2} = \left| \frac{\mu_{1/2}(1/2,q)}{\mu_{1/2}(3/2,q)} \right|^2 \qquad (22)$$

For s-wave detachment, $\Delta J = J' - J = \pm 1/2, \pm 3/2$. Expressions for the line strength factors for transitions from $\Omega=0$ to $\Omega=1/2$ (X1/2 and II1/2 states) and to $\Omega=3/2$ (I3/2 state) for each of the allowed branches are given in Tables V. Note that $S_{1/2}(J', J)$ vanishes for the $\Delta J=\pm 3/2$ branches of the transitions to $\Omega=1/2$ states and for all branches of transitions to the $\Omega=3/2$ state.

One can calculate a rotational stick spectrum by multiplying Eq. (21) by a Boltzmann factor, treating the coefficient $C_{1/2}$ (for the $\Omega=1/2$ neutral states) as an adjustable parameter. To obtain realistic peak shapes, the rotational lines must be convoluted with the empirically determined ZEKE instrumental line shape. Based on our results for the atomic halides,[25] the ZEKE line shape is represented by a linearly rising edge on the low energy side followed by an exponentially decaying tail:

$$y = 1 - k \bullet (E_0 - E), \quad \left(E_0 - \frac{1}{k}\right) \le E < E_0$$

$$y = \exp(a \bullet ((E - E_0) - b)^2) - 1, \quad E_0 \le E < (E_0 + b); \qquad (23)$$

where

$$b = 3.1895xFWHM, \quad a = \ln 2 / b^2, \quad k = 2 / FWHM$$

Here E, E_0, and FWHM are all in units of meV, and E_0 is the calculated energy of the rovibronic transition.

Figure 5 shows how both of these effects contribute to a single vibrational feature in the KrI$^-$ ZEKE spectrum. The solid lines show the effect of rotational structure alone. These were obtained by adding up the rotational sticks within each energy interval of 0.5 cm^{-1}. The

rotational constants used reflect the anion and neutral r_m values for KrI, for which $r_X < r_{an} < r_I < r_{II}$ (see below). A rotational temperature of 40 K is assumed, consistent with previous experiments in which we were able to resolve individual rotational transitions.[25] The peaks are shaded towards the blue in the X1/2 band and towards the red in the I3/2 band and II1/2 band. The dotted lines in Figure 5 show the result of convoluting the individual rotational lines with the ZEKE instrumental peak shape; the FWHM of the ZEKE peak is assumed to be 4.0 cm^{-1}. This makes the X1/2 band shade further towards the blue and makes the other two bands more symmetrical, in qualitative agreement with experiment.

In simulating the experimental spectra, a least-squares fit is used to determine the parameters FWHM, $C_{1/2}$ (Eq. (21)), and C_{IX}, which determines the relative intensities of the I3/2 and X1/2 bands. The rotational temperature was fixed at 40 K; this procedure was used because the ZEKE linewidth and rotational temperature are highly correlated, and the ZEKE linewidth is the parameter more likely to vary with experimental conditions. B_e is determined from the results of vibrational analysis.

The simulated spectra are shown superimposed on the experimental spectra in Figures 1, 2, and 3. The potential parameters with which we obtain the best simulations are tabulated in Table VI, VII, and VIII. The potentials for the neutral X1/2, I3/2 and II1/2 states and the anion state are shown in Figure 6. The vibrational temperatures of the anions, the rotational constants of each electronic state, FWHM of the ZEKE peak, C_{IX}, and $C_{1/2}$ of each band are tabulated in Table IX.

D. Error analysis

It is important to consider the error bars in the potential energy parameters. Estimated error bars were obtained by systematically varying the parameters and observing when the agreement between the simulated and experimental spectra deteriorates. The accuracy of ε and r_m for each state are of particular interest. Our spectra are very sensitive to differences in ε and r_m among the various electronic states, but, since only the first 2-3 vibrational levels for each state are observed, absolute values of these parameters for any state cannot be determined to better than $\pm 10\%$ accuracy. This is why, in the case of ArBr and KrI, ε and r_m for the X1/2 ground state are assumed to be the same as in the potentials obtained by Lee and coworkers.[7] For ArBr their estimated error bars are ± 1 meV for ε and ± 0.2 Å for r_m; for KrI the error bars are ± 2 meV for ε and ± 0.4 Å for r_m. Once ε and r_m for the X1/2 state are fixed, the additional relative errors in ε and r_m for the anion and other neutral states are quite small, on the order of 1-2%. It was necessary to modify Lee's other potential parameters slightly to fit our spectra; his X1/2 potentials predict vibrational frequencies that are too high in case of ArBr.

The situation for ArI is more problematic as there are no potentials available as a reference point. Hence, both r_m and ε for the II1/2 state were fixed as discussed in Section IVb. Since r_m for ArI certainly lies between the values for ArBr and KrI, its error bars are about $\pm 5\%$. To find the error bars for ε(II1/2), we performed several simulations in which this parameter was varied and all II1/2 and anion parameters were adjusted to optimize the fit to experiment. Based on this, the maximum error bars for ε(II1/2) are $\pm 10\%$ (± 2.3 meV). Again, the additional relative error bars in ε and r_m for the anion and other neutral states are 1-2%. Error bars for the other potential parameters have also been estimated. The results for β_1, β_2, x_1, x_2, B_4, B_6, C_6, and C_8 are $\pm 7\%$, $\pm 4\%$, $\pm 6\%$, $\pm 9\%$, $\pm 15\%$, $\pm 25\%$, $\pm 15\%$, and $\pm 30\%$,

77

respectively. These were obtained by varying only the parameter in question and testing the effect on the overall fit; these are thus lower bounds to the error bars because all other parameters were fixed. One conclusion we draw from the error analysis is that changes in the parameters representing the long-range interactions (*i.e.*, B_4, B_6, C_6 and C_8) are not sensitive to the spectral features observed in our spectra. We are more sensitive to the bottom of the potential than to the long-range attractive region. This situation differs from our earlier study of I^-CO_2 in which more extended vibrational progressions were observed.[5]

As for the parameters involved in the least-square fitting of the peak shapes, their error bars are directly determined from the fitting procedure. The error bars in FWHM are ± 0.5 cm^{-1}, those in C_{IX} are ± 0.04, while those in $C_{1/2}$ are typically much larger, ranging up to several hundred percent. Hence, this last parameter plays a small role at best in determining the peak shapes; the observed variations in peak shapes are primarily due to the differences in rotational constants among the various electronic states.

V. Discussion

In this section, we examine in more detail some features of the RgX^- and RgX potential energy curves obtained in the previous section. Several different trends in the ε and r_m parameters will be summarized. The first point to consider is the change in the Rg-X bond length upon photodetachment. For weakly bound molecules or ions, the length of the weak bond is determined by the strength of the attractive interaction and the sizes of the atoms involved in the bond. In our case, these two factors compete: the anion is more strongly

78

bound than the neutral, but I^- (or Br^-) is larger than I (or Br). Our results show the same trend in relative bond lengths for each Rg-X system: $r_{X1/2} < r_{anion} < r_{III/2} < r_{B/2}$. The trend in well depths for each system is $\varepsilon_{B/2} < \varepsilon_{III/2} < \varepsilon_{X1/2} < \varepsilon_{anion}$.

The above trend in bond lengths differs from the $I \bullet CO_2$ system, for which $r_{anion} < r_{X1/2} < r_{III/2} < r_{B/2}$.[5] The relatively shorter bond length in $I^- CO_2$ is consistent with the large binding energy of $I^- CO_2$ ($\varepsilon = 212$ meV), compared to the X1/2 $I \bullet CO_2$ well depth of 44.5 meV. In contrast, the differences between the RgX^- and RgX well depths are not as large. The $I \bullet CO_2$ system shows the same trends in well depths as the RgX systems: $\varepsilon_{B/2} < \varepsilon_{III/2} < \varepsilon_{X1/2} < \varepsilon_{anion}$.

A comparison of the different RgX systems with each other shows that for each neutral state, r_m (ArBr) $< r_m$ (ArI) $< r_m$ (KrI), and ε (ArBr) $< \varepsilon$ (ArI) $< \varepsilon$ (KrI). The trend in anion r_m values is the same as in the neutral: r_m (ArBr$^-$) $< r_m$ (ArI$^-$) $< r_m$ (KrI$^-$). However, the ordering of the anion well depths is ε(ArI$^-$) $< \varepsilon$(ArBr$^-$) $< \varepsilon$(KrI$^-$), which differs from the neutrals. The trends in anion and neutral bond lengths are consistent with the atomic sizes. The neutral well depths follow the same trends as in the interactions between the analogous closed shell atoms, namely that ε (ArKr) $< \varepsilon$ (ArXe) $< \varepsilon$ (KrXe).[2]

The ordering of the anion well depths can be understood considering that the well depth for a Rg-X$^-$ complex is determined by the balance between short range repulsion and the long range attraction between the charge of X$^-$ and the polarizability of the rare gas atom. Since the amount of charge for Br$^-$ and I^- is the same, and the polarizability of Kr is larger than that of Ar, we expect KrI$^-$ to have the deepest potential well. Comparing ArBr$^-$ and ArI$^-$, we have the same amount of charge interacting with the same polarizability. However, since Br$^-$ is smaller than I^-, Br$^-$ should lie closer to Ar than I^- does, resulting in a slightly larger well depth

for ArBr⁻. These considerations would lead one to predict that $\varepsilon(KrI^-) < \varepsilon(KrBr^-)$, and we have recently confirmed this.[42]

The only other detailed experimental results for the ArBr and KrI potentials come from the differential cross section measurements of Lee and coworkers.[7] In Tables VI and VIII, our potential functions for the X1/2 and I3/2 states of ArBr and KrI are compared to those derived from the scattering experiments. These experiments are fundamentally different from ours in that (a) in principle, they probe the entire Rg-X potential including the long-range attraction and repulsive wall (at least up to the collision energies used in their experiments), and (b) they provide absolute values for r_m and ε. For example, the rainbow maximum in the differential cross section (only partially resolved in Ref. 7) is directly related to the well depth. In contrast, our experiment is more sensitive to the Franck-Condon region near the potential energy minimum and less sensitive to the repulsive wall above the dissociation limit and, for the complexes reported in this paper, the long-range attractive part of the potential. Also, in our experiment, the contributions of the X1/2 and I3/2 states are clearly separated, whereas this is not the case in the scattering experiments. Finally, as mentioned earlier, the molecular beam experiments provide no information on the II1/2 state because of the negligible Br* and I* populations in the halogen atom beams, so our experiments provide the first detailed characterization of these potentials.

In spite of the differences between the two sets of experiments, our potential functions for the X1/2 and I3/2 states are quite similar to those obtained by Lee. This is perhaps not so surprising for the X1/2 states. As discussed above, the ε and r_m values for our X1/2 states were fixed at the values obtained by Lee. However, it was necessary to change β_1 and β_2 for

80

ArBr slightly in order to reproduce our vibrational frequencies. These parameters affect the curvature at the bottom of the potential energy well.

For the I3/2 states, the largest discrepancy between the spectroscopy and scattering experiments is in the KrI well depths (16.7 vs. 15.6 meV). Once the X1/2 well depth is known, the I3/2 well depth is determined by Eq. (7), so we believe our value is more accurate. We also obtained a better fit to our spectra using slightly different values for β_1 and β_2. Nonetheless, the overall agreement from the two experiments is quite good, providing strong support for the validity of the potential functions.

Our results for the anion potentials can be compared to those based on the gaseous ion transport data which were reported by Albritton[20] and McDaniel.[22] McDaniel and Viehland[23] obtained the interaction potentials on some of RgX⁻ complexes from the inversion of the mobility measurement results. McDaniel's results on ArBr⁻ (ε=59 meV, r_m=3.72 Å) agree reasonably well with our results (ε=54 meV, r_m=3.78 Å), while Viehland's results on ArBr⁻ (ε=82 meV, r_m=3.39 Å) and ArI⁻ (ε=76 meV, r_m=3.62 Å) represent significantly stronger binding than our values (for ArI⁻, ε=45.7 meV, r_m=4.07 Å). The error bars in the ε and r_m parameters from the ion transport data were estimated to be ±20-25%, but our values for ε are still outside the range of Viehland's values.

There has been a considerable effort over the years to develop predictive models for key features of the potential function between weakly interacting species.[2] These include (a) the development of combining rules,[43,44,45] in which one aims to predict r_m and ε for two unlike rare gas atoms based on the results for the homonuclear dimers, (b) the search for "universal" potential functions that can be applied to a large variety of systems by changing only a small

number of parameters,[46] and (c) the development of simple expressions for r_m and ε based on the properties of the separated atoms.[38] While most of this work is aimed at rare gas dimers, some of the results can be applied to the isotropic component of the interaction between rare gas and halogen atoms, and to the rare gas-halide interaction as well.

To compare our results for the neutral RgX potentials with any of these models, we need to extract the isotropic component of the potential energy function from the three experimental potentials. This is done as follows. In the absence of spin-orbit coupling, the interaction potential between a rare gas and a halogen atom can be written as[4]

$$V(r,\theta) = V_0(r) + V_2(r) P_2(\cos\theta), \tag{24}$$

where r is the internuclear distance and θ is the angle between the unfilled p-orbital on the halogen atom and the internuclear axis. Here, $V_0(r)$ represents the spherical component of the interaction potential, while $V_2(r)$ represents the anisotropic component due to the half-filled p-orbital on the halogen atom. Haberland[3] and Aquilanti et al.[4] showed that, if the spin-orbit coupling Δ is assumed independent of the internuclear distance, then the three potentials V(X1/2), V(I3/2), and V(II1/2) are related to $V_0(r)$ and $V_2(r)$ by (with $\Delta>0$)

$$\tag{25}$$

$$V(X1/2) = V_0 + \frac{V_2}{10} + \frac{\Delta}{2} - \frac{1}{2}\left(\frac{9}{25}V_2^2 + \Delta^2 - \frac{2}{5}V_2\Delta\right)^{\frac{1}{2}}$$

$$V(I3/2) = V_0 - \frac{V_2}{5}$$

$$V(II1/2) = V_0 + \frac{V_2}{10} + \frac{\Delta}{2} + \frac{1}{2}\left(\frac{9}{25}V_2^2 + \Delta^2 - \frac{2}{5}V_2\Delta\right)^{\frac{1}{2}}$$

Hence, from any two of the three experimental potentials, one can determine the isotropic and anisotropic components $V_0(r)$ and $V_2(r)$ of the Rg-X electronic interaction. These are shown in Figure 7 for the three systems. At long range, $V_2(r)$ is small but slightly positive, but at shorter range it becomes strongly negative. Also, for $|V_2|<<\Delta$, as in the cases considered here, $V(\Pi 1/2) \sim V_0$ (compare Tables VI-VIII with Table X).

The isotropic component, $V_0(r)$, can be directly compared to the experimental and theoretical potentials for rare gas dimers. Figure 7 shows the trend in the V_0 binding strength (the larger ε value and shorter r_m indicate the stronger binding) of the three Rg-X systems, *ie.*, KrI > ArI > ArBr. This trend is consistent with the change of polarizabilities of the interacting atoms. It has been noted that the strength of the isotropic van der Waals interaction is proportional to the product of the polarizabilities of the interacting atoms. We therefore expect, for example, ε and r_m values of the KrI V_0 potential to be somewhere between those values for the Kr-Xe and Xe-Xe complexes. This prediction is in agreement with the results in Table X, in which ε and r_m for the ArBr, ArI, and KrI V_0 potentials are compared to several rare gas dimers.[47]

Pirani and coworkers[38] have proposed particularly simple formulae for ε and r_m in terms of the polarizabilities of the separated atoms. The interaction between two neutral atoms A and B is given by Eq. 8, discussed in Section IVb. Table X shows comparison of the predicted values of ε and r_m for ArBr, ArI, and KrI with the values obtained from our $V_0(r)$ potentials. The table shows that the predicted r_m values are 3-5% too long, while the predicted ε values are too small by about 8%. We note that the scaling factors in Eq. 8 are derived from considering several rare gas dimers. While these formulae predict r_m and ε for other rare gas

83

dimers very accurately, one might encounter problems in extending them to open shell interactions.

Pirani and co-workers[38] have also proposed formulae analogous to Eq. 8 for the A^--B (negative ion-neutral) interaction:

$$R_m = 1.767 \frac{\alpha_{A^-}^{\frac{1}{7}} + \alpha_B^{\frac{1}{7}}}{[\alpha_{A^-} \alpha_B (1+\rho)]^{\gamma}} \quad (\mathring{a});$$

$$\varepsilon = 5.20 \times 10^3 \frac{\alpha_B}{R_m^4} (1+\rho) \quad (meV); \tag{26}$$

$$where \quad \rho = \frac{\alpha_{A^-} \alpha_B}{\left[1 + (2\alpha_{A^-}/\alpha_B)^{\frac{2}{3}}\right] \alpha_B^{\frac{3}{7}}}$$

Again the predicted r_m values are too large by 3-5 %, and the calculated ε values for A^--B interactions are *ca.* 30% too large. These discrepancies are not surprising given that there is little prior reference data on ion geometries from which to construct accurate scaling factors, and we hope that the data presented here will help alleviate this situation.

We next consider the anisotropic part of the Rg-X potential. Figure 7 shows that at long r_{Rg-X} range, the anisotropy, is very small, while at shorter range, V_2 becomes increasingly more negative. The small long-range anisotropy is from the anisotropy in the polarizability of the halogen atom, while the much larger shorter range anisotropy is attributed to significant state mixing between the ground covalent states and the strongly-bound excited ionic states.[4,7,19] As pointed out by Hay and Dunning,[19] in lowering the ionic $Rg^+ + X^-$ asymptote relative to the covalent Rg + X limit, the amount of the ionic character mixed into the covalent

states is increased. Given the values of electron affinity of Br and I [EA(Br)>EA(I), see Section IVb] and the ionization potentials of Ar and Kr [IP(Ar)=15.76 eV, IP(Kr)=14.00 eV], the separation of the ionic and neutral asymptotes increases according to KrI < ArI < ArBr. One therefore expects the magnitude in the shorter range anisotropies to be KrI > ArI > ArBr. This is confirmed in Figure 7. KrI has the largest magnitude of V_2 due to the lower IP value of Kr atom.

We close the discussion by comparing the KrI^- results to our earlier study of I^-CO_2.[5] The isotropic polarizability of CO_2 is 2.911 $\mathring{A}^3$, which is slightly larger than that of Kr. In applying the analysis of Eqs. 24 and 25 to the neutral potentials of $I\bullet CO_2$, we found that for $V_0(r)$, $r_m = 4.08$ $\mathring{A}$ and $\varepsilon = 32$ meV. These values indicate somewhat stronger binding than in KrI (see Table X), probably due to the interaction of the CO_2 quadrupole moment with the I atom polarizability in $I\bullet CO_2$. There is a much greater difference in the binding strength between I^-CO_2 (ε=212 meV, r_m=3.77 $\mathring{A}$) and KrI^- (ε=67 meV, r_m=4.11 $\mathring{A}$). This can not simply been explained on the basis of the extra charge - quadrupole interaction present in I^-CO_2. In fact, our photoelectron spectrum of I^-CO_2[48] shows that the CO_2 moiety is slightly bent in the anion. One might expect this to significantly increase the attractive interaction with the I^-, since bent CO_2 has a dipole moment, and the comparison with the KrI^- results strongly suggests that this is indeed the case.

VI. Conclusions

We have used anion ZEKE spectroscopy to study the ArBr⁻, ArI⁻, and KrI⁻ rare gas halide anions and corresponding open shell van der Waals complexes resulting from photodetachment of these anions. The open shell complexes have three low-lying states resulting from the electronically anisotropic interaction of Br or I($^2P_{3/2,1/2}$) with a rare gas atom (Ar or Kr), and all three are accessible by anion photodetachment. The ZEKE spectra show well-resolved vibrational progressions in the low frequency modes of the anion and the three neutral electronic states. These results represent the first observation of vibrational structure for these anion and neutral states. From the spectra, we are able to construct potential energy curves for the anion and the three neutral electronic states for these three complexes. These are compared to the potentials previously determined for ArBr and KrI from scattering experiments, and for the rare gas halides from ion mobility measurements.

We plan to apply this technique to study more of Rg-X complexes and larger clusters involving multiple rare gas atoms bound to a halide ion. Preliminary experimental results have already been obtained on KrBr⁻, XeBr⁻, ArCl⁻, KrCl⁻, and XeCl⁻ in our laboratory, as well as polyatomic Br⁻(Ar)ₙ and I⁻(Ar)ₙ clusters. The trends resulting from this work will provide significant insight into the nature of the interactions in weakly bound neutral and anion complexes.

Acknowledgments

References:

1. G. C. Maitland, M. Rigby, E. B. Smith and W. A. Wakeham, "Intermolecular Forces" (Oxford Univ. Press, Oxford, 1981).

2. R. A. Aziz, in "Inert Gases", M. L. Klein, Ed. (Springer Verlag, 1984) pp. 5-86.

3. H. Haberland, Z. Phys. A **307**, 35 (1982).

4. V. Aquilanti and G. Grossi, J. Chem. Phys. **73**, 1165 (1980); V. Aquilanti, G. Liuti, F. Pirani, and F. Vecchiocattivi, J. Chem. Soc., Faraday Trans. 2 **85**, 955 (1989).

5. Y. Zhao, C. C. Arnold, and D. M. Neumark, J. Chem. Soc. Faraday trans. **89**, 1449 (1993).

6. (a) C. H. Becker, P. Casavecchia, and Y. T, Lee, J. Chem. Phys. **69**, 2377 (1978); (b) ibid. **70**, 2986 (1979); (c) C. H. Becker, J. J. Valentini, P. Casavecchia, S. J. Sibener and Y. T. Lee, Chem. Phys. Lett. **61**, 1 (1979).

7. (a) P. Casavecchia, G. He, R. K. Sparks, and Y. T. Lee, J. Chem. Phys. **75**, 710 (1981); (b) P. Casavecchia, G. He, R. Sparks, and Y. T. Lee, ibid. **77**, 1878 (1982).

8. V. Aquilanti, R. Condori, and F. Pirani, J. Chem. Phys. **89**, 6157 (1988).

9. (a) V. Aquilanti, E. Luzzatti, F. Pirani, and G. G. Volpi, J. Chem. Phys. **89**, 6165, (1988); (b) V. Aquilanti, R. Condori, D. Cappelletti, V. Lorent and F. Pirani, Chem.Phys. **145**, 293 (1990).

10. (a) V. Aquilanti, D. Cappelletti, V. Lorent, E. Luzzatti and F. Pirani, Chem. Phys. Lett. **192**, 153, (1992); (b) V. Aquilanti, D. Cappelletti, V. Lorent, E. Luzzatti, and F. Pirani, J. Chem. Phys. **97**, 2063, (1993).

11. J. E. Velazco and D. W. Setser, J. Chem. Phys. **62**, 1990 (1975); G. Inoue, J. K. Ku, and D. W. Setser, J. Chem. Phys. **76**, 733 (1982); G. Lo and D. W. Setser, J. Chem. Phys. **100**, 5432 (1994).

12. J. J. Ewing and C. A. Brau, Phys. Rev. A **12**, 129 (1975); C. A. Brau and J. J. Ewing, J. Chem. Phys. **63**, 4640 (1975); J. J. Ewing and C. A. Brau, Appl. Phys. Lett. **27**, 350 (1975); C. A. Brau and J. J. Ewing, ibid. **27**, 435 (1975).

13. J. Tellinghuisen, J. M. Hoffman, G. C. Tisone, and A. K. Hays, J. Chem. Phys. **64**, 2484 (1976); J. Tellinghuisen, G. C. Tisone, J. M. Hoffman, and A. K. Hays, ibid. **64**, 4796

(1976); J. Tellinghuisen, A. K. Hays, J. M. Hoffman, and G. C. Tisone, *ibid.* **65**, 4473 (1976); P. C. Tellinghuisen, J. Tellinghuisen, J. A. Coxon, J. E. Velazco, and D. W. Sester, *ibid.* **68**, 5187 (1978); A. Sur, A. Hui, and J. Tellinghuisen, J. Mol. Spectrosc. **74**, 465 (1979).

14.   M. F. Golde and B. Thrush, Chem. Phys. Lett. **29**, 486 (1974); M. F. Golde, J. Mol. Spectrosc. **58**, 261 (1975); M. P. Casassa, M. F. Golde, and A. Kvaran, Chem. Phys. Lett. **59**, 51 (1978); M. F. Golde and A. Kvaran, J. Chem. Phys. **72**, 434(1980); 442 (1980).

15.   A. L. Smith and P.C. Kobrinsky, J. Mol. Spectrosc. **69**, 1 (1978).

16.   C. Jouvet, C. Lardeux-Dedonder, and D. Solgadi, Chem. Phys. Lett. **156**, 569 (1989).

17.   D. L. Monts, L. M. Ziurys, S. M. Beck, M. G. Liverman, and R. E. Smalley, J. Chem. Phys. **71**, 4057 (1979).

18.   R. B. Jones, J. H. Schloss, and J. G. Eden, J. Chem. Phys. **98**, 4317 (1993); J. H. Schloss, R. B. Jones, and J. G. Eden, *ibid.* **99**, 6483 (1993).

19.   (a) T. H. Dunning and P. J. Hay, Appl. Phys. Lett. **28**, 649 (1976); (b) P. J. Hay and T. H. Dunning, Jr., J. Chem. Phys. **66**, 1306 (1977); (c) T. H. Dunning and P. J. Hay, J. Chem. Phys. **69**, 134 (1978); (d) P. J. Hay and T. H. Dunning, Jr., J. Chem. Phys. **69**, 2209 (1978).

20.   I. Dotan and D. L. Albritton, J. Chem. Phys., **66**, 5238 (1977).

21.   M. G. Thackston, F. L. Eisele, H. W. Ellis, E. W. McDaniel, and I. R. Gatland, J. Chem. Phys. **73**, 3183 (1980).

22.   D. R. Lamm, R. D. Chelf, J. R. Twist, F. B. Holleman, M. G. Thackston, F. L. Eisele, W. M. Pope, I. R. Gatland, and E. W. McDaniel, J. Chem. Phys. **79**, 1965 (1983).

23.   C. C. Kirkpatrick and L. A. Viehland, Chem. Phys. **98**, 221 (1985).

24.   Y. S. Kim and R. G. Gordon, J. Chem. Phys. **61**, 1 (1974); R. Ahlrichs, H. J. Bohm, S. Brode, K. T. Tang, and J. P. Toennies, J. Chem. Phys. **88**, 6290 (1988); V. Kello and A. D. Sadlej, Chem. Phys. **157**, 123 (1991); E. J. Mansky and M. R. Flannery, J. Chem. Phys. **99**, 1962 (1993).

25.   T. N. Kitsopoulos, I. M. Waller, J. G. Loeser, and D. M. Neumark, Chem. Phys. Lett. **159**, 300 (1989); C. J. Chick, Y. Zhao, and D. M. Neumark, J. Chem. Phys. **97**, 6121 (1992).

26.   J. M. Bakker, J. Phys. E **6**, 785 (1973).

27.   K. Müller-Dethlefs, M. Sander, and E. W. Schlag, Z. Naturforsch **39a**, 1089 (1984); Chem. Phys. Lett. **12**, 291 (1984); K. Müller-Dethlefs and E. W. Schlag, Ann. Rev. Phys. Chem. **42**, 109 (1991).

28. D. O. Harris, G. G. Engerholm, and W. D. Gwinn, J. Chem. Phys. **43**, 1515 (1965).

29. J. C. Light, I. P. Hamilton, and J. V. Lill, J. Chem. Phys. **82**, 1400 (1985).

30. R. B. Metz, Ph.D Thesis, University of California, Berkeley, 1991.

31. J. C. Slater and J. G. Kirkwood, Phys. Rev. **37**, 682 (1931); see also K. S. Pitzer, Adv. Chem. Phys. **61**, 2372 (1974).

32. "Handbook of Chemistry and Physics," **74**th ed. (CRC Press, Florida: 1994) p. 10-198.

33. J. S. Cohen and R. T. Pack, J. Chem. Phys. **61**, 2372 (1974).

34. A. D. Koutselos and E. A. Mason, J. Chem. Phys. **85**, 2154 (1986).

35. H. Coker, J. Phys. Chem., **80**, 2078 (1976).

36. C. Blondel, P. Cacciani, C. Delsart, and R. Trainham, Phys. Rev. A **40**, 3698 (1989).

37. H. Hotop and W. C. Lineberger, J. Phys. Chem. Ref. Data **14**, 731 (1985).

38. (a) G. Liuti and F. Pirani, Chem. Phys. Lett. **122**, 245 (1985); (b) D. Cappelletti, G. Liuti and F. Pirani, Chem. Phys. Lett. **183**, 297 (1991); (c) R. Cambi, D. Cappelletti, G. Liuti, and F. Pirani, J. Chem. Phys. **95**, 1852 (1991).

39. J. Xie and R. N. Zare, J. Chem. Phys. **93**, 3033 (1990); J. Xie and R. N. Zare, *ibid.*, **97**, 2891 (1992).

40. A. D. Buckingham, B. J. Orr, and J. M. Sichel, Phil. Trans. R. Soc. London, Ser A **268**, 147 (1970).

41. R. N. Zare, "Angular Momentum" (Wiley, New York, 1988).

42. G. Reiser, I. Yourshaw, Y. Zhao, and D. M. Neumark, to be published.

43. K. T. Tang and J. P. Toennies, J. Chem. Phys. **80**, 3725 (1984); K. T. Tang and J. P. Toennies, Z. Phys. D **1**, 91 (1986).

44. J. Bzowski, E. A. Mason, and J. Kestin, Int. J. Thermophys. 9, 131 (1988).

45. C. Douketis, G. Scoles, S. Marchetti, M. Zen, and A. J. Thakkar, J. Chem. Phys. **76**, 3057 (1982); G. Scoles, International J. of Quantum Chem. S**24**, 475 (1990).

46. A. D. Koutselos, E. A. Mason, and L. A. Viehland, J. Chem. Phys. **93**, 7125 (1990).

47. D. A. Barrow, M. J. Slaman, and R. A. Aziz, J. Chem. Phys. **91**, 6348 (1989).

48.   D. W. Arnold, S. E. Bradforth, E. H. Kim, and D. M. Neumark, J. Chem. Phys. **97**, 9468 (1992).

Table I. Peak positions, relative energies and assignments for Fig. 1 (ZEKE spectrum of ArBr⁻).

Band	Peak	Position (cm^{-1})	Relative Energy (cm^{-1})	Assignment
A	1	27429.6	0.0	**0 ← 0**
	a_1	27418.3	-11.3	1 ← 1
	b_1	27405.2	-24.5	2 ← 2
	c_1	27392.0	-37.7	3 ← 3
B	2	27467.4	0.0	**0 ← 0**
	a_2	27490.0	22.7	1 ← 0
	b_2	27509.0	41.6	2 ← 0
C	3	31132.3	0.0	**0 ← 0**
	a_3	31155.7	23.3	1 ← 0
	b_3	31116.8	-15.5	1 ← 1

Table II. Peak positions, relative energies and assignments for Fig. 2 (ZEKE spectrum of ArI$^-$).

Band	Peak	Position (cm^{-1})	Relative Energy (cm^{-1})	Assignment
A	1	24888.3	0.0	$0 \leftarrow 0$
	a_1	24916.0	27.7	$1 \leftarrow 0$
	b_1	24905.3	17.1	$2 \leftarrow 1$
	c_1	24882.1	-6.2	$1 \leftarrow 1$
	d_1	24875.9	-12.4	$2 \leftarrow 2$
	e_1	24866.6	-21.7	$3 \leftarrow 3$
	f_1	24858.0	-30.3	$4 \leftarrow 4, 0 \leftarrow 1$
B	2	24925.5	0.0	$0 \leftarrow 0$
	a_2	24947.3	21.8	$1 \leftarrow 0$
	a_1	24916.0	-9.5	$1 \leftarrow 1$
C	3	32512.6	0.0	$0 \leftarrow 0$
	a_3	32504.1	-8.5	$1 \leftarrow 1$
	b_3	32495.2	-17.4	$2 \leftarrow 2$
	c_3	32485.1	-27.4	$3 \leftarrow 3$

Table III. Peak positions, relative energies and assignments for Fig. 3 (ZEKE spectrum of KrI⁻).

Band	Peak	Position (cm^{-1})	Relative Energy (cm^{-1})	Assignment
A	1	25020.6	0.0	**0 ← 0**
	a_1	25042.5	21.9	1 ← 0
	b_1	25031.6	11.0	2 ← 1
	c_1	25012.8	-7.8	1 ← 1
	d_1	25005.0	-15.7	2 ← 2
	e_1	24997.2	-23.4	3 ← 3
	f_1	24987.8	-32.8	4 ← 4
B	2	25073.9	0.0	**0 ← 0**
	a_2	25092.8	18.9	1 ← 0
	b_2	25110.1	36.2	2 ← 0
	c_2	25125.9	52.0	3 ← 0
	d_2	25042.5	-31.4	0 ← 1
C	3	32650.7	0.0	**0 ← 0**
	a_3	32676.3	25.6	3←1, 5←2
	b_3	32672.1	21.4	1 ← 0
	c_3	32661.4	10.7	2 ← 1

d_3	32640.1	-10.7	$1 \leftarrow 1$
e_3	32631.5	-19.2	$2 \leftarrow 2$
f_3	32620.9	-29.9	$0 \leftarrow 1$
g_3	32612.3	-38.4	$1 \leftarrow 2$
h_3	32603.8	-46.9	$2 \leftarrow 3$
i_3	32595.3	-55.4	$3 \leftarrow 4$
j_3	32584.7	-66.0	$4 \leftarrow 5$

Table IV. Quantum number nomenclature for rotational analysis.

Angular Momentum	Molecule-Fixed Projection	Space-Fixed Projection	Description
J	Ω	M	Total angular momentum of neutral
J^-	Ω^-	M^-	Total angular momentum of anion
j	ω	m	Total photoelectron angular momentum (orbital+spin)
1	μ	μ_0	Angular momentum of photon
k	q	p	Vector sum of photon and photoelectron angular momenta (multipole moment)

Table V. Rotational line strengths for transitions to three neutral states.

ΔJ	$S_{1/2}(J',J)$		$S_{3/2}(J',J)$	
	I3/2	X1/2 or II1/2	I3/2	X1/2 or II1/2
$+\dfrac{1}{2}$	0	$J'+1$	$\dfrac{3(J'+1)(J'+2)}{2(2J'+3)}$	$\dfrac{J'(J'+1)}{2(2J'+3)}$
$-\dfrac{1}{2}$	0	J'	$\dfrac{3J'(J'-1)}{2(2J'-1)}$	$\dfrac{J'(J'+1)}{2(2J'-1)}$
$+\dfrac{3}{2}$	0	0	$\dfrac{(J'+2)(J'+3)}{2(2J'+3)}$	$\dfrac{3(J'+1)(J'+2)}{2(2J'+3)}$
$-\dfrac{3}{2}$	0	0	$\dfrac{(J'-1)(J'-2)}{2(2J'-1)}$	$\dfrac{3J'(J'-1)}{2(2J'-1)}$

97

Table VI. Potential parameters for the anion and the neutral states of the ArBr system obtained from the simulation (the potential forms are those discussed in the text).

Electronic State	X1/2	X1/2 [7]	I3/2	I3/2 [7]	II1/2	Anion
ε (meV)	16.5	16.5	11.5	11.3	13.8	54.0
r_m (Å)	3.73	3.73	3.94	3.93	3.89	3.78
β_1	6.80	7.10	7.72	7.90	6.70	5.10
β_2	6.50	7.30	7.10	7.50	6.35	4.45
x_1	1.02	1.0255	1.012	1.0166	1.01	1.065
x_2	1.59	1.70	1.63	1.70	1.58	1.66
C_6 (eV•Å^6)	65.2	65.2	70.2	70.2	68.8	
C_8 (eV•Å^8)	379.	379.	379.	379.	379.	
B_4 (eV•Å^4)						12.5
B_6 (eV•Å^6)						120.5

Table VII. Potential parameters for the anion and the neutral states of the ArI system obtained from the simulation.

Electronic State	X1/2	I3/2	II1/2	Anion
ε (meV)	18.8	13.7	15.9	45.7
r_m (Å)	3.95	4.18	4.11	4.07
β_1	7.15	7.25	6.90	5.70
β_2	6.18	6.30	6.40	4.45
x_1	1.01	1.04	1.04	1.08
x_2	1.62	1.62	1.64	1.62
C_6 (eV•Å^6)	98.4	98.4	98.4	
C_8 (eV•Å^8)	715.	715.	715.	
B_4 (eV•Å^4)				12.8
B_6 (eV•Å^6)				162.

Table VIII. Potential parameters for the anion and the neutral states of the KrI system obtained from the simulation.

Electronic State	X1/2	X1/2 [7]	I3/2	I3/2 [7]	II1/2	Anion
ε (meV)	23.85	23.85	16.7	15.6	20.2	67.2
r_m (Å)	4.05	4.05	4.32	4.32	4.20	4.11
β_1	5.80	5.70	6.72	6.80	6.38	5.44
β_2	6.12	6.10	6.48	6.30	6.25	4.55
x_1	1.08	1.1136	1.11	1.11	1.09	1.04
x_2	1.77	1.85	1.64	1.70	1.70	1.54
C_6 (eV•Å^6)	141.	141.	141.	141.	141.	
C_8 (eV•Å^8)	908.	908.	908.	908.	908.	
B_4 (eV•Å^4)						20.2
B_6 (eV•Å^6)						238.

Table IX. Vibrational temperatures of the anions and FWHM of the ZEKE instrumental peak shapes resulting from the simulation of each individual bands. The $C_{1/2}$ and C_{IX} parameters are explained in the text.

Electronic State		$B_e(cm^{-1})$	$T_{vib}(K)$	FWHM(cm^{-1})	C_{IX}	$C_{1/2}$
ArBr	Anion	0.045				
	X1/2	0.046	68	5.0		10.0
	I3/2	0.041	68	5.0	0.39	-
	II1/2	0.042	88	4.5		0.6
ArI	Anion	0.034				
	X1/2	0.036	55	3.2		0.4
	I3/2	0.032	55	3.2	0.84	-
	II1/2	0.033	55	5.3		10.0
KrI	Anion	0.020				
	X1/2	0.021	55	4.2		0.8
	I3/2	0.018	55	4.2	0.29	-
	II1/2	0.019	80	4.0		0.1

Table X. Comparison of our ε and r_m values for the V_0 potentials of ArBr, ArI and KrI complexes with those for a few Rg-Rg species[47], and those calculated from Pirani et al.'s[38] correlation formulae.

Molecules	Pirani et al.[38]		Experimental	
	R_m (Å)	ε (meV)	R_m (Å)	ε (meV)
ArBr⁻	3.91	70.0	3.78	54.0
ArI⁻	4.11	63.0	4.07	45.7
KrI⁻	4.17	90.0	4.11	67.2
ArKr			3.881	14.42
ArBr	3.98	12.9	3.89	13.8
ArXe			4.067	16.25
KrKr			4.011	17.35
ArI	4.20	14.7	4.11	15.9
KrXe			4.174	20.12
KrI	4.30	18.5	4.20	20.2
XeXe			4.366	24.37

Figure Captions

Figure 1. Threshold photodetachment spectrum (solid lines) and simulated spectrum (dotted lines) of ArBr⁻. The arrows indicate where the band origins are.

Figure 2. Threshold photodetachment spectrum (solid lines) and simulated spectrum (dotted lines) of ArI⁻. The arrows indicate where the band origins are.

Figure 3. Threshold photodetachment spectrum (solid lines) and simulated spectrum (dotted lines) of KrI⁻. The arrows indicate where the band origins are.

Figure 4. Illustration of the energetics of all the potential energy curves involved in our analysis of the spectrum. ε_X and ε_a are the well depths for the neutral X1/2 state and the anion state, respectively; v_{00} is the origin transition energy for band A; EA is the electron affinity of the X (Br or I) atom; Δ is the X(^{2}P) spin-orbit splitting constant.

Figure 5. The rotational profiles of three different electronic bands for the KrI system. The solid lines are obtained by adding up all the rotational sticks within each energy region of 0.5 cm⁻¹. The dotted lines are obtained by convoluting the rotational sticks with the ZEKE instrumental peak shape.

Figure 6. The anion and neutral adiabatic potential energy curves resulting from our fit to the ZEKE spectrum of ArBr⁻, ArI⁻ and KrI⁻.

Figure 7. The V_0 and V_2 potentials calculated from the three adiabatic potentials according to Haberland, Aquilanti *et al.*'s formulae for all three systems. The solid lines are the potentials for the ArBr system; The dotted lines are the potentials for the ArI system; the dashed lines are the potentials for the KrI system.

Figure 3.1

105
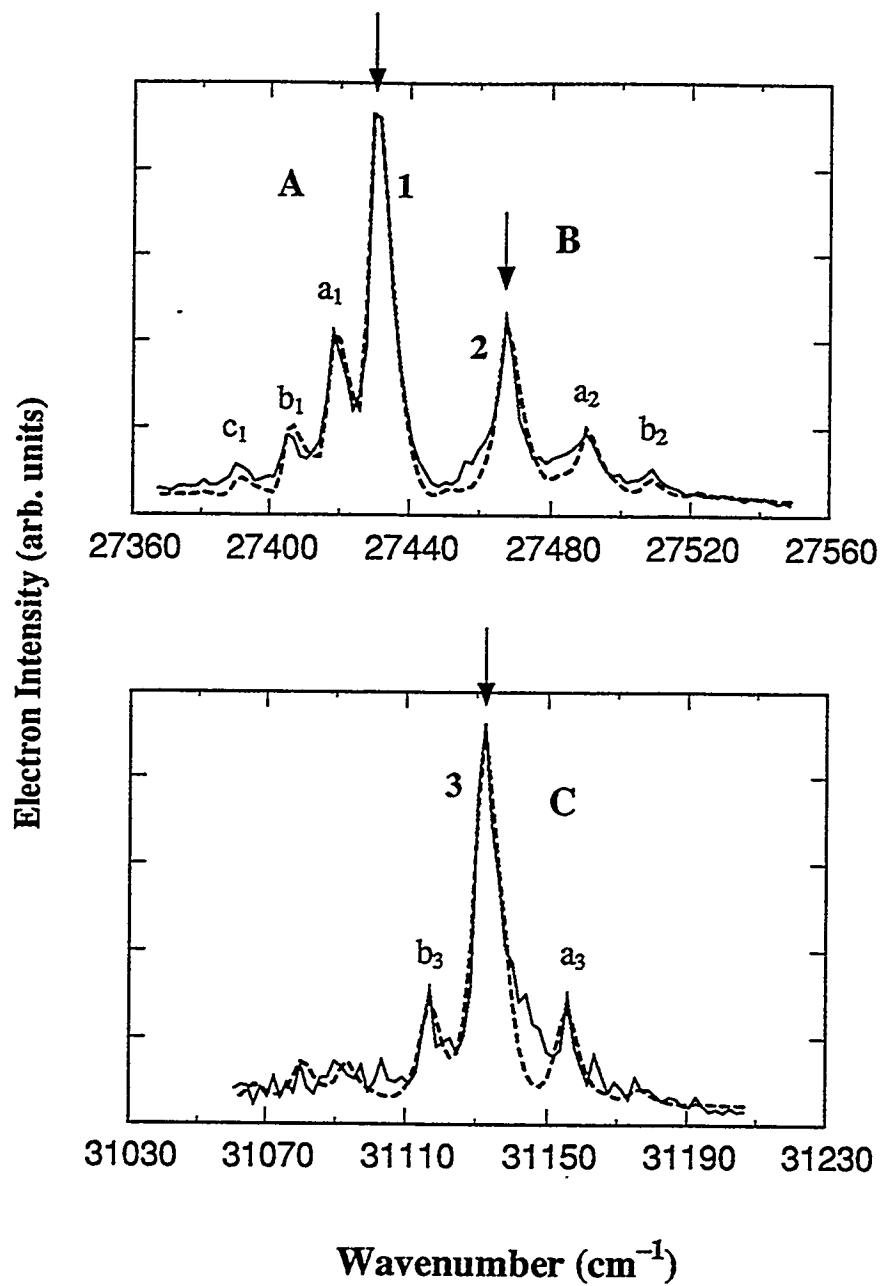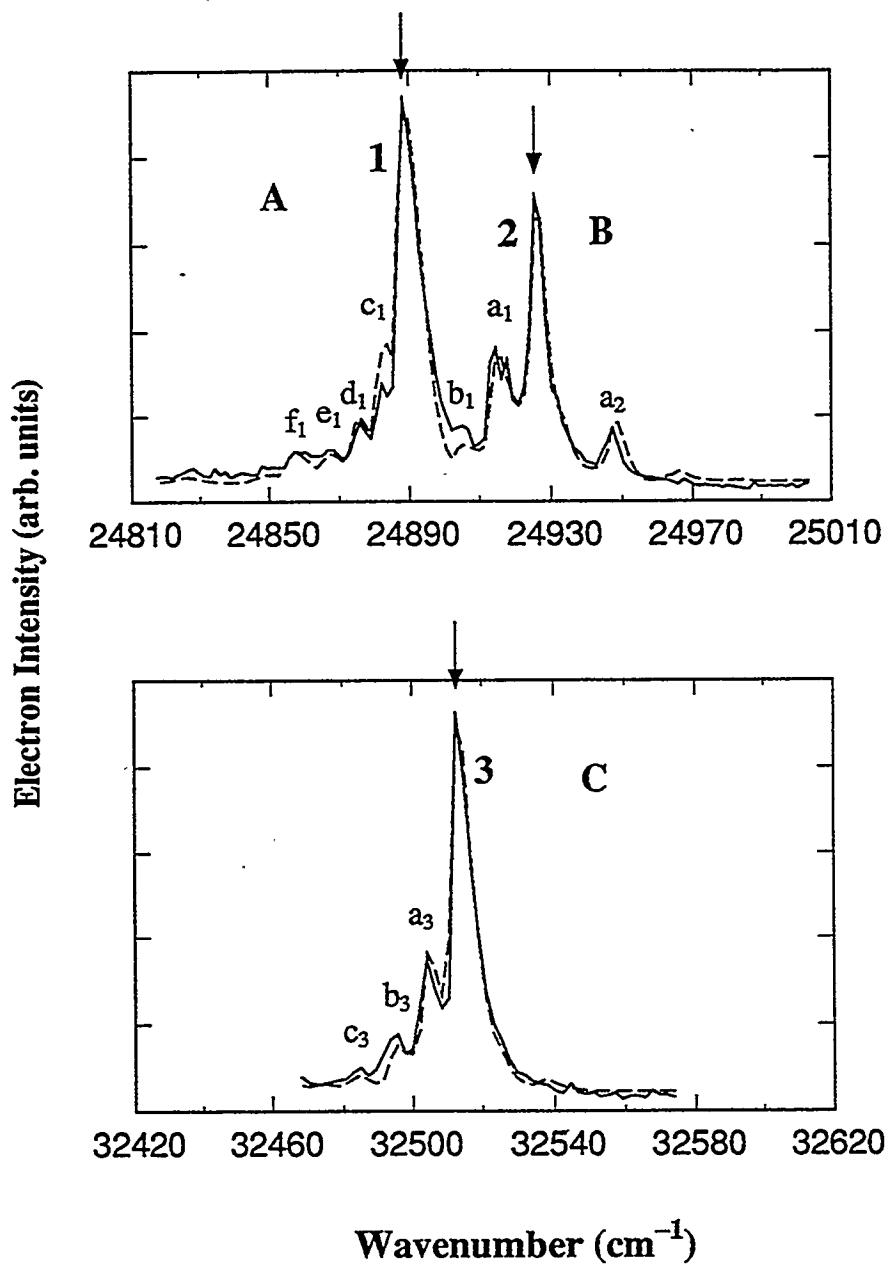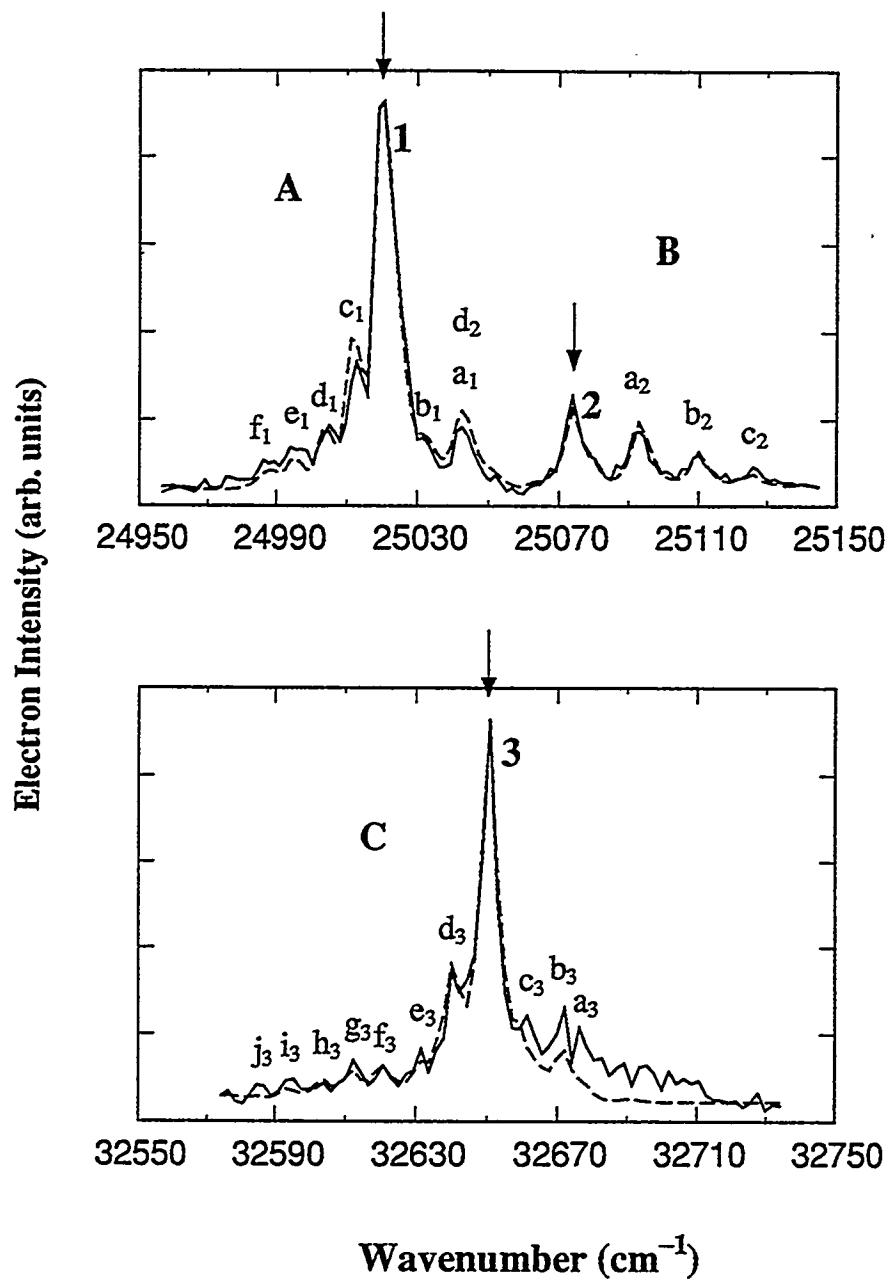
Figure 3.2

Figure 3.3
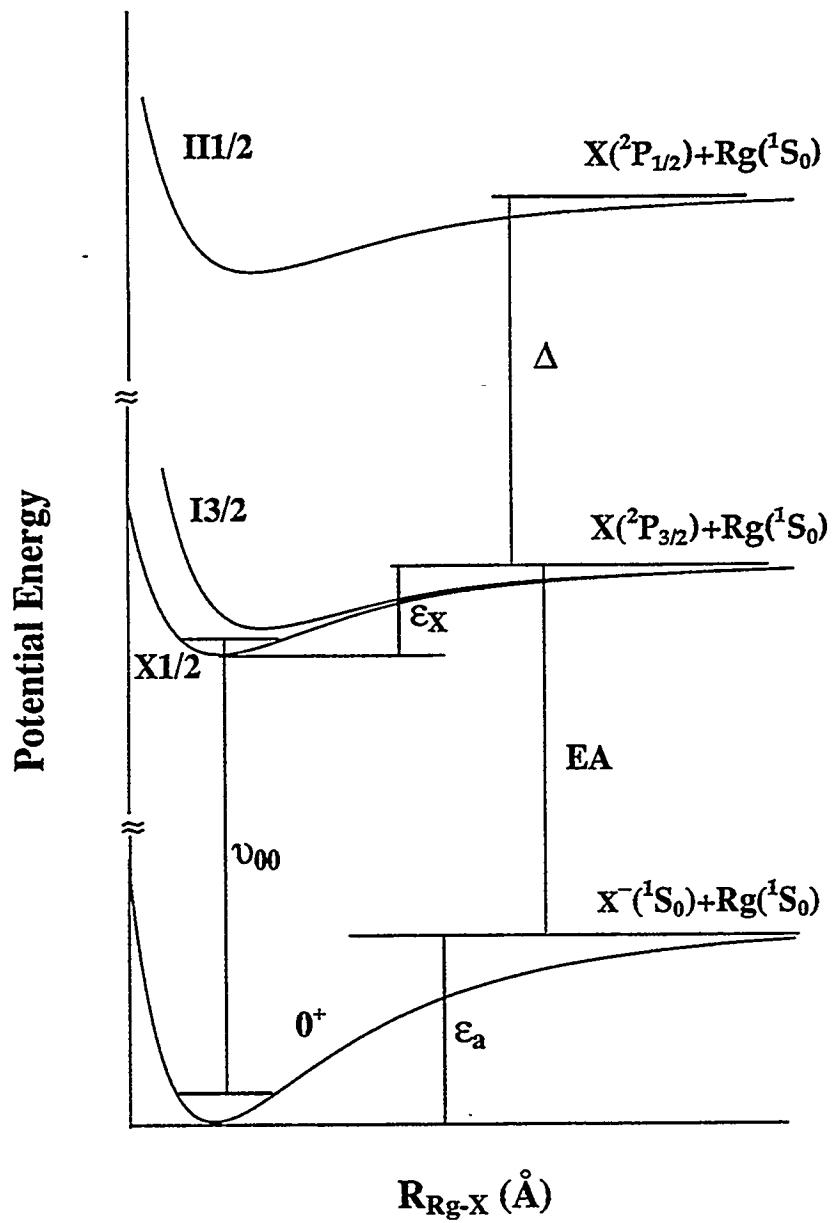
Figure 3.4
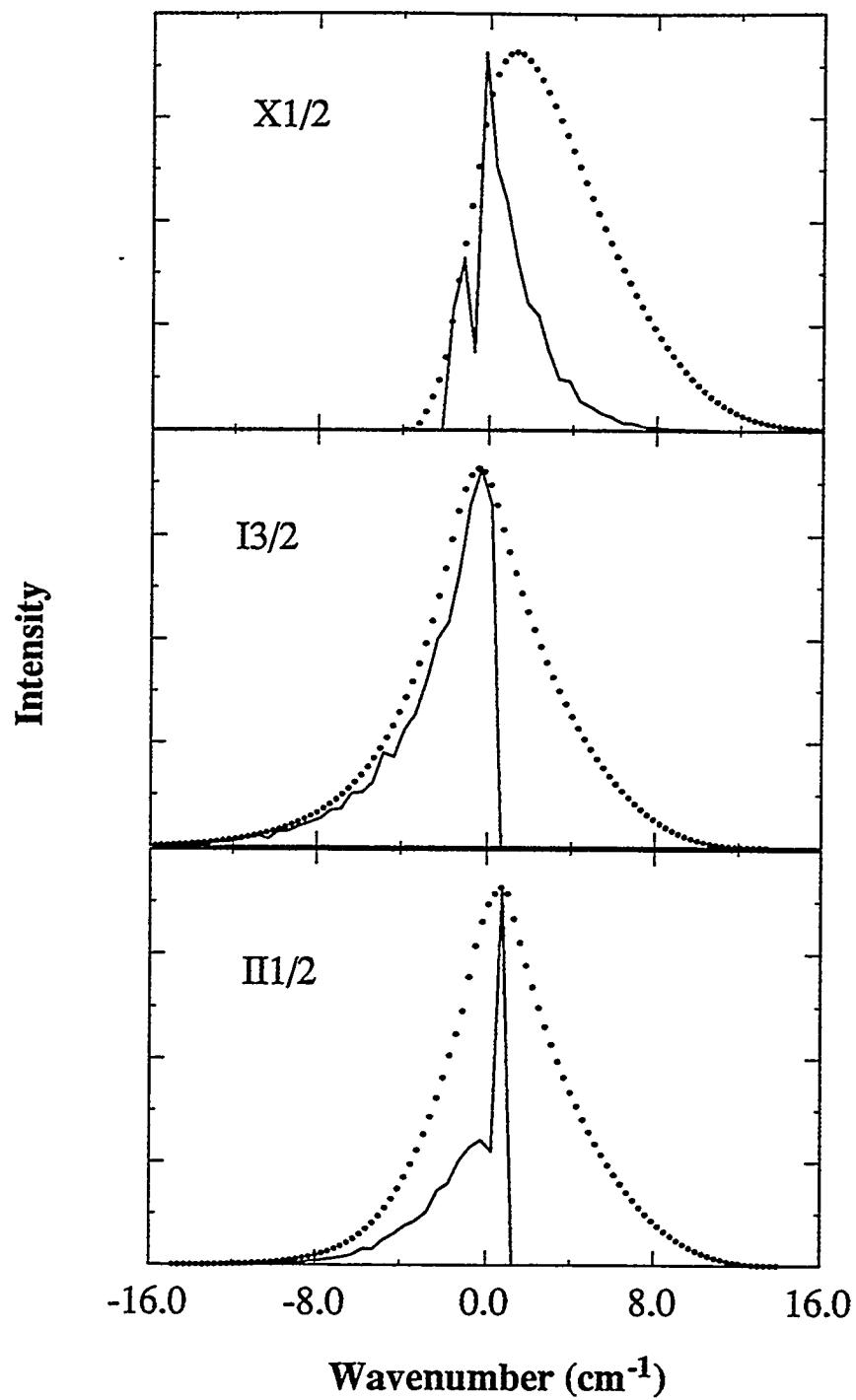
Figure 3.5
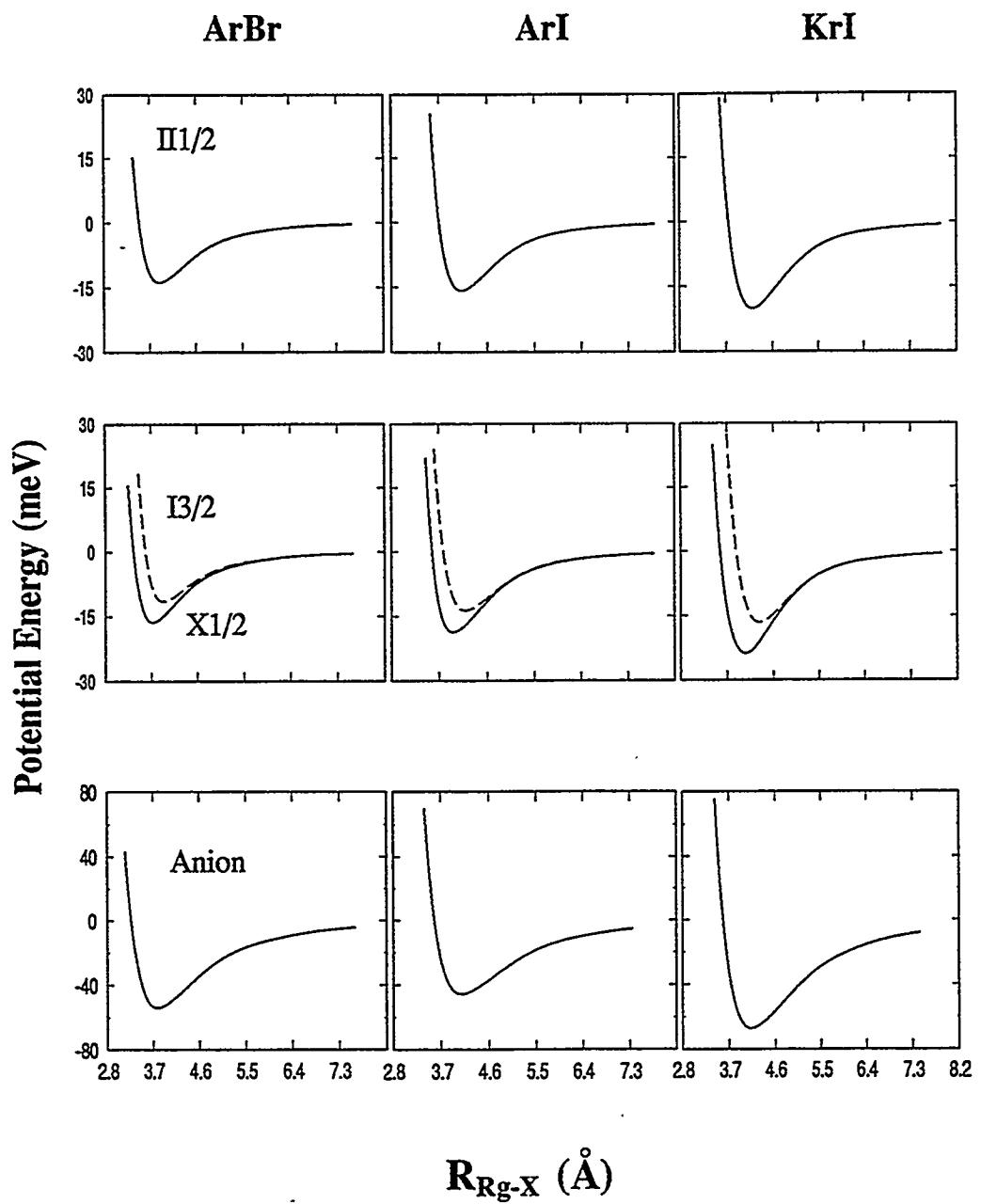
Figure 3.6
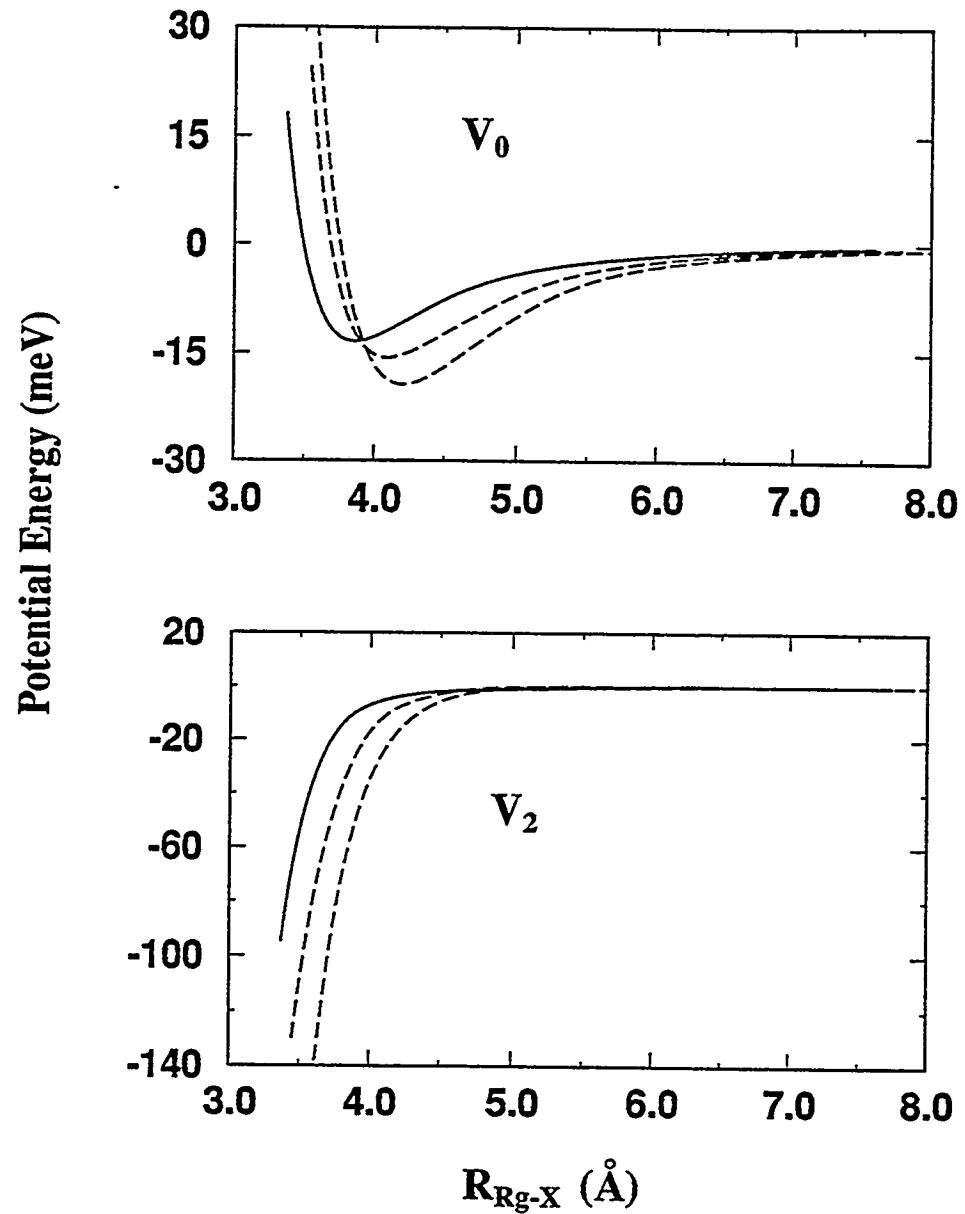
110

Figure 3.7

111

Chapter 4. Study of the Low-Lying Electronic States of GaAs and GaAs⁻ Using Negative Ion Photodetachment Spectroscopy

Abstract

The properties of the low-lying electronic states of GaAs and GaAs⁻ are probed using negative ion photoelectron spectroscopy (PES) and zero electron kinetic energy (ZEKE) spectroscopy. The vibrationally-resolved ZEKE spectrum of GaAs⁻ is presented along with the PES taken with lower resolution. The PES and ZEKE spectra of GaAs⁻ show vibrational progressions due to transitions from the anion ground state to the low-lying neutral $^3\Pi$, $^1\Pi$, and $^1\Sigma^+$ states. The $^2\Sigma^+$ state was found to be the anion ground state. Transitions from the low-lying anion state, the $^2\Pi_{3/2}$ state, were also observed. Relative term energies and vibrational frequencies obtained for these states were found to be in good agreement with *ab initio* calculations at the CASSCF/SOCI level. The spectra of GaAs⁻ reveal the electronic similarity between GaAs/GaAs⁻ and the isoelectronic Ge_2/Ge_2^- species.

I. Introduction

Due to its technological importance, bulk GaAs has been studied extensively.[1] However, very little is known about the small GaAs clusters and their ions, even though it was pointed out that gaseous GaAs may play a role in the mechanism of pyrolytic epitaxial deposition of GaAs films.[2]

Experimental work on these semiconductor clusters are difficult largely due to the lack of mass selection of most cluster sources. Most of the experiments done on these species are related to some kind of mass selection, such as negative ion photodetachment techniques[3] and resonant multiphoton ionization spectroscopy.[4,5]

Smalley and coworkers have studied Ga_xAs_y clusters using photoelectron spectroscopy of their corresponding anions which are generated via laser vaporization of GaAs crystals.[6] These studies revealed an even-odd alternation in electron affinity values.

The $^3\Pi(III) \leftarrow X\ ^3\Sigma^-$ band system of GaAs was studied by Lemire *et al.* in a resonant two-photon ionization spectroscopy experiment.[5] Their spectrum was rotationally resolved, resulting in the determination of the bond length and other spectroscopic constants for these two electronic states. Weltner and coworkers also determined the vibrational frequency of the ground state in a far infrared spectrum of matrix isolated GaAs species.[7]

The diatomic GaAs and its ionic species have been studied extensively by *ab initio* theoreticians. Balasubramanian[8] carried out very high level calculations on these species, the spectroscopic constants he obtained for the $X^3\Sigma^-$ state of GaAs are in excellent

agreement with the experimental results. In his study, many low-lying electronic states of GaAs, GaAs$^-$, and GaAs$^+$ were investigated using complete active space SCF (CASSCF) followed by full second-order configuration interaction (SOCI) calculations. Meier *et al.*[9] and Al-Laham and Raghavachari[10] also studied these species using *ab initio* methods. Based on Balasubramanian's calculations, a $^3\Pi$ excited state is supposed to be very low-lying, within 2000 cm^{-1} of the $X^3\Sigma^-$ state of GaAs. Three singlet states ($^1\Pi$, $^1\Sigma$, and $^1\Delta$) are predicted to lie approximately 0.5 eV to higher energy. The $^2\Sigma^+$ state is predicted to be the anion ground state, however, a $^2\Pi$ state is expected to lie within 0.1 eV.

In our group, we study the electronic and vibrational structures of small semiconductor clusters using anion photoelectron spectroscopy[11,12,13] and zero electron kinetic energy (ZEKE) spectroscopy.[3,14,15] In both techniques, negative ions are mass selected prior to spectroscopic investigations; thus eliminating any ambiguity about the species being studied. Moreover, by detaching an electron from a valence orbital of a cluster anion, both the ground and low-lying excited states of the neutral can be probed. The spectroscopic resolution afforded by time-of-flight photoelectron spectroscopy is typically around 8 meV; much spectroscopic information can be obtained from this type of photoelectron spectrum (PES). However, for clusters with many low-lying electronic states, vibrational structure of each electronic state can hardly be resolved in the time-of-flight PES. On the other hand, negative ion ZEKE spectroscopy is well suited to study the electronically complex species, as it combines mass-selection with good spectroscopic resolution (3 cm^{-1}). Often it is the combination of these two techniques that is most powerful in probing the complex electronic and vibrational structures of small

semiconductor clusters. For example, we have previously applied these two techniques to the study of the low-lying electronic states of Si_2 [16] and Ge_2. [17]

In this paper, we first present photoelectron spectrum (PES) of GaAs⁻ which shows partly resolved vibrational structure. A laser polarization dependence study of the photoelectron spectrum provides useful information in distinguishing features belonging to different electronic transitions. We then present the vibrationally resolved ZEKE spectrum of GaAs⁻. From the ZEKE spectrum, the relative term energies and vibrational frequencies of several low-lying electronic states in GaAs and GaAs⁻ are obtained; the splittings between the Ω components of the low-lying $^3\Pi$ state of GaAs are also determined. Transitions from both the $X^2\Sigma^+$ and $^2\Pi_{3/2}$ anion states are observed.

II. Experimental

The operation of the PES and the ZEKE spectrometer are similar in principle. In both experiments, a beam of cluster anions is generated in a Smalley-type[18] of laser vaporization/pulsed-molecular beam source. The negative ions are then mass-selected by time-of-flight and photodetached. However, the electron detection schemes are different.

A. Photoelectron spectrometer

The anion time-of-flight photoelectron spectrometer has been described in detail elsewhere. [12,19] A beam of cold gallium arsenide anions is generated by vaporizing the

surface of a translating and rotating GaAs rod with 4-6 mJ/pulse output of the second harmonic output of a Nd:YAG laser operated at 20 Hz repetition rate. The resulting plasma is entrained in a pulse of 90% Ne and 10% He carrier gas from a piezoelectric valve, and expanded through a clustering channel into the source vacuum chamber of the apparatus. A relatively short clustering channel (3 mm long) is used to produce sufficient quantity of the diatomic GaAs⁻. Longer clustering channel tends to produce larger clusters. The cluster anions are then injected with a pulsed electric field into a Wiley-McLaren-type[20] time-of-flight mass spectrometer. The ion of interest is selectively detached by a properly timed pulse of light from a second YAG laser beam. After photodetachment, a dual microchannel plate detector at the end of a 1m field-free flight tube detects a small fraction of the photoelectrons. Time-of-flight analysis yields electron kinetic energies (eKE); the instrumental resolution is 8 meV at 0.65 eV and degrades as $(eKE)^{3/2}$ at higher electron kinetic energy.

B. ZEKE spectrometer

The zero electron kinetic energy spectrometer used in this experiment has been described in detail elsewhere.[21] Briefly, the anions are generated in a similar manner to that described above. After the expansion through the clustering channel, those anions passing through a 2 mm skimmer are collinearly accelerated to 1 keV and are then separated into bunches according to their masses in a 1-meter time-of-flight tube.

116

After they enter the detector region, the anions of interest are photodetached by an excimer-pumped dye laser. Only those photoelectrons produced with near zero kinetic energy in the center-of-mass frame are detected. The detection scheme we adapt here is based on the design of Müller-Dethlefs *et al.* for ZEKE photoionization of neutral species.[22] Once the photoelectrons are produced, a time delay between 200-350 ns is applied before they are extracted coaxially by a DC electric field of approximately 3 V/cm. During this time delay, those electrons with a velocity component in the perpendicular direction move off axis and do not make through the apertures *en route* when they are extracted. For those electrons which are scattered on-axis, the amount of energy they acquire during extraction depends on their location in the extraction field, which is in turn determined by their initial kinetic energy. In the subsequent time-of-flight, electrons extracted on axis are separated in time. By using a gated detection scheme, we can selectively collect only the ZEKE electrons. The resolution of this spectrometer in absence of rotational broadening is 2-3 cm^{-1}.

The electron signal is normalized to laser power and ion signal, and averaged over 1200 laser shots per point. The dyes used to obtain the ZEKE spectrum of GaAs⁻ were Coumarin 440, Coumarin 460, Coumarin 480, Coumarin 540, Rhodamine 590, and Rhodamine 610. The dye laser wavelength is calibrated by measuring the absorption spectra of an iodine cell or a Fe-Neon cathode lamp.

III. Results

A. Photoelectron spectrum

Figure 1 shows the photoelectron spectrum (PES) of GaAs$^-$ taken with 2.98 eV photon energy (wavelength 416 nm) at three different laser polarization angles. The spectrum clearly divides into two bands separated by several thousands of wavenumbers in energy. This resembles the similarly obtained PES of Ge$_2^-$, which is isoelectronic to GaAs$^-$. The band at lower energy is more congested; this is the triplet band, corresponding to transitions from GaAs$^-$ to the low-lying triplet states of GaAs. The band at higher binding energy corresponds to transitions to the neutral singlet states which are predicted by *ab initio* calculations to lie thousands of wavenumbers above the triplet states.

Laser polarization dependence of the PES spectrum helps to sort out overlapping electronic transitions. If the relative intensities of two sets of peaks depend on the laser polarization angle, these two sets of peaks most likely belong to two different electronic transitions. Based on the varying peak intensities at three different laser polarization angles, the following information can be definitely obtained: peak CP has very different laser polarization dependence than the neighboring peaks such as peaks AP and BP; peak JP has very different polarization dependence than its neighboring peaks such as IP and HP; peak MP has different polarization dependence than peak HP.

B. ZEKE Spectrum

The triplet band of zero electron kinetic energy (ZEKE) spectrum of GaAs⁻ is shown in the middle panel of Figure 2; the singlet band of ZEKE spectrum of GaAs⁻ is shown in the middle panel of Figure 3. In Figure 2 and Figure 3, the top part shows part of the PES within the same energy region as the ZEKE spectrum. These are primarily to indicate the correspondence between the peaks in PES and ZEKE spectrum.

In the triplet band of the ZEKE spectrum, two progressions, both with spacings of *ca.* 260 cm^{-1}, are observed. These two progressions are labeled as A_n, n=0,1,2,...; and D_n, n=0,1,2,..., respectively. Peak B and C are 300 cm^{-1} and 400 cm^{-1} to the red of peak A_0, respectively. Between the members of the two main progressions, many more peaks are seen. The peak positions, labels, are shown in Table I. Peak AP in the PES corresponds to peak A_0 in the ZEKE spectrum, peak BP in the PES corresponds to peak B in ZEKE spectrum, peak CP in the PES corresponds to peak C in the ZEKE spectrum.

In the singlet band of the ZEKE spectrum, two progressions, both with spacings of *ca.* 290 cm^{-1}, are observed. These two progressions are labeled as H_n, n=0,1,2,...; and M_n, n=0,1,2,..., respectively. Peaks I and J are 300 cm^{-1} and 400 cm^{-1} to the red of peak H_0, respectively. The peak positions, labels, are shown in Table II. Peak HP in PES corresponds to peak H_0 in the ZEKE spectrum; peak IP in the PES corresponds to peak I in the ZEKE spectrum, peak JP in the PES corresponds to peak J in the ZEKE spectrum. Several peaks observed in the PES, including peak JP, have much smaller intensities in the ZEKE spectrum.

Peak widths in the ZEKE spectrum are typically around 11 cm^{-1}, significantly narrower than those in the PES. More features are observed in the PES than in the ZEKE

119

spectrum; and some peaks are more intense in the PES than in the ZEKE spectrum. For example, peaks BP and CP are more intense than peaks B and C. These differences in the two spectra are possibly due to the different source conditions. Indeed, we found that the intensities of peaks B and C depended on source conditions such as the vaporization laser power and the time delay between the laser pulse and the carrier gas pulse. The source temperature in the PES appears to be hotter than that in the ZEKE spectrum.

IV. Analysis

In this section, we try to assign the peaks in the ZEKE spectrum and obtain molecular parameters such as term energies, vibrational frequencies, etc.. Laser polarization dependence information obtained from the PES will be used to distinguish peaks belonging to different electronic transitions. For a molecule like GaAs, which has complicated electronic structure due to the overlapping low-lying electronic states, high level *ab initio* calculations are of great help in making electronic and vibrational assignments. The complete active space SCF coupled with second-order configuration interaction (CASSCF/SOCI) study done for GaAs and its ionic forms by Balasubramaniam[8] should yield highly accurate results on molecular constants including bond lengths, electronic term energies, vibrational frequencies, etc.. For example, the calculated molecular constants[8] for the ground electronic state of GaAs are in excellent agreement with the experimental results.[5]

Based on the *ab initio* calculation results,[8] Figure 4 shows the electronic states that might be involved in our spectra. Taking into consideration relativistic effects, the different Ω components of each electronic state split according to the extent of spin-orbit interactions. For a molecule consisting heavy atoms such as Ga and As, relativistic effects are significant; and Hund's case (c) notation, shown on the left in Figure 4, is more appropriate for the electronic states. For Ge_2, the spin-orbit splitting between different Ω components was found to be in the region of 800-1000 cm^{-1}. One would reasonably expect the extent of this effect in GaAs to be in the same range. For each electronic species, the dominant molecular orbital configuration is also shown.

A. Triplet band

Figure 5 shows the relevant electronic states and the one-electron allowed transitions for the triplet band. The ordering of electronic states are those given by *ab initio* calculations.[8] Photodetachment usually is only sensitive to the transitions that involve the removal of only one electron form the anion molecular orbital configuration. In the triplet band of the ZEKE spectrum, peak A_0 can be clearly assigned as the origin peak ($v=0 \leftarrow v=0$ transition) of some electronic transition. A fairly extended progression, peaks A_0 - A_4, is observed. However, peak A_0 has quite high intensity; if peak A_0 were not the origin transition, one would expect to see a peak *ca.* 260 cm^{-1} to the red. Now, since the vibrational frequency of the $^3\Sigma^-$ state of GaAs has been experimentally determined to be 214 cm^{-1},[5] the neutral state in this progression must be the $^3\Pi$ state,

whose calculated frequency is 236 cm^{-1}. Having assigned peak A$_0$ to the origin transition, we assign peaks B and C hot band transitions. This assignment is consistent with the fact that the intensities of peaks B and C are source condition dependent. Laser polarization study of the PES shows that peak C belongs to a different electronic transition than peak A$_0$, so we assign peak C to a transition from an excited anion state to the $^3\Pi$ neutral state, and the A peaks to transitions from ground anion state to the $^3\Pi$ neutral state. Peak B is then assigned to vibrational hot band transition (0 $\leftarrow$ 1) of the same electronic transition as the A peaks, resulting in vibrational frequency for the ground anion state of 300 cm^{-1}. This is in excellent agreement with the calculated frequency for the $^2\Sigma^+$ state of 303 cm^{-1}. The calculated frequency for the $^2\Pi$ state is much lower, 216 cm^{-1}; it would be unreasonable to assign the 300 cm^{-1} spacing to the vibrational frequency of the $^2\Pi$ anion state. We therefore conclude that the $^2\Sigma^+$ state is the ground state of GaAs$^-$. Our assignment of 300 cm^{-1} as the anion vibrational frequency will be reconfirmed when analyzing the singlet band. By comparison with the *ab initio* results, peak C is due to a transition from the low-lying $^2\Pi_{3/2}$ anion state.

The lowest Ω component of the $^3\Pi$ state is the 2 state, therefore the A progression is assigned to the 2 $\leftarrow$ X 1/2 transition. We now try to assign the peaks between the members of the two main progressions. The ordering of the different Ω components of the GaAs $^3\Pi$ state is shown in Figure 4. The 0$^+$ state is higher-lying than the 0$^-$ state due to the form of the (off-diagonal) spin-spin interaction.[23] Peaks E and G are separated by 300 cm^{-1}, we assign them to the $v=0\leftarrow v=1$, and $v=0\leftarrow v=0$ transitions of the 1 $\leftarrow$ X 1/2 electronic transition, respectively. The spacing between peak F and peak Q is again *ca.*

300 cm^{-1}, these two peaks are therefore assigned to the v=0←v=1, and v=0←v=0

transitions of the 0$^-$ ← X 1/2 electronic transition, respectively. Since the 0$^+$ state is

highest-lying among the four Ω components, the D progression can then be assigned to 0$^+$

← X 1/2 transition. Based on these assignments, The energies for the 1, 0$^-$, and 0$^+$

components relative to the 2 state are 464 cm^{-1}, 615 cm^{-1}, and 1098 cm^{-1}, respectively.

The 2-0$^+$ splitting is 1098 cm^{-1}; for Ge$_2$, this splitting for the $^3\Pi_u$ state was found to be

968 cm^{-1}.

Extended vibrational progressions are seen for transitions to the 2 and 0$^+$ states;

therefore, we are certain about the assignments of the peaks in these two (A and D)

progressions. However, assignments of the rest of features to the transitions to the 1 and

0$^-$ states are more speculative because no vibrational progressions are observed. The

spectrum is congested in this energy region, which may be part of the reason why no

vibrational progressions can be resolved for the transitions to the 1 and 0$^-$ states.

The spectrum in the energy region higher than the energy of peak Q becomes

rather congested, this is not surprising considering that at least three electronic transitions

from the anion ground state are active in this region, transitions from the 3/2 state of the

anion may also have non-negligible intensities. Since much of the useful information on

the molecular constants have already been obtained, we shall not attempt to assign

individual peaks in the rest of the triplet band.

The vibrational frequencies and relative electronic term energies obtained for the

neutral triplet states 2, 1, 0$^-$ and 0$^+$ of the $^3\Pi$ state and the anion X1/2 and a3/2 states are

shown in Table III.

As shown in Figure 5, the $X^3\Sigma^-$ (1 and 0^+) ← a3/2 transition is also a one-electron allowed transition. Since this is an electronic hot band transition, intensities should be smaller. Its transition energy is less than that of the 2 ← X1/2 transition; in other words, these features should lie to the red of peak C. No features are seen in the ZEKE spectrum to the red of peak C, however, there are definitely intensities in the PES to the red of peak CP which may be attributed to transitions in the $X^3\Sigma^-$ (1 and 0^+) ← a3/2 band. This difference in the PES and the ZEKE spectrum may be due to different vibrational temperatures in two sources. According to *ab initio* calculations,[8] the $X^3\Sigma^-$ (1 and 0^+) ← a3/2 transition involves large bond length change (*ca.* 0.11 Å); one then expects an extended Franck-Condon progression. This is consistent with the PES in this region, in which intensity gradually decreases towards the red. Based on the onset of the electron signal in the PES at the lowest binding energy, which is approximately 14500 cm^{-1} (see Figure 1), one can estimate the electron affinity of GaAs. Assuming the electron signal onset corresponds to the origin of $X^3\Sigma^-$ (1 and 0^+) ← a3/2 band, the electron affinity is equal to that energy plus the energy separation between the anion a3/2 and X1/2 states, which is 400 cm^{-1} (see Figure 5). Based on this analysis, the electron affinity of GaAs is (1.85±0.10) eV. The calculated electron affinity of GaAs at the CASSCF/SOCI level is 1.3 eV.[8] Based on the same features in the PES, the energy separation between the X1 ($^3\Sigma^-$) state and the 2 ($^3\Pi$) state of GaAs is estimated to be 0.2±0.10 eV.

B. Singlet band

Figure 6 shows the relevant electronic states and the one-electron allowed transitions for the singlet band. The ordering of electronic states are those predicted by *ab initio* calculation.[8] Different laser polarization dependences between the HP_n (n=0,1,2,...), and MP_n (n=0,1,2,...) progressions suggest that they belong to two different electronic transitions. Peak H_0 corresponds to the origin transition of the H progression, and peak I is 300 cm^{-1} to the red of H_0. Peak M_0 corresponds to the origin transition of the M progression, and peak K is 300 cm^{-1} to the red of M_0. By comparison with Figure 6, the H and M progressions are assigned to 1 ($^1\Pi$) $\leftarrow$ X1/2 (transition *b*) and 0^+ ($^1\Sigma^+$) $\leftarrow$ X1/2 (transition *d*) electronic transitions, respectively. Similar to peak B in the triplet band, peak I and peak K are assigned to the $v=0 \leftarrow v=1$ vibrational hot band transitions in H and M progressions, respectively. Based on these assignments, the vibrational frequency of the 1 state is then 288 cm^{-1} and that of the 0^+ state is 291 cm^{-1}. These two frequencies are in good agreement with *ab initio* frequencies calculated for these two states, which are 277 cm^{-1} and 279 cm^{-1} for the 1 and 0^+ states, respectively. On the other hand, the *ab initio* frequency calculated for the 2 ($^1\Delta$) state is much lower, 214 cm^{-1}.

Peak J is 400 cm^{-1} to the red of peak H_0, and polarization dependence suggests that peak J and progression H belong to different electronic transitions. Peak J is therefore assigned to the 1 ($^1\Pi$) $\leftarrow$ a3/2 transition (*a* in Figure 6). The resulting a3/2 − X1/2 splitting in the anion and the vibrational frequency of the X1/2 state are consistent with those obtained from the triplet band.

Compared to the PES, the hot band transitions, such as peaks I and J are much smaller in the ZEKE spectrum, this is again attributed to the different source conditions in

these two experiments. For this reason, more transitions are observed in the PES. For example, electronic transitions a and c in Figure 6, the transitions from the anion a3/2 state, are hardly observed in the ZEKE spectrum, additional features in the PES are likely due to these hot band transitions. For example, peaks JP, LP can be assigned to the first two members of the 1 ($^1\Pi$) ← a3/2 progression. The relatively poor resolution in PES does not allow a complete assignment of the rest of unassigned features.

The vibrational frequencies and relative electronic term energies obtained for the neutral singlet states 1 and 0^+ are shown in Table III.

C. Franck-Condon simulation

We can simulate the vibrational structures in 2, 0^+ ($^3\Pi$) ← X 1/2 transitions of the triplet band and the 1, 0^+ ← X 1/2 transitions of the singlet band within the Franck-Condon approximation. In the simulation, we assume that the intensities of individual vibrational transitions within a single electronic transition are proportional to their Franck-Condon factors,

$$Intensity \propto \left|\left\langle v'|v''\right\rangle\right|^2. \tag{1}$$

The vibrational wave functions of the neutral and anion, v' and v'', respectively, are taken to be harmonic oscillators with the frequencies determined from the ZEKE spectrum. The relative bond distances of the anion and neutral are then varied until the extension of the simulated progression matches the observed progression.

The A, D, H, and M progressions are simulated. The result of simulation of A and D progressions is shown as the dashed line in the bottom half of Figure 2, and the result of simulation of H and M progressions is shown as the dashed line at bottom of Figure 3. From the simulation, the difference of bond distance between the anion and neutral electronic states is obtained. Assuming the bond distance of the anion X1/2 state is 2.27 Å, the value from CASSCF/SOCI *ab initio* calculation,[8] one can obtain the bond distances for the four neutral states. However, since the direction of bond length change can not be determined from the simulation using harmonic oscillators, we need to resort to *ab initio* calculation to figure out if the neutral bond distance should be shorter or longer relative to the anion bond length. The neutral bond distances thus obtained are shown in Table III. From the simulation, an anion vibrational temperature of 425 K was required to match the hot band intensities.

V. Discussion

A. Comparison with Ge$_2$

The overall appearances of the ZEKE spectra of Ge$_2^-$ and GaAs$^-$ are similar. For example, features all show up in the same energy regions; each spectrum can be divided into the triplet band and the singlet band; vibrational spacings are also similar for these two species. These similarities suggest the similar electronic structures between these two species both in the anions and the neutrals. This is not surprising because Ge$_2$ and GaAs

are isoelectronic. Moreover, since the atoms have similar weights, the relativistic effects in these two species are also similar. From the present work on GaAs/ GaAs⁻and our previous work on Ge_2/ Ge_2^-,[17] it has been shown that the same electronic states present in GaAs (or GaAs⁻) are also present in Ge_2 (or Ge_2^-).

However, in Ge_2/ Ge_2^-, the g/u symmetry, which is the symmetry of the electronic wavefunction with respect to the inversion through the center of the internuclear bond, is present; while this type of symmetry does not apply to GaAs/ GaAs⁻. This difference has profound implications for the ordering of the low-lying electronic states as well as the allowed electronic transitions in the ZEKE spectra. The ordering of these low-lying electronic states in each species may be greatly affected by the interaction among the states with the same symmetry. In Hund's case (c), the good quantum number is Ω, the projection of electronic angular momentum along the molecular axis. In GaAs/ GaAs⁻, the states with same value of Ω will interact with each other; through this interaction, the lower-lying state will be pushed to even lower energy while the higher-lying state will be pushed to higher energy. In the case where more than two states have the same Ω value, the state lying in the middle may be pushed upwards or downwards. In Ge_2/ Ge_2^-, however, only those states with the same Ω value and the same g/u symmetry will interact; for example, a 1_g and a 1_u state do not interact with each other because they do not have the same symmetry. Much of the differences we found for the ordering of the low-lying electronic states between these two species can be explained on this ground. For the purpose of comparison with Figure 4, the energetic orderings of the low-lying electronic states in Ge_2/Ge_2^- based on reference 17 are shown in Figure 7.

128

Compared to Ge_2, the splitting between the 0^- and 0^+ components, based on our assignments, is rather large. This splitting was determined to be 112 cm^{-1} for Ge_2;[17] but it is 483 cm^{-1} for GaAs. On one hand, this large 0^- - 0^+ splitting in GaAs may be attributed to the different extent of interaction these two states experience with other 0^- or 0^+ states; on the other hand, our assignment of the origin transition to the 0^- state is somewhat speculative, we need to view this splitting obtained based on the assignment with caution.

The g/u symmetry also imposes more strict selection rules for ZEKE spectroscopy due to the Wigner threshold law.[24] Near threshold, the detachment cross section rises sharply only for $l=0$, or s-wave detachment, where l is the angular momentum of the ejected electron. As ZEKE spectroscopy relies on detaching electrons near a detachment threshold, it is sensitive only to s-wave transitions. Geltman and coworkers extended the threshold law to diatomics.[25] Given the angular momentum of molecular orbitals in a diatomic anion, the end result is that only transitions involving the detachment from π_u, σ_u orbitals of a homonuclear diatomic, and π, σ orbitals of a heteronuclear diatomic yield s-wave photoelectrons. The two highest occupied molecular orbitals of Ge_2^- are π_u and σ_g; photodetachment involving removal of an electron from the σ_g orbital yields p-wave electrons. For GaAs$^-$, removal of an electron from either σ orbital or π orbital results in s-wave detachment. Therefore, in the case of Ge_2^-, some transitions that are active in the PES can not be observed in the ZEKE spectrum, such as the $^3\Pi_u \leftarrow {}^2\Pi_u$, and the $^1\Pi_u \leftarrow {}^2\Pi_u$ transitions. In the case of GaAs$^-$, all the transitions observed in the PES but the $^3\Sigma^- \leftarrow {}^2\Pi$ transition are also observed in the ZEKE spectrum.

B. Comparison with *ab initio* calculations

By comparison with the experimentally determined spectroscopic constants, the best *ab initio* calculation was done by Balasubramanian at the CASSCF/SOCI level.[8] In fact, the results of this *ab initio* calculation is essential in assigning our spectra. This *ab initio* calculation correctly predicts the energetic orderings of the low-lying electronic states in GaAs and GaAs⁻. The relative bond lengths between the anion ground state and the neutral states obtained from Franck-Condon simulation of the ZEKE spectrum are also in good agreement with the *ab initio* calculation. The calculated vibrational frequencies are 10-25 cm^{-1} too small for the neutral states, and in good agreement with the experiment for the anion X1/2 state.

VI. Conclusions

The work presented here again shows the combination of anion PES and ZEKE spectroscopy provides a powerful probe of electronically complicated species. The relative term energies and vibrational frequencies obtained for several low-lying electronic states of GaAs and GaAs⁻ were found to be consistent with *ab initio* values.

The $^2\Sigma^+$ state ($\omega_e=300\pm5$ cm^{-1}) was found to be the ground state of GaAs⁻; and the $^2\Pi_{3/2}$ state lies 402 cm^{-1} above the ground state. From the triplet band of the ZEKE spectrum, the relative term energies of the 2, 1, 0⁻, 0⁺ components of the $^3\Pi$ state, with their 264±8 cm^{-1} vibrational frequency, were found to be 0, 464, 615, 1098 cm^{-1},

respectively. From the singlet band of the ZEKE spectrum, the term energies of the $^1\Pi$ ($\omega_e=288\pm5$ cm^{-1}) and $^1\Sigma$ ($\omega_e=291\pm5$ cm^{-1}) states relative to the 2 ($^3\Pi$) state were determined to be 4615 and 5513 cm^{-1}, respectively. Based on the features observed at low binding energies in the PES spectrum, the electron affinity of GaAs is estimated to be 1.85$\pm$0.10 eV. From the same features, the energy separation between the X1 ($^3\Sigma^-$) state and the 2 ($^3\Pi$) state of GaAs is estimated to be 0.2$\pm$0.10 eV. Based on this estimate, the term energies of the neutral states relative to the ground state can also be determined.

Acknowledgments

[1] *Gallium Arsenide: Materials, Devices, and Circuits*, edited by M. J. Howes and D. V. Morgan (Wiley, New York, 1985).

[2] C. A. Larsen, N. I. Buchan, and G. B. Stringfellow, Appl. Phys. Lett. **52**, 480 (1988).

[3] For example, C. C. Arnold and D. M. Neumark, Advances in Metal and Semiconductor Clusters, Vol. III, Edited by M. Duncan, JAI Press, Greenwich (1994).

[4] K. D. Kolenbrander and M. L. Mandich, J. Chem. Phys. **92**, 4759 (1990); Phys. Rev. Lett. **65**, 2169 (1990); K. -D. Rinnen, K. D. Kolenbrander, A. M. DeSantolo, and M. L. Mandich, J. Chem. Phys. **96**, 4088 (1992).

[5] G. W. Lemire, G. A. Bishea, S. A. Heidecke, and M. D. Morse, J. Chem. Phys. **92**, 121 (1990).

[6] C. Jin, K. J. Taylor, J. Conceicao, and R. E. Smalley, Chem. Phys. Lett. **175**, 17 (1990).

[7] S. Li, R. J. Van Zee, and W. Weltner, Jr., J. Phys. Chem. **97**, 11393 (1993).

[8] K. Balasubramanian, J. Mol. Spec. **139**, 405 (1990).

[9] U. Meier, S. D. Peyerimhoff, P. J. Bruna, and F. Grein, J. Mol. Spec. **134**, 259 (1989).

[10] M. A. Al-Laham and K. Raghavachari, Chem. Phys. Lett. **187**, 13 (1991).

[11] C. Xu, E. de Beer, D. W. Arnold, C. C. Arnold, and D. M. Neumark, J. Chem. Phys. **101**, 5604 (1994).

[12] D. W. Arnold, S. E. Bradforth, T. N. Kitsopoulos, and D. M. Neumark, J. Chem. Phys. **95**, 8753 (1991).

[13] T. N. Kitsopoulos, C. J. Chick, A. Weaver, and D. M. Neumark, J. Chem. Phys. **93**, 6108 (1990).

[14] C. C. Arnold and D. M. Neumark, Can. J. Phys. **72**, 1322 (1994).

[15] C. C. Arnold and D. M. Neumark, J. Chem. Phys. **100**, 1797 (1994); **99**, 3353 (1993).

[16] C. C. Arnold, T. N. Kitsopoulos, and D. M. Neumark, J. Chem. Phys. **99**, 766 (1993); T. N. Kitsopoulos, C. C. Arnold, Y. Zhao, and D. M. Neumark, J. Chem. Phys. **95**, 1441(1991).

[17] C. C. Arnold and D. M. Neumark, J. Chem. Phys. **102**, 6982 (1995).

[18] T. G. Dietz, M. A. Duncan, D. E. Powers, and R. E. Smalley, J. Chem. Phys. **74**, 6511 (1981).

[19] R. B. Metz, A. Weaver, S. E. Bradforth, T. N. Kitsopoulos, and D. M. Neumark, J. Chem. Phys. **94**, 1377 (1990).

[20] W. C. Wiley and I. H. McLaren, Rev. Sci. Instrum. **26**, 1150 (1955).

[21] T. N. Kitsopoulos, I. M. Waller, J. G. Loeser, and D. M. Neumark, Chem. Phys. Lett. **159**, 300 (1989); C. C. Arnold, Y. Zhao, T. N. Kitsopoulos, and D. M. Neumark, J. Chem. Phys. **97**, 6121 (1992).

[22] K. Müller-Dethlefs, M. Sander and E. W. Schlag, Z. Naturforsch **39a**, 1089 (1984); Chem. Phys. Lett. **12**, 291 (1984); K. Müller-Dethlefs and E. W. Schlag, Ann. Rev. Phys. Chem. **42**, 109 (1991).

[23] G. Herzberg, Molecular Spectra and Molecular Structure Vol. I - Spectra of Diatomic Molecules 2nd Ed., (Krieger, Malabar, Florida, 1989), p. 338.

[24] E. P. Wigner, Phys. Rev. **73**, 1002 (1948).

[25] S. Geltman, Phys. Rev. **112**, 176 (1958); L. M. Branscomb, D. S. Burch, S. J. Smith, and S. Geltman, Phys. Rev. **111**, 504 (1958).

Table I. Peak positions, labels, electronic and vibrational assignments of the triplet band of ZEKE spectrum.

Peak	Energy (cm^{-1})	Spacing (cm^{-1})	Assignment	
			$\Omega' \leftarrow \Omega''$	$v' - v''$
C	16109	-402	$2 - 3/2$	$0 - 0$
B	16211	-300	$2 - 1/2$	$0 - 1$
	16368	-143	$2 - 3/2$	$1 - 0$
A$_0$	16511	0	$2 - 1/2$	$0 - 0$
E	16677	166	$1 - 1/2$	$0 - 1$
	16736	225	$2 - 1/2$	$2 - 1$
A$_1$	16775	264	$2 - 1/2$	$1 - 0$
F	16832	321	$0^- - 1/2$	$0 - 1$
G	16975	464	$1 - 1/2$	$0 - 0$
A$_2$	17033	522	$2 - 1/2$	$2 - 0$
Q	17126	615	$0^- - 1/2$	$0 - 0$
	17250	739		
A$_3$	17286	775	$2 - 1/2$	$3 - 0$
	17308	797	$0^+ - 1/2$	$0 - 1$
	17364	853		
	17440	929		
	17501	990		
A$_4$	17529	1018	$2 - 1/2$	$4 - 0$
	17547	1036		
D$_0$	17609	1098	$0^+ - 1/2$	$0 - 0$
	17694	1183		
A$_5$	17782	1271	$2 - 1/2$	$5 - 0$

D_1	17865	1354	$0^+ - 1/2$	$1 - 0$
	17968	1457	$0^- - 1/2$	$2 - 0$
	18032	1521		
D_2	18124	1613	$0^+ - 1/2$	$2 - 0$
	18340	1829		
D_3	18384	1873	$0^+ - 1/2$	$3 - 0$

135

Table II. Peak positions, labels, electronic and vibrational assignments of the singlet band of ZEKE spectrum.

Peak	Energy (cm^{-1})	Spacing (cm^{-1})	Assignment	
			$\Omega' \leftarrow \Omega''$	$v' - v''$
J	20724	-402	$1 - a\,3/2$	$0 - 0$
I	20827	-299	$1 - X\,1/2$	$0 - 1$
H$_0$	21126	0	$1 - X\,1/2$	$0 - 0$
H$_1$	21414	288	$1 - X\,1/2$	$1 - 0$
	21678	552		
H$_2$	21702	576	$1 - X\,1/2$	$2 - 0$
K	21725	599	$0 - X\,1/2$	$0 - 1$
H$_3$	21976	850	$1 - X\,1/2$	$3 - 0$
M$_0$	22024	898	$0 - X\,1/2$	$0 - 0$
	22273	1147		
M$_1$	22315	1189	$0 - X\,1/2$	$1 - 0$
M$_2$	22602	1476	$0 - X\,1/2$	$2 - 0$
	22617	1491		

Table III. Molecular constants obtained for the neutral and anion electronic states based on the assignment of spectra.

State		T_0 (cm^{-1}) [a]	ω (cm^{-1})	r (Å)
GaAs	2 ($^3\Pi_2$)	0	264	2.36
	1 ($^3\Pi_1$)	464		
	0$^-$ ($^3\Pi_{0-}$)	615		
	0$^+$ ($^3\Pi_{0+}$)	1098	262	2.36
	1 ($^1\Pi$)	4615	288	2.34
	0$^+$ ($^1\Sigma^+$)	5513	291	2.22
	2 ($^1\Delta$)			
GaAs$^-$	X1/2 ($^2\Sigma^+$)	0	300	(2.27) [b]
	a3/2 ($^2\Pi_{3/2}$)	402		

[a] Term energies relative to the zero point energy of the 2 ($^3\Pi_2$) state.

[b] Calculated bond length of the X1/2 state of GaAs$^-$ (from reference 8).

137

Figure Captions

Figure 1. Photoelectron spectra of GaAs⁻ at three different laser polarization angles.

Figure 2. The triplet band of the ZEKE spectrum of GaAs⁻; (top) PES: (middle) experimental ZEKE spectrum; (bottom) simulation as described in the text.

Figure 3. The singlet band of the photoelectron and ZEKE spectra of GaAs⁻; (top) PES; (middle) experimental ZEKE spectrum; (bottom) simulation as described in the text.

Figure 4. Diagram of the low-lying electronic states of GaAs and GaAs⁻ as calculated by Balasubramanian.

Figure 5. The electronic states and one-electron allowed transitions relevant to the triplet band.

Figure 6. The electronic states and one-electron allowed transitions relevant to the singlet band.

Figure 7. Diagram of the low-lying electronic states of GaAs and GaAs⁻ based on the results in Reference 17.

Figure 4.1

139

Figure 4.2

Figure 4.3

GaAs

2 —————————— $^1\Delta\ (\sigma^2\pi^2)$

0^+ —————————— $^1\Sigma^+\ (\sigma^0\pi^4)$

1 —————————— $^1\Pi\ (\sigma^1\pi^3)$

0^+ ——————————

0^- ——————————

1 —————————— $\Big\}\ ^3\Pi\ (\sigma^1\pi^3)$

2 ——————————

0^+ ——————————

X 1 —————————— $^3\Sigma^-\ (\sigma^2\pi^2)$

GaAs⁻

1/2 ——————————

3/2 —————————— $\Big\}\ ^2\Pi\ (\sigma^2\pi^3)$

X 1/2 —————————— $^2\Sigma^+\ (\sigma^1\pi^4)$
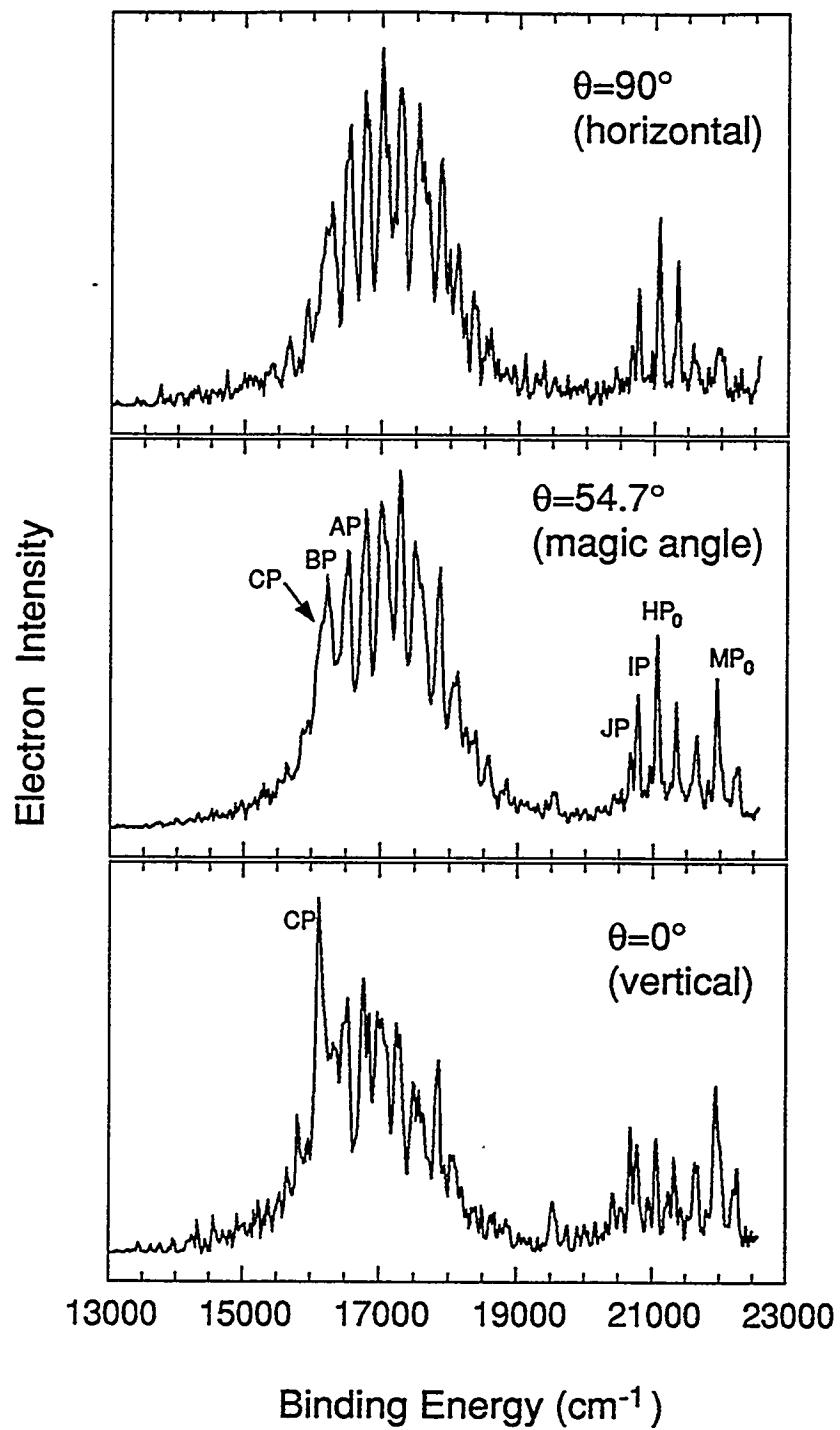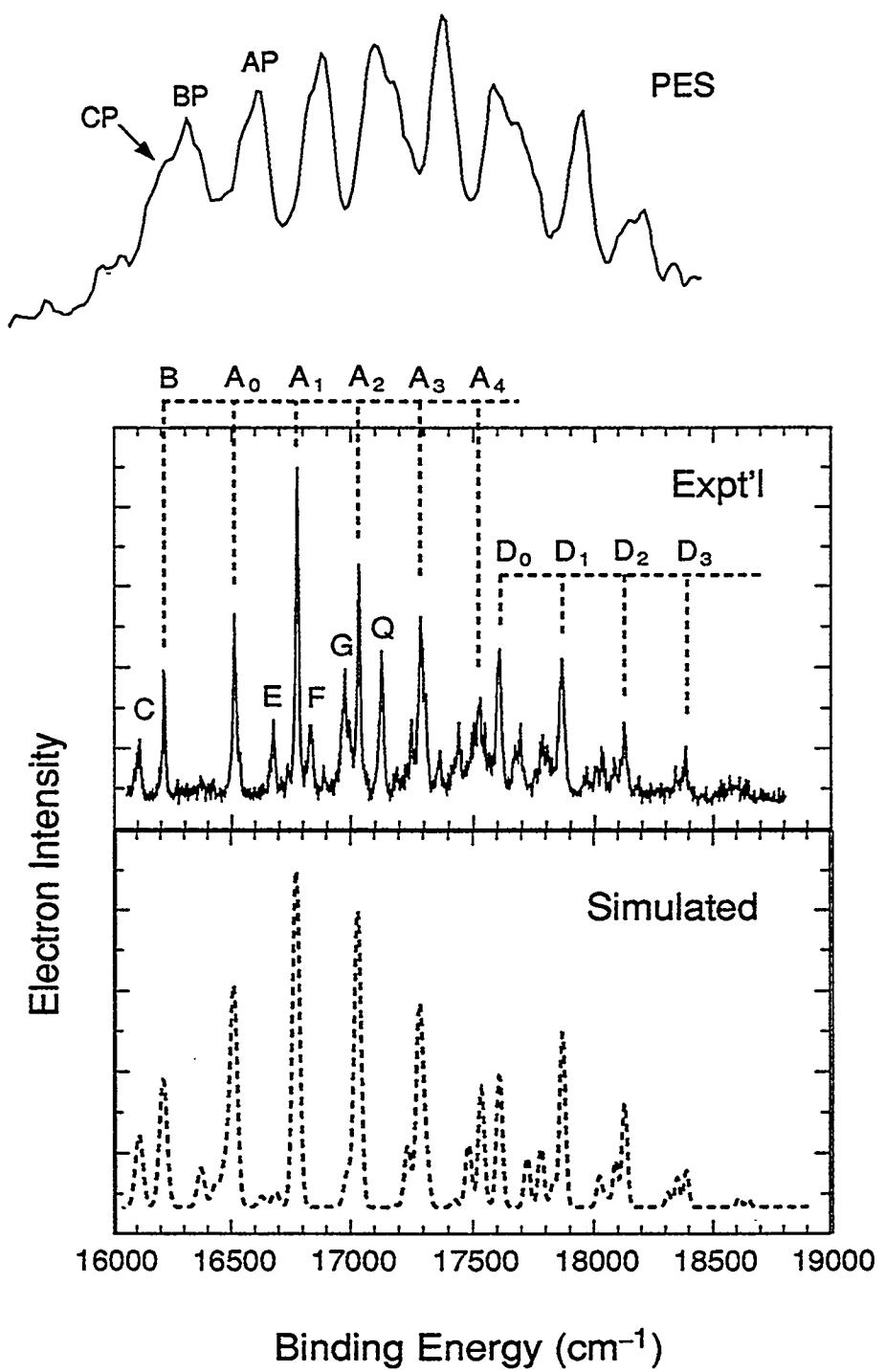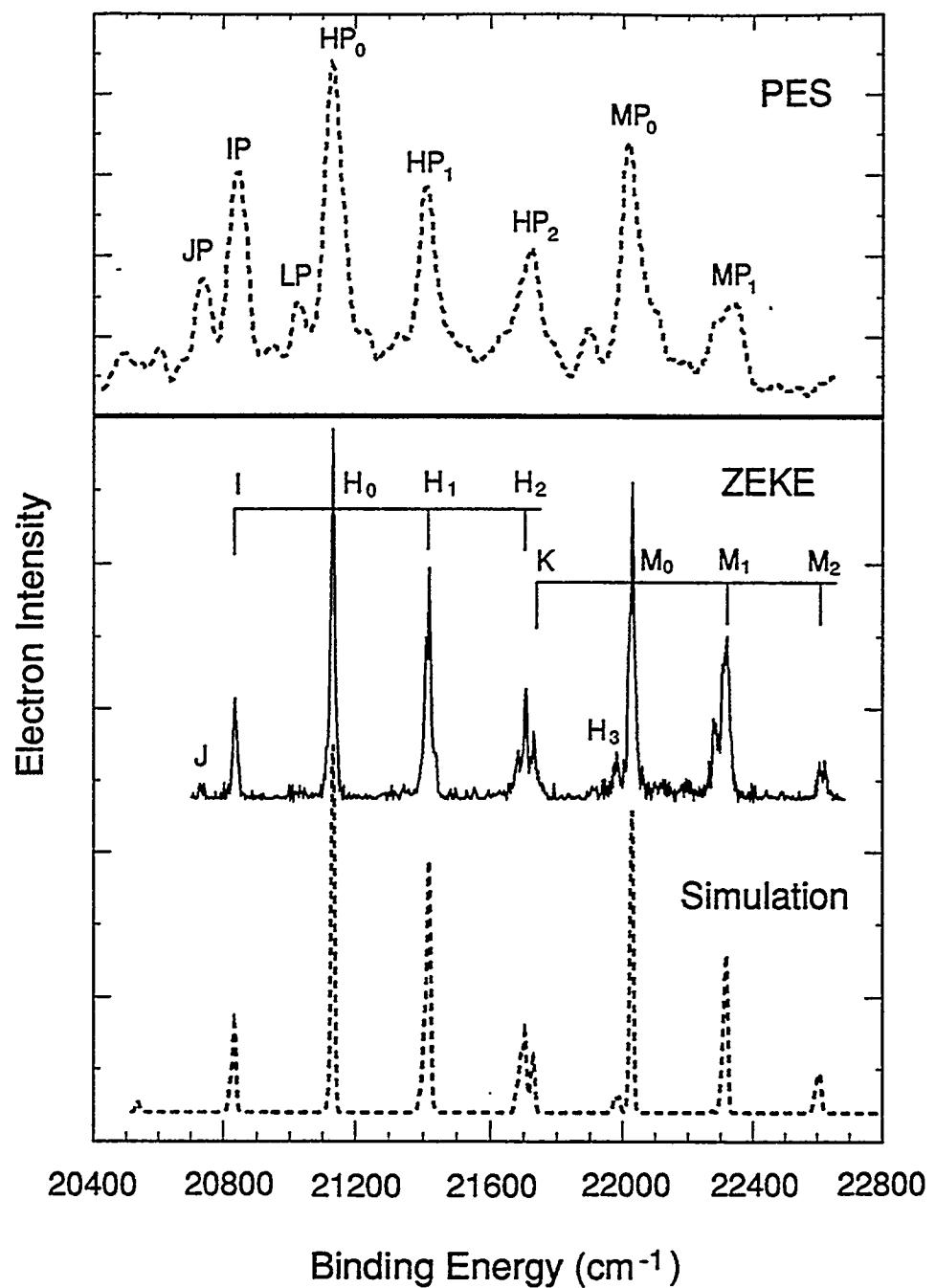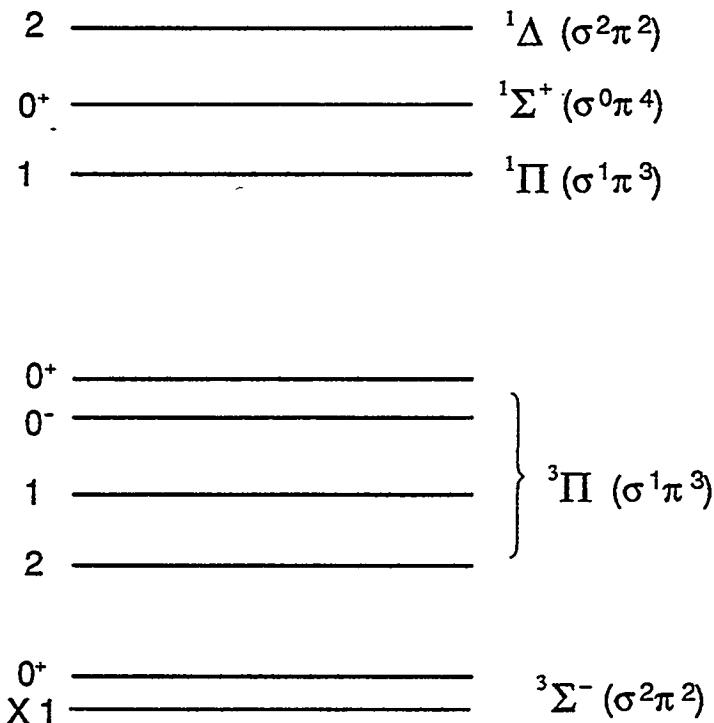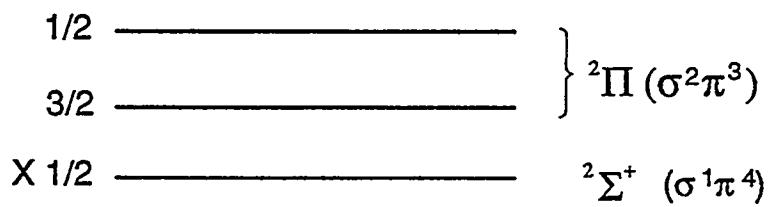
Figure 4.4

Figure 4.5

Figure 4.6
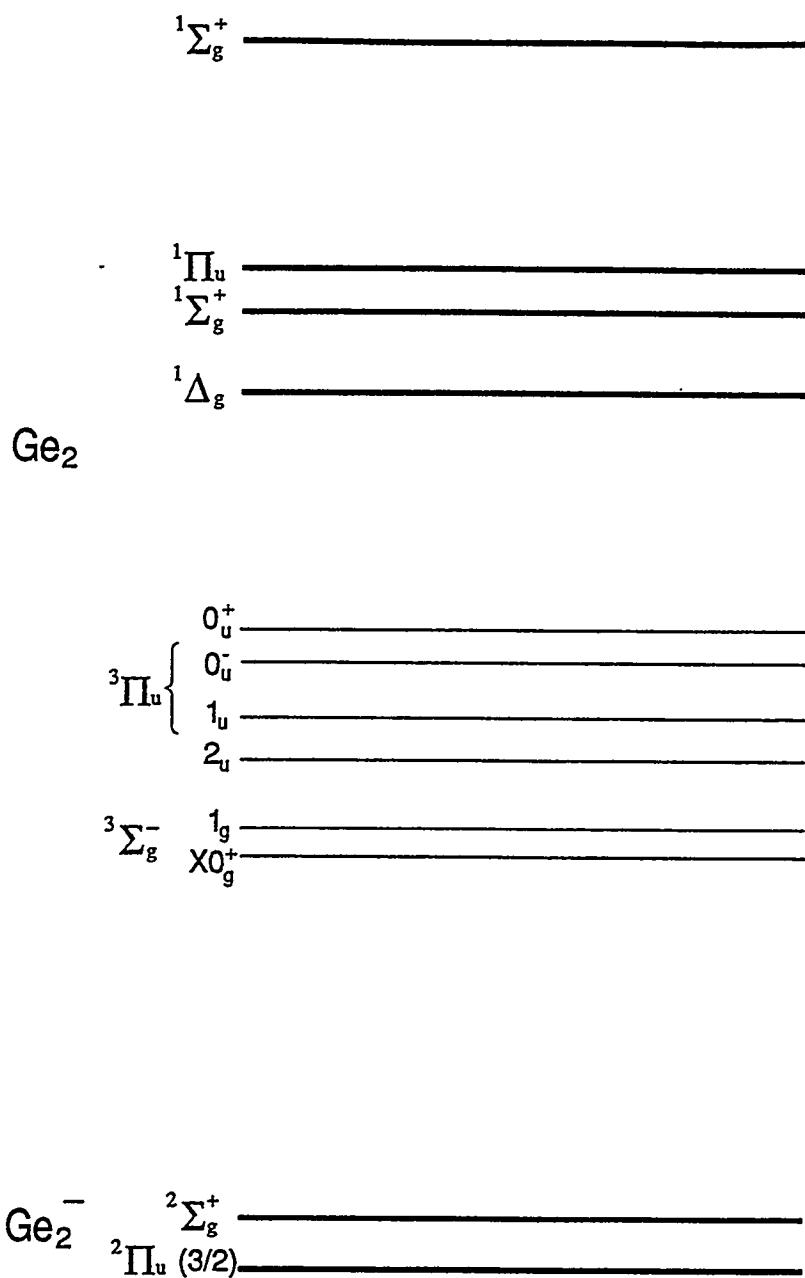
144

$^1\Sigma_g^+$ _____

$^1\Pi_u$ _____
$^1\Sigma_g^+$ _____

$^1\Delta_g$ _____

Ge$_2$

0_u^+ _____
$^3\Pi_u$ { 0_u^- _____
1_u _____
2_u _____

$^3\Sigma_g^-$ 1_g _____
X0_g^+ _____

Ge$_2^-$ $^2\Sigma_g^+$ _____
$^2\Pi_u$ (3/2) _____

Figure 4.7

145

Chapter 5. Rotationally resolved spectrum of the C $^2\Pi_u$ ← X $^2\Pi_g$ electronic transition of C_4^- via resonant 2-photon detachment spectroscopy

Abstract

The C $^2\Pi_u$ ← X $^2\Pi_g$ electronic transition of C_4^- has been studied by both one-color and 2-color resonant 2-photon detachment spectroscopy. The one-color resonant 2-photon detachment spectrum reveals vibrational structure in the excited anion state. Transitions due to excitations in one of the symmetric stretching modes as well as the bending modes are observed. The rotationally resolved spectra of the origin transition and the 2_0^1 transition of this electronic band have been obtained by resonant 2-color 2-photon detachment spectroscopy. The 2-color scheme makes it feasible to significantly reduce the laser fluence of the excitation laser beam, thus avoid the laser power-broadening associated with the one-color scheme. Fitting of the rotational line positions to the eigenvalues of the appropriate molecular Hamiltonian results in accurate determination of the molecular constants for these two electronic states.

I. Introduction

Among the family of small carbon clusters, C_4 has attracted a particularly great deal of attention because theory has predicted the existence of two different structures (the linear form and the rhombic form) as candidates for the ground state.[1] Experimentally, only the linear structure has been definitely observed. Among other experimental results, rotationally resolved infrared spectrum of linear C_4 has been reported.[2]

Compared to the neutral C_4, anion C_4^- is much less well-characterized. Experimentally, anion photoelectron spectroscopy[3,4,5,6,7] and ion chromatography studies[8] indicate that C_4^- has a linear structure. In a recent article by Maier and coworkers,[9] a low-lying excited state was reported for C_4^-; and this state was assigned to the C $^2\Pi_u$ state based on the comparison with *ab initio* calculation.[10] Electron affinities of both the linear C_4 and rhombic C_4 have been calculated by Bartlett and coworkers[11] and others[12] using high level *ab initio* theories. Adamowicz[13] calculated the vertical excitation energies of several low-lying excited states of C_4^-. Recently, Schmatz and Botschwina[10] performed large-scale open-shell coupled cluster calculations on C_4^-, and obtained spectroscopic constants of the lowest four doublet states

However, no high-resolution spectroscopic investigation has been carried out for any carbon cluster anions other than C_2^-, for which accurate spectroscopic constants have been determined for the three lowest doublet states through high resolution spectroscopic studies.[14,15,16,17,18] Based on the recently obtained absorption spectrum of C_4^- in a neon

matrix by Maier and coworkers[9], and high level *ab initio* calculations by Botschwina,[10] the energy of the $C\,^2\Pi_u \leftarrow X\,^2\Pi_g$ electronic transition is found to be about 2.7 eV — more than one half of the electron affinity (3.8 eV) of linear C_4. This electronic transition is therefore suitable for resonant two-photon detachment study. With sufficient laser resolution, one can expect to resolve detailed spectroscopic structure of C_4^- using resonant 2-photon detachment spectroscopy.

In this paper, we report two types of resonant 2-photon detachment spectra of C_4^-. The lower-resolution (0.3 cm^{-1}) spectrum in the wavelength region of 400-465 nm, obtained in the one-color detachment experiments, shows vibrationally resolved structure. Our spectrum is in qualitative agreement with Maier's matrix results[9]. However, additional features due to vibrational excitation in the bending modes are also observed in our spectrum. The higher-resolution (0.05 cm^{-1}) spectrum, obtained in the two-color experiments, shows rotationally resolved structure in two selected wavelength regions: the origin transition and the 2_0^1 transition of the observed electronic band. Molecular constants are accurately determined for both electronic states by fitting the observed rotational line positions.

II. Experimental

The apparatus used in these experiments is the threshold photodetachment spectrometer which has been described in detail elsewhere.[7,19] The mode of operation we

employ here is most similar to the *total photodetachment cross section measurements* described in reference 7.

Carbon cluster anions are generated in a pulsed discharge source which has been described previously.[20] Briefly, a gas mix of 3% acetylene, 1% CO_2 in Ne is pulsed from a piezoelectric valve and enters the discharge region where the molecules are dissociated. The discharge electrodes and the insulating Teflon plates, each of which has a channel of 2.5 mm I.D. in the center, are held together and attached to the face plate of the piezoelectric valve. The last piece of the discharge assembly, a snout with a 5 mm long, 2.5 mm I.D. channel in the center, is held at float voltage of the source. This snout serves as a clustering channel for the mix of species resulted from discharge. To improve stability of the ion signal, a 1 keV electron beam intersects the expanding molecular beam. The free expansion length of the molecular beam, which is the distance between the discharge assembly and the skimmer, strongly affects the temperature of the negative ions. The further this distance, the colder the ions become.

Negative ions that pass through a 2 mm skimmer are collinearly accelerated to 1 keV. Ions are separated according to their mass-to-charge ratios in a 2 meter long beam-modulated time-of-flight mass spectrometer before they are detected by multichannel plates. The negative ions interact with the laser beams in the detector region, approximately 20 cm before the ions reach the ion detector. All the electrons generated via photodetachment of the negative ions are extracted perpendicularly by a weak electric field and collected by the electron detector. The electron signal is normalized to the ion signal and laser power. The low resolution spectra, which cover a wide photon energy

region, are taken with the one-color scheme. The high resolution spectra, which reveal rotationally resolved structure, are taken with the two-color scheme. In the one-color experiments, the same color is used to excite the bound − bound transition and to photodetach the excited anion. In the two-color experiments, two different colors are used for the excitation and photodetachment steps.

In the one-color experiments, the output of a dye laser pumped by a XeCl excimer laser is used. The tuning element of this laser system is the grating of the dye laser. The measured bandwidth is *ca.* 0.3 cm^{-1}. The laser fluence used in this type of experiments is typically around 30 mJ/cm^2. To obtain the wavelength scans reported here, the following laser dyes are used: Coumarin 460, Coumarin 440, Exalite 416, and DPS.

In order to achieve sufficient detachment, high photon fluence is needed in the one-color detachment experiments. This high laser fluence saturates the excitation transition which results in power-broadening in the spectrum. This problem is solved by carrying out a resonant two-color two-photon detachment experiment. In a two-color experiment, the first laser pulse, which has weak photon fluence, excites the ion from its ground state to the excited electronic state; the second laser pulse, with smaller photon energy but much higher photon fluence, then detaches the electron from the excited anion. During the experiment, the frequency of the first laser pulse is tuned while that of the second pulse is fixed.

In the two-color experiments, the first laser pulse comes from the same excimer-pumped dye laser. However, in order to obtain rotationally resolved spectra, a solid state intracavity etalon is used to obtain a narrower bandwidth. The laser bandwidth from the

intracavity etalon is 0.04 - 0.07 cm^{-1}. This laser beam is used to photoexcite C_4^- to an excited electronic state. To prevent lifetime broadening due to laser power saturation, the laser fluence is significantly reduced, typically down to 1 mJ/cm^2. No detectable C_4^- ions are detached with this amount of laser fluence. The second laser beam, either from a YAG-pumped dye laser or the second harmonic output of a YAG laser, is used to detach the photoexcited ions. The wavelength of the second laser beam is fixed at either 588 nm or 532 nm during the two-color experiments. Typical laser fluence of this laser beam is *ca.* 40 mJ/cm^2 . At this amount of laser fluence, this laser beam alone does not detach C_4^-. In other words, no detectable electrons are observed when the first laser beam is blocked. This is because, at either 588 nm or 532 nm, the detachment laser is not resonant with the electronic transition. During the experiment, electrons generated by the second laser beam are collected as a function of the wavelength of the first laser beam. We find that electron signal intensity changed very little when the time delay between the two laser pulses is varied from 0 to 200 ns. This observation along with the multiphoton detachment mechanism will be discussed in detail in a related paper.[21] For the spectra reported here, the two laser pulses are separated by 120 ns temporally. In order to assure both laser beams interact with the same ions, the laser beams are also spatially separated by 6 mm along the axis of ion beam. The diameter of the second laser beam is larger than that of the first laser beam to ensure good spatial overlap with the excited C_4^- ions.

During the two-color scans, the intracavity etalon is stepped in intervals of about 0.02 cm^{-1} every 80-100 laser shots. A total of 3-5 such scans are summed up. Wavelength calibrations are performed immediately after the scans are taken. Absolute

151

wavelength calibration is obtained by taking the absorption spectrum of a Fe-Neon discharge lamp. Relative wavelength calibration between the observed neon lines is obtained by recording the fringe spectrum of a solid state monitor etalon with a free spectral range of 0.67 cm^{-1}. The fringe spectrum shows peaks that are separated from each other by the free spectral range of the monitor etalon.

III. Results

The low resolution, one-color resonant multiphoton detachment spectrum of C_4^- is shown in Figure 1. The wavelength region between 400 nm and 470 nm was scanned. The most prominent feature of this spectrum is a single progression with a spacing of *ca.* 750 cm^{-1}. The first large peak in this progression at 21872 cm^{-1} (or 457.2 nm) appears to be the origin transition. Additional features with smaller intensities are observed between members of the main progression. Each main peak consists of several partially resolved features.

Two small sections of the one-color spectrum are selected for the high resolution two-color experiments: the origin transition near 457.2 nm and the next strong transition near 442 nm. The rotationally resolved two-color spectra for these two energy regions are shown in Figure 2. In each of these two spectra, there are two band heads, labeled as $R_{3/2}$ and $R_{1/2}$, towards higher photon energy. For the resolved peaks, the peak width at FWHM is *ca.* 0.1 cm^{-1}. The peak spacings, ranging from 0.1 cm^{-1} to 1.0 cm^{-1}, increase towards smaller photon energies. The most remarkable difference between these two

152

bands is the separation between the two band heads, which is significantly larger in the 2_0^1 band than in the origin band. Also, the signal-to-noise ratio appears to be worse in the 2_0^1 band.

We also attempted to look at the transition near 448 nm with two-color detachment, but our resolution was not sufficient to resolve the individual rotational lines in this band.

IV. Analysis and discussion

A. One-color spectrum

The energy of the origin transition is 21872 cm^{-1}, or 2.71 eV. The vibrational frequency, based on the peak spacings in the main progression, is 750 cm^{-1}. Schmatz and Botschwina[10] calculated the electronic term energy of the $C^2\Pi_u$ state to be 2.8 eV, and one of its totally symmetric vibrational frequencies, the v_2 mode, to be 777 cm^{-1}. By comparison, we assign the structures in our spectrum to the $C\ ^2\Pi_u \leftarrow X\ ^2\Pi_g$ electronic transition of C_4^-. This assignment is also consistent with that of the C_4^- absorption spectrum obtained in a neon matrix.[9] The main progression, as indicated in Figure 1, is assigned to transitions from the $v_2=0$ state of the X state to $v_2= 0,1,2,...$ states of the C state. The v_2 mode is a totally symmetric stretching mode. This progression is consistent with what one would predict based on the calculated bond length changes calculated for this electronic transition.[10]

Compared to Maier's matrix results,[9] additional features are observed in our spectrum. The most significant discrepancies are the features between the totally symmetric stretching peaks observed in our spectrum. These additional features are assigned to transitions due to double-quanta excitations in the low frequency bending modes. The bending frequency thus obtained, 223 cm^{-1}, is in fair agreement with the *ab initio* ν_5 frequency of the C$^2\Pi_u$ state. The calculated frequency at UHF/6-31G* level is 250 cm^{-1}.

Our explanation of this discrepancy is based on the fact that different light sources are employed in these two experiments. In Maier's experiment, a xenon or arc lamp was used as the light source. In our experiment, the laser fluence used in the one-color experiments is so high that it saturates the excitation process. The strong transitions are more saturated than the weak transitions. In a two-color experiment, the excitation laser fluence can be greatly reduced; therefore, the intensity ratio should resemble Maier's results more closely. In our C_6^- C $^2\Pi_u \leftarrow$ X $^2\Pi_g$ spectrum, which is published elsewhere,[21] a similar situation occurs. The decrease in bending mode intensity relative to stretching mode intensity was experimentally observed in the two-color spectrum of C_6^-.

The peak positions, spacings and assignments are given in Table I. Vibrational frequencies of the C $^2\Pi_u$ state determined from our spectrum are compared with the calculations. The ν_2 mode frequency was calculated by Schmatz and Botschwina[10] and the ν_5 frequency is that from a Gaussian92 calculation at UHF/6-31G* level.

The resolution at which we obtain our one-color detachment spectrum is significantly better than the bandpass of the light source used in Maier's work. Our

spectrum shows more vibrational features. In each vibrational transition, partly resolved structures are observed. These finer structures are mostly likely due to unresolved rotational transitions and other types of interactions among molecular eigenstates such as the Renner-Teller effect and spin-orbit interaction. The sharp lines on top of the unresolved broad features may correspond to unresolved rotational band heads. A few of these band heads actually become resolved in the two-color experiments which we will analyze in the next section.

B. Two-color spectrum

Before analyzing the high resolution data, a brief discussion of C_4^- spectroscopy of the $C\,^2\Pi_u \leftarrow X\,^2\Pi_g$ transition is in order. Although the spin-orbit splitting constant of C_4^- is not known, one would expect it to be close to that of C_5^- and C_6^-. The spin-orbit splitting constants are known for the $^2\Pi_u$ states of C_5^- and C_6^- from ZEKE spectroscopy of these two negative ions.[6,7] The spin-orbit splittings are 26 cm^{-1} and 29 cm^{-1} for C_5^- and C_6^-, respectively. The rotational constant of C_4^- is calculated to be around 0.16 cm^{-1} — very small compared to the spin-orbit splitting. Therefore, the rotational fine structure of C_4^- should belong to Hund's case (a). Because the molecular orbital configurations of the $X\,^2\Pi_g$ and $C\,^2\Pi_u$ states are $...1\pi_u^4\,1\pi_g^3$ and $...1\pi_u^3\,1\pi_g^4$, respectively, the $\Omega=3/2$ state of each electronic state should be lower-lying than the $\Omega=3/2$ state. In a $^2\Pi_u \leftarrow ^2\Pi_g$ electronic transition, if both electronic states belong to Hund's case (a), each of the $^2\Pi_{3/2} \leftarrow ^2\Pi_{3/2}$, $^2\Pi_{1/2} \leftarrow ^2\Pi_{1/2}$ manifolds should have six branches (two P, two Q and two R).

155

However, due to nuclear spin statistics, in the case of a $^2\Pi$ state of a linear carbon chain, for each J level, one of the Λ doublet levels is missing. The consequence of this is that one member of each pair of branches will be missing, resulting in only one P, one Q and one R-branch for each spin-orbit manifold. Therefore, there will be six branches in total, with two band heads. Band heads form because of the different rotational constants for these two states. The energy separation between the band heads should approximately equal to the difference in spin-orbit splitting between the two electronic states.

Figure 3 shows the first few rotational levels for the $^2\Pi_u$ and $^2\Pi_g$ states. The rotational levels are labeled by the total angular momentum J. The F_1 and F_2 manifolds correspond to the $^2\Pi_{3/2}$ and $^2\Pi_{1/2}$ spin-orbit states, respectively. The dashed lines represent the levels that are not populated due to nuclear spin statistics. The *e/f* parity labeling for each J level is determined using a scheme suggested by Kopp and Hougen,[22] and Brown *et al.*.[23] The six transitions from the $J=7/2$ levels are shown; each of these transitions represents one transition in each of the six branches.

From Figure 3, it is easy to see that Λ-doubling does not occur in the C_4^- spectrum due to nuclear spin statistics. However, a phenomenon called *staggering* arises as a combined consequence of nuclear spin statistics and Λ-type doubling. Herzberg discussed this phenomenon for diatomic molecules.[24] The staggering effect refers to the situation in which the even-numbered lines are displaced to one side and the odd-numbered lines to the other side of a mean value. For P and R branches, this effect is proportional to the difference in the Λ-doubling parameters between the upper and lower states. For the Q branch, it is proportional to the sum of Λ-doubling parameters of the states. Therefore,

one expects that staggering may play a more significant role in determining the line positions in the Q-branch.

In the origin band of the rotationally resolved C_4^- spectrum, as shown in the top half of Figure 2, all six branches, i.e., $P_{3/2}$, $Q_{3/2}$, $R_{3/2}$, $P_{1/2}$, $Q_{1/2}$, and $R_{1/2}$-branches, are present. However, the $Q_{1/2}$-branch, i.e., the Q-branch of the $^2\Pi_{1/2} \leftarrow {}^2\Pi_{1/2}$ manifold, is buried underneath the $P_{3/2}$ branch. The P and R-branches are rotationally resolved; the $Q_{3/2}$-branch is partially resolved.

With one-quanta of excitation in a totally symmetric stretching mode, one would expect the same type of rotational branches as in the origin band. As shown in the bottom half of Figure 2, the same type of rotational branches are indeed observed for the 2_0^1 band.

In the origin band, peaks in P and R-branches are assigned using the combination differences method. The peak positions and J level assignments are listed in Table II. Notice that the first transition in the $P_{3/2}$-branch is P(5/2). This observation confirms our assignment of the $^2\Pi_{3/2}$ state as the ground state. The $Q_{3/2}$ branch is only partly resolved, the assignment of peaks in the Q-branch is aided by the molecular parameters estimated from fitting the peaks in the P and R branches.

Once the peak assignments have been completed, the line position data are fit to the effective rotational Hamiltonian derived by Zare $el\ al.$[25] using a nonlinear least-squares fitting program. The parameters used for each electronic and vibrational state were T_v, the electronic and vibrational term energy (with T_0 of X $^2\Pi_g$ state set to 0); B_v and D_v, the rotation and distortion constants, respectively; p_v and q_v, the Λ-doubling parameters as

defined in Ref. 25; and A_v, the spin-orbit coupling constant. The appropriate Hund's case (a) matrix elements for a $^2\Pi$ molecule were shown in a paper by Neumark *el al.*.[26]

The fitting procedure is as follows: (1) first, the matrix elements of the upper and lower state Hamiltonians are calculated for each J value; (2) both Hamiltonians are numerically diagonalized and the resulting sets of eigenvalues are used to construct a set of calculated line positions; and (3) from a least-squares fit of the calculated to the observed line positions, an improved set of molecular constants is obtained. This nonlinear least-squares procedure is repeated until a satisfactory set of molecular constants is obtained. This least-squares procedure is based on the method of Marquardt that combines the Gauss method and the method of steepest descent.[27]

The origin band and the 2_0^1 band are fit separately. All the lines listed in Table II and Table III are included in the fitting. Line positions were weighted according to their uncertainties, typically 0.02-0.03 cm^{-1}. The origin band is fit first. Some of the best-fit parameters are shown in Table IV. These parameters are obtained by simultaneously fitting all the molecular parameters. In fitting the 2_0^1 band, the ground state parameters are held fixed at the values obtained from the origin band. These two bands both originate from the ground electronic state, but many more lines are resolved in the origin band and the signal to noise ratio is also better in the origin band. The differences between the observed and calculated line positions are displayed in Table II and Table III. Table IV also-shows the results of the *ab initio* calculation by Schmatz and Botschwina.[10] Notice that the *ab initio* parameters are calculated for the equilibrium geometry.

Since no transitions between F_1 and F_2 manifolds were observed, A'' and A' are highly correlated, and this is the origin of their very large error bars. However, the difference between these two, $(A'' - A')$, is accurately determined. In the 2_0^1 band, peaks due to transitions in the F_2 manifold can not be assigned. Not only because these peaks are less intense but also because they overlap with peaks in the P-branch of F_1 manifold. Since all the assigned transitions are due to the F_1 manifold, the spin-orbit splitting constant can not be obtained through this fitting. In fitting the 2_0^1 band, A_I of the C state is obtained from ΔA, the band head separation, and the best-fit A_0 value of the X state.

The values of the Λ-doubling parameters, p_v and q_v, and the centrifugal distortion constants, D_v, are not shown in Table IV. This is because, based on the fitting in which all the parameters are adjustable, the uncertainties in these parameters are several times as large as their fitted values. However, these values may be estimated with smaller error bars if the fitting procedure is modified.

Because the staggering effect is most significant in Q-branch, these parameters can be estimated if we fit the Q-branch lines alone. However, the Q-branch in our spectrum is only partially resolved and only a few lines can be assigned. In order to obtain a rough estimate of the Λ-doubling parameters, we fit the line position data by heavily weighting the Q branch lines and making the P and R branch lines much less important. The procedure gives the following estimates: for the X state, $p_0 = (1.2\pm3.0)\times10^{-2}$ cm^{-1}, and $q_0 = (-4.4\pm3.3)\times10^{-3}$ cm^{-1}; for the C state, $p_0 = (1.3\pm3.3)\times10^{-2}$ cm^{-1}, and $q_0 = (-5.3\pm4.0)\times10^{-3}$ cm^{-1}.

The centrifugal distortion constants, D_V, for the X and C states are found to be around 7×10^{-7} cm^{-1}. This is close to the value of D_V for the ν_3 (σ_u) mode of C_4 which was found to be 9×10^{-7} cm^{-1}.[2] During the fitting, D_0 of the X state and D_0 of the C state are found to be strongly correlated. In a slightly modified fit, their difference can be determined with much smaller uncertainty. This is done by (1) first obtaining the best-fit parameters; and (2) then keeping one of the D_0 values fixed at the best-fit value while fitting the rest of the parameters again. The difference in D_0 values between the X and C states is shown in Table IV.

The rotational constants are in excellent agreement with *ab initio* calculations.[10] The α constant for the ν_3 (σ_u) mode of C_4 was found to be 5×10^{-4} cm^{-1}.[2] The α constant for the ν_2 mode of C_4^- is smaller (*ca.* 2×10^{-4} cm^{-1}), indicating that the potential energy surface is fairly symmetric about the equilibrium geometry for this vibrational mode.

Based on the different band head separation in the origin band and the 2_0^1 band, one obtains two different ΔA values, 1.54 cm^{-1} and 6.45 cm^{-1}, respectively. We interpret this to mean that the two spin-orbit components of the C state have different ν_2 frequencies. The ν_2 frequency of the $^2\Pi_{3/2}$ state is 4.9 cm^{-1} larger than that of the $^2\Pi_{1/2}$ state. This discrepancy in vibrational frequency may be due to some type of perturbation of the vibrational states. One very likely possibility is Fermi interaction between vibronic states of the same symmetry species. Fermi interactions are commonly observed in polyatomic molecules. Depending on the extent of coupling and the closeness of the interacting states in energy, Fermi interaction can shift vibrational levels by significant amounts. In C_4^-, the most likely vibronic levels to have Fermi interaction with the $\nu_2=1$

state are the $v_5=2$, 4 and $v_6=2$ states, which are all within 300 cm^{-1} in energy. The v_5 and v_6 modes are the two bending modes of C_4^-.

A good analogy to C_4^- is the linear NCO radical.[28] The two spin-orbit components of the (100) vibrational state of NCO B$^2\Pi$ electronic state experience different amount of Fermi interaction with the (020) bending levels. Consequently, in the B $\leftarrow$ X electronic transition, the splitting between $\Omega=3/2$ and $\Omega=1/2$ manifolds for the origin band is 19 cm^{-1}, while this splitting becomes 64 cm^{-1} for the 1_0^1 band.

The extent of Fermi interaction in C_4^- is not known. From our experiment, we do not have enough information to determine whether the vibrational frequency without Fermi interaction would be higher or lower. Botschwina's calculation gives this frequency as 777 cm^{-1} — higher than the average frequency obtained in our fit, which is the difference between T_0 and T_1, i.e., 752.4 cm^{-1}.

Having obtained the spectroscopic constants, we tried to simulate our spectrum by assuming a Boltzmann distribution for the anion population. Relative line intensities in each manifold are calculated from the product of the line strength, determined by Hönl-London formulae[29] for a $^2\Pi \leftarrow {}^2\Pi$ transition, and the Boltzmann factor. The simulated spectrum of the origin band, along with the experimental spectrum, is shown in Figure 4. A very good simulation is obtained compared to the experimental spectrum. A rotational temperature of 35 K and spin-orbit temperature of 45 K were used in calculating Boltzmann factors. Peak width in the simulation at FWHM is 0.10 cm^{-1}. We believe this width is instrument limited, with the laser bandwidth and Doppler broadening making the largest contributions to this value.

V. Conclusions

Resonant 2-photon detachment spectroscopy provides a means of studying electronic transitions in the negative ions. The one-color detachment spectrum of C_4^- reveals vibrational structure of the excited anion state. The two-color detachment spectrum shows rotationally resolved structure of the $C^2\Pi_u \leftarrow X^2\Pi_g$ electronic transition. The observed rotational structure confirms the assignment of these two electronic states of C_4^-. The molecular constants obtained for these two states are in good agreement with the results of high level *ab initio* calculations.

From this work, it has been shown that the excitation and detachment processes have quite different cross sections; the first step is much more easily saturated by laser power. However, through a 2-color scheme, the power-broadening associated with the one-color experiments can be avoided by exciting the electron transition with a laser beam of low photon fluence and then detaching the excited anion with a second laser beam of much higher photon fluence. This technique can be applied to study other negative ions with allowed electronic transition below the electron affinity; one such example is C_6^- and other even-numbered carbon cluster anions.

Acknowledgments

[1] W. Weltner, Jr. and R. J. van Zee, Chem. Rev. **89**, 1713 (1989).

[2] J. R. Heath and R. J. Saykally, in *On Clusters and Clustering, From Atoms to Fractals*, edited by P. J. Reynolds (Elsevier, Amsterdam, 1993), p.7; J. R. Heath and R. J. Saykally, J. Chem. Phys. **94**, 3271 (1991).

[3] S. Yang, K. J. Taylor, M. J. Craycraft, J. Conceicao, C. L. Pettiette, O. Cheshnovsky, and R. E. Smalley, Chem. Phys. Lett. **144**, 431 (1988).

[4] S. H. Yang, C. L. Pettiette, J. Conceicao, O. Cheshnovsky, and R. E. Smalley, Chem. Phys. Lett. **139**, 233 (1987).

[5] D. W. Arnold, S. E. Bradforth, T. N. Kitsopoulos, and D. M. Neumark, J. Chem. Phys. **95**, 8753 (1991).

[6] T. N. Kitsopoulos, C. J. Chick, Y. Zhao, and D. M. Neumark, J. Chem. Phys. **95**, 5479 (1991).

[7] C.C. Arnold, Y. Zhao, T. N. Kitsopoulos, and D. M. Neumark, J. Chem. Phys. **97**, 6121 (1992).

[8] G. V. Helden, P. R. Kemper, N. G. Gotts, and M. T. Bowers, Science **259**, 1300 (1993).

[9] P. Freivogel, J. Fulara, M. Jakobi, D. Forney, and J. P. Maier, J. Chem. Phys. **103**, 54 (1995).

[10] S. Schmatz and P. Botschwina, (*manuscript from the authors*, 1995).

[11] J. D. Watts, I. Cernusak, and R. J. Bartlett, Chem. Phys. Lett. **178**, 259 (1995).

[12] L. Adamowicz, J. Chem. Phys. **94**, 1241 (1995).

[13] L. Adamowicz, Chem. Phys. 156, 387 (1991).

[14] G. Herzberg and A. Lagerqvist, Can. J. Phys. **46**, 2363 (1968).

[15] P.L. Jones, R. D. Mead, B. E. Kohler, S. D. Rosner, and W. C. Lineberger, J. Chem. Phys. **73**, 4419 (1980).

[16] U. Hefter, R. D. Mead, P. A. Schulz, and W. C. Linberger, Phys. Rev. A **28**, 1429 (1983).

[17] R. D. Mead, U. Hefter, P. A. Schulz, and W. C. Lineberger, J. Chem. Phys. **82**, 1723 (1985).

[18] B. D. Rehfuss, D.-J. Liu, B. M. Dinelli, M.-F. Jagod, W. C. Ho, M. W. Crofton, and T. Oka, J. Chem. Phys. **89**, 129 (1988).

[19] T. N. Kitsopoulos, I. M. Waller, J. G. Loeser, and D. M. Neumark, Chem. Phys. Lett. **159**, 300 (1989).

[20] D. L. Osborn, D. J. Leahy, D. R. Cyr, and D. M. Neumark , in press.

[21] Y. Zhao, E. de Beer, and D. M. Neumark, (manuscript in preparation).

[22] I. Kopp and J. T. Hougen, Can. J. Phys. **45**, 581 (1967).

[23] J. M. Brown, J. T. Hougen, K.-P. Huber, J. W. C. Johns, I. Kopp, H. Lefebvre-Brion, A. J. Merer, D. A. Ramsay, J. Rostas, and R. N. Zare, J. Mol. Spectrosc. **55**, 500 (1975).

[24] G. Herzberg, *Molecular Spectra and Molecular Structure, Vol. I*, p. 268, D. Van Nostrand Company, Princeton (1950).

[25] R. N. Zare, A. L . Schmeltekopf, W. J. Harrop, and D. L. Albritton, J. Mol. Spectrosc. **46**, 37 (1973).

[26] D. M. Neumark, K. R. Lykke, T. Andersen, and W. C. Lineberger, J. Chem. Phys. **83**, 4364 (1985).

[27] W. H. Press, S. A. Teukolsky, W. T. Vetterling, and B. P. Flannery, *Numerical Recipes in Fortran*, 2nd ed. (Cambridge, 1992) p. 678-683

[28] R. N. Dixon, Can. J. Phys. 38, 10 (1960);   D. R. Cyr, R. E. Continetti, R. B. Metz, D. L. Osborn, and D. M. Neumark, J. Chem. Phys. **97**, 4937 (1995).

[29] G. Herzberg, *Molecular Spectra and Molecular Structure, Vol. I*, p. 208, D. Van Nostrand Company, Princeton (1950).

Table I. Peak positions, relative energies, assignments, and vibrational frequencies from one-color multiphoton detachment spectrum of C_4^-.

Peak Position (nm)	Peak Position (cm^{-1})	Relative Energies (cm^{-1})	Assignment	Frequencies (cm^{-1})	
				Expt	Calc
457.2	21872	0	Origin		
448.2	22311	445	5_0^2	π_u 223	250[a]
441.9	22630	750	2_0^1	σ_g 750	777[b]
433.4	23073	1198	$2_0^1 5_0^2$		
428.0	23364	1490	2_0^2		
422.6	23663	1792			
418.8	23878	2005			
414.8	24108	2234	2_0^3		

[a] the calculated π_u frequency at UHF/6-31G* level using GAUSSIAN 92;

[b] from Reference 10.

Table II. Observed transitions of the origin band of the C $^2\Pi_u \leftarrow$ X $^2\Pi_g$ transition of C_4^- from the 2-color multiphoton detachment spectrum (in cm^{-1}).

F_1 manifold (Ω=3/2)		
	Observed	(Obs - Calc) $\times 10^2$
P(2.5, f→f)	21871.45(2)	1
P(3.5, e→e)	21871.06(2)	0
P(4.5, f→f)	21870.66(2)	0
P(5.5, e→e)	21870.23(2)	0
P(6.5, f→f)	21869.80(2)	1
P(7.5, e→e)	21869.32(2)	-1
P(8.5, f→f)	21868.83(3)	-1
P(9.5, e→e)	21868.34(2)	0
P(10.5, f→f)	21867.80(3)	-2
P(11.5, e→e)	21867.26(2)	-1
P(12.5, f→f)	21866.73(3)	2
P(13.5, e→e)	21866.12(2)	-1
P(14.5, f→f)	21865.53(2)	1
P(15.5, e→e)	21864.90(2)	0
P(16.5, f→f)	21864.26(2)	0
P(17.5, e→e)	21863.60(2)	1
P(18.5, f→f)	21862.91(2)	0
P(19.5, e→e)	21862.21(2)	0
P(20.5, f→f)	21861.49(2)	0
P(21.5, e→e)	21860.75(3)	1
P(22.5, f→f)	21859.98(2)	0
P(23.5, e→e)	21859.19(2)	-1
P(24.5, f→f)	21858.40(3)	0

167

P(25.5, e→e)	21857.61(5)	3
P(26.5, f→f)	21856.77(5)	1
R(1.5, e→e)	21873.05(3)	0
R(2.5, f→f)	21873.31(3)	-1
R(3.5, e→e)	21873.55(2)	-1
R(4.5, f→f)	21873.78(2)	0
R(5.5, e→e)	21873.98(2)	0
R(6.5, f→f)	21874.16(2)	0
R(7.5, e→e)	21874.32(2)	0
R(8.5, f→f)	21874.46(2)	0
R(9.5, e→e)	21874.59(2)	1
R(10.5, f→f)	21874.69(2)	0
R(11.5, e→e)	21874.78(3)	1
Q(2.5, f→e)	21872.24(3)	2
Q(3.5, e→f)	21872.16(2)	1
Q(4.5, f→e)	21872.06(2)	0
Q(5.5, e→f)	21871.97(3)	2
Q(6.5, f→e)	21871.81(2)	-1
F_2 manifold (Ω=1/2)		
	Observed	(Obs - Calc) $\times 10^2$
P(3.5, f→f)	21869.48(2)	-1
P(4.5, e→e)	21869.06(5)	-3
P(5.5, f→f)	21868.68(3)	2
P(6.5, e→e)	21868.22(2)	1

P(9.5, f→f)	21866.79(6)	4
P(10.5, e→e)	21866.22(2)	0
P(11.5, f→f)	21865.67(2)	0
P(12.5, e→e)	21865.10(2)	0
P(13.5, f→f)	21864.52(2)	1
P(14.5, e→e)	21863.91(2)	0
P(15.5, f→f)	21863.27(2)	-1
P(16.5, e→e)	21862.63(2)	0
P(17.5, f→f)	21861.96(2)	0
P(18.5, e→e)	21861.27(2)	0
P(19.5, f→f)	21860.56(2)	0
P(20.5, e→e)	21859.84(3)	1
P(21.5, f→f)	21859.07(2)	-1
R(5.5, f→f)	21872.43(2)	-1
R(6.5, e→e)	21872.63(3)	1
R(7.5, f→f)	21872.80(3)	2
R(8.5, e→e)	21872.90(3)	-2

Table III. Observed transitions of the 2_0^1 band of the C $^2\Pi_u \leftarrow$ X $^2\Pi_g$ transition of C_4^- from the 2-color multiphoton detachment spectrum (in cm^{-1}).

F_1 manifold (Ω=3/2)		
	Observed	(Obs - Calc) $\times 10^2$
P(2.5, f$\rightarrow$f)	22626.30(6)	-3
P(3.5, e$\rightarrow$e)	22625.94(4)	-1
P(4.5, f$\rightarrow$f)	22625.54(2)	0
P(5.5, e$\rightarrow$e)	22625.13(2)	1
P(6.5, f$\rightarrow$f)	22624.66(3)	-1
P(7.5, e$\rightarrow$e)	22624.19(4)	-2
P(8.5, f$\rightarrow$f)	22623.70(3)	-2
P(9.5, e$\rightarrow$e)	22623.19(3)	-2
P(10.5, f$\rightarrow$f)	22622.67(2)	-1
P(11.5, e$\rightarrow$e)	22622.14(2)	1
P(12.5, f$\rightarrow$f)	22621.59(5)	3
P(13.5, e$\rightarrow$e)	22620.98(4)	1
P(14.5, f$\rightarrow$f)	22620.35(3)	0
P(15.5, e$\rightarrow$e)	22619.72(2)	0
P(16.5, f$\rightarrow$f)	22619.07(2)	1
P(17.5, e$\rightarrow$e)	22618.38(2)	0
P(18.5, f$\rightarrow$f)	22617.68(2)	0
P(19.5, e$\rightarrow$e)	22616.97(2)	1
P(20.5, f$\rightarrow$f)	22616.22(3)	0
R(1.5, e$\rightarrow$e)	22627.97(5)	3
R(2.5, f$\rightarrow$f)	22628.23(5)	3
R(3.5, e$\rightarrow$e)	22628.46(4)	2

170

R(4.5, f→f)	22628.68(5)	2
R(5.5, e→e)	22628.88(5)	2
R(6.5, f→f)	22629.03(3)	-1
R(7.5, e→e)	22629.19(3)	0

Table IV. Best-fit parameters for C_4^-. All parameters are in cm^{-1}. Uncertainties in parentheses are 1σ.

	Parameters	Present Work	*Ab initio* Theory [a]
X $^2\Pi_g$ State:	B_0	0.16663(22)	0.16610(40)
	A_0	-39(9)	
C $^2\Pi_u$ State:	T_0	21871.525(7)	22599
	B_0	0.15651(25)	0.15520(40)
	A_0	-37(9)	
Between States:	$B_0(X) - B_0(C)$	0.01012(13)	0.01090(60)
	$A_0(X) - A_0(C)$	-1.536(7)	
	$D_0(X) - D_0(C)$	11(3) e-8	
	T_1	22623.96(11)	
2_0^1 C $^2\Pi_u$ State:	B_1	0.15634(26)	
	A_1	-33(9)	
	α_2	17(16) e-5	
	$A_0(X) - A_1(C)$	-6.45(10)	

[a] from Reference 10.

172

Figure Captions

Figure 1. One-color resonant 2-photon detachment spectrum of C_4^-.

Figure 2. High resolution two-color resonant multiphoton detachment spectrum of C_4^-.

Figure 3. Energy levels of the $X\,^2\Pi_g$ and $C\,^2\Pi_g$ states C_4^-. The six possible transitions originating from $J''=7/2$ are shown.

Figure 4. Simulated rotational spectrum of the origin band using fitted molecular constants.

Figure 5.1

174
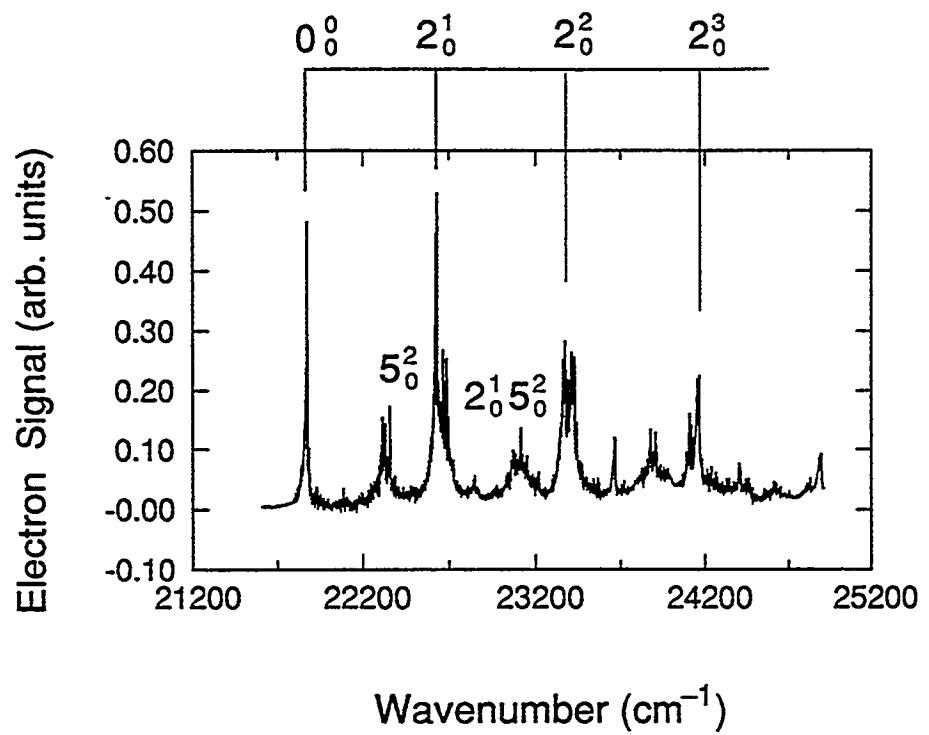
Origin Band:

2_0^1 Band:

Wavenumber (cm^{-1})

Figure 5.2

175

Figure 5.3

176
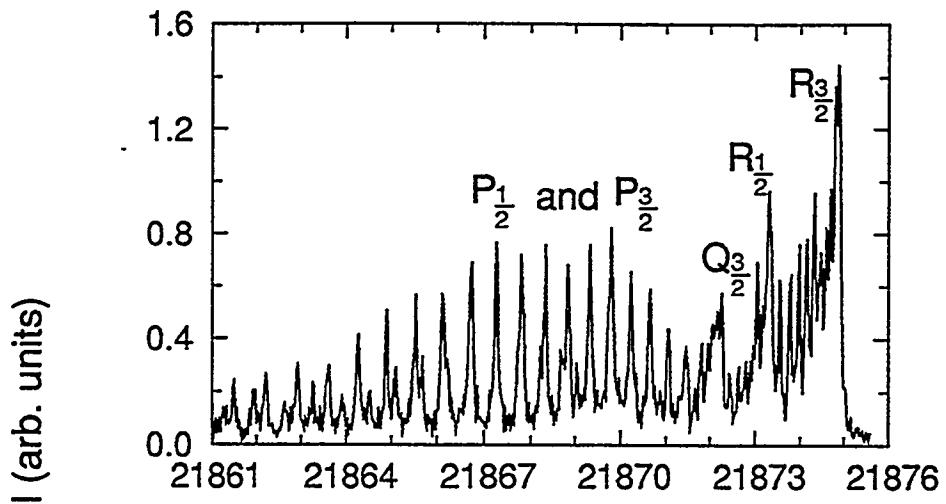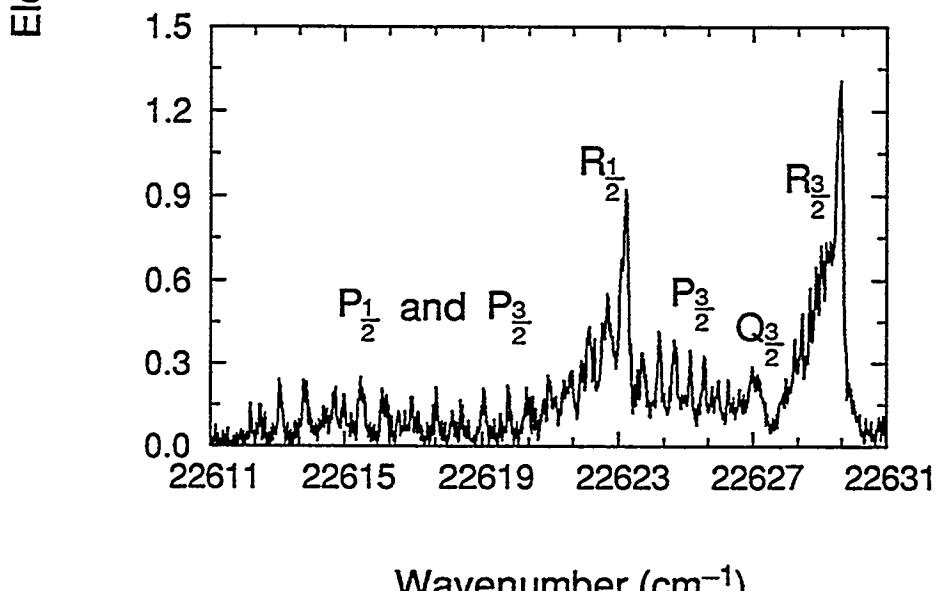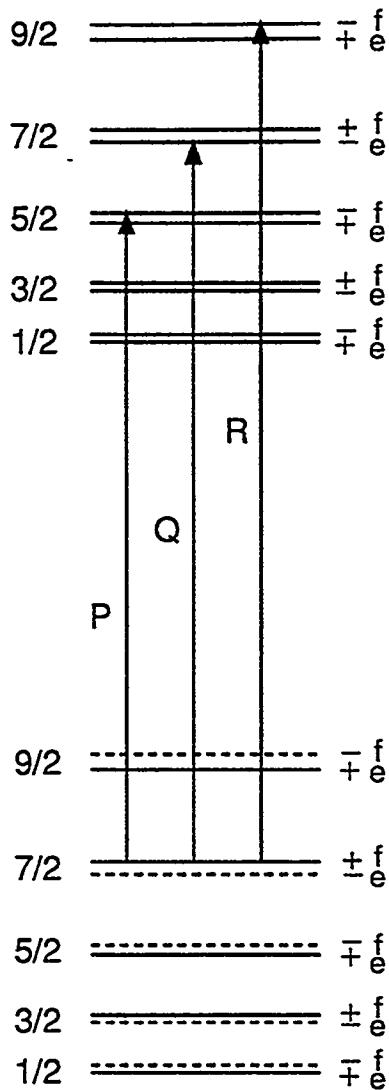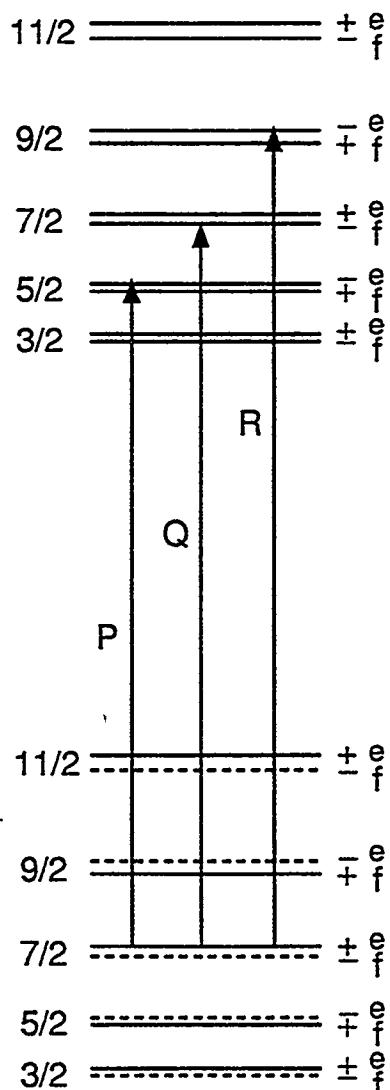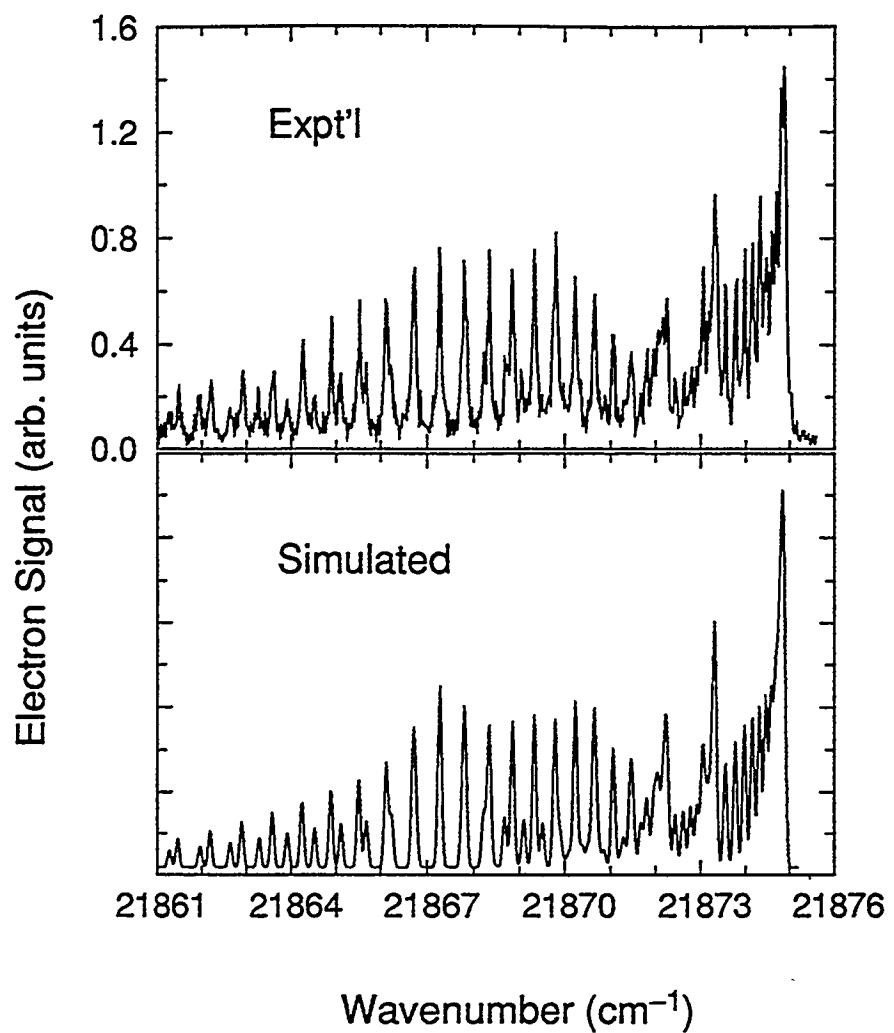
Figure 5.4

Chapter 6. Spectroscopy and electron detachment dynamics of small carbon cluster anions (C_4^-, C_6^-, C_8^-)

Abstract

Resonant multiphoton detachment spectroscopy has been employed to obtain vibrationally resolved spectra of the $^2\Pi \leftarrow X\ ^2\Pi$ electronic transitions of C_4^-, C_6^-, and C_8^-. Transitions due to vibrational excitations in the totally symmetric stretching modes as well as the bending modes are observed. The electron detachment dynamics in the multiphoton detachment processes of these species is studied by measuring the electron kinetic energy distributions and electron signal time profiles. The electron kinetic energy distributions of multiphoton detachment qualitatively differ from those of one-photon direct photodetachment, suggesting an indirect multiphoton detachment mechanism. Delayed electron emission is observed in multiphoton detachment of C_6^- and C_8^-. A two-color multiphoton detachment experiment allows the determination of the exact number of photons absorbed in the multiphoton detachment process. The electron emission rate constant is found to increase as the total photon energy absorbed by the anion increases. It is concluded that electron detachment occurs via thermionic emission following multiple

steps of photon absorption and rapid internal conversion and energy randomization. For C_6^- and C_8^-, the thermionic emission rate constants are determined as a function of total photon energy; and these rate constants are compared to the theoretical rate constants calculated using microcanonical rate theory.

I. Introduction

In this paper, we report the results of experimental studies of the spectroscopy and electron detachment dynamics of C_4^-, C_6^-, and C_8^-. The $C^2\Pi \leftarrow X^2\Pi$ electronic transition of each anion has been studied by resonant multiphoton detachment spectroscopy. In addition, the electron detachment dynamics of these negative ions is studied by measuring the electron kinetic energy distributions and the electron signal time profiles. Our experiments show that thermionic emission is the responsible mechanism for electron detachment following resonant multiphoton detachment.

Small carbon clusters have been a subject of intense experimental and theoretical research in recent years.[1] Much information has been obtained on the neutral carbon clusters through various spectroscopic studies and high level *ab initio* calculations.[2] For C_4, theory has predicted the existence of two different structures (the linear form and the rhombic form) as candidates for the ground state. For C_6 and C_8, the cyclic form is predicted to become increasingly more stable relative to the linear structure. Experimentally, only the linear structure has been definitely observed.

Much less is known about the negatively charged carbon clusters. Anion photoelectron spectroscopy[3,4,5,6,7] and ion chromatography studies[8] indicate that small carbon cluster anions, C_n^- (n<10) have linear structures. Photoelectron spectroscopy shows an even-odd alternation in the EA values of linear C_n (n<10) with the even-numbered clusters having significantly larger EA than the neighboring odd-numbered clusters.

Resonance enhanced multiphoton ionization spectroscopy, which has proved so valuable in studying the electronic transitions of neutral species, has not yet been widely applied to negative ions. Electronic transitions within negative ions are not commonly observed mainly because most known negative ions do not have bound electronic states. However, the large electron affinities of even-numbered small carbon clusters give rise to the possibilities of valence bound electronic states of the anions. In the case of C_2^-, accurate spectroscopic constants have been determined for the three lowest doublet states through high resolution spectroscopic work.[9,10,11,12,13] In our group, an excited state of C_6^- whose origin lies right below the linear C_6 ground state was studied by autodetachment spectroscopy.[7] Schmatz and Botschwina performed large-scale open-shell coupled cluster calculations on C_4^-,[14] C_6^-,[15] and C_8^-.[16] Spectroscopic constants of the four lowest doublet states were obtained for C_4^- and C_6^-. The two lowest $^2\Pi$ states of C_8^- were also studied. These states all lie below electron affinities of the linear neutral clusters. In two recent articles by Maier and coworkers,[17,18] one low-lying excited state of each even-numbered carbon cluster anion C_{2n}^- (n=2 - 10) was discovered. The absorption spectrum of the $^2\Pi \leftarrow X^2\Pi$ transition was studied as a function of cluster size in neon matrices.

In this work we have studied the $^2\Pi \leftarrow X^2\Pi$ electronic transitions of C_4^-, C_6^-, and C_8^- via resonant multiphoton detachment of the mass selected anions. In these experiments, the first photon excites the $^2\Pi \leftarrow X^2\Pi$ electronic transition, and subsequent photon absorption detaches the excited anion. The spectrum is obtained by measuring the electron signal as a function of the excitation laser wavelength. Our spectra are in

qualitative agreement with Maier's results[17,18] in neon matrix. However, our spectra show more detailed vibrational structure and additional features due to vibrational excitation in the bending modes. The spectroscopy of C_4^- has been reported in a separate paper,[19] in which a rotationally resolved resonant 2-color multiphoton detachment spectrum, as well as the vibrationally resolved one-color spectrum, were presented and analyzed. In this paper, we present the resonant multiphoton detachment spectra of C_6^- in the wavelength region of 420-660 nm and of C_8^- in the wavelength region of 420-780 nm.

Besides the spectroscopy of these negative ions, the electron detachment dynamics of the photoexcited anions are also studied. In the one-photon detachment process of small carbon cluster anions, when the photon energy is significantly larger than the electron affinity of the neutral species, direct detachment occurs, resulting in prompt electron signal and a discrete photoelectron spectrum.[5] In a resonant 2-photon detachment process in which the single-photon energy is smaller than electron affinity, the first photon excites an electronic transition; the second photon can either detach the excited anion via direct detachment; or excite the anion to an energy level that lies above the neutral plus an electron continuum. In the latter case, electron detachment then occurs via autodetachment, through a non-adiabatic coupling process between the anion and the continuum. For this process, if energy randomization among various electronic and vibrational degrees of freedom occurs on a time scale faster than electron detachment, the coupling between the anion and the continuum becomes a statistical process. The electron then detaches from the *hot* anion, and this process is appropriately referred to as *thermionic emission.*

182

Thermionic emission can be described as direct ejection of electrons as the result of heating the material, which raises the electron energy beyond the binding energy that holds the electron to the material. The temperature dependence of the electron emission rate from hot surfaces is well described by the Richardson-Dushman equation.[20] In the last few years, delayed electron ionization following multiphoton absorption, i.e., ionization taking place after the laser pulse has been turned off, has been observed for the atomic clusters of several refractory metals (tungsten, niobium, and tantalum) and it has been attributed to thermionic emission.[21,22,23] The small ratio of ionization potential to cohesive energy per atom for these refractory metals favors ionization over atomic evaporation after photon absorption. The time constants of delayed ionization have been measured at various photon energies. Recently, delayed electron emission has also been observed for the W_n^- anions as a result of photon absorption.[24] For these species, the electron kinetic energy distribution measured by Weidele et. al. showed the characteristics of thermionic emission. Delayed electron emission from C_6^- and several other C_n^- and Si_n^- clusters has been observed by Whetten et al. after surface collisions of these species at low impact energies.[25]

Smalley and coworkers discovered delayed electron emission from C_{60}^- after absorption of 353 nm photons.[26] Thermionic emission was thought to be partly responsible. At about the same time, Hertel and coworkers discovered delayed ionization from photoexcited C_{60} and C_{70}.[27] Since then, the exact mechanism of delayed ionization from fullerenes following multiphoton absorption has been debated.[28,29,30,31] Two models exist: stored electronic energy (long-lived triplet manifolds) as opposed to stored

vibrational energy in the thermionic emission description. Recent ionization experiments using cw laser supports the thermionic emission model.[32] Comparison to statistical modeling of the electron emission rate assuming a thermionic emission mechanism is hampered by the lack of knowledge about how many photons are absorbed.

In this paper, we report the observation of delayed electron emission from C_6^- and C_8^- following resonant multiphoton absorption. The electron emission rate constants are measured as a function of photon energy. The number of photons absorbed are exactly determined by a two-color measurement of the electron emission rate. The electron kinetic energy distributions of C_4^- and C_6^- multiphoton detachment show the characteristics of thermionic emission. The mechanism involved in the resonant multiphoton detachment of C_4^-, C_6^- and C_8^- will be discussed. The multiphoton detachment process is not direct, rather it occurs via thermionic emission following fast internal conversion and energy randomization. Calculated rate constants for thermionic emission using microcanonical rate theory are in reasonable agreement with the experimentally measured values.

The rest of paper is organized as follows. Section II describes the experimental details involved in the measurements; In Section III we present the experimental results; These results are analyzed and explained in Section IV; Section V is discussion; Section IV summarizes the findings from this work.

II. Experimental

For each negative ion, three types of measurements were performed: (1) wavelength scans, in which the resonant multiphoton detachment spectrum was obtained by scanning the laser wavelength; (2) at fixed wavelengths, the electron signal time profiles were recorded, resulting in the determination of electron emission rate at various photon energies (C_6^- and C_8^-). Two-color measurement of electron emission rate was also performed; (3) at fixed wavelengths, the electron kinetic energy distributions of C_4^- and C_6^- were measured using a time-of-flight electron energy analyzer.

In all three types of experiments, carbon cluster anions are generated in a pulsed discharge source which has been described previously.[33] Briefly, a gas mix of 3% acetylene, 1% CO_2 in Ne, typically at a backing pressure of 25 psi, is pulsed from a piezoelectric valve and enters the discharge region where the molecules are dissociated. The discharge electrodes and the insulating Teflon plates, each of them has a channel of 2.5 mm I.D. in the center, are held together and attached to the face plate of the piezoelectric valve. The last piece of the discharge assembly, a snout with a 5 mm long, 2.5 mm I.D. channel in the center, is at the float voltage of the source (-1000 V). This snout serves as a clustering channel for the mix of species resulted from discharge. To improve stability of the ion signal, a 1 keV electron beam intersects the expanding molecular beam. The free expansion length of the molecular beam, which is the distance between the discharge assembly and the skimmer, is found to strongly affect the temperature of the negative ions. The further this distance, the colder the ions become.

The apparatus used in the first two types of experiments has been described in detail elsewhere.[7,34] Briefly, negative ions that pass through the skimmer are collinearly

accelerated to 1 keV. Ions are separated according to their mass-to-charge ratios in a beam-modulated time-of-flight mass spectrometer.[35] The negative ions of interest interact with the laser beams in the detector region, approximately 20 cm before the ions reach the ion detector. All the electrons generated via photodetachment of the negative ions are extracted perpendicularly by a weak electric field and collected by a multichannel plate electron detector. The electron signal is normalized to the ion signal and laser power.

One-color resonant multiphoton detachment spectra, i.e., measurements of type (1), are obtained by measuring the electron signal intensity while scanning the laser wavelength of a dye laser pumped with a XeCl excimer laser. Electron signal intensity is measured by using a gated detection scheme; electron signal appearing inside of a 60-ns wide gate is integrated and converted into digital signal using a CAMAC analog-to-digital converter. Each spectrum is the result of signal averaging over 500 laser shots/point. The measured bandwidth of the laser beam is $ca.$ 0.3 cm^{-1}. The laser is calibrated by measuring the absorption spectra of an iodine cell or a Fe-Neon cathode lamp. The laser fluence used in this type of experiment is typically in the range of 30-60 mJ/cm^2. The time width of the laser pulse is approximately 30 ns FWHM. To obtain the wavelength scans reported here, the following laser dyes were used: Oxazine 750, Pyridine I, DCM, Rhodamine 640, Rhodamine 610, Rhodamine 590, Coumarin 540, Coumarin 503, Coumarin 480, Coumarin 460, Coumarin 440, Exalite 416, and DPS.

Electron signal time profiles, i.e., measurements of type (2), are recorded at various fixed photon energies. This is achieved by collecting all the electron signal using a 500 MHz digitizing oscilloscope, typically signal averaging over 10 k laser shots. The

electrons that detach after the ion package fly out of the electron detector region can not be collected; therefore, those electrons that detach more than *ca.* 700 ns after laser interaction can not be detected. In the two-color measurements of electron emission time profiles, the first laser pulse comes from the same excimer pumped dye laser. This laser beam is used to photoexcite C_n^- to an excited electronic state. The second laser beam, generated from a YAG pumped dye laser, is used to detach the photoexcited ions. We shall refer these two lasers as the excitation laser and the detachment laser, respectively. These two laser pulses can be separated temporally and spatially. Notice that both laser pulses should coincide with the same ion package, and the ions have 1 keV kinetic energy. If the two laser beams are temporally separated, they should also be separated spatially along the axis of ion beam. For example, in the case of C_6^-, a temporal separation of 200 ns corresponds to a spatial separation of 9 mm.

The electron kinetic energy distributions, i.e., experiments of type (3), are measured in an anion time-of-flight photoelectron spectrometer which has been described in detail elsewhere. [5, 36] Ions are produced in the same manner as we just described. Anions generated from the discharge source are injected with a pulsed electric field into a Wiley-McLaren-type time-of-flight mass spectrometer equipped with a linear reflectron. [37] The ion of interest is selectively detached by a properly timed pulse of light from the excimer-pumped dye laser or a YAG laser. After photodetachment, a dual microchannel plate detector at the end of a 1 m field-free flight tube detects a small fraction of the photoelectrons. Time-of-flight analysis yields electron kinetic energies (eKE); the instrumental resolution is 8 meV at 0.65 eV and degrades as $(eKE)^{3/2}$ at higher electron

187

kinetic energy. The time-of-flight analysis has a cut-off for electrons with less than 0.2 eV kinetic energy; in other words, the detection efficiency deteriorates for electrons with kinetic energy below 0.2 eV.

III. Results

A. Resonant multiphoton detachment spectra of C_4^-, C_6^- and C_8^-

The one-color resonant multiphoton detachment spectra of C_4^-, C_6^-, C_8^- are shown in Figure 1. From C_4^-, C_6^-, to C_8^-, the spectrum becomes more complex, and peak width also increases. The C_4^- spectrum has been discussed in detail elsewhere,[19] it is included here for comparison.

For C_6^-, the wavelength region between 430 nm and 665 nm was studied. The most intense peak at 607 nm (or 16476 cm^{-1}) appears to be the origin transition. Hot band transitions with significantly smaller intensities are observed to the red of the origin transition. To the blue of the origin transition, the most prominent feature is a progression with a spacing of *ca.* 600 cm^{-1}. Besides this progression, many other features are also observed. The origin peak actually consists of 3-4 partially resolved peaks which are separated from each other by *ca.* 25 cm^{-1}. The width of peaks in the spectrum (typically 10-15 cm^{-1} at FWHM) is significantly broader than the laser bandwidth. Peaks become

even broader at the blue end of the spectrum. Figure 2 shows in more detail the C_6^- spectrum along with vibrational assignments in the energy region of 16200-19200 cm^{-1}.

The C_6^- spectrum in the wavelength region of 589 nm - 584 nm (16978-17123 cm^{-1}) obtained through a two-color scan is shown in Figure 3. The set-up of two-color multiphoton detachment has been described in detail elsewhere.[19] The laser fluence of the excitation laser (589-584 nm) is reduced to *ca.* 2 mJ/cm^2, while the laser fluence of the detachment laser is *ca.* 40 mJ/cm^2. The detachment laser wavelength is fixed at 635.5 nm which is non-resonant with any transition. The peak intensity at 589.4 nm in the two-color scan (solid line) is much smaller than that in the one-color (high laser fluence) scan (shown in dashed line).

The C_8^- multiphoton detachment spectrum in the wavelength region of 420-780 nm is shown. This spectrum is complicated. First, peaks are broad, typically 15-20 cm^{-1} at FWHM. Second, the intensity distribution is not typical of a Franck-Condon progression in a single electronic band. Third, peak spacings are irregular, no progression of any particular spacing is observed. Last, the baseline of the spectrum is well above zero all the way across the photon energy region shown.

B. Electron kinetic energy distributions of C_4^- and C_6^-

Electron kinetic energy (eKE) distributions of C_4^- and C_6^- direct one-photon detachment are shown in the top half of Figure 4 and Figure 5, respectively. The photon energy was 4.66 eV (or 266 nm) for C_4^- detachment, and 5.82 eV (or 213 nm) for C_6^-

189

detachment, both of which are above the electron affinities (EA) of the corresponding neutrals. EA for C_4 and C_6 are 3.88 eV and 4.18 eV, respectively.[5] The C_4^- spectrum has been discussed in an earlier publication.[5] The C_6^- spectrum will be analyzed in a later publication.[38] The previously published photoelectron spectrum of C_6^- was taken with 4.66 eV photon energy.[5] The most intense peak at 0.78 eV in the C_4^- spectrum corresponds to the EA (3.88 eV) of C_4, and the most intense peak at 1.64 eV in the C_6^- spectrum corresponds to the EA (4.18 eV) of C_6. The peaks in these spectra correspond to vibrational and electronic excitations in the neutral species.

Electron kinetic energy (eKE) distributions from resonant multiphoton detachment of C_4^- and C_6^- are shown in the bottom half of Figure 4 and Figure 5, respectively. In both cases, the laser photon energy is resonant with its corresponding origin transition of the $^2\Pi \leftarrow X\ ^2\Pi$ electronic band. The eKE distribution of C_4^- at photon energy 2.71 eV (or 457.2 nm) is a continuous function with a maximum near 0.1 eV; it is roughly an exponential decay towards higher eKE. Compared to the C_4^- data, the eKE distribution of C_6^- at photon energy 2.04 eV (or 607 nm) is very similar except the electron signal decreases faster towards higher eKE. As we mentioned in the previous section, the transmission efficiency of the electron time-of-flight tube decreases for slower electrons with eKE below *ca.* 0.2 eV. The observed maximum might be due to this instrumental cut-off for slow electrons.

C. Electron emission time profiles

1. One-color measurements

Electron emission time profile of C_4^- multiphoton detachment at all scanned photon energies appears to be *prompt*, i.e., the time profile of the electron signal is identical to the laser pulse time profile, which is *ca.* 30 ns wide.

Delayed electron emission, electron signal appearing well after the laser pulse, is observed in certain photon energy regions in the C_6^- and C_8^- multiphoton detachment process. The electron signal time profiles of C_6^- measured at various photon energies are shown in Figure 6. At 565.6 nm, and all the longer wavelengths, the electron signal is prompt. When the photon energy is increased, delayed electron emission starts to appear. For example, at 501.4 nm, both delayed electrons and prompt electrons are seen. At 483.2 nm, delayed electron emission becomes faster, i.e., the signal decreases faster towards longer time. The delayed electron signal time profile is an exponential decay. Eventually, at 446.2 nm, delayed electron emission becomes so fast that it appears to be prompt; the prompt component and the delayed component converge to the same time scale — within the time width of the laser pulse.

Rate constants can be obtained by fitting the exponential decay with a first-order rate constant. The sudden decrease of the delayed electron signal beyond 550 ns, particularly at 501.4 nm, is due to anions flying out of the electron detector region. The electron emission rate constants and the corresponding laser wavelengths are shown in Table III.

For C_6^-, the rate of delayed electron emission appears to monotonically increase with increasing photon energy. However, the situation with C_8^- multiphoton detachment is more complicated. Figure 7 shows some typical electron signal time profiles of C_8^- at

various laser wavelengths. At 773 nm, delayed electron signal is observed; then at 738 nm, the delayed electron emission rate is almost as fast as prompt electrons; However, slow electron emission rate reappears at 630 nm, which gradually becomes faster when the photon energy is further increased. The electron emission rates and the corresponding laser wavelengths are shown in Table IV.

To further characterize delayed electron emission, two additional experiments were performed: (1) laser power dependence studies of delayed electron emission and prompt electron emission; (2) two-color measurement of rate constant for delayed electron emission.

Figure 8 shows the laser power dependence of the delayed electron signal and the prompt electron signal in C_6^- multiphoton detachment. At 498.2 nm, as shown in the top half of Figure 8, the delayed electron signal is approximately linearly proportional to laser power, while the prompt electron signal has almost a quadratic laser power dependence. In the bottom half of Figure 8, the time profile at 483.2 nm is measured at three different laser powers. The relative intensity of the delayed electron signal versus prompt electron signal increases when laser power decreases, which also suggests that the prompt electron signal has a steeper laser power dependence than the delayed electron signal.

2. Two-color measurements

In the top half of Figure 9, the solid trace is the electron signal time profile of a two-color experiment. The two-laser beams are separated temporally by *ca.* 200 ns and spatially by *ca.* 9 mm. The two peaks correspond to the timing of the two laser pulses. The photon energies are: $E(\lambda_1) = 2.12$ eV (at 585.6 nm); $E(\lambda_2) = 2.83$ eV (at 437.2 nm);

192

The first peak is the electron signal due to multiphoton detachment by the first laser pulse (λ_1) alone. The dashed trace shows the electron signal when the first laser pulse is blocked, i.e., the signal due to multiphoton detachment by the second laser pulse (λ_2) alone. In the bottom half of Figure 9, the two-color electron signal time profile (solid trace) is compared to the one-color electron signal time profile at 501.0 nm (λ_3), where $E(\lambda_3) = 2.47$ eV. Note that:

$$2E(\lambda_3) = E(\lambda_1) + E(\lambda_2) \tag{1}$$

These two traces show the same delayed electron emission rate. The significance of this observation will be discussed in the next section.

IV. Analysis

A. Assignment of resonant multiphoton detachment spectra of C_6^- and C_8^-

1. C_6^- spectrum

The energy of the origin transition is 2.07 eV in the C_6^- spectrum. Schmatz and Botschwina[15] calculated the term energy of the C $^2\Pi_u$ electronic state of C_6^- to be 2.12 eV. Based on this comparison, we assign the features in our spectrum to the C $^2\Pi_u \leftarrow$ X $^2\Pi_g$ electronic transition of C_6^-. This assignment is consistent with Maier's assignment for the C_6^- absorption spectrum in a neon matrix.[17] Again, based on the same *ab initio* calculation, in which the vibrational frequency of the ν_3 mode of the C $^2\Pi_u$ state was found

193

to be 599 cm^{-1}, the progression of *ca.* 600 cm^{-1} is assigned to excitation in the v_3 mode of the C $^2\Pi_u$ state. This progression is also observed in the matrix absorption spectrum.[17]

To the blue of the origin transition, the spectrum appears congested. However, most features in the wavelength region between 607 nm - 530 nm (16475 - 18868 cm^{-1}) can be assigned to transitions from the $v=0$ state of the X $^2\Pi_g$ electronic state to vibrationally excited states of the C $^2\Pi_u$ state. Unlike Maier's matrix results, additional features assigned to double-quanta excitations in the low-frequency bending modes are also observed in our spectrum. Excitation in the other two totally symmetric modes are also observed, giving vibrational frequencies in reasonable agreement with theoretical predictions.[15] However, we are uncertain about the assignment of the peak at 18243 cm^{-1} to v_2 excitation in the C state. In Schmatz and Botschwina's calculation [15], only the vibrational frequencies of the totally symmetric stretching modes were calculated. The remaining features in 16475 - 18868 cm^{-1} region can be assigned to combination bands of different vibrational modes.

In addition, hot band transitions observed in our spectrum give vibrational frequencies of the X $^2\Pi_g$ electronic state. The partially resolved peaks around the origin transition may be assigned to sequence band transitions in the low-frequency bending modes, such as 9_1^1, 8_1^1, or 9_2^2 transitions. The observed peak width (10-15 cm^{-1} FWHM) is due to lifetime broadening in the upper state and unresolved rotational and vibrational structure. The rotational constant of C_6^- is *ca.* 0.047 cm^{-1}, the laser resolution (*ca.* 0.3 cm^{-1}) is much too low to resolve the rotational structure.

Peak positions, relative energies, assignments and vibrational frequencies of the C_6^- spectra are shown in Table I.

Compared to Maier's matrix results,[17] the most significant discrepancies are the features due to transitions in double-quanta bending excitations. Our explanation of this discrepancy is related to the fact that different light sources are employed in these two experiments. In Maier's experiment, a xenon or arc lamp was used as the light source. In our experiment, in order to achieve sufficient detachment, the laser fluence used in the one-color experiments is so high that it saturates the first excitation process, i.e., the $C\,^2\Pi_u$ $\leftarrow X\,^2\Pi_g$ electronic transition, which is a strongly allowed optical transition. However, in order to achieve sufficient detachment, this power saturation is necessary in one-color experiments. Under these conditions, transitions that would otherwise be weak could show up with significant intensities. In other words, the intensity ratio of a weak transition to a strong transition is increased due to laser fluence saturation. The stronger transitions, such as the excitations in the ν_3 mode, are more saturated than the weaker transitions, such as the excitations in the bending modes. In the two-color experiment, the excitation laser fluence can be greatly reduced, therefore according to the above argument, the intensity ratio should resemble Maier's results more closely. Figure 3 shows the decrease in the bending mode intensity (7_0^2 transition) relative to the stretching excitation (3_0^1 transition) when the excitation laser fluence is reduced from 30 mJ/cm^2 to 2 mJ/cm^2.

2. C_8^- spectrum

The multiphoton detachment spectrum of C_8^- resembles the matrix absorption spectrum[18] only at the red end of the spectrum. Many more features are observed in our

spectrum at photon energies higher than 16300 cm^{-1}. Without help from high level *ab initio* calculations on C_8^-, the vibrational assignment for the matrix absorption spectrum was somewhat speculative. Recently, a paper by Schmatz and Botschwina appeared which reported high level *ab initio* calculations on the two lowest $^2\Pi$ states of C_8^-.[16] The equilibrium excitation energy of the C $^2\Pi_u$ state of C_8^- is calculated to be 13634 cm^{-1}. The harmonic wavenumbers of the four symmetric stretching vibrations for C_8^- C $^2\Pi_u$ state are calculated to be 2178, 1903, 1218, and 471 cm^{-1}. Based on the calculated vibrational frequencies and Franck-Condon factors for the C $^2\Pi_u \leftarrow$ X $^2\Pi_g$ transition, the peaks at 12963, 13416 cm^{-1}, 13920 cm^{-1}, and 15050 cm^{-1} are assigned to origin, 4_0^1, 4_0^2, and 1_0^1 transitions, respectively.

The peak at 16305 cm^{-1} probably marks the onset of another excited electronic state of C_8^-. However, other factors may contribute to the complexity of this spectrum. For example, the intensity of electron signal in the resonant multiphoton detachment spectrum not only depends upon the first photon absorption step, but also each of the subsequent photon absorption steps.

Peak positions, relative energies, assignments and vibrational frequencies of the C_8^- spectrum are shown in Table II.

B. Resonant multiphoton detachment mechanism of C_4^- and C_6^-

As shown in Figure 4 and Figure 5, the time-of-flight photoelectron spectrum of the one-photon direct detachment and that of the resonant multiphoton detachment are

strikingly different, which suggests a fundamental difference between the two photodetachment mechanisms. The eKE distribution for resonant multiphoton detachment is characteristic of a thermionic emission mechanism.[24] Similar eKE distribution profiles have been observed for thermionic emission of photoexcited W_n^- clusters.[24]

First we consider the resonant multiphoton detachment mechanism of C_4^-. After absorbing the first photon at 457.2 nm, the anion is in the ground vibrational state of the C $^2\Pi_u$ state. Energetically, the second photon should be able to directly detach it. The total energy of two photons is 5.42 eV, or 1.54 eV above EA of linear C_4. However, this can not be the mechanism responsible for our observation. First, the transition from the C $^2\Pi_u$ state of C_4^- (molecular orbital configuration $...1\pi_u^3 1\pi_g^4$) to the linear ground state(X $^3\Sigma_g^-$, $...1\pi_u^4 1\pi_g^2$) of neutral C_4 plus an electron is not one-electron allowed. The first excited state of linear C_4 which can be accessed from C $^2\Pi_u$ state of C_4^- via one-electron transition is the $^3\Pi_u$ state $(..5\sigma_g^1 1\pi_u^3 1\pi_g^4)$. According to Adamowicz's calculation,[39] this state lies *ca.* 1.8 eV above the ground state; it may not be energetically accessible via 2-photon detachment. Moreover, if multiphoton detachment occurred via such a direct mechanism, one would expect to observe discrete peaks in the eKE distribution, similar to the one-photon direct detachment spectrum shown in the top half of Figure 4.

Based on this analysis, we propose an indirect mechanism, shown in Figure 10, for the resonant 2-photon detachment of C_4^-. This mechanism includes the following sequence of events which lead to detachment of the negative ion: (1) absorption of the 1st photon, (2) internal conversion back to the ground electronic state, (3) absorption of the 2nd photon, (4) internal conversion back to the ground electronic state and energy

randomization, (5) thermionic emission. In this mechanism, each photon absorption is a C $^2\Pi_u \leftarrow$ X $^2\Pi_g$ electronic transition. Thermionic emission occurs from the highly vibrationally excited states of the C_4^- X $^2\Pi_g$ state following fast internal conversion. The transition from the X $^2\Pi_g$ state of C_4^- (...$1\pi_u^4 1\pi_g^3$) to X $^3\Sigma_g^-$ state (...$1\pi_u^4 1\pi_g^2$) of C_4 plus an electron is one-electron allowed.

Since the laser pulse width is 30 ns, the first internal conversion step should take place within 30 ns for the second photon to be absorbed. The thermionic emission rate of C_4^- is not known for the photon energy region studied. However, its lifetime must be shorter than 30 ns, since no delayed electron emission is observed.

Second, we consider the resonant multiphoton detachment mechanism of C_6^-. Having understood the C_4^- mechanism, one would expect a similar mechanism to be proposed for C_6^-. However, we realize that the total energy of 2-photon absorption at 607 nm is 4.08 eV, about 0.1 eV less than the EA of linear C_6. Without further investigation, two possible explanations exist: (1) electrons are generated via 3-photon detachment, or (2) 2-photon detachment that results in cyclic C_6 neutral. Theory has predicted that the cyclic form of neutral C_6 lies below the linear C_6.[1, 40] Experimentally, only the linear form has been observed. Laser power dependence studies at several photon energies show that the delayed electron signal approximately has a linear laser power dependence and prompt electron signal approximately has a square laser power dependence. Therefore, laser power dependence study alone suggests the existence of the lower-lying neutral cyclic state. Assuming the prompt electron signal is due to a 2-photon process, one would then attribute the delayed electron signal to a one-photon process.

198

Because delayed electron signal is observed at photon energy as low as *ca.* 2.4 eV, the energetic of the cyclic C_6 has to be at least about 1.8 eV below that of the linear C_6. This cyclic-linear energy separation is much larger than what *ab initio* calculations predicted. For example, Raghavachari *et al.* calculated that the linear $^3\Sigma_g^-$ structure to lie about 0.4 eV higher in energy.[40]

C. Determination of the number of photons absorbed

To determine whether the cyclic neutral C_6 state needs to be invoked to explain multiphoton detachment at 607 nm, it is important to determine exactly how many photons are involved in the multiphoton detachment process. In addition, in order to study the dependence of the delayed electron emission rate on the total internal energy of the anion cluster, one needs to know the total photon energy absorbed at a given laser wavelength, i.e., the number of photons times the photon energy.

Laser power dependence gives useful information regarding the number of photons absorbed. Figure 8 shows that the delayed electron signal and the prompt electron signal have different laser power dependencies and the prompt electrons are due to a higher order photon absorption process than the delayed electrons. However, one can hardly determine the number of photons conclusively from laser power dependence alone due to the differing extent of power saturation at each photon absorption step.

We determine the number of photons absorbed for the delayed electron emission using a two-color measurement of the electron emission rate for C_6^-. The idea is as

199

follows: thermionic emission is an activated statistical process whose rate is determined by the full internal energy of the cluster. In other words, the thermionic emission rate is a monotonic function of total internal energy. If there are two different means of achieving same total internal energy, the same electron emission rate should be observed.

The solid trace, particularly the tail at longer time, in Figure 9 (top) is clearly a result of two-color $(\lambda_1 + \lambda_2)$ multiphoton detachment. The tail disappears when the first laser pulse (λ_1) is blocked. Based on the results shown in Figure 9 (bottom), the same delayed electron emission rate has been observed for the one-color and two-color detachment. Ignoring the contribution of thermal energy, which should be small compared to photon energy, one has:

$$n_1 \times E(\lambda_1) + n_2 \times E(\lambda_2) = n_3 \times E(\lambda_3) \tag{2}$$

n is the number of photon(s) absorbed for each laser pulse, E is the corresponding photon energy. Compared to Eq. (1), one obtains:

$$n_1 = 1$$
$$n_2 = 1$$
$$n_3 = 2$$

This means that the delayed electron emission at $\lambda_3(501 \text{ nm})$ is due to a two-photon process.

Since the prompt electron signal has a higher order of laser power dependence, we conclude the prompt electrons are due to three-photon or even higher-order process. Four-photon process should be much weaker than three-photon process unless very high photon fluence is applied. At 607 nm, since electron signal is prompt, it must be due to a

three-photon absorption process. The total photon energy absorbed is three times of the photon energy (2.04 eV), i.e., 6.12 eV, which is 1.94 eV above EA of linear C_6.

Having determined the number of photons involved, we propose a mechanism, similar to that for C_4^- resonant multiphoton detachment, for the multiphoton detachment process of C_6^-. For detachment at 607 nm, this is schematically shown in Figure 11. The basic ideas behind this mechanism are the same as those proposed for the C_4^- mechanism.

Thermionic emission is thought to be an activated statistical process, and our experiment provides direct confirmation of this. The two-color experiment shows that it does not matter how the energy is pumped into the ions, as long as the total internal energy is a constant, the same rate constant is observed.

We now consider the number of photons involved in C_8^- multiphoton detachment. The electron affinity of linear C_8 is 4.38 eV; at 773 nm (photon energy 1.60 eV), it takes at least three photons to see electron signal if linear neutral C_8 is produced. As shown in Figure 7 or Table IV, the electron emission rate constant is almost the same for 773 nm (λ_1) and 578.5 nm (λ_2). In analogy to the analysis of C_6, the total photon energies at these two wavelengths should be the same, i.e.,

$$n_1 \times E(\lambda_1) = n_2 \times E(\lambda_2) \tag{3}$$

where $E(\lambda_1)$=1.60 eV, and $E(\lambda_2)$=2.14 eV, the only reasonable solution to this equation is

$$n_1 = 4$$
$$n_2 = 3$$

201

Knowing the number of photons absorbed for the delayed electrons, those for the prompt electrons can be deduced accordingly. For example, the prompt component at 629.5 nm is due to absorption of at least four photons.

Figure 12 shows the rate constant as a function of total photon energy for C_6^- and C_8^-. The total photon energies corresponding to the measured rate constants are also shown in Table III and Table IV.

D. Analysis using microcanonical rate theory

Thermionic emission rate constants for C_6^- and C_8^- have been measured at various photon energies. At each photon energy, the number of photons absorbed has been exactly determined. The available information presents a good opportunity for the statistical modeling of this process. Rate constants can be calculated as a function of molecular constants and total photon energy and the results of statistical calculations can then be compared to the experimentally determined values. In this section, we try to analyze quantitatively, using microcanonical rate theory, the thermionic emission rate constant and electron kinetic energy distribution as a function of quantities such as total internal energy, vibrational frequencies and other molecular constants.

Klots has derived an expression for the rate constants of thermionic emission from isolated aggregates of matter based on a modified hard-sphere model.[41] Briefly, he started from the standard quasiequilibrium rate constant for particle emission expression:

$$k(E) = \sum_f (\sigma / \pi \lambda^2)_f / h\rho(E), \qquad (4)$$

where E is the total internal energy of the negative ion after photon absorption, $\rho(E)$ is the density-of-states of the hot anion, σ is the cross-section for the reverse of the emission, and λ is the de Broglie wavelength associated with the pair of separating fragments. For electron emission, Klots concluded that the following expression can be evaluated to obtain the total number of product states:

$$W(E, E_0) \equiv \sum_f (\sigma / \pi \lambda^2)_f$$

$$W(E, E_0) = \int_0^{E-E_0} \rho_v(x)dx \left\{ 1 + 2\left[2\mu b^2(E - E_0 - x)/\hbar^2\right]^{1/2} + \left[2\mu b^2(E - E_0 - x)/\hbar^2\right] \right\}, \qquad (5)$$

where μ is the reduced mass, essentially equal to the mass of electron; E_0 is the energy threshold for electron ejection, i.e., the electron affinity; b is classical hard-sphere collision radius. ρ_v is the density of vibrational states of the neutral species. In Klots' treatment, the rotational degrees of freedom have been included in deriving Eq. (5). In addition, in order to make the calculation of $W(E, E_0)$ complete, a spin-degeneracy factor for the outgoing electron and an electronic degeneracy factor for anion and neutral have to be included.

Klots also suggested an expression for the unnormalized distribution of kinetic energies, ε, of the emitted electrons:

$$p(\varepsilon) = \rho_v(E - E_0 - \varepsilon)(L_{max} + 1)^2 \qquad (6)$$

where,

$$L_{max} + 1 = (\lambda + b) / \lambda,$$

For s-wave emission, L_{max} is equal to 0. The s-wave emission model has frequently been considered in the context of autodetachment by negative ions.[42] In the case when the slow electrons are dominant, λ becomes much larger than b; therefore, the s-wave emission model is particularly appropriate. As shown in Figure 4 and Figure 5, slow electrons are indeed dominant in resonant multiphoton detachment of these carbon cluster anions.

We have used the above expressions to calculate the thermionic emission rate constants from multiphoton excited C_6^- and C_8^- and the electron kinetic energy distributions from C_4^- and C_6^- thermionic emission.

An essential part in carrying out these calculations is the calculation of the density of vibrational levels. First, the vibrational frequencies of the neutral and anion ground state are obtained through *ab initio* calculations using GAUSSIAN 92 at the UHF/6-31G* level. For the neutral species, our calculated frequencies are identical to those reported by Martin *et al.*[43] at the same level of calculation. For C_8^-, one of the bending frequencies (the ν_{13} mode) came out negative; this is discarded. Instead, the frequency of the same mode of neutral C_8 is substituted. One of the π_g bending frequencies (the ν_{10} mode) of C_8 is calculated to be imaginary at UHF/6-31G* level— this frequency is discarded; and the frequency of the same mode obtained in an *Ad hoc* MNDO calculation is used.[43] Second, these frequencies, except the *Ad hoc* MNDO frequency, are scaled by 90%, a commonly accepted scaling factor for this level of *ab initio* calculation. The vibrational frequencies after scaling are shown in Table V. Third, instead of direct counting, the Whitten-Rabinovith approximation[44] is used to calculate the vibrational density of states. Each

stretching mode is considered as a one-dimensional harmonic oscillator, and each doubly degenerate bending mode is treated as two one-dimensional harmonic oscillators with the same frequency.

Electron affinity values are known from previous work; The value of b, the classical hard-sphere collision radius is taken to be one half of the total carbon chain length; The spin multiplicity is equal to 2, the neutral electronic multiplicity (of the $^3\Sigma_g^-$ state) is 3, and the anion electronic multiplicity (of the $^2\Pi$ state) is 4. If nuclear spin statistics is taken into account, both the number of neutral states and the density of anion states should be divided by a factor of 2; therefore, the rate, which is given by Eq. (4), unchanged.

When comparing the calculated rate constant to the experimental value, one should be aware of the possible effect of thermal energy in the cluster anion prior to photon excitation. Since the rate constant is a strongly increasing function of the total internal energy, which is the sum of total photon energy and initial thermal energy, thermal energy may affect the rate constant significantly, especially at low total photon energy. As a rough estimate, we calculate the thermal energy using the following simple formula:

$$E_{thermal} = (3N - 5)k_B T_{vib} \qquad (7)$$

The vibrational temperature of the negative ions in our source, T_{vib}, as estimated from the observed hot band transition intensities in the C_6^- multiphoton detachment spectrum (see Figure 1), is somewhere between 100-150 K. Adding the $E_{thermal}$ to the total internal energy approximately doubles the calculated rate constant in the photon energy region of interest if one assumes T_{vib} equals to 100 K.

The rate constant values for the photon energy region for which thermionic emission rate constants were experimentally measured are calculated using the parameters described above, including thermal energy at 100 K. Figure 13 shows the result of calculation vs. the experimental results in a *log(k) - photon energy* plot. In the case of C_6^-, two calculations are shown, the dotted line and the solid line. The experimental result is shown as solid circles connected by a dashed line. The dotted line is the result of a calculation using the parameters described above; when compared to the experiment, it is roughly one order of magnitude too high. The solid line, which is a much improved fit compared to the experiment, is the result of a calculation using scaled bending frequencies. The lowest vibrational frequency (ν_9) of C_6^-, initially at 119 cm^{-1}, is scaled down to 37 cm^{-1}, at which point the calculated rate constant at photon energy 41390 cm^{-1} (483.2 nm) matches the experimentally measured value. We then calculate the rate constants at other photon energies using this modified vibrational frequency while leaving the rest of parameters unchanged. The result is the solid line in the top half of 13. The purpose here is not to correct the possible error in this particular vibrational frequency, rather, we use this frequency to collect most of the errors involved in all parameters. In fact, the modified ν_9 frequency, 37 cm^{-1}, is too low to be realistic. Among the parameters used in the calculation, the rate constant is most sensitive to the vibrational frequencies of the lowest-frequency modes. In the case of C_8^-, the calculation (solid line) is in agreement with the experiment (solid circles connected by a dashed line) within a factor of two;

The electron kinetic energy (eKE) distributions for C_4^- at 457.2 nm and C_6^- at 607 nm are calculated using Equation (6) assuming the s-wave emission model. The results of

the calculation (dashed lines) are shown in Figure 14 along with the experimental results (solid curves). Apparently the calculated eKE distribution does not match the experimental results, especially at low eKE. Experimentally, electrons tend to be ejected with smaller eKE than what Equation (6) predicts. One possible explanation is that the density of neutral vibrational levels at higher energy, i.e., smaller eKE, is underestimated. Anharmonicity and coupling within each bending mode increases the density of states at higher internal energy. These effects are not taken into account in the calculation.

In brief, the calculated thermionic emission rate constants based on the statistical models are in agreement with the experimental values within one order of magnitude; and the calculated eKE distributions are also in qualitative agreement with the experimental observations.

V. Discussion

A. Microcanonical rate constant calculation

One of the principal assumptions in treating a rate process using statistical mechanics methods is the ergodicity hypothesis: the internal energy in the reactant is randomized rapidly compared to the time scale of electron detachment. For thermionic emission, this means that vibronic coupling and the coupling between the various vibrational degrees of freedom are sufficiently strong for excitation energy to be randomized amongst the active degrees of freedom on the time scale of reaction. These

active degrees of freedom include all the vibrational modes as well as the electronic degree of freedom.

As shown in the last section, the result of a thermionic emission rate constant calculation using microcanonical rate theory is in agreement with the experiment within one order of magnitude. The ability to reproduce the experimental rate constants over a wide range of photon energy with reasonable values of parameters justify the current treatment of thermionic emission as an activated statistical process and the overall validity of this approach to quantitatively calculate the thermionic emission rate constant. In the case of the C_8^- calculation, quantitative agreement with the experiment is achieved with *ab initio* vibrational frequencies; while for C_6^-, *ab initio* frequencies have to be substantially adjusted to achieve agreement with the experiment. However, in general, vibrational frequencies of the bending modes are less likely to be calculated with high accuracy for larger molecules than for smaller molecules. In a calculation involving many parameters, one should realize that a good fit between experiment and calculation can hardly be taken to imply the goodness of individual parameters.

In both C_6^- and C_8^-, the calculation using *ab initio* frequencies overestimates the rate constant at a given photon energy. Among all the factors which may contribute to the error of calculated rate constants, the following two factors, if taken into account, may have significant effects on the calculated rate constants. First, vibrational anharmonicity and coupling within each bending mode increases the density of states at higher internal energy. Since the total internal energy above the ground state is much higher in the photoexcited anion than in the neutral, the anion density of states would be increased

208

much more than the neutral. According to Eq. (4), taking this effect into account would lower the calculated rate constants and may improve the agreement between the calculated and experimental rate constants. Second, in our treatment, we assume that the energy is fully equipartitioned between the electronic and nuclear degrees of freedom. However, as Schalg and Levine have argued,[45] this may not be a realistic assumption for large molecules. They suggested that the electronic energy is not fully thermalized; it is damped and coupled to what is effectively a heat bath, but it is not equilibrated with it. Assuming energy randomization is incomplete in the photoexcited carbon cluster anions, the calculated rate constants should be higher, resulting in even larger discrepancy between the calculated and experimental values. It appears that our results support the notion that, at least for these small carbon cluster anions, energy randomization between the electronic and nuclear degrees of freedom is rather complete. The rate constant of this energy dissipation process is a function of cluster size and also of the energy. The rovibrational density of states of the photoexcited anion is so high that even weak coupling between electronic and nuclear degrees of freedom suffices to damp the motion of electron.

With this theoretical approach, we can now explain why delayed electron emission is not observed for C_4^- in the photon energy region studied in this work. In the photon energy region studied, it takes at least two photons to photodetach C_4^-. However, even for the lowest photon energy at origin transition (457.2 nm), the thermionic emission rate constant with the energy of two photons is calculated to be faster than 1×10^8 per second, or 10 ns lifetime. The total photon energy at which the thermionic emission lifetime is on

the observable time scale (*ca.* 50 ns - 1 µs) is expected to be around (33300 ± 1500) cm^{-1}, or 0.25 eV above electron affinity.

The amount of energy above the electron affinity required to give rise to thermionic emission rate observable in the experiment (faster than *ca.* 5×10^5 per second) is called the kinetic shift. The kinetic shift for C_4^- is calculated to be around 0.25 eV, for C_6^- and C_8^- it is experimentally determined to be around 0.50 eV and 1.4 eV, respectively. This is in agreement with the notion that kinetic shift increases with the size of molecule.

B. Photodissociation versus electron emission

For most of the neutral metal clusters studied by others,[21,22,23] the dissociation channels after multiphoton absorption may compete with thermionic emission as an alternative decaying channel of the hot clusters. In the negative ion carbon clusters, this is hardly the case mainly due to the fact that the threshold for electron ejection, i.e., the electron affinity, is significantly smaller than the bond dissociation energy of linear carbon clusters. For example, the binding energy of C_6^- relative to the lowest energy channel C_3 + C_3^- is around 5.5 eV based on *ab initio* calculation.[46]

The small ratio of electron detachment threshold to the atomic binding energy makes carbon cluster anions good candidates as thermionic emitters. Thermionic emission should also be observed from the larger clusters as long as there is an intermediate state that can be reached via an allowed electronic transition. Even-numbered carbon clusters have low-lying excited electronic states, thermionic emission after multiphoton absorption

should be a common phenomenon. However, for larger molecules, in order to overcome the increasingly larger kinetic shift, the number of photons absorbed should be increased. This means a more powerful laser may be required. As we have shown in the 2-color experiment, after absorbing the first photon, the anion can absorb the second photon 200 nanoseconds later without losing the excitation energy from the first photon. Thermionic emission intensity strongly depends upon the laser fluence (mJ/cm^2), rather than upon the laser flux density ($mJ/sec \, cm^2$). Therefore, more than one laser beams can be lined up along the axis of the ion beam to excite the same ions and facilitate the resonant multiphoton absorption process.

C. Thermionic emission versus autodetachment

Both autodetachment and thermionic emission involve the coupling between the anion states lying above electron detachment threshold and the neutral plus electron continuum. The same coupling mechanisms that lead to autodetachment, such as vibronic coupling, are also responsible for thermionic emission. However, these two processes differ in the following way. If electron detachment occurs via coupling between a discrete anion state and one or more discrete neutral states plus an electron , such as in the case of C_2^-,[11] the process is autodetachment, and the rate constant can be calculated using Fermi's golden rule; On the other hand, if energy in the excited anion state is first randomized among many vibrational and electronic degrees of freedom, electron detachment occurs via coupling between a dense set of anion levels and many neutral states plus an electron;

this process becomes statistical, and the concept of thermionic emission is invoked. For a statistical process, the rate content can hardly be evaluated using Fermi's golden rule. Instead, it can be calculated using microcanonical rate theory.

Once the energy in the excited anion becomes randomized, a thermally *hot* anion is created, and electrons can *boil off* with small kinetic energy, this process is equivalent to thermionic emission from hot metal surfaces. For small clusters, energy has to be added through processes such as photon absorption. However, when the cluster size increases, the number of vibrational degrees of freedom increases, pure thermal energy may play a larger role in contributing to the total content of internal energy.

In reference 7, we reported the discovery of an excited anion electronic state whose origin lies only 46 cm^{-1} below the linear C_6 neutral ground state. Laser power dependence study shows that electron detachment at photon energies below the electron detachment threshold, e.g., at 297 nm, occurs via a 2-photon process; and that above the threshold, e.g., at 296 nm, it occurs via a one-photon process. Electron signal is prompt at photon energies both below and above the threshold.

The present work provides some insight regarding the electron detachment dynamics of this C_6^- excited electronic state. Without knowing the exact number of photons absorbed, one has two possible situations for electron detachment at photon energies above the threshold, e.g., at 296 nm. With one photon absorption at 296 nm, which is slightly above the detachment threshold, according to the results obtained from this work, the internal energy of C_6^- is clearly less than what is required to drive thermionic emission to an observable rate. If electron signal at 296 nm were due to 2-

212

photon absorption, one would expect to observe the same laser power dependence for the electron signal below and above the threshold. This is inconsistent with the result of laser power dependence studies. Based on this analysis, we conclude that thermionic emission can not be the responsible mechanism for electron detachment from this C_6^- electronic state. In addition, we have shown[7] that, although the two photon energies differ only by several tens of wavenumbers, electrons detached by the 297 nm light appeared to be far more energetic than those detached by the 296 nm light. This observation is also inconsistent with thermionic emission mechanism which would predict that slow electrons dominate at both laser energies.

This particular anion state is found to have similar vibrational structure as the linear neutral ground state. In this anion state, the electron is probably only loosely bound to the neutral core; therefore, the coupling between the excited anion state and the neutral continuum can be fairly strong. This strong coupling results in autodetachment that is even faster than the time scale of energy randomization among the various anion states. In this case, the electronic energy is not quite damped into the nuclear degrees of freedom. Therefore, the rate constant estimated from the quasiequilibrium rate theory is too small.

D.   Implications on other photodetachment studies of carbon cluster anions

Zajfman *et al.* have reported electron photodetachment cross sections of small carbon cluster anions.[47] In their experiments, the negative ion beam was overlapped with

213

a laser beam within a 2-mm-diameter aperture and along a path that was longer than 10 cm. The photodetachment cross section was measured both as a function of laser photon energy and as a function of laser power at fixed photon energy. Based on the low electron detachment thresholds observed in these experiments, nonlinear isomers of anion and neutral carbon clusters ($n=3$, ..., 8) were suggested. For example, C_8^- was found to photodetach at photon energy as low as 1.16 eV. Furthermore, they concluded the photodetachment process was a single-photon event based on laser power dependence which showed a linear dependence at lower laser power and saturation at higher laser power.

Our experimental results clearly showed that laser power dependence alone yielded misleading information on the number of photons involved in a multiphoton process. On the other hand, due to the existence of excited electronic states, the carbon cluster anions can be photodetached through resonant multiphoton detachment process. Photodetachment of C_n^- at low photon energies may well be due to multiphoton detachment process. Multiphoton absorption would be particularly feasible in Zajfman *et al.*'s experimental set-up. One can hardly reach any conclusion about electron affinity values of different isomers based on the onset of photodetachment as the photon energy is increased. For instance, at a fixed laser power, if one scans the photon energy region from 2.6 - 2.8 eV while monitoring the photodetachment signal from C_4^-, one sees a clear threshold at 2.71 eV. This threshold corresponds to the origin of the $C\ ^2\Pi_u \leftarrow X\ ^2\Pi_g$ transition in C_4^-, instead of the electron affinity of the cyclic isomer.

In this work, it has been shown that only the linear forms of these carbon clusters are definitely involved in the multiphoton detachment process.

VI. Conclusions

Resonant multiphoton detachment spectroscopy of C_4^-, C_6^- and C_8^- has provided valuable spectroscopic information on the low-lying $^2\Pi$ electronic states of these negative ions. Vibrational frequencies and term energies of the upper $^2\Pi$ electronic state of each anion are found to be in good agreement with those of the *ab initio* calculations.

The electron detachment dynamics of this multiphoton process is studied in detail. Based on the experimental results, we conclude that resonant multiphoton detachment occurs via thermionic emission following multiple steps of photon absorption and fast internal conversion.

Delayed electron emission from C_6^- and C_8^- following photoexcitation has been observed, and this process is attributed to thermionic emission. For each measured rate constant, the number of photons associated with multiphoton detachment was exactly determined. The electron emission rate constants at various photon energies have been calculated using microcanonical rate theory. The rates were found to be sensitive to a host of molecular parameters; reasonable agreement with experiment was achieved using *ab initio* vibrational frequencies and experimentally known electron affinities of the linear neutrals.

Acknowledgments

[1] W. Weltner, Jr. and R. J. van Zee, Chem. Rev. **89**, 1713 (1989).

[2] For example, see the references in this review article: J. R. Heath and R. J. Saykally, in *On Clusters and Clustering, From Atoms to Fractals*, edited by P. J. Reynolds (Elsevier, Amsterdam, 1993).

[3] S. Yang, K. J. Taylor, M. J. Craycraft, J. Conceicao, C. L. Pettiette, O. Cheshnovsky, and R. E. Smalley, Chem. Phys. Lett. **144**, 431 (1988).

[4] S. H. Yang, C. L. Pettiette, J. Conceicao, O. Cheshnovsky, and R. E. Smalley, Chem. Phys. Lett. **139**, 233 (1987).

[5] D. W. Arnold, S. E. Bradforth, T. N. Kitsopoulos, and D. M. Neumark, J. Chem. Phys. **95**, 8753 (1991).

[6] T. N. Kitsopoulos, C. J. Chick, Y. Zhao, and D. M. Neumark, J. Chem. Phys. **95**, 5479 (1991).

[7] C.C. Arnold, Y. Zhao, T. N. Kitsopoulos, and D. M. Neumark, J. Chem. Phys. **97**, 6121 (1992).

[8] G. V. Helden, P. R. Kemper, N. G. Gotts, and M. T. Bowers, Science **259**, 1300 (1993).

[9] G. Herzberg and A. Lagerqvist, Can. J. Phys. **46**, 2363 (1968).

[10] P.L. Jones, R. D. Mead, B. E. Kohler, S. D. Rosner, and W. C. Lineberger, J. Chem. Phys. **73**, 4419 (1980).

[11] U. Hefter, R. D. Mead, P. A. Schulz, and W. C. Linberger, Phys. Rev. A **28**, 1429 (1983).

[12] R. D. Mead, U. Hefter, P. A. Schulz, and W. C. Lineberger, J. Chem. Phys. **82**, 1723 (1985).

[13] B. D. Rehfuss, D.-J. Liu, B. M. Dinelli, M.-F. Jagod, W. C. Ho, M. W. Crofton, and T. Oka, J. Chem. Phys. **89**, 129 (1988).

[14] S. Schmatz and P. Botschwina, manuscript from the authors (1995).

[15] S. Schmatz and P. Botschwina, Chem. Phys. Lett. **235**, 5 (1995).

[16] S. Schmatz and P. Botschwina, Chem. Phys. Lett. **245**, 136 (1995).

[17] D. Forney, J. Fulara, P. Freivogel, M. Jakobi, D. Lessen, and J. P. Maier, J. Chem. Phys. **103**, 43 (1995).

[18] P. Freivogel, J. Fulara, M. Jakobi, D. Forney, and J. P. Maier, J. Chem. Phys. **103**, 54 (1995).

[19] Y. Zhao and D. M. Neumark, (manuscript in preparation).

[20] C. Kittle, Introduction to solid state physics, 6th ed. (Wiley, New York, 1986) p. 536.

[21] A. Amrein, R. Simpson, and P. Hackett, J. Chem. Phys. **94**, 4663 (1991); **95**, 1781 (1991).

[22] T. Leisner, K. Athanassenas, D. Kreisle, E. Recknagel, and O. Echt, J. Chem. Phys. **99**, 9670 (1993).

[23] B. A. Collings, A. H. Amrein, D. M. Rayner, and P. A. Hackett, J. Chem. Phys. **99**, 4174 (1993).

[24] H. Weidele, D. Kreisle, and E. Recknagel, G. Schulze Icking-Konert, H. Handschuh, G. Ganteför, and W. Eberhardt, Chem. Phys. Lett. **237**, 425 (1995).

[25] P. M. St. John, C. Yeretzian, and R. L. Whetten, J. Phys. Chem. **96**, 9100 (1992).

[26] L.-S. Wang, J. Conceicao, C. Jin, and R. E. Smalley, Chem. Phys. Chem. **182**, 5 (1991).

[27] E. E. B. Campbell, G. Ulmer, and I. V. Hertel, Phys. Rev. Lett. **67**, 1986 (1991).

[28] P. Wurz and K. R. Lykke, J. Chem. Phys. **95**, 7008 (1991).

[29] P. Sandler and C. Lifshitz, Chem. Phys. Lett. **200**, 445 (1992).

[30] D. Ding, R. N. Compton, R. E. Haufler, and C. E. Klots, J. Phys. Chem. **97**, 2500 (1993).

[31] Y. Zhang and M. Stuke, Phys. Rev. Lett. **70**, 3231 (1993).

[32] D. Ding, J. Huang, R. N. Compton, C. E. Klots, and R. E. Haufler, Phys. Rev. Lett. **73**, 1084 (1994).

[33] D. L. Osborn, D. J. Leahy, D. R. Cyr, and D. M. Neumark , (in press).

[34] T. N. Kitsopoulos, I. M. Waller, J. G. Loeser, and D. M. Neumark, Chem. Phys. Lett. **159**, 300 (1989).

[35] J. M. Bakker, J. Phys. E **6**, 785 (1973); J. Phys. E **7**, 364 (1974).

[36] R. B. Metz, A. Weaver, S. E. Bradforth, T. N. Kitsopoulos, and D. M. Neumark, J. Chem. Phys. **94**, 1377 (1990).

[37] To be described in a later publication.

[38] C. Xu, T. Taylor, and D. M. Neumark, (manuscript in preparation).

[39] L. Adamowicz, Chem. Phys. **156**, 387 (1991).

[40] K. Raghavachari, R. A. Whiteside, and J. A. Pople, J. Chem. Phys. **85**, 6623 (1986).

[41] C. Klots, Chem. Phys. Lett. **186**, 73 (1991).

[42] R. N. Compton, L. G. Christophorou, G. S. Hurst, and P. W. Reinhardt, J. Chem. Phys. **45**, 4634 (1967); C. E. Klots, *ibid.* **46**, 1197 (1967).

[43] J. M. L. Martin, J. P. Francois, and R. Gijbels, J. Chem. Phys. **93**, 8850 (1990).

[44] G. Z. Whitten and B. S. Robinovitch, J. Chem. Phys. **38**, 2466 (1963).

[45] E. W. Schlag and R. D. Levine, J. Phys. Chem. **96**, 10608 (1992).

[46] J. D. Watts and R. J. Bartlett, J. Chem. Phys. **97**, 3445 (1992).

[47] D. Zajfman, H. Feldman, O. Heber, D. Kella, D. Majer, Z. Vager, and R. Naaman, Science **258**, 1129 (1992).

Table I. Peak positions, relative energies, assignments, and vibrational frequencies from one-color multiphoton detachment spectrum of C_6^-

Peak Position (nm)	Peak Position (cm^{-1})	Relative Energies (cm^{-1})	Assignment	Frequencies (cm^{-1})	
				Expt'l	Calculated
628.47	15912	-564	3_1^0	σ_g'' 564	637
622.09	16075	-401	7_2^0	π_g'' 201	
606.94	16476	0	Origin		
598.93	16696	220	9_0^2	π_u 110	
589.46	16965	489	7_0^2	π_g 245	
585.54	17078	602	3_0^1	σ_g 602	600
577.50	17316	840	$3_0^1 9_0^2$		
565.45	17685	1209	3_0^2		
557.77	17929	1453	$3_0^2 9_0^2$		
548.17	18243	1767	2_0^1	σ_g 1767	1805
546.64	18294	1818	3_0^3		
539.73	18528	2052	1_0^1	σ_g 2052	2189
530.65	18845	2369			
522.78	19129	2653	$1_0^1 3_0^1$		
501.50	19940	3464	2_0^2		
497.80	20088	3612			
483.16	20697	4221			
445.88	22428	5952			

Table II. Peak positions, relative energies, assignments, and vibrational frequencies from one-color multiphoton detachment spectrum of C_8^-

Peak Position (nm)	Peak Position (cm^{-1})	Relative Energies (cm^{-1})	Assignment	Frequencies (cm^{-1})
773.93	12921	-42		
771.43	12963	0	Origin	
767.86	13023	60		
763.60	13096	133		
748.40	13362	399		
745.36	13416	453	4_0^1	σ_g 453
718.40	13920	957	4_0^2	
664.43	15050	2087	1_0^1	σ_g 2087
639.14	15646	2683		
613.29	16305	3342	Origin	
596.43	16766	3803		
578.29	17292	4329		
551.71	18125	5162		
543.71	18392	5429		
495.00	20202	7239		
490.00	20408	7445		
483.04	20702	7739		
446.43	22400	9437		

221

Table III. Thermionic emission rate constants for C_6^- at various photon energies

Wavelength (nm)	Number of Photons	Total Photon Energy (cm^{-1})	Rate Constant ($second^{-1}$)
522.8	2	38256	$1.00(40) \times 10^6$
501.35	2	39892	$2.42(20) \times 10^6$
498.2	2	40145	$2.86(16) \times 10^6$
491.2	2	40717	$4.70(15) \times 10^6$
488.8	2	40917	$6.10(15) \times 10^6$
487.2	2	41051	$5.90(15) \times 10^6$
483.2	2	41391	$7.60(15) \times 10^6$
477.0	2	41929	$1.06(3) \times 10^7$
475.2	2	42088	$1.30(4) \times 10^7$
472.8	2	42301	$1.38(4) \times 10^7$
464.5	2	43057	$1.92(7) \times 10^7$
457.0	2	43764	$2.60(27) \times 10^7$
446.15	2	44828	$3.70(40) \times 10^7$

Table IV. Thermionic emission rate constants for C_8^- at various photon energies

Wavelength (nm)	Number of Photons	Total Photon Energy (cm^{-1})	Rate Constant (second^{-1})
622.8	3	48170	1.40(30)×10^6
620.5	3	48348	1.50(30)×10^6
619.8	3	48403	1.70(30)×10^6
607.5	3	49383	2.50(20)×10^6
604.5	3	49628	2.90(20)×10^6
601.5	3	49875	3.50(20)×10^6
598.0	3	50167	4.10(20)×10^6
596.5	3	50293	4.50(20)×10^6
587.0	3	51107	7.70(30)×10^6
582.0	3	51546	1.08(6)×10^7
578.5	3	51858	1.23(7) ×10^7
575.5	3	52129	1.63(14)×10^7
773	4	51746	1.18(10)×10^7
768	4	52083	1.45(12) ×10^7

Table V. Vibrational frequencies (in cm^{-1}) used in microcanonical rate constant calculations.

C_4^- $(X^2\Pi_g)$	C_4 $(X^3\Sigma_g^-)$	C_6^- $(X^2\Pi_u)$	C_6 $(X^3\Sigma_g^-)$	C_8^- $(X^2\Pi_g)$	C_8 $(X^3\Sigma_g^-)$
π_u 240	π_u 188	π_u 119	π_u 105	π_u 60	π_u 60
π_g 505	π_g 367	π_g 261	π_g 238	π_g 68	π_g 501
σ_g 893	σ_g 919	π_u 437	π_u 331	π_u 265	π_u 153
σ_u 1884	σ_u 1566	π_g 540	π_g 496	π_g 284	π_g 203
σ_g 2084	σ_g 2111	σ_g 628	σ_g 649	π_u 546	π_u 264
		σ_u 1167	σ_u 1194	π_g 515	π_g 320
		σ_g 1823	σ_g 1661	σ_g 481	σ_g 497
		σ_u 1943	σ_u 1971	σ_u 918	σ_u 944
		σ_g 2171	σ_g 2176	σ_g 1303	σ_g 1346
				σ_u 1783	σ_u 1680
				σ_g 1915	σ_g 1945
				σ_u 2083	σ_u 2097
				σ_g 2151	σ_g 2154

Figure Captions

Figure 1. One-color resonant multiphoton detachment spectra of C_4^-, C_6^-, and C_8^-.

Figure 2. The expanded C_6^- spectrum and vibrational assignments.

Figure 3. Two-color and one-color resonant multiphoton detachment spectra of C_6^-. Solid line: two-color spectrum, laser wavelength of the first laser is scanned while the second laser is fixed at 635.5 nm; the laser fluence for the first laser is 2 mJ/cm^2. Dashed line: one-color spectrum, laser fluence is 30 mJ/cm^2.

Figure 4. Time-of-flight photoelectron kinetic energy measurement from C_4^- photodetachment. (top) one-photon direct detachment with photon energy of 4.66 eV; (bottom) resonant multiphoton detachment with photon energy of 2.71 eV. The electron affinity of linear C_4 is 3.88 eV.

Figure 5. Time-of-flight photoelectron kinetic energy measurement from C_6^- photodetachment. (top) one-photon direct detachment with photon energy 5.82 eV; (bottom) resonant multiphoton detachment with photon energy 2.04 eV. The electron affinity of linear C_6 is 4.18 eV.

Figure 6. Electron signal time profiles from resonant multiphoton detachment of C_6^- at various photon energies. The time width at FWHM of the laser pulse is 30 ns.

Figure 7. Electron signal time profiles from resonant multiphoton detachment of C_8^- at various photon energies. The time width at FWHM of the laser pulse is 30 ns.

Figure 8. Laser power dependence for the prompt electron signal and for the delayed electron signal of C_6^- multiphoton detachment. At 498.2 nm or 483.2 nm, both prompt electrons and delayed electrons are observed. These two types of electrons have different laser power dependence.

Figure 9. Two-color measurement of the electron emission rate constant for C_6^- multiphoton detachment, as compared to the rate constant from one-color measurement. (top) solid trace is the electron signal time profile after C_6^- interacts with two separated laser pulses: (1) 585.6 nm + (2) 437.2 nm; dashed trace is the electron signal time profile when the first laser pulse is blocked off. (bottom) the two-color electron signal time profile (solid line) is compared to the one-color electron signal time profile (dashed line) at 501 nm. Intensity is normalized to show the almost identical delayed electron emission traces from these two different experiments.

Figure 10. Schematic drawing of C_4^- resonant 2-photon detachment mechanism. *IC* stands for internal conversion, *TE* stands for thermionic emission.

Figure 11. Schematic drawing of C_6^- resonant multiphoton detachment mechanism. *IC* stands for internal conversion, *TE* stands for thermionic emission. The 3-photon absorption process is shown, as this is the case for electron signal at 607 nm, the origin transition of $^2\Pi_g \leftarrow X\,^2\Pi_u$ transition. The electron affinity of linear C_6 is 4.18 eV, and the photon energy at 607 nm is 2.04 eV.

Figure 12. Measured electron emission rate constants at various total photon energies. Dashed lines are drawn to guide eyes. The error bars in the measurement are as indicated in the figure; for some data points, error bars are smaller than the size of solid circles that are used to represent the data points.

Figure 13. Calculated thermionic emission rate constants using quasiequilibrium rate theory. The y-axis is the log value of k_{TE}, the x-axis is the total photon energy absorbed. Experimental results are shown in solid circles connected by a dashed line. For C_8^-, only one type of calculation is shown (solid line); For C_6^-, two types of calculations (dotted line and solid line) differing in calculation parameters are shown.

Figure 14. Calculated electron kinetic energy distributions (dashed lines) using Equation (6) and assuming s-wave detachment, as compared to experimental results (solid lines).
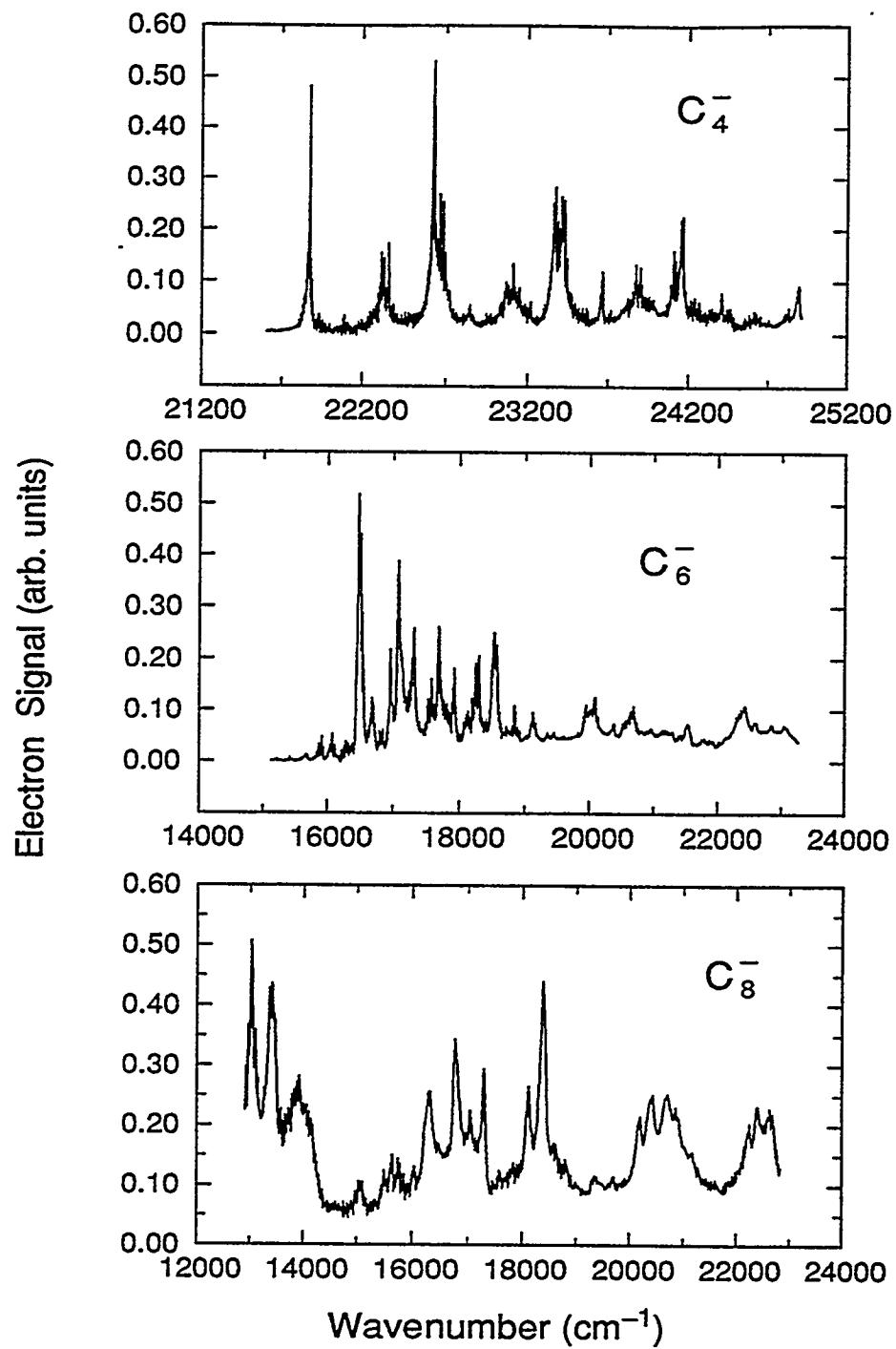
Figure 6.1
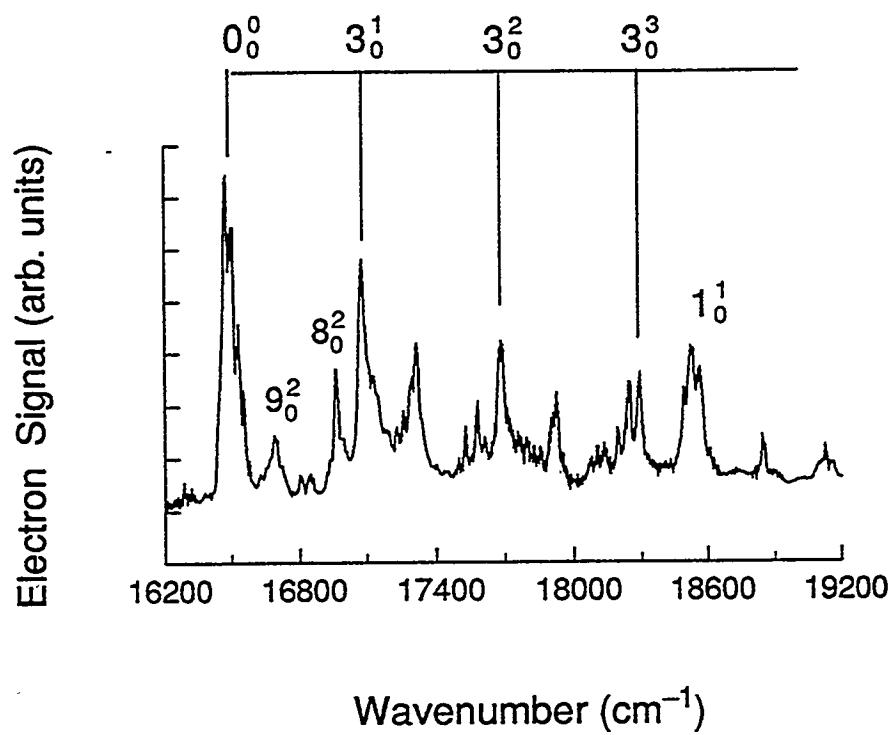
Figure 6.2

Figure 6.3

229
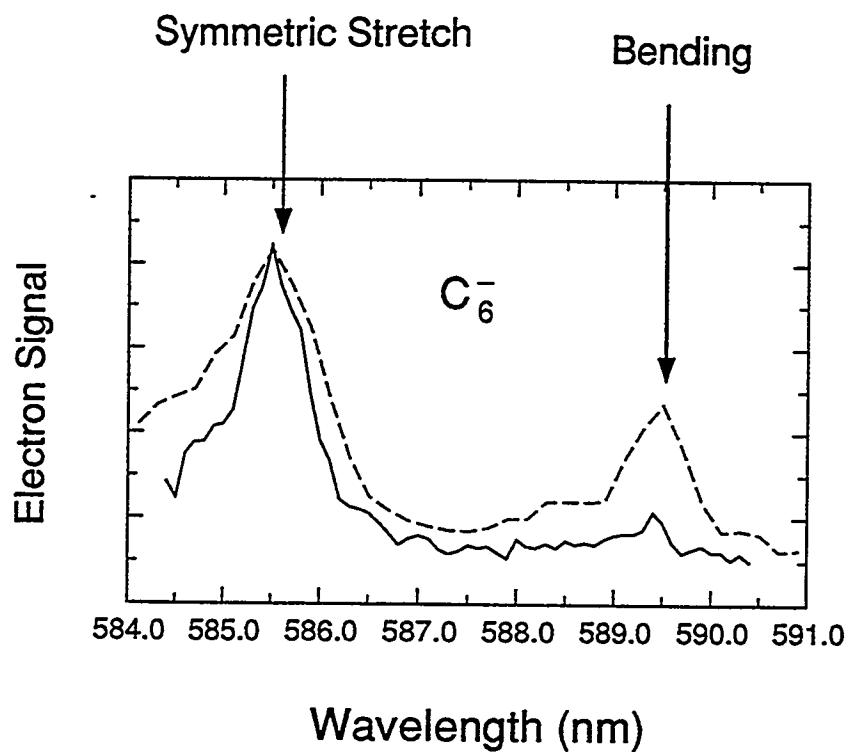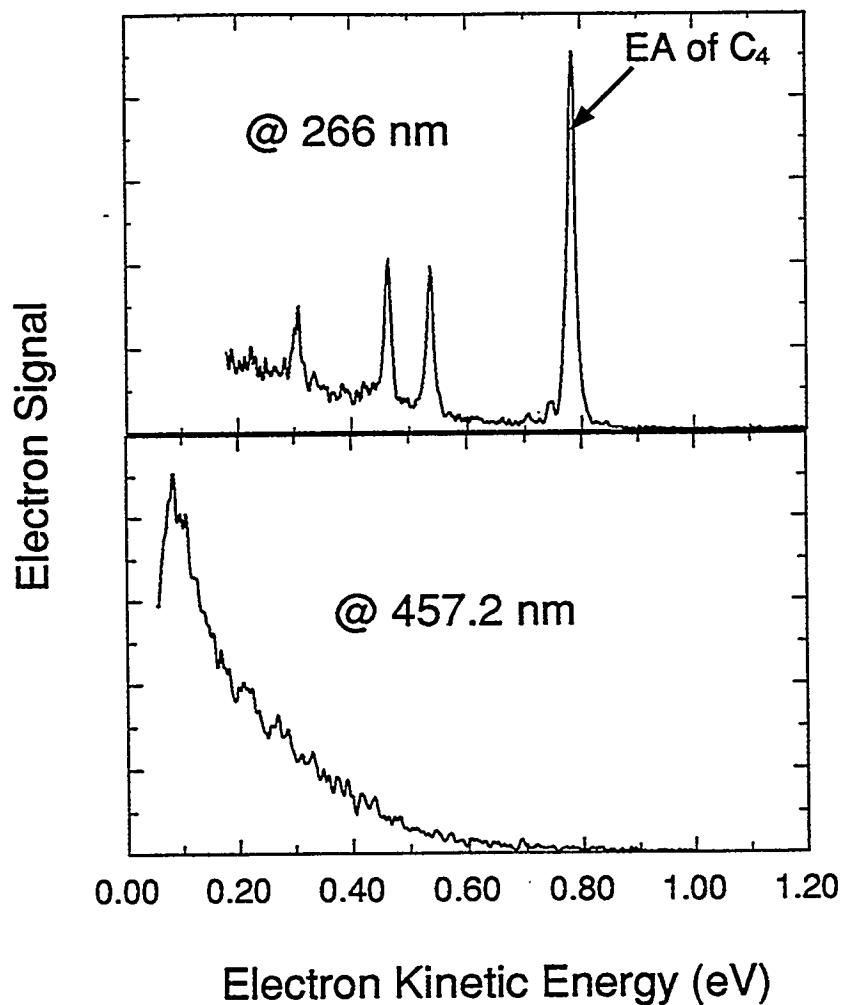
Figure 6.4

**Figure 6.5**

231
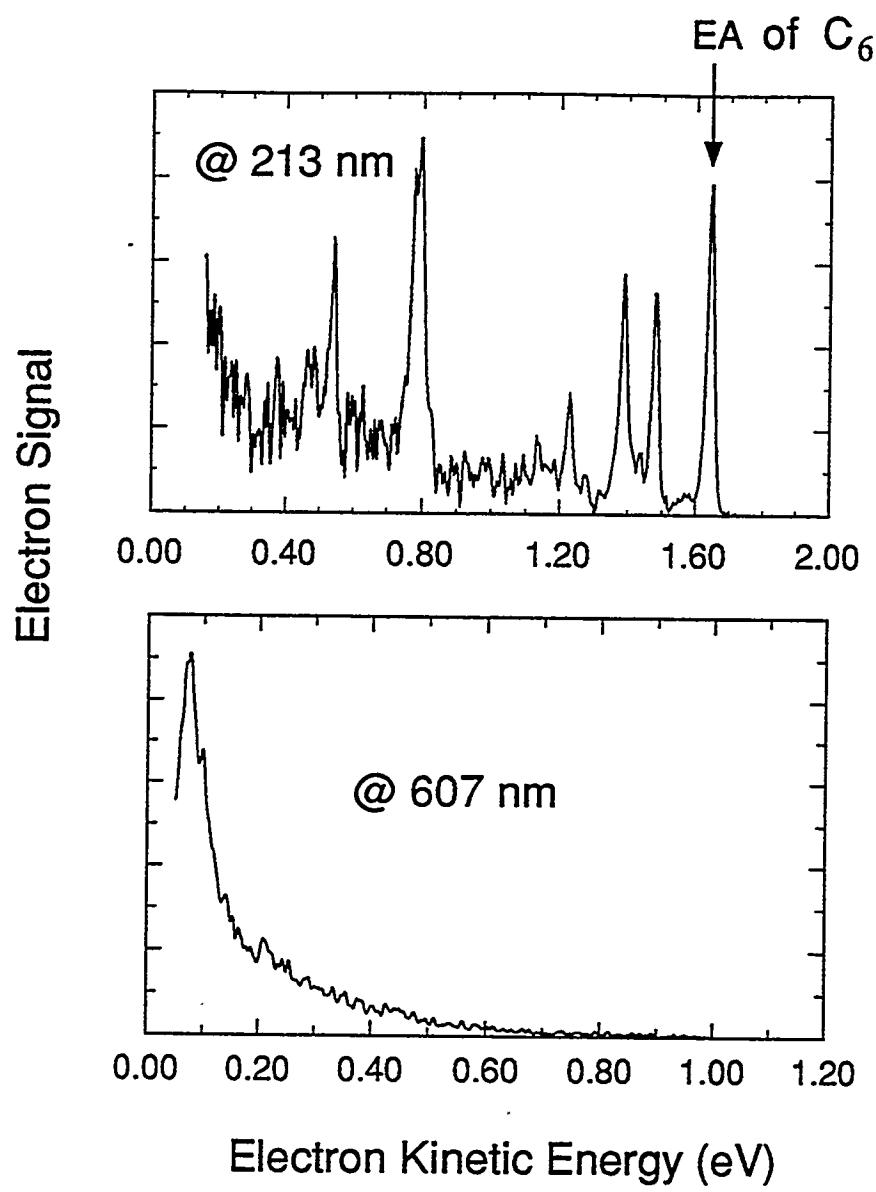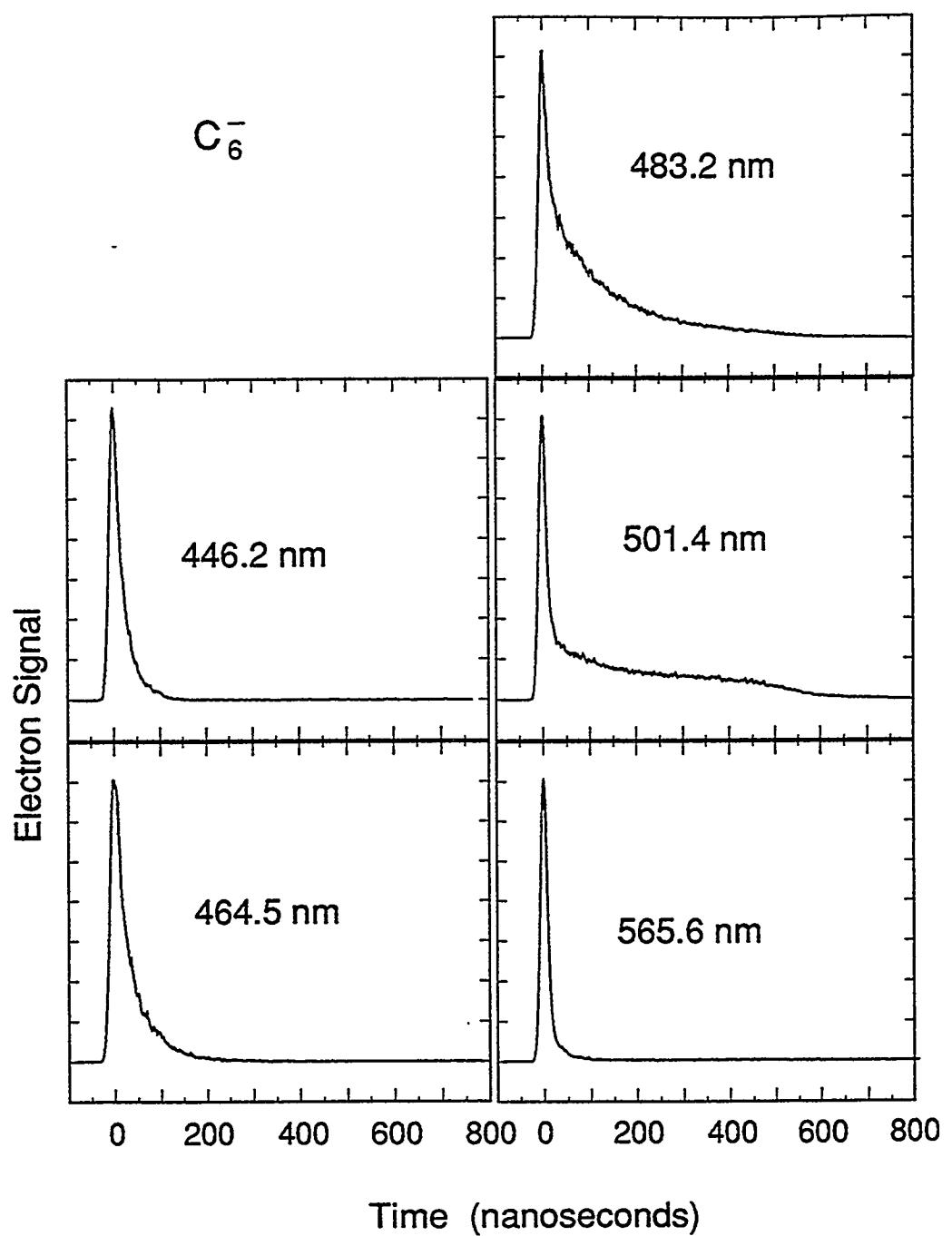
Figure 6.6

Figure 6.7

233
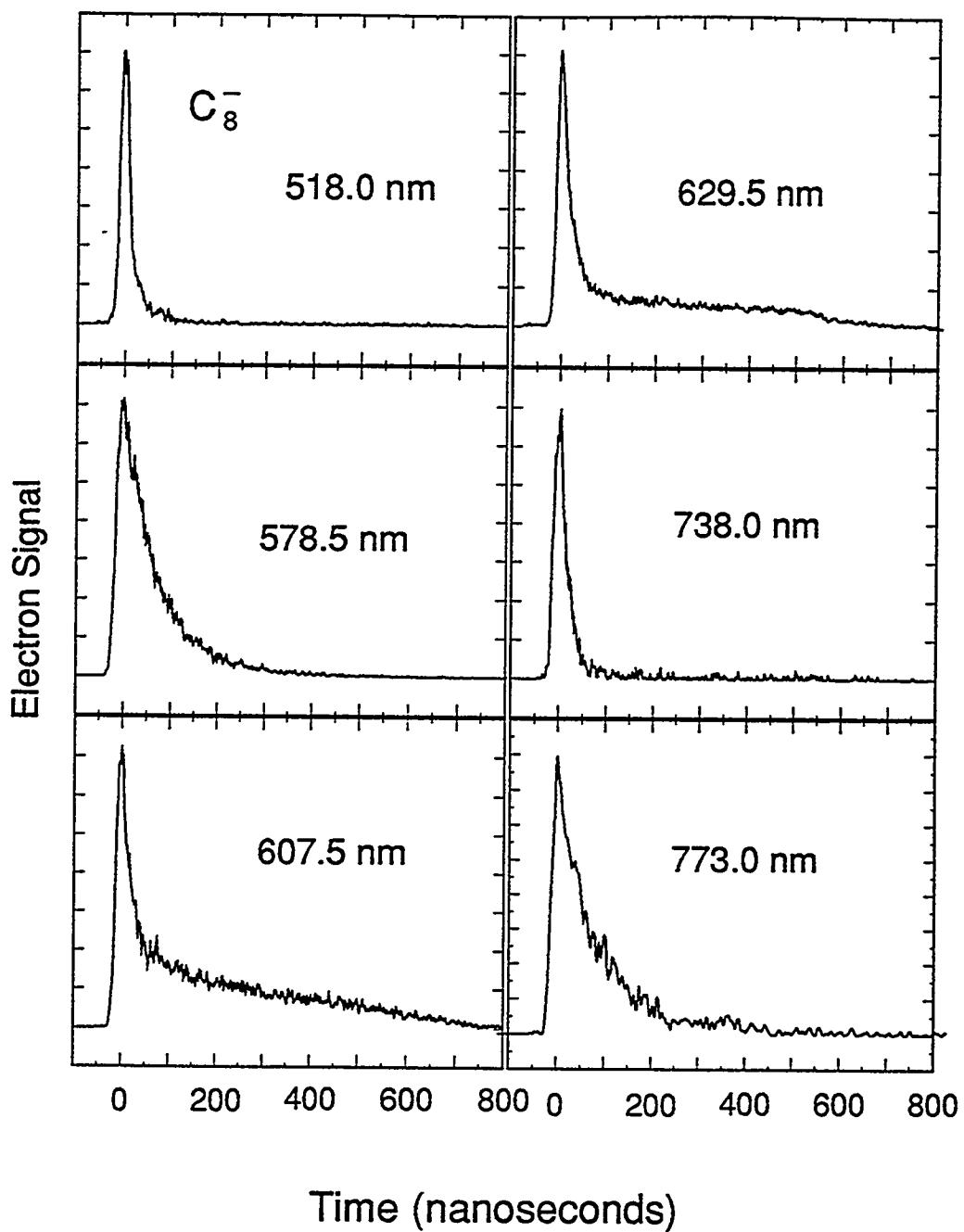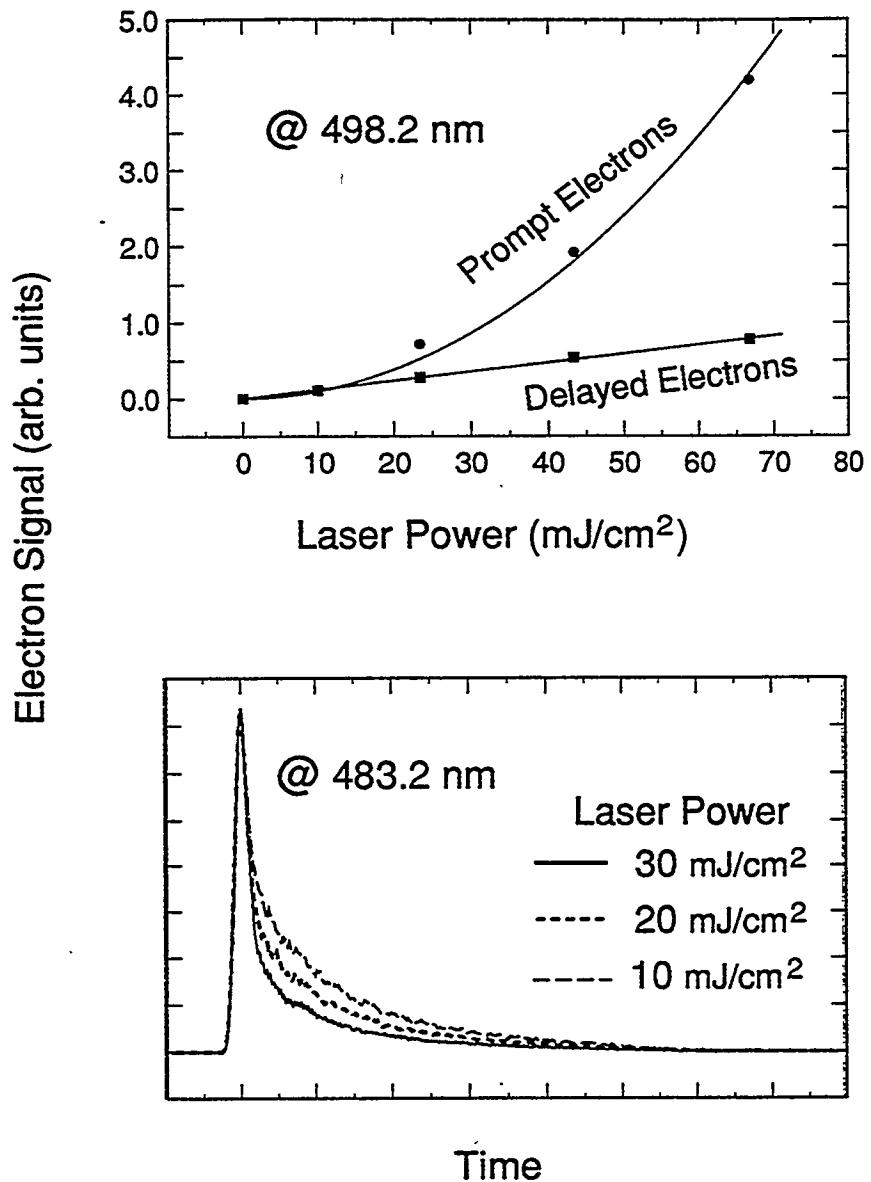
Figure 6.8

Figure 6.9

235

Figure 6.10

236
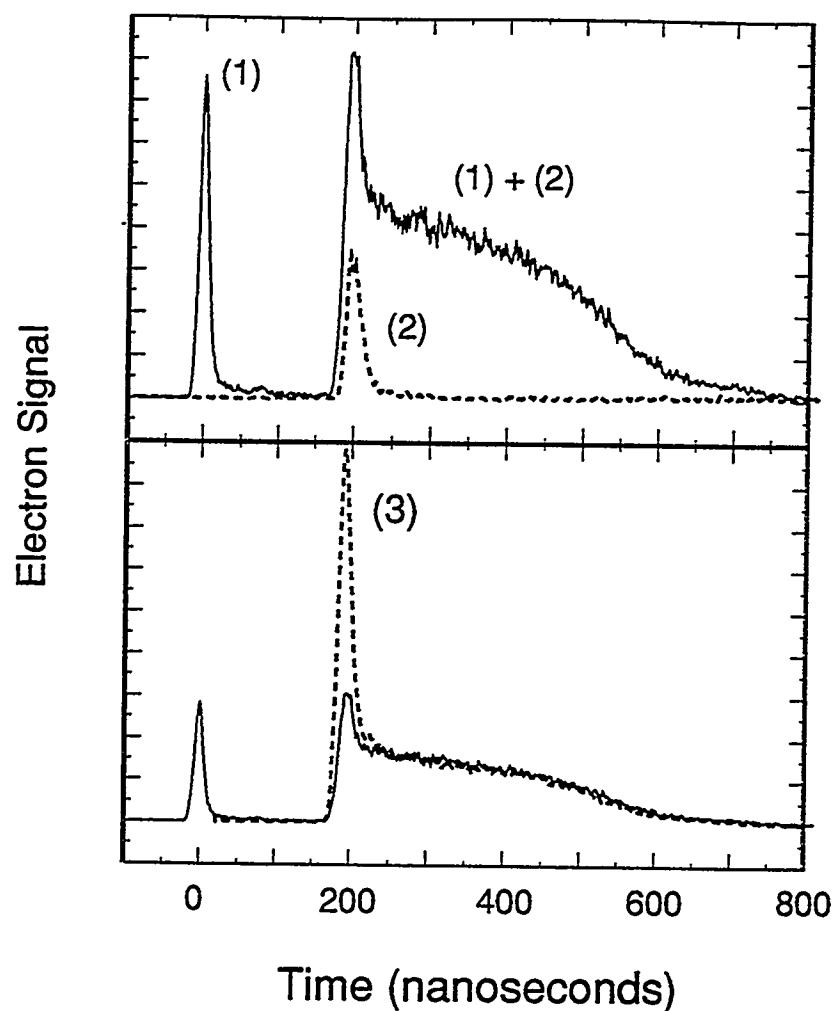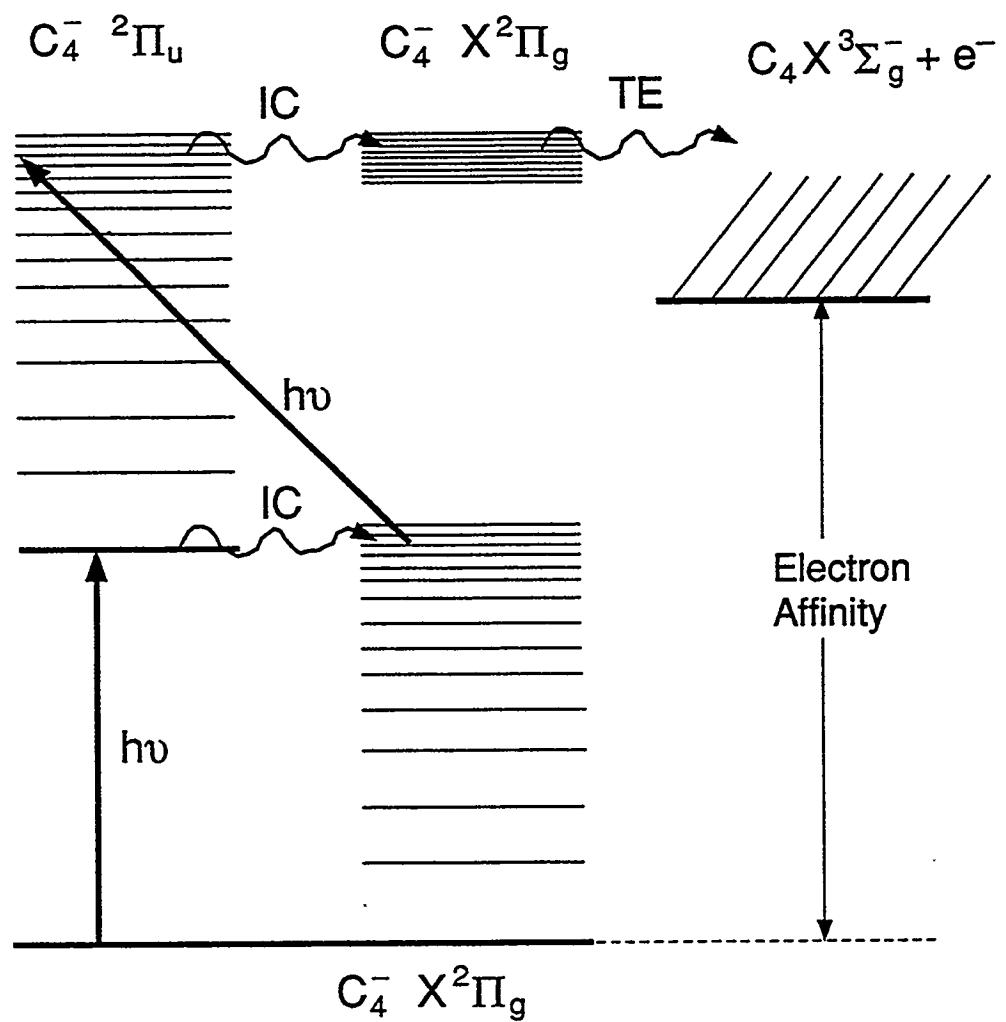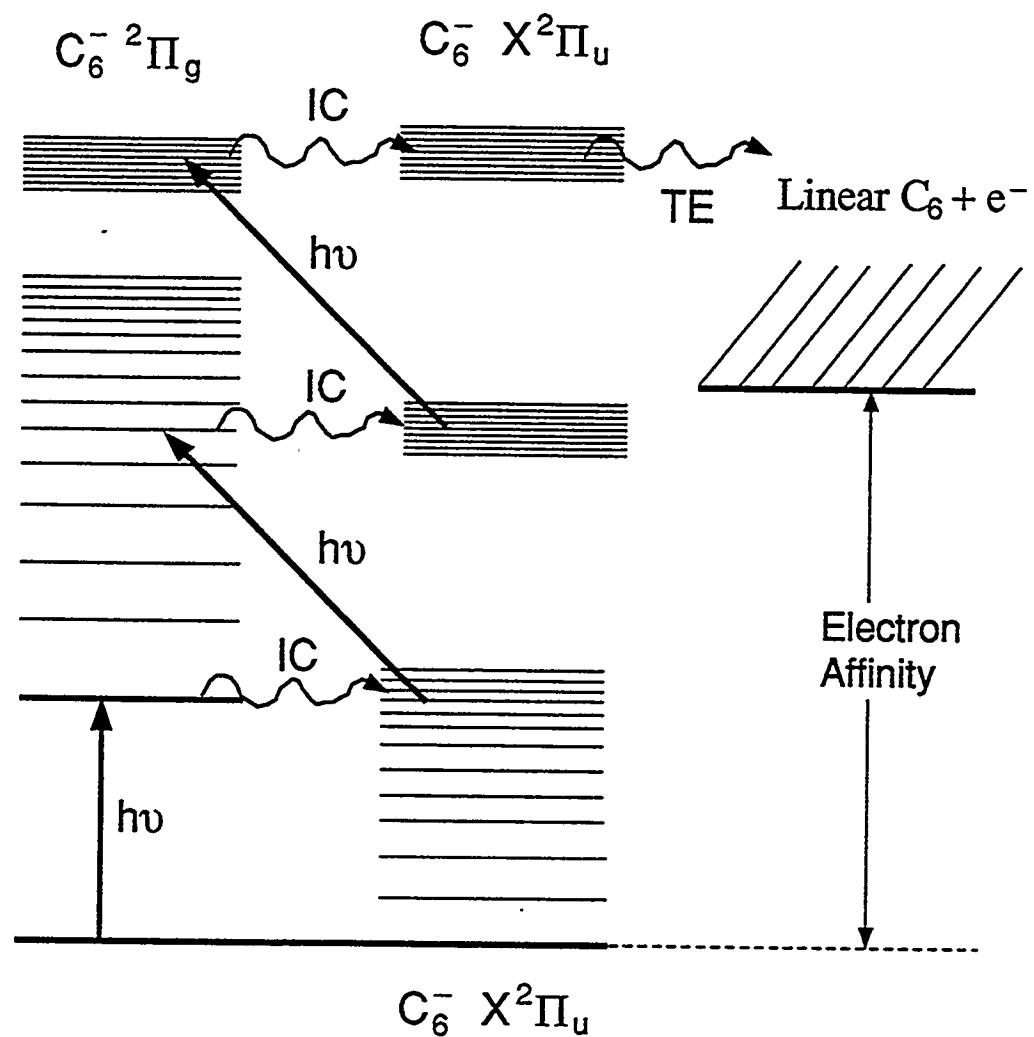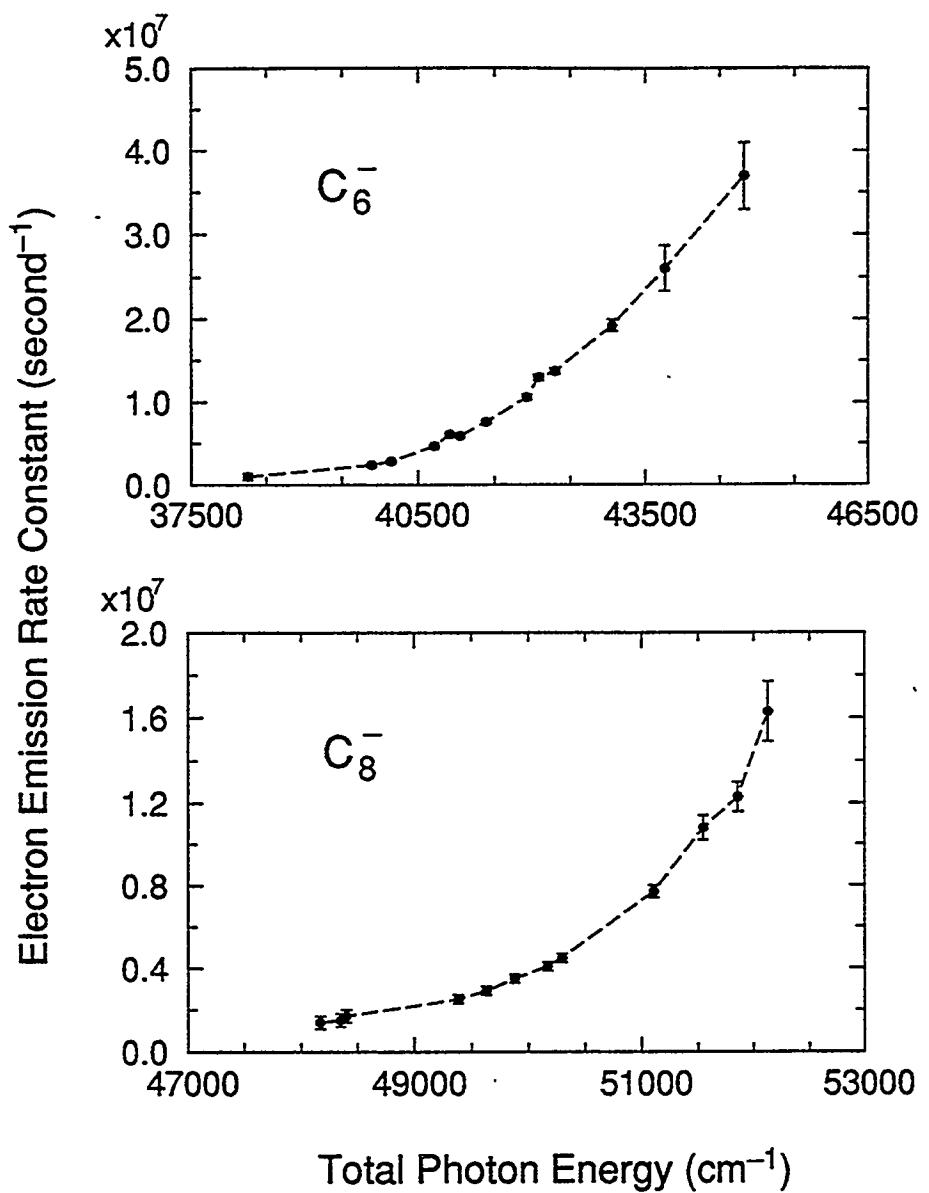
Figure 6.11

Figure 6.12
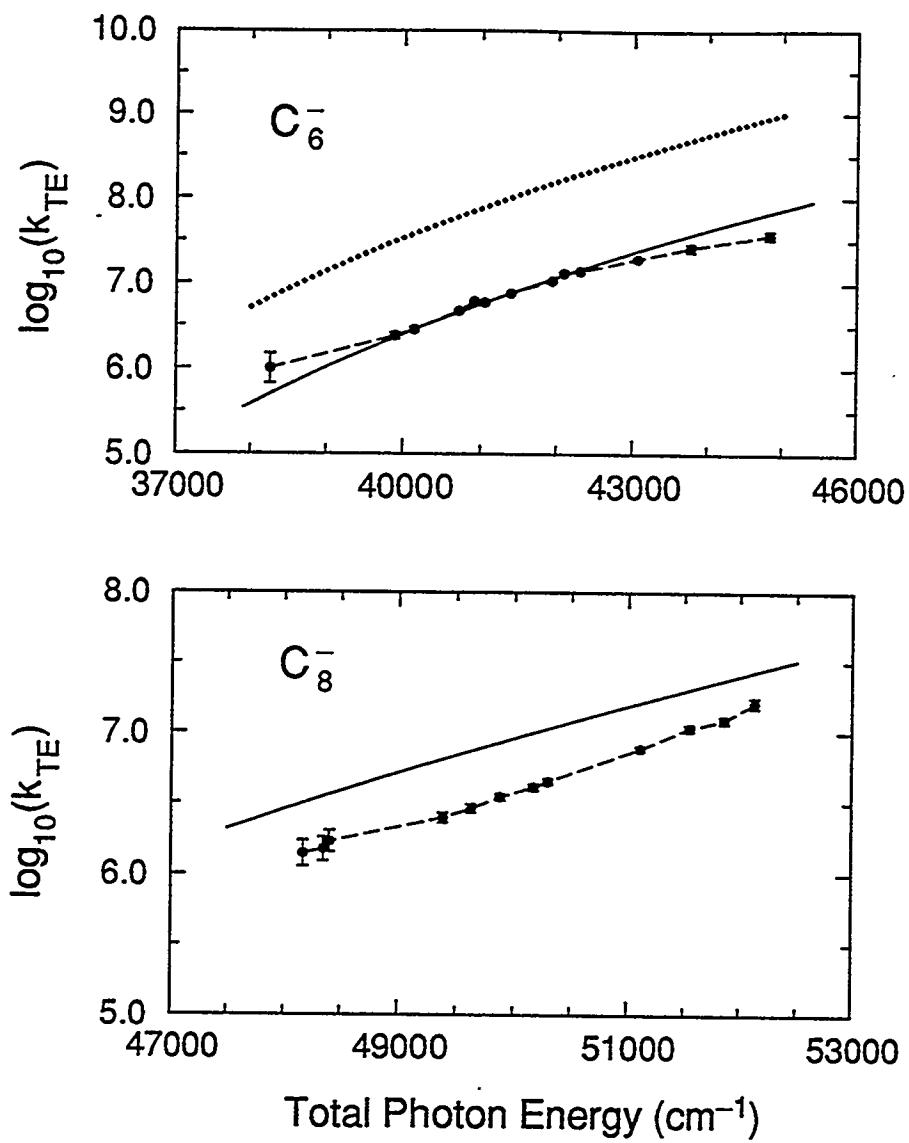
Figure 6.13

Figure 6.14

240
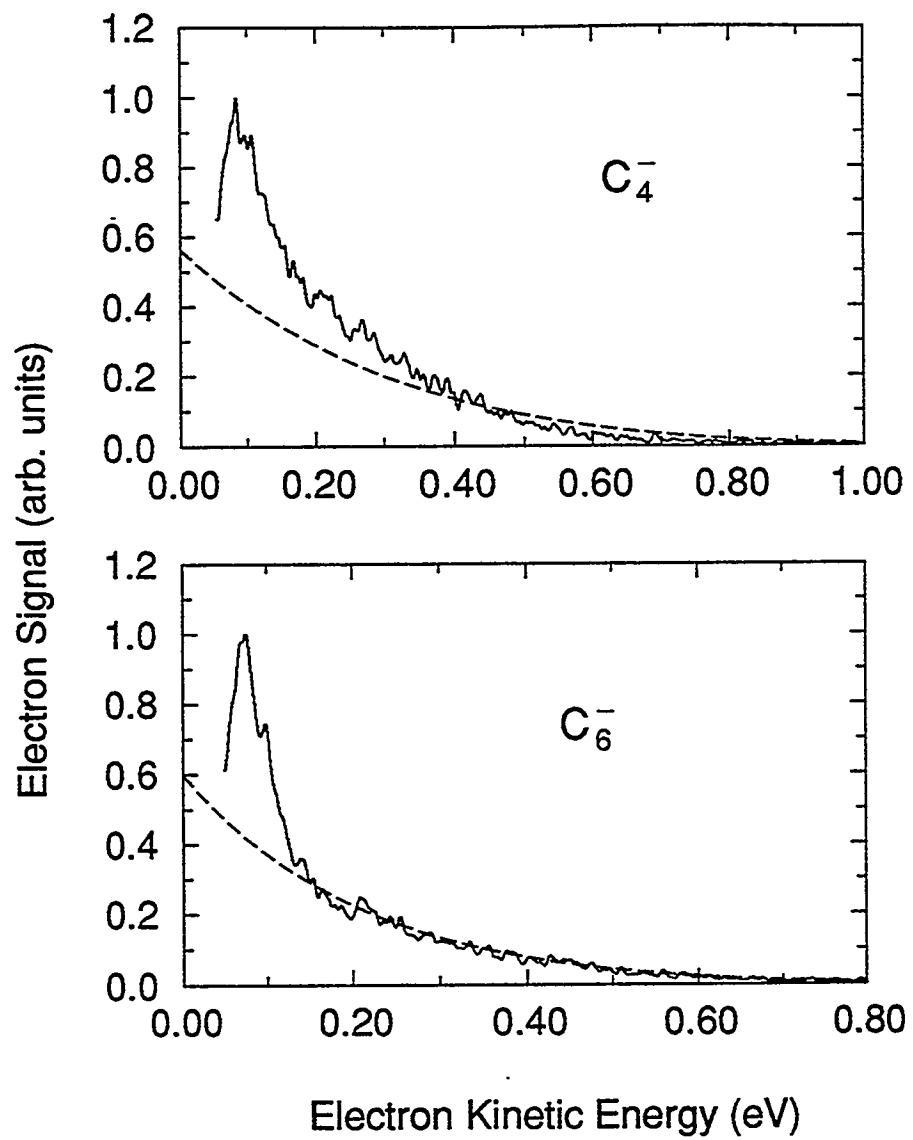
Appendix I

Rotation line position fitting code (FORTRAN)

Program Zare_Fit

```
C    This program generates a set of best-fit molecular constants by fitting
C    the observed rotational line positions in a doublet PI to doublet PI
C    electronic transition to the solution of the appropriate molecular
C    Hamiltonian.  This method is first suggested by Professor Richard N.
C    Zare and co-workers in a 1974 J. Mol. Spec. paper.

C    Some details are taken into account to accommodate the specifics relevant
C    to the C4- spectroscopy; these include the nuclear spin statistics and
C    Hund's case (a) energetics.

C    To run this program, one supplies (1) an input file with rotational
C    assignments and line positions; (2) an initial set of molecular
C    constants and information regarding which are to be fitted, which are
C    to be held constant.

     implicit double precision (a-h,o-z)
     CHARACTER*20 DATAFILE
     PARAMETER (NMAX=500,MA=12,NTRY=100)
     INTEGER ia(MA),ix1(NMAX),ix2(NMAX),ix3(NMAX),ndata
     DOUBLE PRECISION y(NMAX),sig(NMAX)
     DOUBLE PRECISION alamda,a(MA),covar(MA,MA), alpha(MA,MA)

        write(*,1)
  1     format(2x,'Name of file with input data: ',$)
        read(*,*)DATAFILE

     open(20,file=DATAFILE)
     do 10 i=1,NMAX
       read (20,*,end=100) ix1(i),ix2(i),ix3(i),y(i),sig(i)
  10 continue
 100 ndata=i-1
     close(20)

   open(4)
     do 260 i=1,MA
       read(4,*) a(i), ia(i)
```

```
260   continue
      close(4)


      alamda=-.1
      call mrqmin(ix1,ix2,ix3,y,sig,ndata,a,ia,MA,covar,alpha,MA,
     *         chisq,alamda)
      tchisq=chisq
      do 250 i=1,NTRY
        call mrqmin(ix1,ix2,ix3,y,sig,ndata,a,ia,MA,covar,alpha,MA,
     *         chisq,alamda)
        if(((tchisq-chisq).gt.0.).and.((tchisq-chisq).lt.
     *      (1.e-4*tchisq))) go to 240
      tchisq=chisq
250   continue
240   call mrqmin(ix1,ix2,ix3,y,sig,ndata,a,ia,MA,covar,alpha,MA,
     *         chisq,0.)


      write(*,*) "
      write(*,*) 'Fitted Parameters: '
      do 185 i=1,MA
        write(*,85) a(i),sqrt(covar(i,i))
 85      format(f18.9,5x,f18.9)
185   continue


c     write(*,*) "
c     write(*,*) 'Covariance Matrix: '
c     do 180 i=1,MA
c       write(*,80) (covar(i,j), j=1,MA)
c 80     format(6e10.2)
c 180   continue



      end

C   The following four subroutines are the least-squares fitting
C   code adapted from NUMERICAL RECIPES FOR FORTRAN, 2nd edition.
C   The non-linear Marquardt algorithm is used.  This fitting yields
C   best-fit parameters, error bars in terms of variance and covariance
C   matrix.  Individual parameters can be chosen to be fixed or varied
C   during the fitting.

      SUBROUTINE MRQMIN(IX1,IX2,IX3,Y,SIG,NDATA,A,IA,MA,
     *  COVAR,ALPHA,NCA,CHISQ,ALAMDA)
      INTEGER ma,nca,ndata,ia(ma),MMAX,IX1(NDATA),
```

```fortran
*        IX2(NDATA),IX3(NDATA)
      DOUBLE PRECISION alamda,chisq,Y(NDATA),
*     SIG(NDATA),A(MA),COVAR(NCA,NCA),ALPHA(NCA,NCA)
      PARAMETER (MMAX=20)
      INTEGER j,k,l,m,mfit
      DOUBLE PRECISION ochisq, atry(MMAX), beta(MMAX), da(MMAX)
      SAVE ochisq,atry,beta,da,mfit
      IF(ALAMDA.LT.0.)THEN
        mfit=0
        DO 11 J=1,MA
          if (ia(j).ne.0) mfit=mfit+1
11    continue
        ALAMDA=0.001
        CALL MRQCOF(IX1,IX2,IX3,Y,SIG,NDATA,A,IA,MA,ALPHA,
*           BETA,NCA,CHISQ)
        write(*,*)'chisq after 1st mrqcof: ',chisq
        OCHISQ=CHISQ
        DO 12 J=1,MA
          ATRY(J)=A(J)
12      CONTINUE
      ENDIF
      j=0
      DO 14 l=1,MA
        if(ia(l).ne.0) then
          j=j+1
          k=0
          do 13 m=1,ma
          if(ia(m).ne.0) then
            k=k+1
            COVAR(J,K)=ALPHA(J,K)
          endif
13        continue
          COVAR(J,J)=ALPHA(J,J)*(1.+ALAMDA)
          DA(J)=BETA(J)
        endif
14    continue
      CALL GAUSSJ(COVAR,MFIT,NCA,DA,1,1)
      IF(ALAMDA.EQ.0.)THEN
        CALL COVSRT(COVAR,NCA,MA,IA,MFIT)
        RETURN
      ENDIF
      j=0
      DO 15 l=1,MA
        if(ia(l).ne.0) then
          j=j+1
```

```fortran
          atry(l)=a(l)+da(j)
        endif
15    continue
      CALL MRQCOF(IX1,IX2,IX3,Y,SIG,NDATA,ATRY,IA,MA,COVAR,DA,
     *       NCA,CHISQ)
      write(*,*) 'chisq after mrqcof: ', chisq
      IF(CHISQ.LT.OCHISQ)THEN
        ALAMDA=0.1*ALAMDA
        OCHISQ=CHISQ
        j=0
        do 17 l=1,ma
          if(ia(l).ne.0) then
            j=j+1
            k=0
            do 16 m=1,ma
              if(ia(m).ne.0) then
                k=k+1
                ALPHA(J,K)=COVAR(J,K)
              endif
16          continue
            BETA(J)=DA(J)
            A(L)=ATRY(L)
          endif
17      continue
      ELSE
        ALAMDA=10.*ALAMDA
        CHISQ=OCHISQ
      ENDIF

      RETURN
      END



      SUBROUTINE
     MRQCOF(IX1,IX2,IX3,Y,SIG,NDATA,A,IA,MA,ALPHA,BETA,NALP,
     *CHISQ)
      INTEGER ma,nalp,ia(ma),MMAX,ix1(ndata),ix2(ndata),ix3(ndata)
      DOUBLE PRECISION chisq,a(ma),ALPHA(NALP,NALP),BETA(MA),
     *       sig(ndata),y(ndata)
      PARAMETER (MMAX=20)
      INTEGER mfit,i,j,k,l,m,ndata
      DOUBLE PRECISION dy,sig2i,wt,ymod,dyda(MMAX)
      mfit=0
      DO 21 J=1,MA
        if (ia(j).ne.0) mfit=mfit+1
```

244

```fortran
21    continue
   do 23 j=1,mfit
      do 22 k=1,j
         alpha(j,k)=0.
22    continue
      BETA(J)=0.
23 continue
   CHISQ=0.
   DO 26 I=1,NDATA
      CALL FUNCS(IX1(I),IX2(I),IX3(I),A,YMOD,DYDA,MA)
      SIG2I=1./(SIG(I)*SIG(I))
      DY=Y(I)-YMOD
      j=0
      DO 25 l=1,MA
         if (ia(l).ne.0) then
            j=j+1
            wt=dyda(l)*sig2i
            k=0
            do 24 m=1,l
               if (ia(m).ne.0) then
                  k=k+1
                  ALPHA(J,K)=ALPHA(J,K)+WT*DYDA(m)
               endif
24          continue
            beta(j)=beta(j)+dy*wt
         endif
25    continue
      CHISQ=CHISQ+DY*DY*SIG2I
26 continue
   DO 28 J=2,MFIT
      DO 27 K=1,J-1
         ALPHA(K,J)=ALPHA(J,K)
27 continue
28 continue

   RETURN
   END



   SUBROUTINE COVSRT(COVAR,NPC,MA,IA,MFIT)
   INTEGER ma, mfit, npc, ia(ma)
   DOUBLE PRECISION COVAR(NPC,NPC)
   INTEGER i,j,k
   DOUBLE PRECISION swap
   DO 32 i=mfit+1,MA
```

245

```fortran
      DO 31 j=1,i
        COVAR(I,J)=0.
        COVAR(J,I)=0.
31    CONTINUE
32    CONTINUE
      k=mfit
      DO 35 j=ma,1,-1
        if (ia(j).ne.0) then
          DO 33 i=1,ma
            swap=covar(i,k)
            covar(i,k)=covar(i,j)
            covar(i,j)=swap
33        continue
          do 34 i=1,ma
            swap=covar(k,i)
            covar(k,i)=covar(j,i)
            covar(j,i)=swap
34        continue
          k=k-1
        endif
35    continue
      RETURN
      END


      SUBROUTINE GAUSSJ(A,N,NP,B,M,MP)
      PARAMETER (LMAX=50)
      DOUBLE PRECISION big,dum,pivinv,A(NP,NP),B(NP,MP)
      INTEGER IPIV(LMAX),INDXR(LMAX),INDXC(LMAX)
      DO 41 J=1,N
        IPIV(J)=0
41    CONTINUE
      DO 52 I=1,N
        BIG=0.
        DO 43 J=1,N
          IF(IPIV(J).NE.1)THEN
            DO 42 K=1,N
              IF (IPIV(K).EQ.0) THEN
                IF (ABS(A(J,K)).GE.BIG)THEN
                  BIG=ABS(A(J,K))
                  IROW=J
                  ICOL=K
                ENDIF
              ELSE IF (IPIV(K).GT.1) THEN
                PAUSE 'Singular matrix'
```

246

```fortran
        ENDIF
42      CONTINUE
        ENDIF
43   CONTINUE
     IPIV(ICOL)=IPIV(ICOL)+1
     IF (IROW.NE.ICOL) THEN
       DO 44 L=1,N
         DUM=A(IROW,L)
         A(IROW,L)=A(ICOL,L)
         A(ICOL,L)=DUM
44     CONTINUE
       DO 45 L=1,M
         DUM=B(IROW,L)
         B(IROW,L)=B(ICOL,L)
         B(ICOL,L)=DUM
45     CONTINUE
     ENDIF
     INDXR(I)=IROW
     INDXC(I)=ICOL
     IF (A(ICOL,ICOL).EQ.0.) PAUSE 'Singular matrix.'
     PIVINV=1./A(ICOL,ICOL)
     A(ICOL,ICOL)=1.
     DO 46 L=1,N
       A(ICOL,L)=A(ICOL,L)*PIVINV
46   CONTINUE
     DO 47 L=1,M
       B(ICOL,L)=B(ICOL,L)*PIVINV
47   CONTINUE
     DO 51 LL=1,N
       IF(LL.NE.ICOL)THEN
        DUM=A(LL,ICOL)
        A(LL,ICOL)=0.
        DO 48 L=1,N
          A(LL,L)=A(LL,L)-A(ICOL,L)*DUM
48      CONTINUE
        DO 49 L=1,M
          B(LL,L)=B(LL,L)-B(ICOL,L)*DUM
49      CONTINUE
       ENDIF
51   CONTINUE
52 CONTINUE
   DO 54 L=N,1,-1
     IF(INDXR(L).NE.INDXC(L))THEN
       DO 53 K=1,N
         DUM=A(K,INDXR(L))
```

247

```
          A(K,INDXR(L))=A(K,INDXC(L))
          A(K,INDXC(L))=DUM
53     CONTINUE
       ENDIF
54   CONTINUE

     RETURN
     END



C    This function calculates the transition frequency in wavenumbers
C    for a given rotational assignment.  The gradient of the transition
C    energy with respect to the fitting parameters are also calculated.

     subroutine funcs(ix1,ix2,ix3,a,omega,dfda,na)
     integer na,ix1,ix2,ix3,ix4(2),ix31,ix32
     double precision a(na),dfda(na),omega,omega2,y1,y2
     call getix4(ix1,ix2,ix3,ix4)
     ix32=ix3
     if(ix2.eq.3) ix31=ix3
     if(ix2.eq.1) ix31=ix3-1
     if(ix2.eq.2) ix31=ix3+1
     call gety(ix1,1,ix4(1),ix31,a,na,y1)
     call gety(ix1,2,ix4(2),ix32,a,na,y2)
     omega=y1-y2
     do 150 i=1,na
       delta=a(i)
       do 120 j=1,12
          delta=0.1*delta
          a(i)=a(i)+delta
          call gety(ix1,1,ix4(1),ix31,a,na,y1)
          call gety(ix1,2,ix4(2),ix32,a,na,y2)
          omega2=y1-y2
          dfda(i)=(omega2-omega)/delta
          a(i)=a(i)-delta
          if(((omega2-omega).gt.-.1).and.((omega2-omega)
     *       .lt..1)) goto 150
120     continue
150   continue
     return
     end

C    This subroutine figures out the e/f parity of the lower and upper
C    states for a given J value.
```

```fortran
      subroutine getix4(ix1,ix2,ix3,ix4)
      integer ix1,ix2,ix3,ix4(2),ixt
      if (ix1.eq.1) then
        if(mod(ix3,2).eq.0) then
           ixt=2
        else
           ixt=1
        endif
      elseif(mod(ix3,2).eq.0) then
           ixt=1
        else
           ixt=2
      endif
      ix4(2)=ixt
      if((ix2.eq.1).or.(ix2.eq.2)) then
        ix4(1)=ixt
      elseif (ixt.eq.1) then
         ix4(1)=2
      else
         ix4(1)=1
      endif
      return
      end
```

C   This subroutine calculates the eigenvalue for a given set of
C   quantum numbers.

```fortran
      subroutine gety(ix1,ix5,ix4i,ix3,a,na,y)
      integer na,ix1,ix3,ix4i,ix5,j
      double precision a(na),y,a11,a22,a12,esmall,elarge
      j=(ix5-1)*6
      a11=a(j+1)-a(j+2)/2.+a(j+4)+(a(j+3)-a(j+4))*ix3**2-a(j+4)*
     *    ix3**4+a(j+5)*(1.+(-1)**ix4i*ix3)/2.+a(j+6)*(1.+(-1)
     *     **ix4i*ix3)**2/2.
      a12=(-1.*a(j+3)-a(j+5)/4.-a(j+6)*(1.+(-1)**ix4i*ix3)/2.+
     *    +2.*a(j+4)*(ix3**2-1.))*sqrt(ix3**2-1.)
      a22=a(j+1)+(a(j+2)+a(j+6))/2.-a(j+4)+(a(j+3)-a(j+4)+a(j+6)
     *    /2.)*(ix3**2-2.)-a(j+4)*(ix3**2-2.)**2
      call eigen(a11,a22,a12,esmall,elarge)
      if(ix1.eq.1) y=elarge
      if(ix1.eq.2) y=esmall
      return
      end
```

C   This subroutine numerically diagonalizes the (2 x 2) matrix.

```
C    The eigenvalues are the energies of a particular J level for
C    the 3/2 and 1/2 manifolds, respectively.

     subroutine eigen(a11,a22,a12,esmall,elarge)
     double precision a11,a22,a12,esmall,elarge,temp
     temp=sqrt((a11+a22)**2-4.*(a11*a22-a12**2))
     elarge=(a11+a22+temp)/2.
     esmall=(a11+a22-temp)/2.
     return
     end
```

Appendix II

Publications

1. "Stimulated Raman Pumping of C_2^- Probed via Resonant Two Photon Detachment", Esther de Beer, Yuexing Zhao, Ivan Yourshaw, and Daniel M. Neumark, Chemical Physics Letters, 244, 400 (1995).

2. "Study of the $ArBr^-$, ArI^-, and KrI^- Anions and the Corresponding Neutral van der Waals Complexes by Anion Zero Electron Kinetic Energy Spectroscopy", Yuexing Zhao, Ivan Yourshaw, Georg Reiser, Caroline C. Arnold, and Daniel M. Neumark, Journal of Chemical Physics 101, 6538 (1994).

3. "Study of $I \bullet CO_2$ van der Waals Complex by Threshold Photodetachment Spectroscopy of I^-CO_2", Yuexing Zhao, Caroline C. Arnold, and Daniel M. Neumark, Journal of the Chemical Society - Faraday Transactions 89, 1449 (1993).

4. "Study of C_6^- and C_6 with Threshold Photodetachment Spectroscopy and Autodetachment Spectroscopy", Caroline C. Arnold, Yuexing Zhao, Theofanis N. Kitsopoulos and Daniel M. Neumark, Journal of Chemical Physics 97, 6121 (1992).

5. "Threshold Photodetachment Spectroscopy of C_5^-", Theofanis N. Kitsopoulos, Caroline J. Chick, Yuexing Zhao and Daniel M. Neumark, Journal of Chemical Physics, 95, 5479 (1991).

6. "Study of the Low-lying Electronic States of Si_2 and Si_2^- Using Negative Ion Photodetachment Techniques", Theofanis N. Kitsopoulos, Caroline J. Chick, Yuexing Zhao and Daniel M. Neumark, Journal of Chemical Physics 95, 1441 (1991).

7. "Spectroscopy and Electron Detachment Dynamics of Small Carbon Cluster Anions (C_4^-, C_6^- and C_8^-)", Yuexing Zhao, Esther de Beer, Cangshan Xu, Travis Taylor, and Daniel M. Neumark, (manuscript in preparation).

8. "Rotationally Resolved Resonant Multi-Photon Detachment Spectra of C_4^-", Yuexing Zhao, and Daniel M. Neumark, (manuscript in preparation).

9. "Study of the low-lying electronic states of GaAs and GaAs⁻ using negative ion photodetachment spectroscopy", Yuexing Zhao, Esther de Beer, Caroline C. Arnold, Cangshan Xu, Gordon R. Burton, and Daniel M. Neumark, (manuscript in preparation).

10. "Observation of many-body effects in Ar_nBr^- (n=2-9) and Ar_nI^- (n=2-19) clusters via anion zero electron kinetic energy spectroscopy and threshold photodetachment spectroscopy", Ivan Yourshaw, Yuexing Zhao, and Daniel M. Neumark, (manuscript in preparation).